

L . . . OF . . . BY . . . ES ON PL . . .  
17 OCTOBER 1980 . . . V. I. BAZHENOV AND M. I. OSIN . . . 1 OF 3

FOR OFFICIAL USE ONLY

JPRS L/9351

17 October 1980

# Translation

LANDING OF SPACE VEHICLES ON PLANETS

By

V.I. Bazhenov and M.I. Osin

**FBIS**

FOREIGN BROADCAST INFORMATION SERVICE

FOR OFFICIAL USE ONLY

NOTE

JPRS publications contain information primarily from foreign newspapers, periodicals and books, but also from news agency transmissions and broadcasts. Materials from foreign-language sources are translated; those from English-language sources are transcribed or reprinted, with the original phrasing and other characteristics retained.

Headlines, editorial reports, and material enclosed in brackets [ ] are supplied by JPRS. Processing indicators such as [Text] or [Excerpt] in the first line of each item, or following the last line of a brief, indicate how the original information was processed. Where no processing indicator is given, the information was summarized or extracted.

Unfamiliar names rendered phonetically or transliterated are enclosed in parentheses. Words or names preceded by a question mark and enclosed in parentheses were not clear in the original but have been supplied as appropriate in context. Other unattributed parenthetical notes within the body of an item originate with the source. Times within items are as given by source.

The contents of this publication in no way represent the policies, views or attitudes of the U.S. Government.

COPYRIGHT LAWS AND REGULATIONS GOVERNING OWNERSHIP OF MATERIALS REPRODUCED HEREIN REQUIRE THAT DISSEMINATION OF THIS PUBLICATION BE RESTRICTED FOR OFFICIAL USE ONLY.

FOR OFFICIAL USE ONLY

JPRS L/9351

17 October 1980

## LANDING OF SPACE VEHICLES ON PLANETS

Moscow POSADKA KOSMICHESKIKH APPARATOV NA PLANETY (Landing of Space Vehicles on Planets) in Russian 1978 signed to press 16 May 78 pp 1-160

[Book by Vladimir Ivanovich Bazhenov and Mikhail Ivanovich Osin, Mashinostroyeniye, 2,500 copies, 160 pages, UDC 629.875.001]

### CONTENTS

Annotation .....	1
Preface .....	1
PART 1. Landing of Space Vehicles on Planets With an Atmosphere.....	2
Chapter 1. Characteristics of Descent to Planets With an Atmosphere	3
Chapter 2. Problems Characteristics for the Return to Earth From Near-Earth and Interplanetary Space Flights .....	28
Chapter 3. Choice of Design-Ballistic Parameters for Landing Vehicles of Martian Planetary Systems .....	49
Chapter 4. Analysis of Trajectory Characteristics for Controlled Entry and Descent Into the Atmosphere of Venus .....	64
Chapter 5. Determining Design Parameters for Descent Vehicles to Sound the Atmosphere of Jupiter.....	71
PART 2. Methods for Studying Soft Landing of Space Vehicles on Planets Lacking Atmospheres.....	81
Chapter 6. Theoretical Analysis of Soft-Landing Dynamics and of Space Landing Vehicles .....	82
Chapter 7. Theoretical Foundations for Physical Modeling of Soft Landing .....	105

- a -

[I - USSR - A FOUO]

FOR OFFICIAL USE ONLY



FOR OFFICIAL USE ONLY

Chapter 8. Experimental Studies of Soft Landings Using Dynamically Similar Models of Space Landing Vehicles .....	129
Chapter 9. Peculiarities of Terrestrial Experimental Development of Soft Landing With the Aid of Full-Scale Mockups of Space Landing Vehicles .....	152
Chapter 10. Several Results of Theoretical and Experimental Studies of Soft Landing .....	164
Bibliography .....	196

- b -

FOR OFFICIAL USE ONLY

FOR OFFICIAL USE ONLY

ANNOTATION

[Text] This book explores problems encountered by developers of space vehicles for descent and landing in studying vehicle structure and conditions of motion. Methods for the parametric calculation of different types of descent vehicles are presented, the problem of searching for optimal parameter values is formulated, and methods of physical modeling are described.

Analytical methods of studying the dynamics of soft landing are presented. The results of applying these methods are fully acceptable for practical engineering computations in terms of accuracy and scope. The book can be useful to designers of space vehicles, to scientists, and to those engaged in studying problems of descent and landing, as well as for graduate and undergraduate students of institutions in the appropriate specialties.

PREFACE

The book is devoted to problems of space vehicles descending to and landing on planets. Success of space engineering in this direction is obvious; man-made space vehicles are landing on the Moon, Venus, and Mars and returning successfully to Earth from orbits and interplanetary trajectories.

Current publications at home and abroad describe methods for calculating trajectories, gas dynamics, and heat transfer during the motion of a space vehicle through the atmosphere. As a rule, these books contain techniques and algorithms that require laborious numerical computational procedures to determine even some of the parameters of such space vehicles. Unfortunately, it is impossible to describe precisely all operations in the process of space-vehicle design and it is necessary in practice to search for analogies and general guidelines in the construction of new space vehicles. Methods of approximate parametric design estimates based on simplified computational models and on the results of experiments using methods based on the theory of similarity and dimensional analysis must be used to determine configuration of space vehicles working under new and unusual conditions.

Obviously, it is impossible to encompass the diversity of problems connected with landing on a planet and returning to Earth within the limitations of a single book. Even a brief enumeration of these problems with a description and formulation of the basic tasks to be carried out during the design and ground-based development of various landing vehicles would require a multi-volume monograph. The authors of this book have therefore limited themselves to considering only the basic questions connected with the design of future descent and landing vehicles and with the illumination of problems that have to be solved in the near future.

FOR OFFICIAL USE ONLY

Problems of descent into the atmospheres of various planets are treated in Part 1, which also presents the results of calculations of design and research tasks connected with determining the configuration and motions of descent vehicles. In particular, for descent to Earth, the conditions of motion based on load-factor criteria for piloted space vehicles are substantiated for entry into the Earth's atmosphere at hyperbolic velocity, and an approximate mathematical model is proposed for calculating a controlled descent trajectory. By using parametric computations, optimum loading on lifting surfaces suitable for a descent to Mars is determined; for Venus, optimal descent trajectories are determined based on the conditions at transition to the subsequent descent into denser layers of the atmosphere; and modern concepts have been formulated for design phase calculations of the characteristics of a planetary sounding vehicle for a descent to Jupiter.

Problems associated with space vehicles making contact with the surfaces of planets and the related problems of landing-gear design can, to a certain known degree, be separated and considered independently of the problem of motion in the atmosphere and during the touchdown braking phase. Part 2 of the book is devoted to the set of problems that arise during the development of landing gears, including theoretical methods of calculating the dynamics of soft landing, methods for modeling and designing support kinematics, designing shock absorbers, and improving the stability of landing systems, and the experimental verification of theoretical results using full-scale mockups and dynamically similar models.

Part 2 of the book substantiates the techniques for the physical modeling of soft landing under Earth conditions. The derivation and analysis of conditions of similarity are presented, which are necessary for the simulation of processes of landing on the Moon and other planets. Such simulations are required for the ground-based development of landing vehicles.

The book can be useful to specialists in designing and developing landing systems for lunar, Venusian, Martian, and other descent vehicles, to those studying the specific problems of the mechanics of landing and thermodynamics of descent, and to students of appropriate specialties.

The authors are grateful to candidates of technical sciences A. F. Yevich and R. P. Belonogov for useful counsel and the comments they made in reviewing the manuscript, and to engineers A. I. Goncharov, A. I. Burtsev, Yu. V. Zakharov, and V. F. Malykhin for help in preparing manuscript materials for publication.

The authors will gratefully accept all comments that readers might have about this book.

FOR OFFICIAL USE ONLY

PART ONE

LANDING OF SPACE VEHICLES ON PLANETS  
WITH AN ATMOSPHERE

This portion of the book is devoted to problems of space-vehicle descent through the atmospheres of Earth and planets. The wide circle of specialists is familiar with books and texts that present methods for computing and generalizing the problems of thermodynamics of descent (for example, Refs. 1, 20, 40, 43). In these works, the emphasis is on obtaining approximate relationships of a general character suitable for qualitative conclusions at the preliminary design stage of analysis. The methods and results of analytical assessments presented in this literature are no doubt useful to persons beginning to study the problems of motion of traditional descent vehicles in an atmosphere.

However, space engineering continues to develop; new vehicles use modern technology and employ many different specialists. These specialists need more than just general information on ballistics and thermodynamics of descent; they are interested in the professional aspects of designing new flight vehicles. It is just for this reason that the present book attempts to throw light on the problems of designing future descent vehicles. The characteristics of descent to each of the planets are considered within only one of the two parts, with the authors intentionally limiting themselves to the exposition of general relationships and basics and to specific engineering aspects of descent under conditions characteristic for each planet. The goal was to capture the problem as a whole, to compare the various possible engineering solutions for each type of descent vehicle, and to establish the general outline inherent to the conditions of motion and shape of future descent vehicles.

Part 1 of the book explores questions of selecting the descent mode and calculating design characteristics of future descent vehicles. To start with, the design features peculiar to descent vehicles and which differ from those of other component systems of space rocket systems are presented in generalized form. The typical design search problem that has to be solved in any mechanized design at the top level of research and design selection is described, that is, in an automated synthesis of the configuration and structure, with consideration given to the conditions of motion in the atmosphere. Methods and results of analysis of the conditions of motion are considered as they apply to the requirements of modeling future vehicles with weight as the control parameter. Such vehicles, in the authors' opinion, include reusable space rocket systems that return to Earth, as well as vehicles for landing on Mars or returning to Earth after an interplanetary expedition. The problem of descent for heavy controlled automated planetary systems to study Mars and Venus and questions of automated sounding of the Jovian atmosphere are decidedly of interest.

All of these problems, to some detail, are sequentially illuminated in Part 1 of the book.

Thus, we will start with the characteristics of descent vehicles that determine the specifics of designing them, in contrast to the design of other space vehicles.

FOR OFFICIAL USE ONLY

## CHAPTER 1

## CHARACTERISTICS OF DESCENT TO PLANETS WITH AN ATMOSPHERE

Landing on planets with an atmosphere or returning to Earth from space is one of the most complex and important stages of space flight. The task of the descent vehicle is to land on the surface of a planet or to return to Earth with some payload. In landing on a planet, the payload consists of the scientific research equipment; with returning to Earth, it can be the fruits of a particular flight program. For manned space vehicles whose payload is the crew and passengers either returning from space or about to land on a planet, the period of descent through the atmosphere represents one of the most critical stages of the expedition. This is because the descent vehicle experiences the extreme effects of space flight. The descent vehicle, as well as orbiting vehicles and interplanetary and planetary space vehicles, operate under conditions of vacuum, weightlessness, solar radiation, and meteoric erosion. However, all these effects, common to all space objects, assume a secondary significance compared to the effects of the atmosphere during descent. Approach to the planet and descent into its atmosphere occur with a speed several times higher than the flight of even the fastest aircraft, and deceleration from that speed is accomplished by aerodynamic braking in the atmosphere. The inertial forces acting on both structure and crew during such braking exceed their weights; heat-shielding of the vehicle protects its airtight cabin from powerful heat flows that emanate from the shock layer of the gas, heated at the forward part of the vehicle to several thousand degrees. Besides static loads, the vehicle experiences vibration and shock loads. The process of braking in the atmosphere is, as a rule, short-lived; however, large gradients in load factor, altitude, flight velocity, heat flow, and temperature in the various parts of the structure appear during braking. The extreme loads thus are the first difference between descent vehicles and other types of space vehicles.

The enumerated characteristics of the process of descent through an atmosphere define yet another difference between descent vehicles and other component systems of space vehicles. These characteristics make considerable demands on the reliability of all systems of the descent vehicle. Thus, while it is possible to abort a flight and return to Earth to save crew and payload, or to evacuate a crew with the aid of a supply space ship, it is almost impossible to rescue the crew from the airtight cabin of a descent vehicle in an emergency during the braking phase of flight in the atmosphere. Let us note that rescue from orbit or from a trajectory of injection into orbit depends on using the very same descent vehicle, and the probability of failure of the descent and landing systems thus determines the safety of flight. Thus, the reliability of the descent and landing systems has to be higher than the reliability of other subsystems and ships of the space rocket system.

The third differentiating characteristic of descent vehicles is determined by the rigid weight limitations placed on the entire space rocket system.

FOR OFFICIAL USE ONLY

## FOR OFFICIAL USE ONLY

As a rule, descent vehicles operate in the concluding phase of space flight and each excess kg of weight is equivalent to several kg of weight in the propulsion systems of the mission system or tens of kg in the initial weight of the booster. For this reason, problems of optimizing the descent and landing system by using the weight criterion are important. Also, problems of minimizing the descent and landing system weight are complex and interesting and require a detailed account of the interplay between the conditions of motion and the configuration of the vehicles. These relationships determine the fourth difference of descent vehicles from orbital and interplanetary ships and stages, namely, the complex dependence of weight characteristics on those geometric parameters that determine the form of the descent vehicle. These parameters determine, on one hand, the distribution of the heat flows and mass of the thermal protection system and, on the other hand, the lift and braking characteristics of the vehicle, which characteristics, in turn, determine the duration, thermal resistance, and load-factor regimes of the descent trajectory, and, in the final accounting, determine the total mass of structure, heat shield, and fuel of the propulsion system for braking and control.

Only an integrated approach to the problem of optimizing the geometric, component, and weight-propulsion parameters of descent vehicles can guarantee the achievement of reliable results in choosing optimal design solutions. Unfortunately, as frequently happens, erroneous conclusions are drawn about the advantages of one or another vehicle configuration during the detailed analysis of nonrelated problems in ballistics, control, or aerodynamics. If the optimizing of descent-vehicle parameters is based on a weight criterion, then the computational model has to provide procedures for describing the configurations, for estimating aerodynamic and centering characteristics, for modeling of the conditions of motion and heat exchange, and for estimating the weights of the structure, heat shield, and landing system, while also considering vehicle loading, detail features, and the requirements placed on the landing site. For each type of flight vehicle, the computational model is constructed differently, and design criteria and limitations are accounted for differently. Examples are shown in subsequent chapters of this book of how allowances are made for limitations placed on vehicles designed for different missions. It is possible to point to several general principles for constructing computational models and to attempt to unify the general statement of the problem of optimizing parameters of different types of descent vehicles. It is assumed that use is made of numerical search methods during optimization and that the choice of design parameters is made using a system for the automated synthesis of descent-vehicle configurations.

The typical algorithm for design or verification calculations used in a system of automated search and selection of design solutions for descent vehicles as a whole must necessarily include the following specialized computational models:

1. A module or group of modules for describing the vehicle configuration, for mathematical modeling of contours, and for computation of dimensional,

FOR OFFICIAL USE ONLY

volumetric-centering, and layout characteristics. For simply-shaped vehicles formed by combining several geometric shapes, a special computational routine has to be provided for the calculation of dimensions, areas, and volumes.

As a rule, the group of modules describing the configuration is combined with a special procedure for generating the vehicle shape by using graphic information display devices (graphic displays, plotters, or digital printing devices).

2. A group of modules for the calculation of aerodynamic characteristics. Different modules are, as a rule, created for different classes of shapes and different regimes of flow.

3. Modules and routines for the computation of the conditions of motion. These routines can differ by the degree of detail in design estimates, they can use different principles and procedures of calculation, and they can form part of the modules for computing aerodynamic and weight-power characteristics.

4. Modules for cumulative calculation of weight-power characteristics. These modules process and summarize information for judging the appearance of the vehicle as a whole. Depending on the formulation of the design search problem, it is possible to include, as part of these modules or separately, procedures for strength calculations, thermodynamic calculations, computations of dynamic processes, estimates of cost, synthesis of design layout, and so forth.

All parameters determining the appearance of a typical descent vehicle can be divided into several groups. The first group ought to contain geometric characteristics that determine the external contour of the body. Parameters in this group are continuous and represent the starting point for calculating aerodynamic characteristics and, therefore, largely determine the ballistic design parameters and the thermal stress for the trajectory, as well as the flow regime around the body and heat exchange in the different zones of the vehicle's surface. The second group should contain parameters that describe the control of motion. Among them are the coefficients that shape the programmed change in the angle of attack or roll, or indicators that determine the instant of transition from one to another type of control, for example, motion along a constant altitude, constant load factor, or constant temperature trajectory.

The third group of design parameters includes the weight-power and design-layout characteristics of the descent vehicle. These are primarily dimensions of the structural elements and of the thermal protection system, power plant parameters, and data that determine the location of compartments and assemblies onboard the vehicle. Among these parameters can be those that change discretely or assume only integer values.

FOR OFFICIAL USE ONLY

## FOR OFFICIAL USE ONLY

The situation becomes more complicated when, combined with an automated search for configuration and structure of the descent vehicle, different internal layout schemes and various arrangements for the instruments and assemblies forming part of the onboard systems are reviewed.

The variables in such a problem of optimization are the configuration parameters whose integer values correspond to certain variants of layout or schematic solutions. In this case, the task of an automated synthesis of the structure of the vehicle is formulated as a problem of discrete programming for whose solution specialized search methods are used as described in Ref. 23, which also contains the formulation of the problem of synthesizing the structure of a space vehicle. In the same book, examples are taken from the practice of space-vehicle design in order to explore the solution to the problem of optimal design through the use of a system of automated search and selection of configurations, descent trajectories, design, and weight-power parameters for different types of descent vehicles. For this reason, we will limit ourselves here to a description of the general formulation for the problem of searching for design parameters of descent vehicles. We will present several of the most interesting applications of design calculations and results from such a search and show the chosen conditions of motion and configuration of future descent vehicles.

The common, most typical problem of search for geometric and trajectory parameters is usually solved at the initial design stage and determines the appearance of the descent vehicle. Only continuous parameters that belong to the first and second groups are varied and their values, corresponding to the minimum of a weight index, are determined. This index can be the mass of the vehicle or the mass of the descent and landing equipment. The question of criteria that determine the goodness of the vehicle in terms of weight will be posed below as part of the discussion on descent-vehicle payload. The simultaneous optimizing of vehicle shape and of the conditions of motion is usually formulated as a problem in nonlinear programming and is solved with the aid of known numerical search methods based on a stepwise progression through the parameter space to arrive at the optimum variant. The values of the design parameters for a descent vehicle determine the state vector of the system to be optimized:

$$\bar{X}(X_1, X_2, \dots, X_1, \dots, X_n).$$

To each value  $\bar{X}^{(k)}$  of this vector corresponds a value  $F^{(k)}$  of the object function  $\phi(\bar{X})$  and the values

$$y_1^{(k)}; y_2^{(k)}, \dots, y_j^{(k)}, \dots, y_m^{(k)}$$

of the functional constraints  $Y_1(\bar{X}), Y_2(\bar{X}), \dots, Y_j(\bar{X}), \dots, Y_m(\bar{X})$ . Here the vector  $X$  is defined over the set  $R$ , which is constrained due to the range of variation of each variable determined by inequalities of the type:

$$B_i \leq X_i \leq A_i \quad (\text{constraints of the first type}) \quad (1.1)$$



## FOR OFFICIAL USE ONLY

and also due to the functional constraints, that is, due to inequalities of the type

$$Y_j(X) \leq y_{j,0} \quad (\text{constraints of the second type}) \quad (1.2)$$

The goal of the optimization is to find the best value of the criterion  $F_{opt}$  for  $\bar{X} \in R$ . The goal of the search is broader and can result in finding a whole family of suboptimal solutions. It is among these solutions, which are close to optimum but differ from it by a number of additional properties and attributes that cannot be formulated, that the developer will look for the best variant for the vehicle design applicable to the design limitations established. By choosing a design variant at the current level of the state of the art, the designer must know to what degree he departs from the strictly optimum solution according to each criterion.

The general goal of design research is broader, and it results in determining the relationships between optimal or suboptimal solutions and the basic initial data and constraints.

In choosing descent-vehicle design parameters, it is necessary to deal with a number of criteria that in part are contradictory. As a rule, one of them determines the achievement of weight goals, a second may target a specific problem, for example, the achievement of maximum cross range, a decrease in load factor, or a decrease in the flight velocity at the end of the descent trajectory before landing. The problem of searching for the best values of descent-vehicle parameters is thus divided into a number of partial problems of optimization, for each of which one of the best solutions for a given criterion is determined with other criteria being considered as constraints.

By letting an optimum "drift" along fundamental constraints, the bounding sets of optimum solution are determined, that is, the bounding relationships of the best solutions in terms of each criterion are found while values of the other criteria are held constant.

Among the criteria or constraints in problems of searching for the best values of descent-vehicle parameters can be indices of weight or mass for the whole vehicle, expenditures of the working medium from systems of attitude control and braking, the value of characteristic velocity of the propulsion systems, speed of flight at a given altitude, or altitude of flight at a given speed, load factor, drag, effect of load factor on the crew, cross range or trajectory turn angle, flight range, temperature, specific heat flows, or erosion of the surface layers at the heat-stressed points of the vehicle, thickness or strength of the heat shield, time of flight, or time of flight through the atmosphere. The choice of criteria and constraints is determined by the specific search problem and depends on the particular mission of the vehicle. The mission of the vehicle determines the method for controlling motion, the type of structure, and class of shapes to be considered in searching for the vehicle configuration.

FOR OFFICIAL USE ONLY

In spite of the brevity of the development period of space engineering, there exists at present a variety of descent vehicles, and this variety produces the need for some kind of classification. The authors do not pretend to have an all-inclusive and definitive system for classifying descent vehicle attributes and grant that there are other ways of grouping descent vehicles into classes and groups; in the future, one ought to expect a more substantiated approach to the classification of descent vehicles.

It is possible, for example, to group descent vehicles arbitrarily according to the character of their payloads, and this will be our first attribute for their classification. The presence of man on board the vehicle, or, more correctly, the presence of systems that provide for his ability to live, work, and participate in the control of the mission, substantially influences the composition of the payload, which then is reflected in the appearance of the vehicle and in the trajectories of descent and landing. Descent vehicles developed for automatic flight can be designed for substantial load factors, as a result of which the requirement for controlled descent and high lift capability of the aerodynamic shape is removed.

The mission of the vehicle should probably be the second classification attribute. The shape of the vehicle depends on the conditions of entry into the atmosphere, on the parameters of the atmosphere and gravitational field of the planet, and on the schedule of operations to be performed during descent and landing.

An additional subdivision according to specific purpose and flight conditions is possible for vehicles intended for operations close to a particular planet. Descent vehicles can enter the atmosphere either from an approach trajectory with hyperbolic velocity or from a low orbit around the planet. In either case, different requirements on the lifting properties of the vehicle frequently arise. In addition, descent vehicles can either penetrate the atmosphere and deliver a payload, or dive through it and return to an orbit around the planet or to a departure trajectory. In the first case, delivery is made to either the surface, in which case a special landing gear is used, or to a predetermined altitude in the atmosphere of the planet.

The external appearance of the vehicle, its configuration, and conditions of motion in the atmosphere depend to a great extent on the manner in which the lift capability of the aerodynamic shape is used. Here we have in mind the maximum attainable lift-to-drag ratio, that is, the available lift-to-drag ratio of a given shape for the assumed layout and centering characteristics. In flight, the vehicle can be trimmed at some angle of attack to produce a lift-to-drag ratio less than the available one.

The relationship between the lifting and braking properties will serve as a third attribute for classification, according to which descent vehicles can arbitrarily be divided into five categories: Vehicles for ballistic descent (with zero lift-to-drag ratio); vehicles with low lift-to-drag ratios ( $K < 0.4$ ); vehicles with modest lift-to-drag ratios ( $K = 0.4-0.7$ ); vehicles

FOR OFFICIAL USE ONLY

FOR OFFICIAL USE ONLY

with significant lifting capabilities ( $K = 0.7-1$ ); and gliding vehicles with high lift-to-drag ratios.

Ballistic descent vehicles, in turn, can have different braking capabilities and two limiting configurations: A shape with a large aerodynamic braking device (as a rule, this is a blunt heat shield) or a pointed shape with high midsection load factor.

There are many methods of classifying aerodynamic shapes having a modest to large lift-to-drag ratio. The classes are obtained by means of transforming various initial configurations to combine several bodies or various conic and spheric shapes. The variety of all conceivable shapes tasks one's ability to count them.

Comparisons of different classes of aerodynamic shapes are useful only in terms of applications to vehicles for specific missions at a given level of the required lift-to-drag ratio.

One of the widespread means for classifying descent vehicles according to the method of flight in the atmosphere is based on the differences in control used during the main segment of the descent trajectory. Descent vehicles can perform a noncontrolled ballistic descent as used in automated vehicles; they can vary the amount of braking either gradually or in steps during the flight, thus controlling the descent trajectory without requiring lift; they can, for a given constant lift that corresponds to the trim angle of attack, change its projection onto the vertical, by controlling the roll angle, that is, by turning about the velocity vector; and, finally, they can change the magnitude and direction of the lifting force by controlling the angles of roll and attack during the flight. Roll control can be achieved relatively simply for blunt-shaped vehicles with a low value of the available lift, inasmuch as rotation about the velocity vector can be achieved with gas jets and without changing the balance of the vehicle. Such a descent, which has been called "slipping," was used for the Soyuz and Apollo spacecraft.

And finally, the various types of descent vehicles can also be divided according to structural attributes, which determine the principle of operation of individual descent and landing systems.

Depending on the manner in which structure and thermal protection of descent vehicles are used, they can be of the single- or multiple-use varieties, with multiple-use descent vehicles, in turn, subdivided according to thermal protection method ("hot structure," ablative thermal protection, thermal protection using heat-sink or radiating screen, and so forth).

The landing systems of descent vehicles also influence their appearance and can be used to differentiate one from another. Thus, we differentiate between devices for prelanding braking and shock-absorbing devices for soft landings. For the latter, use can be made of landing gears with different

FOR OFFICIAL USE ONLY

FOR OFFICIAL USE ONLY

energy absorbers in the support mechanism, inflatable balloons, or soft-landing thrusters, which provide a vertical impulse at the moment of contact with the surface. The prelanding maneuver devices and braking systems can consist of wings, liquid-propellant rockets, turbojet or turbofan power plants, rotor systems with different methods of driving the blades, parachute and paraballoon braking devices, and collapsible soft-envelope wings with either an inflatable or a rigid airframe.

There are many other ways for differentiating among descent vehicles by structural features of individual systems. Let us now try to define general criteria for comparing descent vehicles intended for the same mission, that is, let us make the transition from the attributes that separate different descent vehicles to the attributes that unite them.

One of the basic nondimensional criteria used in comparing descent vehicle characteristics is the weight criterion for descent and landing systems. The widely-used form of the weight criterion for the descent and landing system, namely, the ratio of the weight (mass) of the descent and landing system,  $G_{CC\Pi}$ , to the total weight (mass) of the vehicle,  $G_0$ , is not correct, inasmuch as the total weight of the vehicle already includes the weight of the descent and landing system. Only the ratio of the weight of the descent and landing system to a reference weight, fixed for all variants of descent vehicles, can objectively describe the weight improvement of the vehicle. Such a reference weight could be the weight (or mass) of the payload,  $G_{\Pi\Pi}$ .

Thus, if for two vehicles the weight efficiency, that is, the ratio  $G_{CC\Pi}/G_0$ , is 50 percent and 70 percent, and at first glance the difference is only 20 percent of the total weight, in actuality, for given uniform constraints placed on the weight of the descent vehicle in terms of total weight of the space system, we have to reduce the payload weight in the second vehicle by nearly a factor of 2 compared to the first vehicle. The ratio

$$\frac{G_{CC\Pi}}{G_{\Pi\Pi}} = \frac{G_{CC\Pi}/G_0}{1 - G_{CC\Pi}/G_0} \quad (1.3)$$

is 100 percent in the first case and 2.33 percent in the second case. Thus, for an identical payload weight fraction, the true difference in actual payload weight is 60 percent.

The payload for a typical descent vehicle can be conveniently thought of as consisting not only of the scientific equipment to be returned to Earth or delivered to a planet but also all onboard systems, which remain fixed during changes of design parameters of the vehicle, that is, in changing from one variant of the vehicle to another.

In this fashion, the payload includes all that does not form part of the descent and landing system. As a rule, the descent and landing system includes the structure of the airtight cabin, the structure of the glider

FOR OFFICIAL USE ONLY

FOR OFFICIAL USE ONLY

or aerodynamic braking equipment, the thermal protection and thermal insulation, propulsion equipment for attitude control and prelanding braking, and systems that provide for a soft landing. The other onboard systems, namely, the collection of life-support systems, systems for thermal control, power generation, and radio communication, and the instrumentation portion of the control system all form part of the payload of the descent vehicle.

The systems mentioned are arranged in the body of the vehicle, and the manner of distributing them in the various sections of a given configuration determines the volume characteristics and mass properties. One of the non-dimensional criteria, which indirectly reflects the increase in vehicle weight with an increase in its lifting capabilities, is defined by the following well-known formula:

$$K_S = (4.85/S) \sqrt[3]{V_p^2} \quad (1.4)$$

where  $V_p$  is the available volume of the vehicle (in terms of the external outline);  $S$  is the total surface of the vehicle. This criterion represents the ratio of the surface of a given vehicle to the minimum possible surface for the given volume and can be thought of as a kind of efficiency in using the vehicle surface.

For vehicles with a fineness ratio close to unity and without wings or other protruding surfaces, this criterion is close to unity. The typical descent vehicle shape with small or moderate lift-to-drag ratios consists of two bodies: A forward volume and an aft volume (Figure 1.1). The forward volume can be a segment or a blunted cone, either circular or elliptical. The aft volume can be spherical or conical. Both volumes are joined at a common surface, which can arbitrarily be considered to be a plane, and all aerodynamic characteristics can be referred to it. This plane, called the lifting plane, is perpendicular to the plane of symmetry of the vehicle, in which, as a rule, lie the vehicle center of mass and the center of balance of aerodynamic forces.

Aerodynamic forces used for braking and controlling the descent trajectory are basically generated by the surface of the forward body. In the hypersonic regime of flow, aerodynamic forces are generated by the pressure in the stream as it is decelerated by the forward part of the vehicle. The front lifting surface is coated with a thermal protection layer and forms the heat shield or screen. Side surfaces of the aft body lie in the base region (region of blanketing), require less thermal protection, and form the fairing about the payload. The main portion of the required volume of the descent vehicle is formed by the volume of the aft body and its surface is larger than the surface of the heat shield, which results in an advantage of weight, inasmuch as the density of a unit of surface of the heat shield is two to three times higher than the density of a unit of surface of the base fairing.

FOR OFFICIAL USE ONLY

FOR OFFICIAL USE ONLY

The centering characteristics for this type of vehicle can be compared to the layout parameters by using the nondimensional criterion  $K_v$ , which is determined for the design trim condition and for the corresponding location of the resultant aerodynamic force. The criterion used is the ratio between the minimum possible volume that can be cut from the vehicle by a plane in which the resultant force lies and one-half of the total available volume. The minimum possible volume is bounded for this situation by the surface of the vehicle on the upstream side and by a plane containing the resultant force acting normal to the surface of symmetry of the vehicle.

The vehicle's center of mass for the design balance condition is located along the resultant aerodynamic force. If, by using active devices for stabilization and control, the attitude of the vehicle relative to the velocity vector can be controlled before entry into the atmosphere, then, as a rule, there is no requirement on where the center of mass is along the resultant. The same has to hold in the case of descent vehicles whose motion is controlled in accordance with the tasks set.

In any case, whether control is used for reducing the cumulative effect of deceleration to an allowable level (descent to Earth), for shaping a shallow trajectory for approaching the surface with minimum velocity (descent to Mars), or the injection of the vehicle into the descent regime at the highest possible altitude (descent into the atmosphere of Venus), the design conditions for the flight are determined by the method chosen for controlling descent. Any deviation from the desired trajectory due to an off-design entry into the atmosphere by the vehicle with an arbitrary angle of attack has to be avoided, as this will lead to failure to achieve the basic flight objectives. A direct consequence of such an approach in choosing the conditions of motion is the main requirement on the location of the center of gravity: Its location has to be along the resultant aerodynamic force for the design angle of attack, and for insignificant deviations from this angle of attack the vehicle has to be statically stable. Let us agree that by normal direction we will mean the direction parallel to the lifting surface of the vehicle and by longitudinal direction we will mean the direction perpendicular to the lifting surface.

Thus, the longitudinal movement of the center of gravity is, as a rule, unlimited for angles of attack close to the design value. The matter stands differently with displacement of the center of gravity in the normal direction, because here we have to relate the centering of the vehicle to the location of the resultant aerodynamic force, which is almost perpendicular to the lifting surface. For vehicles with a moderate lift-to-drag ratio, such a displacement of the center can cause certain difficulties. If the surface, which passes through the resultant, divides the vehicle volume in half, then the necessary centering can be achieved without any weight loss. On the other hand, depending on the degree to which the required location for the resultant is moved away from the geometric center of the volume of the vehicle, layout difficulties arise and the ballast weight goes up. The criteria stated above indirectly reflect the possibilities that exist for

FOR OFFICIAL USE ONLY

FOR OFFICIAL USE ONLY

some forms of vehicles to use the internal volume to attain improved lift-to-drag ratios. This is particularly important for those cases where the required magnitude of the lift-to-drag ratio approaches 0.5 to 0.7. Achieving such a lift-to-drag ratio with traditional segmented conic forms, which retain a good ratio of surface to volume and a relatively small surface of the heat shield, is difficult for a number of reasons, among them the displacement of the resultant and the attendant poor use of the volume while maintaining the necessary lateral centering.

To improve further the shape of controlled vehicles for entry into the atmospheres of Earth, Venus, and Jupiter at hyperbolic velocities, let us recall the relationship between convective and radiative heat flows and the requirement for more pointed heat shields. In such circumstances, we have to consider shapes with conic heat shields in a zero angle-of-attack flow.

By replacing the segmented shield of traditional segmented-conic shapes in a zero angle-of-attack flow (Figures 1.2, 1.3) by a shield shaped like an obliquely-cut elliptical cone, a shape will result that has the same volume and surface as the segmented cone but with a number of advantages. The main advantages are: Increased lift-to-drag ratios for given angles of attack; smaller angles of attack of the lifting surface for equal lift-to-drag ratios; lower structural weight for the lifting envelope of the heat shield and lower weight of the thermal protection system in those cases where the radiative heat flows from the shock layer exceed the convective ones (for vehicles entering the atmospheres of Earth, Venus, and Jupiter at hyperbolic velocity); and a more advantageous location of the resultant aerodynamic force from the point of view of the required lateral centering.

The latter circumstance becomes especially important in those cases where it is necessary to achieve a higher value of the lift-to-drag ratio ( $K = 0.7$  to  $0.8$ ). Obtaining such ratios in a shape with a segmented shield (Figure 1.4) is difficult, due to the rigid requirements on the location of the center of gravity, which has to follow the resultant in moving to the upstream side of the generatrix of the payload fairing.

The centering advantages of the shapes considered can be seen in Figure 1.2, where the initial and transformed shapes and the location of the resultant for various angles of attack, corresponding to lift-to-drag ratios of 0.3 and 0.4, are shown.

These advantages are even more apparent for shapes intended for achieving higher values of the lift-to-drag ratio ( $K = 0.7$  to  $0.8$ ). One of the possible nonsymmetrical segmented-conic shapes and a bi-conic shape are shown in Figure 1.4. They were generated by substituting an obliquely-cut elliptical conic shield for the segmented heat shield.

The curves in Figures 1.3 and 1.5 show the aerodynamic characteristics for different angles of attack of the initial and resultant shapes and demonstrate the first two advantages of the new shapes. We must mention another

FOR OFFICIAL USE ONLY

FOR OFFICIAL USE ONLY

advantage of the bi-conic form, in which the axis of the forward cone, which forms the surface of the heat shield, is parallel to the velocity vector of the impinging flow. The heat shield is in a flow at zero angle of attack, and for such a symmetrical flow it is fairly easy to calculate the aerodynamic characteristics and the parameters that determine the heat transfer at the surface of the heat shield. For vehicles that have to fly in night conditions and particularly for those entering the atmospheres of Earth and planets at hyperbolic velocities, the latter advantage is considerable.

Zero angle-of-attack flow implies that the forward cone has to be elliptical with its oblique cut either elliptical or circular, as, for example, in the shape shown in Figure 1.2. Fairings in the base regions of vehicles are, as a rule, circular cones. Thus, these difficulties in production engineering of the fuselage and application of thermal protection surfaces are peculiar only to heat shields with the new shapes.

Neither can we remain silent about such a property of the above bi-conic shapes as their ability to preserve centering characteristics while the lift-to-drag ratio is increased. The derivatives  $dK/d\alpha$  and  $dK/dY_T$  for these shapes are significantly larger than for segmented-conic ones. If we consider the influence of the scatter in centering properties on aerodynamic characteristics of the finished product, then the mentioned property has to be classified as a shortcoming. If, however, we consider the system for controlling centering before flight as part of the flight process, or if we consider a property such as adaptation of shape and layout to changing regimes of balancing (as, for example, for increasing the available lift-to-drag ratio) as important to the design process, then the property indicated has to be considered an advantage.

To avoid repeating descent trajectory calculations when changing the mass or dimensional properties of a vehicle without changing the vehicle shape, it is useful to develop a method that permits the determination of the trajectory characteristics without having to integrate the equations of motion, if the descent control is known only in general. Such estimates are also needed in problems of optimizing vehicle shape when the type of descent trajectory is known, that is, the variation of load factor is known as a function of time or as a function of flight velocity. In the above-mentioned problems of optimization for each variant of descent vehicle considered, a design calculation is done that culminates in estimating the weight characteristics of the descent and landing system for different constraints. An iterative procedure is used to determine the weight during design calculations, because, in order to determine weight, it is necessary to know the descent trajectory, which, in turn, makes it necessary to know the loading on the lifting surface, which, in turn again, depends on the weight of the vehicle. Also, the computational cases for the majority of descent and landing systems consider the extreme conditions of flight. The determination of extreme conditions of load factor, heat flow, temperature, time, and range of flight is dependent on a series of iterations, in each of which a specific descent trajectory is calculated.

FOR OFFICIAL USE ONLY



FOR OFFICIAL USE ONLY

The material presented above dictates the basic need for methods to permit economical use of machine time and approximate determination of trajectory parameters. Known methods (Refs. 6, 20, 40) are not convenient for design purposes, as they do not give values for thermal flow loading along the trajectory but only at the end of the calculation. This removes the basic advantage of such methods for purposes of design search; specifically, the opportunity is lost to proceed in these calculations directly to the extreme conditions of flight in terms of load factor and heat transfer. In the proposed method of calculating motion, the type of trajectory is given by a combination of control laws that include constant load-factor laws; programs that, by following the given relationship between load factor and flight velocity, can shape a constant-altitude trajectory or assure that the trajectory will remain within given constraints of temperature and flight range.

The unified sequence of control laws defines a whole set of trajectories, and each trajectory in the set differs only by one design-ballistic parameter, namely, the loading on the lifting surface. The independent variable is flight velocity and, by specifying the switching instants (on the velocity scale) makes it possible to combine all possible trajectories into a single class and to establish general ranges for controlling interactions.

It is sufficient to obtain the variation of speed and altitude of flight as a function of time in order to estimate the parameters of motion, loading, heat flow, and temperatures, and, consequently, ablation and heating of the thermal protection surface.

By integrating the four basic equations of motion, we can determine the indicated relationships with a precision sufficient for design calculations. These equations based on generally accepted assumptions (Refs. 1, 6) and written in the velocity coordinates in a unified form suitable for any planet are

$$\frac{dV}{dt} = -\frac{QV^2}{2P_x} g_3 - g_n \sin \theta; \quad (1.5)$$

$$\frac{d\theta}{dt} = \frac{KQV}{2P_x} g_3 + g_n \cos \theta \left( \frac{V}{g_n R_n} - \frac{1}{V} \right); \quad (1.6)$$

$$\frac{dH}{dt} = V \sin \theta; \quad (1.7)$$

$$\frac{dL}{df} = V \cos \theta, \quad (1.8)$$

FOR OFFICIAL USE ONLY

FOR OFFICIAL USE ONLY

where  $V$  is the flight velocity;  $\theta$  is the flight-path angle with respect to the horizon;  $g_3$  is the free-fall acceleration at the Earth's surface;  $g_H$  is the free-fall acceleration at the altitude of flight in the atmosphere of a given planet;  $R_H$  is the distance from the center of the planet to the altitude at which the vehicle is moving;  $H$  is the altitude of flight;  $L$  is the range of flight;  $\rho$  is the density of the atmosphere, evaluated at the given altitude of flight;  $P_x$  is the loading on the lifting surface. Here  $P_x = G/(C_x S)$  or  $P_x = mg_3/(C_x S)$  where  $G$  is the total weight of the vehicle;  $C_x$  is the drag;  $S$  is the area of lifting surface; and  $m$  is the mass of the vehicle.

It is assumed that the law according to which density varies with altitude of flight is known and that by determining the density we have an estimate of altitude.

The magnitude of the effective lift-to-drag ratio  $K$  at any instant of time determines the control of descent. For a constant angle of attack, the loading  $P_x$  of the vehicle practically does not change along the trajectory and the magnitude of the effective lift-to-drag ratio is determined by the roll angle  $\gamma$  and the available lift-to-drag ratio of the vehicle,  $K_p$ , namely,

$$K = K_p \cos \gamma \quad (1.9)$$

As will be shown in later chapters, the preferable trajectories of motion of future descent vehicles entering the atmospheres of Earth, Mars, and Venus will include leveling-off regimes with constant altitude or constant load-factor plateaus. Transition to the leveling-off regime is achieved after the atmospheric entry segment, that is, after achieving maximum load factor or heat-shield surface temperature. Control during the atmospheric entry phase (permitting flexible response to changes in entry conditions and the attendant change in vehicle characteristics) uses control algorithms or a collection of programmed relationships between load factor and time or between load factor and flight velocity, in order to bring the controlled object to within established load factor and temperature bounds.

In the simplest case, the atmospheric entry phase can be modeled by a linear relationship between load factor and time. By assuming the angle of entry into the atmosphere to be small (controlled descent), we assume  $\theta \approx 0$ ;  $\cos \theta \approx 1$  and  $\sin \theta \approx 0$  in the equations of motion and obtain the following relationships for the flight phase with a constant rate of increase in load factor:

$$V = V_{bx} - \frac{1}{2} c \tau^2 \frac{1}{\sqrt{1 + K_p^2}}; \quad (1.10)$$

FOR OFFICIAL USE ONLY

FOR OFFICIAL USE ONLY

$$Q = \frac{n_{e, \max}}{\Delta \tau_B} \frac{2P_x}{V^2} \tau, \quad (1.11)$$

$$n_i = \frac{n_{e, \max}}{\Delta \tau_B} \tau; \quad (1.12)$$

$$L = V_{BX} \tau - \frac{c}{6\sqrt{1+K_p^2}} \tau^3, \quad (1.13)$$

where  $V_{BX}$  is the velocity of entry into the atmosphere;  $c = (n_{e, \max}/\Delta \tau_B)g_3$  is the gradient of the change in acceleration during braking;  $n_{e, \max}$  is the maximum load factor characteristic for the given entry corridor and the available lift-to-drag ratio of the vehicle;  $\Delta \tau_B$  is the interval of time from the instant of entering the atmosphere (load factor of 0.05 to 0.1 g's) to the instant of experiencing maximum load factor. If, during the period of atmospheric entry, a flexible algorithm is used that permits obtaining a general relationship between the required acceleration and the apparent velocity for all conditions of entry, then a maneuver will result that provides for capture of the vehicle (for motion along the upper boundary of the entry corridor) and injection of the vehicle into a permissible level in terms of load factor or temperature. Let us assume that we are following a linear relationship between the longitudinal acceleration  $\dot{V}_x$  and the apparent velocity ( $V_{BX} - V$ ), that is, a relationship of the type

$$\dot{V}_x = a + b (V_{BX} - V) \quad (1.14)$$

This relationship for the longitudinal acceleration is now substituted into Equation 1.5.

The nominal, or reference, trajectory is common for all conditions of entry, and in such a case is determined by the following equations, obtained by integrating the equations of motion with the condition of Equation 1.14 and using the same assumptions as in the preceding case:

$$V = V_B - \frac{a}{b} (e^{bt} - 1); \quad (1.15)$$

$$Q = \frac{2P_x a e^{bt}}{g_3 \left[ V_{BX} - \frac{a}{b} (e^{bt} - 1) \right]^2}; \quad (1.16)$$

$$n_i = [a + b (V_{BX} - V)] \frac{g_3}{\sqrt{1 + K_p^2}}; \quad (1.17)$$

$$L = V_{BX} \tau - \frac{a}{b} \tau - \frac{a}{b^2} e^{bt} + \frac{a}{b^2}. \quad (1.18)$$

FOR OFFICIAL USE ONLY

## FOR OFFICIAL USE ONLY

Immediately after passing the maximum load factor, that is, at the instant the vehicle is in a state to move further by skipping with a maximum effective lift-to-drag ratio, the trajectory angle approaches zero and then changes sign and becomes positive.

The time interval from the moment of entry into the atmosphere to the instant of passing peak load factor will be designated by  $\Delta\tau_B$ , and flight velocity at this same instant by  $V_B$ . The constant altitude regime of leveling off should be started at this time, as the control program generates an effective lift-to-drag ratio starting with a zero value for the derivative of the trajectory flight-path angle. Taking this into account, we can integrate Equation 1.5 by assuming the density of the atmosphere to be constant. We obtain the following expression for the velocity of flight during the constant-altitude phase:

$$V = [(1/V_B) + (\rho g_3/2P_x)(\tau - \Delta\tau_B)]^{-1} \quad (1.19)$$

The density of the atmosphere during the constant-altitude phase of flight equals

$$\rho = (2P_x n_{\epsilon \max}) / (V_B^2 \sqrt{1 + K_p^2}) \quad (1.20)$$

Load factor is determined from the expression

$$n_{\epsilon} = (n_{\epsilon \max} V^2) / V_B^2 \quad (1.21)$$

The increase in flight range along the trajectory is determined by using the formula

$$\Delta L = L - L_s = \frac{2P_x}{\rho g_3} \left[ \ln \left( \frac{1}{V_s} - \frac{\rho g_3}{2P_x} \Delta\tau_s + \frac{\rho g_3}{2P_x} \tau \right) - \ln \frac{1}{V_s} \right] \quad (1.22)$$

Motion along a constant-temperature trajectory usually begins when the limiting temperature is attained. We will consider that at the instant of transition to the isotherm the flight time is  $\Delta\tau_B$  and the velocity is  $V_B$ . The condition that the equilibrium temperature remain constant means that along this trajectory there is preserved a constant heat flow in the thermally stressed zone of the vehicle. A formula like the following one is usually used to estimate the magnitude of the convective heat flow:

$$q = C_q \rho^m V^n \quad (1.23)$$

We will assume that the magnitude of heat flow will be maintained at the attained value  $q_0$ . With the control system providing for motion along the isotherm, the density of the atmosphere in this case will depend on flight velocity in the following fashion:

FOR OFFICIAL USE ONLY

$$Q = \left( \frac{q_0}{C_q} \right)^{\frac{1}{m}} \frac{1}{V^{\frac{n}{m}}} \quad (1.24)$$

Integration of the equation of motion (Equation 1.5), with the condition of Equation 1.24 and assuming that the flight-path angle is zero, yields the following relationship between flight velocity and time:

$$V = \left[ V_0^{\frac{n-m}{m}} - \frac{n-m}{m} \left( \frac{q_0}{C_q} \right)^{\frac{1}{m}} \frac{g_3}{2P_x} (\tau - \Delta\tau_0) \right]^{\frac{m}{n-m}} \quad (1.25)$$

Load factor as a function of time for a constant-temperature trajectory varies in the following fashion:

$$n_i = \sqrt{1 + K_p^2} \left( \frac{q_0}{C_q} \right)^{\frac{1}{m}} \frac{1}{2P_x} \times \left[ V_0^{\frac{n-m}{m}} - \frac{n-m}{m} \left( \frac{q_0}{C_q} \right)^{\frac{1}{m}} \frac{g_3}{2P_x} (\tau - \Delta\tau_0) \right]^{\frac{2m-n}{n-m}} \quad (1.26)$$

The range for flight along a constant-temperature segment of the trajectory can be determined approximately by the following formula:

$$\Delta L = L - L_0 \approx - \frac{1}{\frac{n-m}{m} \left( \frac{q_0}{C_q} \right)^{\frac{1}{m}} \frac{g_3}{2P_x} \left( \frac{m}{n-m} + 1 \right)} \times \left\{ \left[ V_0^{\frac{n-m}{m}} - \frac{n-m}{m} \left( \frac{q_0}{C_q} \right)^{\frac{1}{m}} \frac{g_3}{2P_x} (\tau - \Delta\tau_0) \right]^{\frac{n}{n-m}} - V_0^{\frac{n}{m}} \right\} \quad (1.27)$$

The constant-load-factor segment begins after the point of leveling off or following flight in the constant-altitude regime. Departure from the isotherm can also be achieved using a constant load-factor trajectory. Assuming that the flight-path angle (between the velocity vector and the local horizontal) is small and assuming a load factor much larger than the

FOR OFFICIAL USE ONLY

FOR OFFICIAL USE ONLY

magnitude of  $g_{\Pi} \sin \theta$ , we obtain the approximate expression for the trajectory parameters for a constant-load-factor plateau;

$$V \approx V_n - \frac{n_s}{\sqrt{1+K_p^2}} g_3 (\tau - \Delta\tau_n); \quad (1.28)$$

$$q \approx \frac{2P_x n_s}{\sqrt{1+K_p^2} V^2}; \quad (1.29)$$

$$\Delta L = L - L_n \approx V_n (\tau - \Delta\tau_n) - \frac{n_s}{\sqrt{1+K_p^2}} g_3 (\tau - \Delta\tau_n)^2, \quad (1.30)$$

where  $L_H$ ,  $V_H$ , and  $\Delta\tau_H$  are the initial values of distance, velocity, and time of flight corresponding to the instant of transition to constant-load-factor flight.

All the above relationships are characteristic for different segments of controlled descent, with the control system using the lift characteristics of the vehicle, shaping a shallow trajectory, and thus implementing a law for varying the load factor as a function of flight velocity.

With the variation of velocity and flight altitude known, it is possible to estimate heat flow and, hence, the required mass of the ablative thermal protection layer.

During the preliminary design stage, when a number of approximate models are used, specific heat flows are computed by correlation formulas. In the general case, correlation relationships for estimating heat flows have the form

$$q_r = k_r q_r^a V^b R^m; \quad (1.31)$$

$$q_k = k_k q_k^c V^d R^n; \quad (1.32)$$

where  $q_r$  and  $q_k$  are the specific radiative and convective heat flows at the stagnation point of the vehicle;  $R$  is the radius of bluntness.

During entry into the atmospheres of Venus and Earth at hyperbolic velocities, radiative heat flows are comparable to convective ones, while during entry into the atmosphere of Jupiter, radiative flows predominate. Under such conditions, the estimation of the optimum radius of bluntness is of some interest at the stage of qualitative analysis of braking in the atmosphere. Finding the optimum radius of bluntness is important for that class of trajectories that have been optimized by using the criterion defining the special problem whose solution determines the conditions of motion. For

FOR OFFICIAL USE ONLY

FOR OFFICIAL USE ONLY

entry into Earth's atmosphere, this problem turns out to be (as will be shown in the next chapter) the search for a minimum integral of load factor; for entry into the atmosphere of Venus, it is the completion of braking in the upper layers of the atmosphere. In this and other cases, trajectories with constant-altitude plateaus are preferred, followed by further shallow descent along a constant-load-factor trajectory. Parameters of trajectories of this type can be determined without integrating the equations of motion; therefore, for vehicles with variable loading on the lifting surfaces, it is possible to estimate an optimum radius of bluntness for different conditions of entry into an atmosphere.

The expression for the optimum radius of bluntness is derived from the condition

$$\frac{d}{dR} (Q_r + Q_k) = 0. \quad (1.33)$$

where  $Q_r$  and  $Q_k$  are the integrated heat flows at the stagnation point.

By considering Equations 1.31 and 1.32, we can determine the optimum radius of bluntness by using the unit integral heat flows, that is, heat flows at the stagnation point with radius 1 m:

$$R_{opt} = \left( -\frac{m}{n} \frac{\int_0^{\tau_k} k_k Q_\infty^c V_\infty^d d\tau}{\int_0^{\tau_k} k_r Q_\infty^d V_\infty^b d\tau} \right)^{\frac{m}{n}}. \quad (1.34)$$

In Figure 1.6, the reader can see a typical variation of the optimum radius of bluntness as a function of speed of entry into the Earth's atmosphere for vehicles with different loading on a lifting surface with the available lift-to-drag ratio equal to 0.6. The curves have been constructed for trajectories corresponding to the lower bounds of the entry corridor with the constraint that after passing through the maximum load factor the conditions of motion correspond to the minimal integrated load factor effect (Chapter 2).

Let us note that the magnitude of the optimum radius of bluntness determined using Equation 1.34 does in no way imply the need to make the vehicle with that exact radius of bluntness but only allows us to assess the correlation of the integral heat flows at the stagnation point for the given type of descent trajectory.

The loss in the total heat flow depends on the optimum radius of bluntness, which is borne out by the curve in Figure 1.7, showing in relative units the magnitude of the loss in the total integrated heat flows for deviations from the optimal radius.

FOR OFFICIAL USE ONLY

FOR OFFICIAL USE ONLY

The true value of the optimal radius of bluntness has to be determined by the mass of the thermal protection material to be ablated and heated at the stagnation point of the heat shield and its vicinity, while also considering the mass of the structure that supports the heat shield.

The magnitude of the radius of bluntness has, as a rule, little influence on the mass of the vehicle. Here the deciding factors are the dimensions of the surface of the heat shield and the general curvature of its surface with respect to the local angles of attack, inasmuch as they determine, on one hand, the drag of the vehicle, its lifting characteristics, and, therefore, the thermal stress of the descent trajectory, and, on the other hand, the mass of the entire shield in terms of the mass-density of a square meter of area.

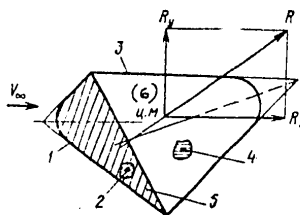


Figure 1.1 General View of Descent Vehicle with Modest Lift-to-Drag Ratio

Key:

1. Heat shield
2. Forward volume
3. Payload fairing
4. Aft volume
5. Lifting surface
6. Center of mass



FOR OFFICIAL USE ONLY

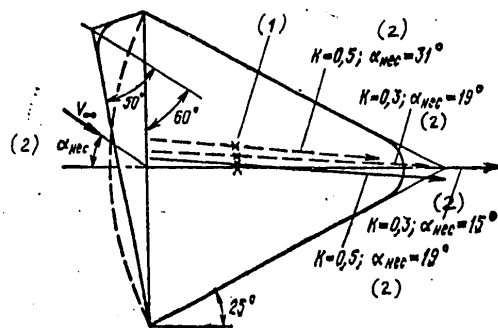


Figure 1.2. External Contours and the Location of the Resultant Aerodynamic Force of Segmented-Conic and Bi-Conic Shapes of Vehicles with Small Lift-to-Drag Ratio

Key:

1. Center-of-mass locations
2. Lifting surface angle of attack
- Vehicle with segmented heat shield
- Vehicle with heat shield in the shape of an obliquely-cut cone

FOR OFFICIAL USE ONLY

FOR OFFICIAL USE ONLY

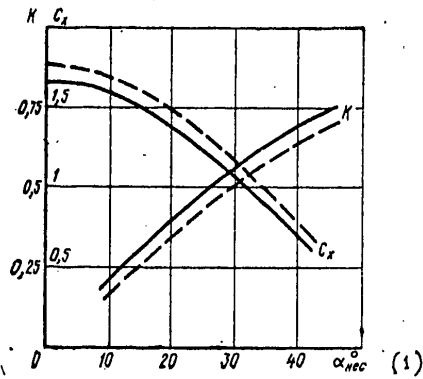


Figure 1.3. Aerodynamic Characteristics of Segmented-Conic and Bi-Conic Shapes at Various Angles of Attack for Vehicles with Small Lift-to-Drag Ratio

Key:

- Vehicle with segmented heat shield
- Vehicle with heat shield in the shape of an obliquely-cut cone
- 1. Lifting surface angle of attack

FOR OFFICIAL USE ONLY

FOR OFFICIAL USE ONLY

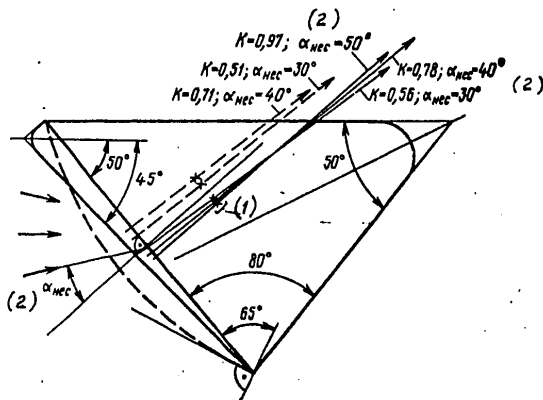


Figure 1.4. External Contours and the Location of the Resultant Aerodynamic Force of Segmented-Conic and Bi-Conic Shapes of Vehicles with a Modest Lift-to-Drag Ratio

Key:

1. Center-of-mass locations
2. Lifting surface angle of attack
- Vehicle with segmented heat shield
- Vehicle with heat shield in the shape of an obliquely-cut cone

FOR OFFICIAL USE ONLY

FOR OFFICIAL USE ONLY

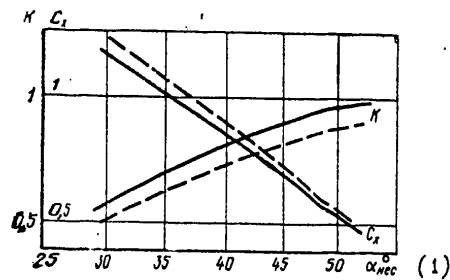


Figure 1.5. Aerodynamic Characteristics of Segmented-Conic and Bi-Conic Shapes at Various Angles of Attack for Vehicles with Modest Lift-to-Drag Ratio

Key:

- Vehicle with segmented heat shield
- Vehicle with heat shield in the shape of an obliquely-cut cone
- 1. Lifting surface angle of attack

FOR OFFICIAL USE ONLY

FOR OFFICIAL USE ONLY

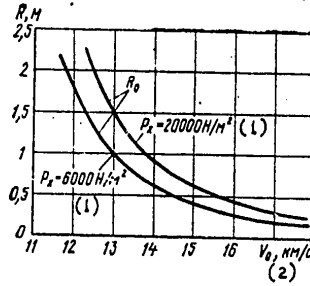


Figure 1.6. Dependence of the Optimum Radius of Bluntness on the Speed of Entering into the Earth's Atmosphere

Key:

1. Loading  $P_x$  on the lifting surface ( $N/m^2$ )
2.  $V_0$  (km/s)

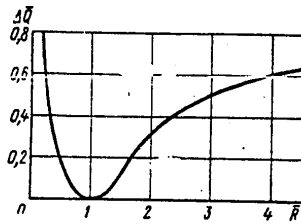


Figure 1.7. Dependence of Total Heat Flow Loss on the Radius of Bluntness ( $Q$  is the heat flow in the bluntness region of radius  $R$ ;  $\bar{R} = R/R_{opt}$ ;  $\Delta Q = (Q - Q_{opt})/Q_{opt}$ )

FOR OFFICIAL USE ONLY

FOR OFFICIAL USE ONLY

## CHAPTER TWO

PROBLEMS CHARACTERISTIC FOR THE RETURN TO EARTH FROM NEAR-EARTH  
AND INTERPLANETARY SPACE FLIGHTS

Most questions related to the development of future descent vehicles deal with problems of descent through the Earth's atmosphere. It is in this atmosphere and in near-Earth space that the majority of new engineering solutions are verified.

The return to Earth for interplanetary, piloted flights is usually related to expeditions involving flight around Mars and Venus, with automated sounding of these planets or landing on the surface of Mars. The velocity of entry into Earth's atmosphere exceeds escape velocity and reaches 16 to 17 km/s. By studying Figure 2.1, we can see how the required magnitude of the lift-to-drag ratio  $K_n$  varies with changes in entry velocity (for a constant maximum total load factor of 10 g's). We also see the variation in magnitude of the maximum load factor  $n_{max}$  for the vehicle (for several constant values of the lift-to-drag ratio  $K$ ). Finally, we also see that the lift capability of the vehicle provides a corridor of entry into the atmosphere with a height of 20 km. The following conclusion can be drawn from calculating the limiting descent trajectories, as generalized in the graph: If we use current estimates of navigation accuracy in the planetary approach portion of the trajectory and if we want to use traditional descent principles (vehicle of modest lift-to-drag ratio with roll control), then we run into load factors during descent whose maximum value will be the same as was experienced during the first flights into space (8-12 g's), with the time of braking in the atmosphere increased by a factor of 2.

If we now turn to the relationship between maximum load factor and time, as, for example, shown in Reference 12 and in Figure 2.2, we can determine by using simple estimates the maximum load-factor effect that can be tolerated by the crew for optimum posture of each crew member with respect to the acceleration vector ( $\sim 78^\circ$  to the spinal column in a chest-to-back direction). The situation is aggravated by the fact that the crew will have become deconditioned due to prolonged flight under weightlessness. In such conditions, the load-factor effect on the crew exercises an essential influence on the choice of the regime for braking in the atmosphere, and to determine the criteria that model the load-factor effect becomes one of the basic tasks of ballistic design research.

Let us first consider those general criteria that describe the maximum permissible level of acceleration. Having seen the relationship between load factor and the limiting time of action (shown in Figure 2.2), we note that the limiting time that man can sustain a certain load factor increases sharply with a decrease in load factor. For example, by reducing the load factor by a factor of 2, from 10 down to 5 g's, the time of tolerance increases from 115 to 650 s, that is, approximately by a factor of 5 to 6. An even more striking change is obtained for a further reduction of the load

FOR OFFICIAL USE ONLY

## FOR OFFICIAL USE ONLY

factor below the level characteristic for the segment of entry into the atmosphere. It is logical to assume that, by having reduced the load factor during the basic stage of braking yet having preserved its maximum value at the moment of entry into the atmosphere, that is, by maintaining the specified corridor of entry for the vehicle with modest lift-to-drag ratio, we will lower the cumulative load-factor effect on the crew.

The quantitative side of the cumulative load-factor effect can be conveniently estimated by introducing the concept of a maximum (permissible) effect impulse  $J_{\Pi p}$ , which is determined as the product of the load factor acting and the limiting time corresponding to this load factor. Determining the effect impulse makes it possible to construct a system of nondimensional cumulative load-factor criteria.

Let us turn to Figure 2.3, which shows two curves for the maximum-effect impulse as a function of load factor, with the lower curve corresponding to a body that has been weakened by the effect of weightlessness. These curves show an interesting relationship, namely: As the velocity of entry into the atmosphere increases, the maximum permissible load factor, that is, the load factor that can be sustained by a body, decreases. Indeed, the dashed horizontal lines in the figure define levels of different required effect impulses that correspond to velocities of entry into the atmosphere of 12, 15, and 17 km/s. The points where the horizontal lines cross the curves of maximum impulse give the maximum load factor for the condition that braking is occurring with a constant load factor of this magnitude, that is, for the condition of isoload-factor braking. It is easy to establish that the maximum load factor for a pilot in top condition drops in this case from 10 g's for a velocity of entry into the atmosphere of 12 km/s down to 8 g's for an entry velocity of 17 km/s (for vehicles that have an available lift-to-drag ratio of 0.5).

The example considered once again shows that in estimating load-factor effects it is not enough to operate solely on the basis of load-factor magnitude but that it is necessary to introduced criteria that, based on the maximum impulse, determine the magnitude of the cumulative load-factor effect.

The relationship between maximum impulse and load-factor magnitude for the optimum posture of the pilot can be approximated by the following formulas:

$$1. \text{ For } 5 < n < 8.67 \quad J_{\Pi p} = 14,000/n - 180 (n - 8) \quad (2.1)$$

$$2. \text{ For } 8.67 < n < 16 \quad J_{\Pi p} = 14,000/n - 120 \quad (2.2)$$

$$3. \text{ For } 16 < n < 20 \quad J_{\Pi p} = 11,500/(n - 0.8) \quad (2.3)$$

FOR OFFICIAL USE ONLY

The decrease in maximum impulse for a body weakened by weightlessness and subjected to conditions of hypokinesia is given approximately by the formula  $J_{\Pi P 0} = (J_{\Pi P} - 450) 0.85$ .

The ratio between the achieved value of effect impulse  $J = n\Delta\tau$  for the constant load factor  $n$  and its maximum permissible magnitude  $J_{\Pi P} = n\Delta\tau_{\Pi P}$  is the basis for the formation of mechanistic nondimensional cumulative load-factor criteria, which account for the accumulation of the load-factor effect with time. If a load factor  $n$  is acting during a brief portion  $\Delta\tau$  of the descent, then the fraction  $m$  of the maximum permissible effect impulse corresponding to this load factor and to the given interval of time will be

$$m = J(n) / J_{\Pi P}(n) = n\Delta\tau / n\Delta\tau_{\Pi P} \quad (2.4)$$

For  $J(n) > J_{\Pi P}(n)$ , that is, for  $m > 1$ , the effect of the load factor will lead to irreversible changes in the body.

By summing the fractions  $m$  of load-factor effects for the separate segments of the trajectory and then integrating in the limit the ratio between load factor and the corresponding maximum permissible impulse, we obtain a nondimensional criterion which is termed the "measure of the cumulative load-factor effect":

$$M = \int_0^{\tau_k} \frac{n}{J_{\Pi P}(n)} d\tau. \quad (2.5)$$

If, for the given method of braking in the atmosphere,  $M < 1$ , then we assume that the cumulative effect is less than the limiting one. This criterion is described in Reference 11. The criterion proposed in a number of works that does not use the concept of a maximum permissible impulse (Ref. 18) has the same physical meaning.

The concept of an effect impulse is methodologically justified inasmuch as tied to it is a construction of more complex criteria that consider the prehistory of the loading process. The matter rests on the fact that the measure of the cumulative effect mechanistically describes the process of accumulating the physiological changes in the human body, as if summing the power of the effect of the loading on the body organs, which are under stress from reacting to the forces of inertia and from external pressure applied by the seat lodgments. Also, this criterion reflects the phenomenon of accumulation of load-factor effects onesidedly, without accounting for the prehistory of the loading process nor for the effect of other load factors on the body. The acceleration effect process is distributed over time, and it is quite significant during which period of loading the body is subjected to the effect of the maximum load factor. We can assume that the form of the load-factor envelope as a function of time influences the

FOR OFFICIAL USE ONLY



FOR OFFICIAL USE ONLY

cumulative load-factor effect. Peak loads at the end of the descent trajectory or repeated peak loads will produce a more severe reaction than the initial load-factor effects at the moment of entry into the atmosphere. The prehistory of the loading process can, to some degree, be accounted for with the aid of a nondimensional criterion that represents the maximum of the ratio between the integral of load factor and the maximum permissible effect impulse corresponding to that load factor. The maximum value of this ratio is chosen from all loads computed in the process. Let us call this criterion the "degree of loading due to load factor impulse," and we will determine it by using the formula

$$C_n^{(J)} = \max \frac{\int_0^{\tau_k} n d\tau}{J_{np}(n)}. \quad (2.6)$$

For  $C_H^{(J)} > 1$ , we should assume that the body has been overstressed, and that for  $C_H^{(J)} < 1$  the degree of residual viability  $C_0^{(J)}$  as a result of action of the load-factor impulse is logically estimated as  $C_0^{(J)} = 1 - C_H^{(J)}$ .

We should note that the criterion considered only incompletely accounts for the loading prehistory, because no information on load-factor gradients nor on how the maximum permissible load factors were reached is used. Therefore, in choosing the descent trajectory by using the cumulative load-factor criterion, the degree of loading is estimated simultaneously with the checking of the maximum permissible load-factor levels, which supplements the basic criterion, which is the measure of the cumulative effect. Determining trajectories that are optimal in terms of load-factor effect is carried out by using numerical search methods and with the optimization problem formulated as a problem in nonlinear programming.

Constraints for this search are: The limiting values of load factor and its gradient, heat flows, ablation of the thermal protection layer, altitude, and speed of flight. These parameters are varied in the course of the search and determine (using apparent flight velocity as the independent variable) the instants of switching from one roll angle to another or the instants of switching to a different load-factor profile, to be followed by the control system.

Two trajectories of atmospheric entry at hyperbolic velocity are shown in Figure 2.4 using altitude and nondimensional flight velocity as the coordinates. One of the trajectories (indicated by the dashed line), which was the initial one in the search, has a short constant-load-factor segment of braking at the maximum permissible load factor, which equals the maximum during atmospheric entry. The figure shows how the cumulative effect grows during the flight. The initial trajectory is optimal in terms of ablative mass and mass of the heat-sink layer. The search computations yielded the

FOR OFFICIAL USE ONLY

FOR OFFICIAL USE ONLY

trajectory shown by solid lines, that is, the trajectory with an extended constant-altitude regime of leveling off, which permits lowering the cumulative load-factor effect without skipping out of the atmosphere, that is, without a substantial increase in range and thermal protection mass, while retaining their maximum values at the instant of entry into the atmosphere.

Results of moving the optimum along one of the constraints are shown in Figure 2.5, namely, along the constraint placed on the angle of atmospheric entry for a descent trajectory for returns from lunar flights or from high-altitude near-Earth orbits. The functional relationship shown represents a family of optimal solutions, and it is possible to determine the limiting angle of entry for a given vehicle with optimal control, that is, the maximum entry angle corresponding to the maximum permissible value of the cumulative-effect measure.

We have thus considered the following criteria: The measure of the cumulative load-factor effect as used in choosing the trajectory only under conditions that the constraints on load factor itself and on its gradient are known. Information on nearing the limiting values of load factor and its time derivative supplement the integral criteria and permit the construction of a system of complex indicators for describing the viability of a body subjected to the effect of changing accelerations.

From a physiological point of view, we can subdivide acceleration effects arbitrarily as follows: (1) Effect on bone-muscle fibers; (2) effect on liquid-filled organs (brain, liver, stomach); (3) effect on blood vessels (changes in hydrostatic pressure in the blood); (4) effect on rhythmic processes in the body (frequency rhythms of heart, breathing); (5) decrease in the working volume of the lungs due to decreased muscle activity; (6) degradation in ideomotor reaction, limitation of motion functions; and (7) decrease in the solid angle of view.

The body reacts differently to the various load-factor effects. Massive inertial forces and external concentrated reactions lead to stresses in the connective, bone, and muscle tissues, thereby limiting mobility. The gradient in load factor affects the rhythmic processes in the body, changing the rhythm of the heartbeat and the frequency of breathing, and acting on the vestibular apparatus. The load-factor impulse affects blood circulation, complicating blood supply to the brain, and causes congestion, increased pressure, and local hemorrhaging. In order to judge the viability of the body to be subjected to the extreme results of all load-factor effects, it is necessary to consider the degree of remaining viability following the action of each effect. Analogously to the load-factor impulse, for which the degree of loading is determined by Equation 2.6, the degree of loading  $C_H^{(n)}$  due to acceleration itself and the degree of loading  $C_H^{(dn/d\tau)}$  due to the gradient of acceleration are determined by

$$C_H^{(n)} = \max \frac{n}{n_{np}} ; C_H^{(dn/d\tau)} = \max \frac{dn/d\tau}{(dn/d\tau)_{np}} .$$

FOR OFFICIAL USE ONLY

FOR OFFICIAL USE ONLY

The degree of remaining viability after the action of the load-factor effects mentioned is determined the same way as for the load-factor effect impulse:

$$C_0^{(n)} = 1 - C_H^{(n)} \quad (2.7)$$

$$C_0^{(dn/d\tau)} = 1 - C_H^{(dn/d\tau)} \quad (2.8)$$

In calculating the remaining viability sequentially after the action of each factor, care must be taken in approaching the maximum permissible values of impulse, load factor, and gradient. The limiting value of load factor is that value which, if a body is exposed to it for even a short period, produces irreversible changes in that body. According to several sets of data, this load-factor value is in the range of 30 to 40 g's. Using this criterion for evaluating the ability of pilots to work, we have to reduce this limit and consider as a threshold value of acceleration the one at which a temporary disturbance of separate functions of the body occurs under conditions such that after removal of the load these functions are restored.

The limiting value of the acceleration gradient is even more vaguely known and, apparently, lies in the range of 5 to 10 m/s<sup>3</sup>.

We must mention that the majority of medical researchers consider the cumulative load-factor effect to be the key one, as provision of normal blood flow to the body is the determining condition for supporting life.

In Reference 12, in which research results on sustaining of load factors by pilots in good condition and out of condition are generalized, it is assured that "one of the leading limiting circumstances of the capability of man to tolerate acceleration is the disturbance of the oxygen balance of the body."

The problem of tolerating load factors is still being investigated and a full definition of a number of questions does not yet exist. This concerns, in first order, determining the relative significance of some of the factors of the load-factor effect, the level of reliability, and questions of precision in estimating the limiting quantities of load factor, gradient, and load-factor impulse.

If we ignore questions of the pilot's ability to function, then we can take the probability for a successful outcome of the loading process for the entire crew as a single criterion for this evaluation of the cumulative load-factor effect. To each component of the load-factor effect, namely, its gradient, the magnitude of inertial forces, and the cumulative effect of acceleration, there corresponds a scatter of values in the neighborhood of the threshold magnitude. This scatter is assumed as given, with the distribution of limiting load-factor values known. In such a case, the determination of the probability  $P_f$  (of exceeding for just one member of the crew the limiting value for a given braking profile with a known load-factor envelope given as a function of time) does not represent much work, if such

FOR OFFICIAL USE ONLY

FOR OFFICIAL USE ONLY

probability is determined for only a single component of the load-factor effect. A calculation made in this fashion will become the basis of an optimistic load-factor-effect model based on the assumption of independence between the effects of load factor, its gradient, and load-factor impulse.

The probability  $P_{\Sigma}$  for a successful outcome of the loading is determined by using such a model in the following fashion:

$$P_{\Sigma} = [(1 - P_1)(1 - P_2)(1 - P_3)]^n, \quad (2.9)$$

where  $P_1$ ,  $P_2$ , and  $P_3$  are the probabilities of exceeding the maximum permissible values of load factor, gradient, and load-factor impulse, based on data for an out-of-condition crew; and  $n$  is the number of crew members.

Models that account for the dependence of load factors on one another and on the prehistory of the loading process are closer to reality. The basis for such a maximum-permissible-value model is a computational scheme for determining the probability of a successful outcome through use of "pessimistic" estimates. Such estimates deal with the correlation of load-factor effects and are made for each of the limiting effects with the condition that the degree of loading is determined by considering the degree of remaining viability for a body subjected earlier to other load-factor effects. Modeling of the cumulative load-factor effect is done by statistical testing.

Each series of tests is conducted for a single, specific descent trajectory, and the results are compared to the goal of choosing the best conditions of motion. In each test, the degree of loading due to the gradient of acceleration during the beginning phase of braking is determined for the given random magnitude of the maximum permissible gradient obtained by using the law for the distribution of threshold values of this gradient.

The measure of the remaining viability becomes the new level corresponding to which there is a decrease in the magnitude of the maximum permissible load factor as obtained from a sequential random test. Having determined the magnitude of the maximum load factor according to the distribution function for the threshold value of this loading and having reduced it in accordance with the measure of remaining viability, we can calculate the degree of loading due to load factor. For this we compare the maximum value of load factor along the trajectory to the decreased value of maximum permissible loading. The newly computed measure of remaining viability will, in this fashion, account for two load-factor effects. In computing each of the trajectories being considered, one should take care to determine ahead of time the maximum value of the relationship between load-factor integral and the maximum permissible impulse corresponding to this load factor. Noting the magnitude of load factor corresponding to this maximum, a random selection is made based on the distribution of the maximum permissible impulse, after which the threshold value obtained for impulse is corrected and reduced in accordance with the measure of remaining viability computed earlier and based on the effect of two other load-factor effects.

FOR OFFICIAL USE ONLY

FOR OFFICIAL USE ONLY

The degree of loading due to the impulse accounts for the prehistory of braking and, in the present case, looks like the ratio between load-factor integral, characteristic for the initial degree of loading calculated for the trajectory, and the newly corrected threshold value of impulse.

The probability for a successful outcome of the loading process for one member of the crew as well as for the crew as a whole can be estimated with a given reliability by repeating the indicated operation for the given descent trajectory and modeling the time of appearance of threshold values of gradient, load factor, and impulse as a random parameter.

If an estimate of pilots' fitness levels, which also affect the successful outcome of the braking process, is required, it is necessary to consider the following parameters, which describe pilots as links in a control system for a flight vehicle in the descent phase:

1. Information lag in the process of operating on signals from control-circuit sensing elements;
2. Pilot lag and lag in the control link connecting pilot and control device.

Nominal values and scatter of these parameters depend on load-factor effects, and in general the probability for a successful outcome of the braking process includes consideration of control system reliability.

Let us consider one more aspect of the problem of returning to Earth from interplanetary expeditions, and in particular let us attempt to determine the possible outline of descent vehicles for the condition that the principles of descent through the atmosphere remain constant.

One of the conditions for choosing the shape of a vehicle will be assumed to be the requirement for using existing methods for braking in the atmosphere and controlling descent. We will consider vehicles of blunted and moderately-pointed shapes, which have minimal available lift-to-drag ratios approximately equal to the required value ( $K_p = 0.65$  to  $0.78$ ). Descent trajectories are chosen using the criterion of minimal cumulative load-factor effect. The maximum load factor following entry into the atmosphere is approximately 10 g's for entry speeds of 17 km/s. Figure 2.6 illustrates one possible path in searching for the best shape of a vehicle intended for entry into the atmosphere with a speed of 17 km/s and carrying a crew of six. Subsequent transition to better shapes is achieved by transforming individual portions of the shapes under consideration while holding the following parameters constant: Volume required, payload weight, maximum permissible load factor, available lift-to-drag ratio, and type of descent trajectory, that is, the set of isoaltitude and isoload-factor segments following occurrence of peak load.

The initial shape, close in shape to existing descent vehicles and with acceptable volume characteristics, does not provide the required

FOR OFFICIAL USE ONLY

FOR OFFICIAL USE ONLY

lift-to-drag ratio and therefore the first stage of transformation of the shape is a change in configuration of the aft volume, having changed the angle of attack of the lifting surface.

Two bounding paths of transformation of the aft volume are shown in Figure 2.6, and they lead to shapes 1 and 2. One of these paths involves an oblique intersection between body and lifting surface (shape 1); the other involves an increase in the apex angle of the aft body and a consequent increase in lifting surface for a symmetrical shape (shape 2). Next to each shape are noted the values for the coefficient of usable volume utilization ( $K_V$ ), as well as the total mass of the thermal protection system and of the descent and landing gear. Mass characteristics are shown in relative units and are referred to the mass of the payload of the descent vehicles, which includes crew, exploration results, life-support systems, thermal control systems, power supplies, control systems (hardware portion), radio systems, and equipment for carrying on operations during the period of approach to the atmosphere and after landing.

Included in the descent and landing gear mass are those remaining descent vehicle systems whose masses either directly or indirectly depend on the vehicle's dimensions and shape, namely: Thermal protection with insulation, structure of the airtight cabin, base fairing, and the forward section with the heat shield, parachute-rocket system for alighting, actuators of the attitude control system, and systems of centering through using the reserves of working fluid.

The path that leads to shapes with significant asymmetry due to the oblique cut leads to configurations of the shape 1 type with a small area for the heat shield and relatively small total surface but with extremely inconvenient centering constraints, which lead to an unacceptable mass for the centering system and to a large total mass of the descent vehicle, while resulting in a small thermal protection and vehicle structure mass.

The compromise solution shown in Figure 2.6 by shape 3 has better centering characteristics.

The use of a symmetrical shape with low fineness ratio (shape 2) gives satisfactory conditions while providing satisfactory lateral centering ( $K_V = 0.75$ ), but due to the enlarged area of the heat shield, substantial total surface, and increase of available volume beyond what is needed, the required mass of the descent and landing gear (which includes the mass of the thermal protection system) is not acceptable.

The characteristics of all three vehicle shapes mentioned are improved if in the next stage of transformation the configuration of the forward part is shaped as an obliquely-cut elliptic cone in a zero angle-of-attack flow. The result of such a change manifests itself in the mass of the centering control system due to the improved volume and centering control characteristics (Chapter 1). In Figure 2.6, we can see what changes are introduced

FOR OFFICIAL USE ONLY

FOR OFFICIAL USE ONLY

under these circumstances in the centering criteria, in the mass of the thermal protection system, and in the descent and landing gear as a whole.

The compromise solution (shape 3a) is attractive not only because of satisfactory mass and centering characteristics but also due to the circumstance that not only the initial segmented-conic but also the resulting bi-conic shapes preserve acceptable and simple outlines for the payload section, which is shaped like a circular cone. Shapes 3 and 3a are shown in Figure 2.6. The landing section, containing the hermetically sealed cabin, which is part of such forms, is shown in Figure 2.6 and can be used as part of other descent vehicles that have the traditional symmetric segmented-cone shape and are intended for entry into the atmosphere from near-Earth orbits and from lunar trajectories.

One of the advantages of vehicles with moderately pointed shapes which enter the atmosphere at hyperbolic speeds (in addition to the volume and weight centering advantages (Chapter 1)) is the lower mass of the thermal protection system and the simple arrangement of the flow past the forward cone, whose angle of attack is close to zero. The optimum radius of bluntness (when radiative heat flows predominate at the stagnation point) is considerably smaller than 1 m. Estimates of the amount of ablation of the surface have to be made considering feedback in the mechanism of breakdown of the thermal protection layer, that is, by considering the blocking of convective flows and the screening of radiative heat flows by the boundary layer of the pyrolytic gas being formed by the products of breakdown in the thermal protection material.

Figure 2.7 shows the change in ablation rate of the thermal protection material during entry into the atmosphere along the lower boundary of the entry corridor for three typical points on the heat shield of a vehicle with shape 3a (Figure 2.6). We can also see how the mass of the ablative coating changes at the stagnation point as a function of time per  $m^2$  of surface.

Let us now consider questions of control during motion along a trajectory that is characterized by constraints on temperature, load factor, or heat flow.

For motion along isotherm trajectories, there occur heat flows with values at or less than the maximum permissible ones; here, a constant value of heat flow indicates a constant temperature equilibrium at the stagnation point (Refs. 20, 40). Motion along an isotherm trajectory (along an isotherm) can be obtained by changing roll attitude without changing the regime of balance. The nominal value of the required roll angle is determined as a function of the value of the effective lift-to-drag ratio.

The equations of motion in velocity coordinates were presented in Chapter 1, from which, by assuming that along the segment of the isotherm of interest, the flight path angle is close to zero, and because  $\sin \theta \approx 0$  and  $\cos \theta \approx 1$ , we obtain the following relationships for the conditions of motion in the Earth's atmosphere:

FOR OFFICIAL USE ONLY

FOR OFFICIAL USE ONLY

$$dt = - (2P_x / \rho g V^2) dV \quad (2.10)$$

$$-V \frac{d\theta}{dV} \frac{QgV^2}{2P_x} = Kg \frac{QV^2}{2P_x} - g + \frac{V^2}{R}. \quad (2.11)$$

Let us express  $d\theta/dV$  in terms of  $\rho$  and  $V$ . By substituting Equation 2.10 in Equation 1.7, we obtain  $dH/dV = - (2P_x / \rho g V) \theta$ . The equation relating density to altitude is differentiated with respect to  $V$  from which we obtain the expression

$$dH/dV = - (d\rho/dV) (1/\beta\rho). \quad (2.12)$$

By equating the right-hand sides of the expressions for  $dH/dV$ , we obtain

$$\theta = (gV/2P_x\beta) (d\rho/dV). \quad (2.13)$$

By differentiating  $\theta$  with respect to  $V$ , we get

$$\frac{d\theta}{dV} = \frac{g}{2P_x\beta} \left( \frac{d^2Q}{dV^2} V + \frac{dQ}{dV} \right). \quad (2.14)$$

Substituting Equation 2.14 in Equation 2.11, we obtain the initial expression for estimating the effective lift-to-drag ratio required for motion in the leveling-off region:

$$K = \frac{QV^2}{2P_x} - 1 + \frac{V^2}{gR} = - \frac{QgV^3}{4P_x^2\beta} \left( \frac{d^2Q}{dV^2} V + \frac{dQ}{dV} \right). \quad (2.15)$$

From Equation 2.15, we obtain the relationship for isoaltitude (Chapter 4), isoload factor, and isotemperature conditions of motion. For the latter, we can obtain the derivative of density with respect to velocity by using the condition of constant heat flow determined by the formula

$$q = C_q \rho^m V^n. \quad (2.16)$$

By taking the derivative of  $q$  with respect to  $V$  and setting it equal to zero, we find the expression for the first derivative of density with respect to velocity:

FOR OFFICIAL USE ONLY



FOR OFFICIAL USE ONLY

$$d\rho/dV = - (n/m) \rho (1/V) \quad (2.17)$$

Differentiating Equation 2.17 again with respect to V, we get

$$d^2\rho/dV^2 = (n/m) (\rho/V^2) (1 + n/m) \quad (2.18)$$

Substituting Equations 2.17 and 2.18 into Equation 2.15 and noting that  $n_x \approx \rho V^2/2P_x$ , we obtain the following formula for the effective lift-to-drag ratio

$$K = \frac{1}{n_x} \left( 1 - \frac{V^2}{gR} - \frac{gn_x^2}{\beta} \frac{n^2}{m^2} \frac{1}{V^2} \right). \quad (2.19)$$

The first two terms inside the parentheses in the expression for determining the required magnitude of the effective lift-to-drag ratio determine the condition of flight along an isoaltitude (at a constant flight-path angle of the trajectory), and the third term expresses the change in lift-to-drag ratio (negative) required for descent into the dense layers of the atmosphere in accordance with the decreased flight speed. In particular, descent along an isoload-factor trajectory corresponds to the condition  $m = 0.5$  and  $n = 2$ , while a descent along isotherms is given by the conditions  $m = 0.5$ ;  $n = 3$  to 3.75.

Analysis of Equation 2.19 shows that for descent from low near-Earth orbits the magnitude of the effective lift-to-drag ratio cannot be negative for motion along an isotherm. At the initial moment of passing the point of leveling off, the angle of roll is close to 60 to 70° and subsequently, according to the degree of penetration into the atmosphere, it will, as a rule, increase further so that later on, when it again decreases, it can provide an increase of the effective lift-to-drag ratio for flight velocities of less than 6 km/s. During flight along an isotherm, the load factor increases, as can be seen, for example, from Equation 1.26.

We have touched on design-ballistic questions related to descent but have not touched on questions of the prelanding maneuver and touchdown, although problems of automated landing at an airport are no less complex and interesting than problems of entry into the atmosphere and the overcoming of temperature and load-factor effects for motion at hypersonic speeds.

Although analysis of the problem of landing a vehicle with a high lift-to-drag ratio and controllable pitch, yaw, and roll is more familiar to aircraft designers, it is difficult to find in the near future any analogies between problems of a gliding landing at an airport and the problems of

FOR OFFICIAL USE ONLY

FOR OFFICIAL USE ONLY

landing on planets. Therefore, we will touch on the question familiar to designers of traditional descent vehicles but also of interest to researchers for reusable rocket-space systems and future heavy descent vehicles. We will discuss well-known landing systems that use parachutes and rocket motors. Systems of this type will doubtless be used for a long time for solving descent and landing problems, and it would be naive to assume that all operations of returning from space will be concluded by a gliding landing at an airport in the near future. Descent vehicles entering the atmosphere from interplanetary trajectories and rocket boosters will land using parachute-rocket systems, which are best from the point of view of weight. Such parachute-rocket systems will permit full use of power plants with onboard propellant storage and will enable landing in different parts of the Earth.

It would be tempting to continue using traditional methods of terminal braking and, in particular, to use parachute systems of existing dimensions for the descent modules of interplanetary vehicles or for reusable rocket assemblies. Let us examine the optimal characteristics of parachute-reaction systems from this point of view. The mass  $M_{C,\Pi}$  of the landing gear, as expressed in relative units (that is, referred to the mass of the landing load  $M_0$ ), will consist of the following components

$$\bar{M}_{C,\Pi} = M_{C,\Pi}/M_0 = \bar{M}_{\Pi,C} + \bar{M}_{D,y} + \bar{M}_{aBT} \quad (2.20)$$

where  $\bar{M}_{\Pi,C}$  is the relative mass of the parachute device;  $M_{D,y}$  is the relative mass of the propulsion-system fuel supply to be used for terminal braking; and  $\bar{M}_{aBT}$  is the relative mass of the automated equipment and apparatus for controlling the operation of the landing gear. Optimal velocity for parachuting corresponding to the minimum mass of the landing gear is quite high and is measured in tens of m/s. Let us convince ourselves of this fact. The parachute descent velocity,  $V_C$ , corresponding to the minimum mass, is determined from the condition

$$d\bar{M}_{C,\Pi}/dV_C = 0. \quad (2.21)$$

Here  $\bar{M}_{aBT}$  is on the order of 0.01 for large values of  $M_0$ . We will assume that  $\bar{M}_{aBT}$  is independent of  $V_C$ . From the condition that the parachute descent has achieved equilibrium, we obtain an expression for the relative mass of the parachute systems:

$$\bar{M}_{nc} = \frac{2\delta(1 + K_1 + K_2)}{C_x Q_0 \cos^2 \theta V_c^2}, \quad (2.22)$$

where  $\delta$  is the specific weight of a square m of the parachute canopy;  $K_1$  is the ratio between the mass of the shroud lines with the strands and the mass of the canopies;  $K_2$  is the ratio between the mass of the attachment elements

FOR OFFICIAL USE ONLY

## FOR OFFICIAL USE ONLY

and the means for deploying the parachute and the mass of the canopies;  $C_x$  is the parachute coefficient of drag;  $\rho_0$  is the density of the atmosphere in the area of landing;  $\theta$  is the angle of deviation of the parachute axis from the velocity vector (for multicanopy systems). The values of all listed coefficients and parameters will be assumed to be independent of the velocity of parachuting. The relative mass of the liquid propulsion rocket-landing systems is determined according to the following equation:

$$\bar{M}_{x,y} = (1 + a_{T,0}) \left( 1 - e^{-\frac{V_x}{Jg}} \right) + \gamma_{x,y} n_0. \quad (2.23)$$

Equation 2.23 is explained in Chapter 3. The relative mass of a solid-propellant rocket can be determined by using the following expression:

$$\bar{M}_{x,y} = \bar{M}_{\text{KOPII}} + \left( 1 - e^{-\frac{V_x}{Jg}} \right), \quad (2.24)$$

where  $\bar{M}_{\text{KOPII}}$  is the relative mass of the rocket-motor casing. The thrust-to-weight ratio at landing will be assumed to be much larger than unity, which, in turn, yields  $V_x \approx V_C$ .

For liquid-propellant rockets, which, as a rule, are used for other stages of flight, the values of  $a_{T,0}$ ,  $\gamma_{x,y}$ , and  $n_0$  are independent of  $V_C$ , with  $a_{T,0} \ll 1$ . For a solid-propellant rocket, the value of  $\bar{M}_{\text{KOPII}}$  depends on  $V_x$ , and for large motors is equal to  $(0.1 \text{ to } 0.2) \times \bar{M}_{x,y}$ . We will assume that  $\bar{M}_{\text{KOPII}} = \text{constant}$ . The magnitude of  $V_C$  does not exceed 100 m/s, and therefore we can assume that

$$1 - e^{-\frac{V_x}{Jg}} \approx \frac{V_x}{Jg}. \quad (2.25)$$

is accurate to within 2 to 4 percent. From the condition given in Equation 2.21 and taking into account Equations 2.22, 2.24, and 2.25, we obtain

$$V_{\text{copt}} \approx \sqrt[3]{\frac{4(1 + K_1 + K_2) \delta J g}{C_x \theta_0 \cos \theta}}. \quad (2.26)$$

FOR OFFICIAL USE ONLY

It is easy to convince ourselves that for any set of values of the quantities that make up Equation 2.26, the optimum parachuting velocity will be in the range of 20 to 30 m/s.

The optimum mass for parachute-rocket systems for such descent velocities will be 5 to 6 percent of the mass of the landing load, that is, about 2 times smaller than for the majority of systems currently used, which are designed for parachute velocities of 7 to 8 m/s. The above considerations on the optimum parachuting velocity are nothing new to persons who deal with landing systems. Implementation of systems with nonoptimal parachute velocities is explained by the fact that it is necessary to allow for the possibility of an emergency landing without propulsive system as well as for difficulties of providing accuracy in a system for controlling the landing for higher descent velocities. Errors in sensors (as a rule, altimeters) depend mainly on the descent velocity, impulse, and altitude at which the propulsion system is turned on.

One of the possible methods for decreasing the scatter of landing velocities is the use of a staircase thrust profile for operating the deceleration rocket, thus achieving a gradual decrease of velocity. The task during the first stage of decreasing velocity is the lowering of the parachute descent velocity to a magnitude on the order of 10 to 15 m/s. The first-stage motor has a thrust-to-weight ratio of less than unity and operates underneath the parachute canopy, thus effectively reducing the landing weight. Errors in switching on the propulsion system (in altitude) are compensated for by increasing its duty cycle, that is, by adding a reserve of fuel for the pre-landing auxiliary braking.

The second phase of braking is accomplished traditionally, that is, by imparting a powerful impulse to the whole system at a low altitude above the Earth's surface.

The main difficulties in implementing a staircase braking profile are connected with the operation of auxiliary braking during the first stage of decreasing velocity, for which it is necessary to formulate a program of rocket motor operation with a gradual increase in thrust, to prevent dynamic effects on the parachute-load system.

Figure 2.8 shows the variation in thrust of solid-propellant rockets for a load weighing 5 tons (force). Also shown is one of several possible shapes for the first-stage motor propellant charge, which provides a progressive burn with transition to constant thrust.

From the thrust curves for the first-stage ( $T_1$ ) and second-stage ( $T_2$ ) motors, it is apparent that there is a parallel-sequential switching on of the motors. In Figure 2.9, we can see how the nominal values of descent velocity and altitude vary as a function of time for the case of programmed braking shown in Figure 2.8.

FOR OFFICIAL USE ONLY

FOR OFFICIAL USE ONLY

In the example given, only one of several possibilities is explored of pre-touchdown braking of parachute-rocket systems, which provide nearly minimal mass characteristics for landing gear.

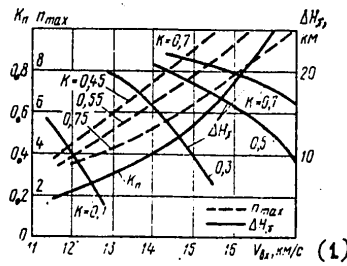


Figure 2.1. The Required Lift-to-Drag Ratio,  $K_n$ ; Maximum Load Factor,  $n_{max}$ ; and Entry Corridor Height,  $\Delta H_{II}$ ; as a Function of the Velocity of Entry into the Earth's Atmosphere,  $V_{BX}$

Key:

1.  $V_{BX}$ , in km/s

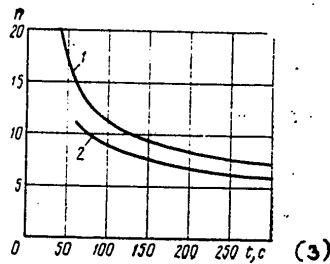


Figure 2.2. Maximum Sustainable Load Factor,  $n$ , As a Function of Time,  $t$ , During Which the Load Factor Acts

Key:

1. Body in condition
2. Body not in condition
3. Time during which maximum load fact is sustained (s)

FOR OFFICIAL USE ONLY

FOR OFFICIAL USE ONLY

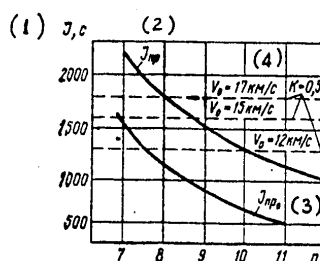


Figure 2.3. Maximum Permissible Impulse as a Function of Load Factor

Key:

1. Impulse, J (s)
2. Maximum permissible impulse,  $J_{\pi p}$
3. Maximum permissible impulse for body weakened by weightlessness,  $J_{\pi p_0}$
4. Velocity of entry (km/s)

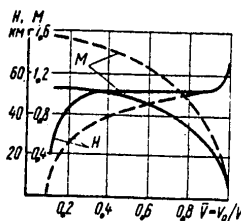


Figure 2.4. Measure M of the Cumulative Effect for Two Descent Trajectories During Atmospheric Entry at Hyperbolic Velocity

Key:

- Initial trajectory
- Optimal trajectory

FOR OFFICIAL USE ONLY

FOR OFFICIAL USE ONLY

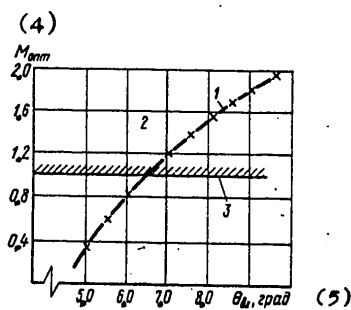


Figure 2.5. Maximum Permissible Values of the Cumulative Effect Measure for Different Angles of Entry into the Atmosphere,  $\theta_{BX}$

Key:

1. Bounding set of optimal solutions
2. Region of possible trajectories
3. Boundary of permissible load-factor effect on crew
4.  $M_{opt}$
5.  $\theta_{BX}$  (deg.)

FOR OFFICIAL USE ONLY

FOR OFFICIAL USE ONLY

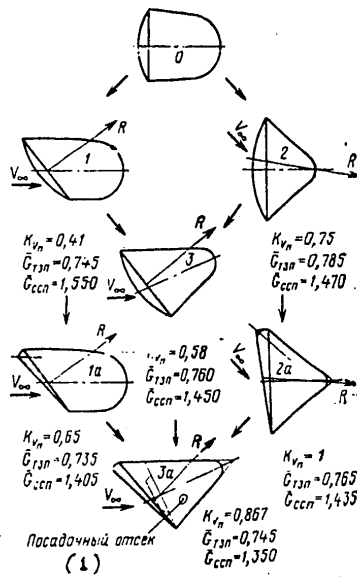


Figure 2.6. Shape Transformation in Searching for the Best Descent Vehicle Configuration

Key:

1. Landing module
2.  $\bar{G}_{T3II}$ : Relative mass of thermal protection system
3.  $\bar{G}_{CCI}$ : Relative mass of descent and landing gear
4.  $K_{V_{II}}$ : Coefficient of usable volume utilization
5.  $\bar{G}$ : Mass expressed as a fraction of descent-vehicle payload

Shape	$K_{V_{II}}$ (4)	$\bar{G}_{T3II}$ (2)	$\bar{G}_{CCI}$ (3)
0	-	-	-
1	0.41	0.745	1.550
2	0.75	0.785	1.470
3	0.58	0.760	1.450
1a	0.65	0.735	1.405
2a	1	0.765	1.435
3a	0.867	0.745	1.350

FOR OFFICIAL USE ONLY



FOR OFFICIAL USE ONLY

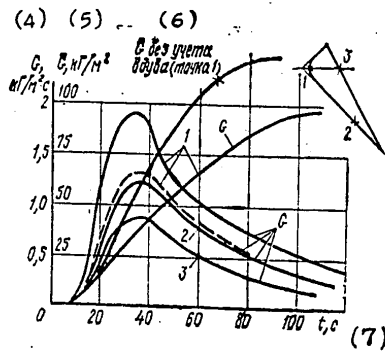


Figure 2.7. Ablation Rate of Thermal Protection Layer as a Function of Flight Time

Key:

- Entry along lower boundary of the entry corridor
- - - Entry along the upper boundary of the entry corridor
- 1, 2, 3. Typical points on the heat shield, as shown in sketch
- 4. Ablation rate per unit of area,  $G$  ( $\text{kg/m}^2/\text{s}$ )
- 5. Cumulative ablation per unit of area,  $\bar{G}$  ( $\text{kg/m}^2$ )
- 6.  $\bar{G}$  without gas injection (at point 1)
- 7. Time (s)

FOR OFFICIAL USE ONLY

FOR OFFICIAL USE ONLY

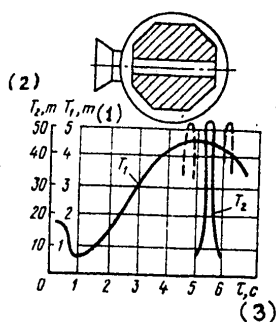


Figure 2.8. Variation in Thrust of Lander Rocket Motors and Typical Charge Shape of the First-Stage Motor

Key:

1.  $T_1$ : First-stage thrust (tons (force))
2.  $T_2$ : Second-stage thrust (tons (force))
3.  $\tau$ : Time (s)

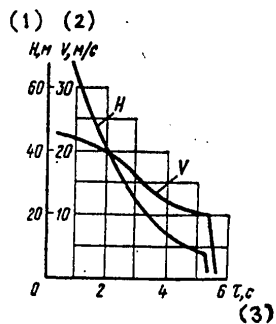


Figure 2.9. Parameters of Motion of a Parachute-Rocket System Using a Staircase Prelanding Braking Profile

Key:

1.  $H$ : Altitude (m)
2.  $V$ : Velocity (m/s)
3.  $\tau$ : Time (s)

FOR OFFICIAL USE ONLY

FOR OFFICIAL USE ONLY

CHAPTER 3

CHOICE OF DESIGN-BALLISTIC PARAMETERS FOR LANDING VEHICLES OF  
MARTIAN PLANETARY SYSTEMS

The basic operational feature of a Mars landing is the rarefaction of the Martian atmosphere. Therefore, during analysis of the problem of descent to the planet, it is necessary to determine the best method for braking, considering both the use of deployable aerodynamic braking devices and the suitability of the vehicle for active prelanding braking by rocket motors.

It is to be expected that heavy descent vehicles, which will make controlled descents to the Martian surface with the aim of delivering large planetary systems, will be developed in the future.

Let us review methods for the practical calculation of optimal design-ballistic parameters for such descent vehicles.

The choice of optimum dimensions and component layout for a Martian descent vehicle is determined, as a rule, through a compromise between vehicle lifting-surface area and propellant reserve for braking before touchdown.

During parametric calculations in the preliminary design stage, it is frequently necessary to determine analytically the optimum ballistic parameters and dimensions of the vehicle for conditions that motion in the atmosphere will be along an optimum-energy trajectory. The problem of optimizing is solved by parts, with a class of optimal control laws for descent determined first. For the set of optimum trajectories, design-ballistic parameters are then determined, namely, load on the midsection and available lift-to-drag ratio. Following such calculations, it is possible to go on to the determination of the brake shroud dimensions for specific configurations of the aerodynamic braking device.

Let us consider the methods for analytical estimation of optimal design-ballistic parameters, solving separately the problem of choosing the optimal control law for descent and the problem of searching for design-ballistic parameters and, in particular, load on the vehicle midsection. For this we will assume that, in the design of the vehicle, use is made of simple and accepted solutions, that is, for aerodynamic braking at hypersonic velocities, a forward heat shield will be used. The heat shield is at an angle of attack sufficient for obtaining a small lift-to-drag ratio, with the angle of attack and magnitude of lift-to-drag ratio, as determined by balance weights or asymmetric shape of the shield, held constant during the descent process. Motion control is achieved by rolling about the velocity vector. It is assumed that all prelanding braking is accomplished by a rocket motor, which is subsequently used for the vernier maneuver and soft landing on the surface.

FOR OFFICIAL USE ONLY

FOR OFFICIAL USE ONLY

moment of switching from one value of effective lift-to-drag ratio to another or from one load factor profile to another.

Four characteristic descent trajectories in altitude versus flight velocity coordinates are shown in Figure 3.1 for a vehicle that has a heat shield with a half-cone angle of  $70^\circ$  and a fineness ratio of 0.9. It is assumed that the vehicle is trimmed at an angle of attack corresponding to a lift-to-drag ratio of  $K = 0.4$  and that it has a midsection loading of  $5,900 \text{ N/m}^2$  ( $600 \text{ kg-force/m}^2$ ). Calculations were made for a model atmosphere approximating the nominal one (Ref. 24) and for a velocity of entry into the atmosphere of  $4.6 \text{ km/s}$ , with the condition that, at the moment of initial entry into the atmosphere, flight with maximum effective lift-to-drag ratio and with maximum permissible load factor of  $5 \text{ g}$ 's is attained.

Trajectory 1, as seen in the figure, is a glancing trajectory; this is the limiting skip trajectory, because the maximum effective lift-to-drag ratio is maintained (angle of roll is constant at zero).

Trajectory 2 is the limiting steepest trajectory, inasmuch as along this trajectory maximum load factor is maintained during the entire time of flight, as a result of which the vehicle does not have enough time for braking and at the surface has a flight velocity corresponding to this load factor ( $1.7$  to  $1.9 \text{ km/s}$ ).

In the first case, the flight velocity at the surface is also large, inasmuch as the second dive into the atmosphere occurs along a steep trajectory.

Flight along a sloping trajectory following the initial dive is preferable, because the vehicle has considerable time for braking in the dense layers of the atmosphere and approaches the surface of the planet along a shallow slope. Two such trajectories are shown in Figure 3.1. In both cases, the vehicle approaches the surface with maximum effective lift-to-drag ratio, in the same manner as is done along the entire length of trajectory 1. However, after passing maximum load factor immediately after atmospheric entry and in contrast to trajectory 1, the effective lift-to-drag ratio, that is, the projection of the lift force on the vertical, is decreased. The shallow skip of trajectory 3 is designed in such a manner that during the period of flight, starting with a velocity of  $3.2 \text{ km/s}$  and ending with a velocity of  $1.2 \text{ km/s}$ , the vehicle moves with a roll angle of  $10^\circ$  corresponding to the value of effective lift-to-drag ratio of  $0.135$ . Trajectory 4 has a flight segment of isoaltitude leveling-off during the same period. The instantaneous value of roll angle during this segment is determined from the condition that the derivative of the flight-path angle be zero.

For both trajectories 3 and 4, a near-minimum value of flight velocity is attained at altitudes of  $2$  to  $4 \text{ km}$ , with the value of this velocity somewhat lower for the shallow-skip trajectory. However, the trajectory with the isoaltitude plateau is preferable, because, due to the shallower approach to altitudes of  $3$  to  $4 \text{ km}$ , the losses in propellant for the prelanding braking will be somewhat lower than for the skipping trajectory.

FOR OFFICIAL USE ONLY

FOR OFFICIAL USE ONLY

Let us now investigate how the speed of approach to the surface varies for such level trajectories when lifting and braking characteristics of the vehicle are varied. The terminal velocity of flight at different altitudes during descent with an isoaltitude segment is shown in Figure 3.2 as a function of the loading on the midsection of the vehicle for different values of the available lift-to-drag ratio for a nominal model of the atmosphere. We note a sharp increase in velocity at low load levels, increasing from 200 to 500 N/m<sup>2</sup> (20 to 50 percent kg-force/m<sup>2</sup>) up to 2,000 to 3,000 N/m<sup>2</sup> (200 to 300 kg-force/m<sup>2</sup>) and a further gradual growth for  $P_x$  greater than 4,000 N/m<sup>2</sup> to 5,000 N/m<sup>2</sup> (400 to 500 kg-force/m<sup>2</sup>).

As we can see from the figure (lower curves), the sensitivity of the trajectory in terms of the terminal velocity criterion as a function of available lift-to-drag ratio is nonlinear. This nonlinearity is more graphically represented in Figure 3.3, where it is shown how, at a 2-km altitude, flight velocity of a trajectory with leveling-off varies with increasing available lift-to-drag ratio for a constant  $P_x$  ( $P_x = 7,850$  N/m<sup>2</sup> or 800 kg-force/m<sup>2</sup>), and also as a function of increase in loading on the midsection for a constant lift-to-drag ratio ( $K = 0.526$ ). We see once again that in the area of large  $P_x$  the terminal velocity increases with  $P_x$  but quite sluggishly. The gradient of the variation of velocity as a function of available lift-to-drag ratio is clearly not constant, and the velocity decreases most when the lift-to-drag ratio increases from 0.2 to 0.6.

Generally speaking, we cannot consider the relationship among terminal velocity,  $P_x$ , and  $K$  in isolation, inasmuch as these characteristics are closely related to one another by the lift-drag polar of the vehicle. For one and the same vehicle having the same aerodynamic shape and dimensions, an increase in lift capability is accompanied by worsening braking characteristics, and it would be more correct to consider the effect of the angle of attack on the magnitude of the terminal velocity. It turns out that for each vehicle shape there exists a zone of best trim angles of attack, and Figure 3.4 shows this zone for a vehicle with a shield in the shape of a symmetric blunted cone with a semicone angle of 70°. Two curves are shown, relating the speed of flight at an altitude of 2 km to the angle of attack for an isoaltitude trajectory, with one curve characterizing a vehicle with an extensive heat shield and the other describing a vehicle of relatively small diameter and fineness ratio close to unity.

It is useful to approximate the value of terminal flight velocity considered above through formulas, which can be used to determine that velocity for the optimal descent trajectory as a function of flight altitude and loading on the midsection of the vehicle for the range of the best regions of trim, that is, for those values of the available lift-to-drag ratio ( $K_p$ ) that are characteristic for blunted and for moderately pointed shapes.

For the majority of atmosphere models, the structure of the formulas can be developed on the basis of steady-state motion, as a result of which these formulas will have the form

FOR OFFICIAL USE ONLY

FOR OFFICIAL USE ONLY

We will also assume that the flow field about the vehicle and the method of generating aerodynamic forces used for braking and control of the descent trajectory are traditional, that is, vehicles with simple aerodynamic shapes having small available lift-to-drag ratios are used. Such a vehicle has a deployed aerodynamic braking shroud carrying the payload enclosed by a lightweight fairing in the shadow zone. The shroud can project beyond the payload, and the shield itself has a blunted or moderately pointed shape. Let us consider the type of descent trajectory for which the best design-ballistic vehicle parameters are to be determined.

The optimal descent control law for a Martian descent vehicle is chosen in accordance with criteria that define the terminal descent phase at the instant the vehicle touches the planet's surface. In general, such a criterion can be the mass of the propulsion system for given dimensions of the aerodynamic braking shroud. By making a number of simplifications permissible for parametric estimates, the weight or mass criterion can be isolated, as it is not necessary to consider the thrust-to-weight ratio and the mass of the combustion chamber, but to work only with the fuel supply for the pre-touchdown braking and landing maneuvers. The choice of optimum thrust-to-weight ratio has to be made considering changes in flight velocity at the various altitudes at which the rocket is ignited and the thrust-control program during braking. Several results of calculations of the optimum thrust-to-weight ratio will be discussed at the end of the chapter. The speed of entry into the atmosphere of Mars is significantly lower than the speed of entry into the atmospheres of Earth or Venus; it varies from 3.6 km/s (descent from low near-planetary orbits) up to 4.8 to 6 km/s (descent from highly elliptical areocentric orbits or approach trajectories). Along such descent trajectories, the maximum convective heat flows (which predominate in the heat transfer) do not, as a rule, exceed  $10^2$  kW/m<sup>2</sup> and thus the constraints of heating and load-factor effects are not the decisive ones for Martian planetary descent vehicles.

If we ignore the thrust-to-weight ratio and take the characteristic velocity of the descent rocket motor as the criterion for searching for the regime of descent control, we can make additional simplifications in the problem, reducing the problem of optimizing the weight-energy characteristics to a problem of minimizing the characteristics of the descent trajectory.

Results of solving such problems appear most graphic if the minimum of just a single, basic characteristic of the trajectory is determined, namely, the velocity at the desired final altitude of passive flight at the moment that the landing rocket motor is ignited.

Strictly speaking, we are not in a position (having optimized the conditions of descent motion by using the criterion of a minimum characteristic velocity) to ignore the peculiarities of the regime of active braking and, in particular, the flight-path angle, which is the angle of inclination of the velocity vector to the horizontal at the end of the aerodynamic braking segment. The characteristic landing velocity  $V_x$  has the following components:

FOR OFFICIAL USE ONLY

FOR OFFICIAL USE ONLY

1.  $V_{H_0}$  is the velocity of flight at altitude  $H_0$  at the end of aerodynamic braking and before ignition of the rocket motor for prelanding braking (the magnitude of  $V_{H_0}$  depends on the type of descent trajectory chosen and on the ballistic characteristics of the vehicle.
2.  $\Delta V_{\Gamma\Pi}$  is the gravitational loss in velocity during the active braking segment (determined by the thrust vector control profile and the length of the braking segment, that is, by the thrust-to-weight ratio of the rocket motor, which, in its turn, depends on the altitude  $H_0$  and the initial flight path angle  $\theta_0$ ). The magnitude of  $\Delta V_{\Gamma\Pi}$  is small and amounts to from 2 to 4 percent of  $V_{H_0}$ ; thus, in parametric studies of the optimal design-ballistic parameters, it is possible to neglect the effect of characteristics of the final segment of the descent trajectory on the value of  $\Delta V_{\Gamma\Pi}$ .
3.  $\Delta V_{\Upsilon\Pi\Pi}$  is the characteristic velocity loss due to control during the segment of active prelanding braking. The total loss due to control amounts to 2 to 5 percent of  $V_{H_0}$ .

The three components mentioned can be combined, inasmuch as they determine the propellant reserves needed for the prelanding braking. Thus,  $\Delta V_x$  for the braking is  $\Delta V_{xTOPM} = V_{H_0} + \Delta V_{\Gamma\Pi} + \Delta V_{\Upsilon\Pi\Pi}$  and  $\Delta V_{xTOPM} = K_V V_{H_0}$ , where

$K_V = 1.04$  to  $1.10$ . The remaining components of the characteristic velocity determine propellant losses during the landing segment ( $\Delta V_{x\Pi OC}$ ) and the amount of unexpended propellant in the tanks ( $\Delta V_{\Gamma AP}$ ). For all practical purposes,  $\Delta V_{x\Pi OC}$  is independent of the descent trajectory characteristics:

$$\Delta V_{x\Pi OC} = \Delta V_{MAH} + \Delta V_{\text{ЮCT}} \quad [3.1]$$

where  $\Delta V_{MAH}$  is the velocity reserve for the prelanding maneuver.  $\Delta V_{MAH}$  depends on the time allotted for the maneuver. For a maneuver time of 60 s, the magnitude of  $\Delta V_{MAH}$  is 270 m/s;  $\Delta V_{\text{ЮCT}}$  are the velocity losses during vernier braking for a soft landing. The magnitude of  $\Delta V_{\text{ЮCT}}$ , as a rule, is small and amounts to between 20 to 60 m/s.  $\Delta V_{\Gamma AP}$  is the component of the characteristic velocity, determined by the guaranteed reserve of propellant in the tanks. The magnitude of  $\Delta V_{\Gamma AP}$  is usually determined by the tank coefficient and, in practice, does not depend on the parameters of the descent trajectory.

Let us observe how the conditions of motion on the aerodynamic-braking segment influence the terminal phase of such braking. Parameters of the trajectory to be varied during optimization are the trim angle of attack for the vehicle of a particular configuration and a set of control actions that determine the variation of the roll angle and, thus, the magnitude of the effective lift-to-drag ratio. These control actions can be in the form of a series of turns, by defining the instants at which the attitude control thrusters are turned on or, which is even more graphic, by defining the

FOR OFFICIAL USE ONLY

FOR OFFICIAL USE ONLY

$$V_{H_0} = K_y \sqrt{\frac{2g_H}{g_3 g_H} \frac{\rho_H^{0.5}}{f(K_p)}} \quad (3.2)$$

where  $K_y$  is the coefficient that determines the control method on the descent segment and the peculiarities of the atmosphere model being used;  $g_H$  is the free-fall acceleration close to the surface of the planet;  $g_3$  is the free-fall acceleration in Earth's atmosphere;  $\rho_H$  is the density of the atmosphere at the terminal altitude of flight; the function  $f(K_p)$ , which defines velocity, depends on the magnitude of the lift-to-drag ratio in the region of optimal values of  $K_p$ .

For an isoaltitude control law, for segmented or conic blunted shapes, and for a nominal atmosphere model, Equation 3.2 has the form

$$V_{H_0} = 0.49 Q_H^{-0.5} P_x^{0.5} (1.26 K_p^2 - 0.77 K_p + 0.45)^{0.5}, \quad (3.3)$$

which describes the magnitude of flight velocity at altitudes from 0 to 4 km; for  $980 \text{ N/m}^2$  ( $100 \text{ kg-force/m}^2$ )  $\leq P_x \leq 6,800 \text{ N/m}^2$  ( $700 \text{ kg-force/m}^2$ ); and for  $0.2 \leq K_p \leq 0.6$ , with an accuracy on the order of 10 percent.

The proposed method for determining the optimal parameters of descent and landing gears is based on parametric calculations, in which widely known terms are used: Midsection loading, specific mass/ $\text{m}^2$  of structure, specific mass for the rocket-motor casings, relative weight of the propulsion system, thrust-to-weight ratio, and others. The authors decided not to use indicators based on mass but to preserve commonly accepted weight criteria, because this is permitted by the GOST [All-union state standard].

The weight of the descent and landing gear,  $G_{\text{CCH}}$ , consists of the following components:

$$G_{\text{CCH}} = G_{\text{KT}} + G_{\text{AY}} + G_{\text{OBOBYD}},$$

where  $G_{\text{KT}}$  is the weight of the structure and thermal protection layer of the aerodynamic braking device;  $G_{\text{AY}}$  is the weight of the propulsion system including the propellant supply; and  $G_{\text{OBOBYD}}$  is the equipment weight.

The third itemized component does not, in practice, depend on the design-ballistic parameters of the vehicle, and for this reason we will determine the optimal loading on the midsection starting with the minimum weight of the structure, thermal protection, and propulsion system.

For heavy descent vehicles intended for missions to Mars, the weight characteristics of the vehicle structure conflict with analogous characteristics

FOR OFFICIAL USE ONLY



FOR OFFICIAL USE ONLY

of the landing propulsion system. Because of this, the parameter used, and the one that relates these two, is the flight speed at the moment the rocket is ignited before landing. The task of optimization is thus the determination of the optimum loading on the midsection. We will determine the optimum weight of the descent and landing gear in relative units, without tying the optimum loading on the midsection to concrete dimensions of the vehicle or relating component weights of the descent and landing gear to the initial weight  $G_0$ , which is characteristic for the vehicle before atmospheric entry.

The weight of structure and thermal protection is usually estimated during parametric design calculations by using specific weight of the lifting or wetted surfaces. We, too, will use the specific weight, defining it as the weight of structure and thermal protection per each  $m^2$  of lifting surface:

$$\bar{G}_{y\Delta} = G_{KT}/S \quad (3.4)$$

By letting  $P_x = G_0/C_x S$ , we obtain as the weight of structure and thermal protection:

$$G_{KT} = \bar{G}_{y\Delta} \frac{G_0}{C_x P_x} \quad (3.5)$$

It should not be assumed, even for parametric design estimates, that  $\bar{G}_{y\Delta}$  will remain constant for vehicles of different configuration and size. Increase in vehicle dimensions and lifting surface area for the same total weight will necessarily lead to a decrease in the weight of each  $m^2$  of lifting surface due to the circumstances listed below. First, for decreased loading on the midsection there will be a decrease in the thermal stress for the descent trajectory, the vehicle will be braked at higher altitudes, and the weight of the thermal protection coating per  $m^2$  of heat-shield surface and bottom fairing will decrease. This decrease is also aided by the additional reduction in convective heat flows due to the increased bluntness radius with an increase in vehicle dimension.

Second, with an increase in dimensions of the lifting surface, there is a decrease in the fraction of structural weight per unit area of the surface. This structure consists of load-carrying elements of the vehicle fuselage, and payload support components and assemblies of airlocks, docking mechanisms, and so forth. Some increase in weight of the lifting envelope of the heat shield affects stability due to increased bluntness radius and counteracts the general trend to reducing the weight per  $m^2$  of lifting surface with an increase in its area.

In the limit, as the dimensions of the shield increase ( $P_x \rightarrow 0$ ), the structural weight per  $m^2$  of such a shield will tend toward very small values.

For vehicles with the customary relationship between diameter and length and with modest dimensions and values of loading on the midsection

FOR OFFICIAL USE ONLY

FOR OFFICIAL USE ONLY

( $P_x = 4,000$  to  $8,000$  N/m<sup>2</sup> or  $400$  to  $800$  kg-force/m<sup>2</sup>), the specific weight of the structure and thermal protection of the body for each m<sup>2</sup> of lifting surface changes little with changes in the diameter of the vehicle.

From the material presented, it follows that first, the specific weight of structure and thermal protection per m<sup>2</sup> of lifting surface is not a constant value for vehicles with lifting surfaces of different dimensions, and, second, this specific weight is a nonlinear function of the midsection loading, increasing with increases in this loading, and with the steepest increase in the specific weight to be expected when midsection loads are small.

In the general case, the relationship between specific weight  $\bar{G}_{yA}$  and the midsection load of bluntly-shaped vehicles can be described using the equation:

$$\bar{G}_{yA} = C_1 P_x^{C_2}, \quad (3.6)$$

where  $C_2$  is an index of degree and lies in the range of 0 to 1.

Typical relationships between specific weight and midsection load are shown in Figure 3.5 and were obtained by approximating the results of design-layout work on vehicles that have different ratios between heat-shield area and total wetted surface. This relationship has the form

$$\bar{G}_{yA} = K_{KT} P_x^{0.5}, \quad (3.7)$$

where  $K_{KT}$  is the coefficient that defines the rate of change in  $\bar{G}_{yA}$  for a structure with thermal protection. Substituting Equation 3.6 in Equation 3.4 and transforming to relative units, we obtain

$$\bar{G}_{KT} = K_{KT}' \frac{1}{C_x P_x^{0.5}}. \quad (3.8)$$

Undoubtedly, the relationships presented reflect more the qualitative than the quantitative side of the relationships between the structural weight and the heat-shield dimensions of a descent vehicle. In each concrete case, the weight characteristics will depend on the power plant of the vehicle, the particulars of loading, the computational cases, the layout of structural components and assemblies of the heat shield, and the materials used for thermal protection and structure. However, for parametric studies, it is usually necessary to neglect specifics of the structure so that, having once determined the range of optimal values of the design parameters, it is possible to estimate their values more precisely through the use of additional, more detailed computational models.

FOR OFFICIAL USE ONLY

FOR OFFICIAL USE ONLY

Let us consider the weight model of the propulsion system for prelanding braking and touchdown. The weight of the power plant has the following components:

$$G_{a,y} = G_{\text{KAM}} + G_{\text{ТОПЛ}} + G_{\text{БАК}}, \quad (3.9)$$

where  $G_{\text{KAM}}$  is the weight of the combustion chamber;  $G_{\text{ТОПЛ}}$  is the weight of the propellant required for landing; and  $G_{\text{БАК}}$  is the weight of the tanks with fittings.

By switching to relative units in Equation 3.9 and referring the weight of the components to the total weight of the vehicle, we obtain

$$\bar{G}_{a,y} = \gamma_{\text{KAM}} n_0 + \frac{G_{\text{ТОПЛ}}}{G_0} (1 + a_{T,0}), \quad (3.10)$$

where  $\gamma_{\text{KAM}}$  is the specific weight of the combustion chamber (kg-force of weight per kg-force of thrust);  $n_0$  is the initial thrust-to-weight ratio of the landing propulsion system;  $a_{T0}$  is the tank coefficient, which is the ratio of the propellant tank system weight to the weight of the propellant.

Since

$$\frac{G_0 - G_{\text{ТОПЛ}}}{G_0} = e^{-\frac{V_x}{Jg}}, \quad (3.11)$$

we have

$$\bar{G}_{a,y} = (1 + a_{T,0}) \left( 1 - e^{-\frac{V_x}{Jg}} \right) + \gamma_{\text{KAM}} n_0. \quad (3.12)$$

At the beginning of this chapter, we considered the components of characteristic velocity and divided  $V_x$  as follows:

$$\begin{aligned} V_x &= V_{H_0} + \Delta V_{r,n} + \Delta V_{\text{YIP}} + \Delta V_{\text{MAK}} + \Delta V_{\text{ЮСТ}} + \Delta V_{\text{ГОР}} = \\ &= \Delta V_{\text{X.TOPM}} + \Delta V_{\text{X.IIOC}} + \Delta V_{\text{ГAP}}. \end{aligned}$$

The magnitude of  $\Delta V_{\text{ГAP}}$  is determined by the tank coefficient and is included in  $a_{T0}$ .

By considering Equation 3.1, we get the relationship between  $V_x$  and  $V_{H_0}$

$$V_x = K_V V_{H_0} + \Delta V_{\text{X.IIOC}} \quad (3.13)$$

where  $\Delta V_{\text{X.IIOC}}$  is independent of  $V_{H_0}$ .

FOR OFFICIAL USE ONLY

FOR OFFICIAL USE ONLY

The magnitude of  $V_x$  does not exceed 1,500 to 2,000 m/s, and therefore it is possible to transform Equation 3.12 into the following expression with only a small error:

$$\bar{Q}_{a,y} = (1 + a_{r,o}) \left( \frac{V_x}{Jg} - \frac{V_x^2}{2g^2J^2} \right) + \gamma_{kam} n_0. \quad (3.14)$$

By considering the expression of Equation 3.3 for  $V_{H_0}$ , we obtain

$$\bar{Q}_{a,y} = (1 + a_{r,o}) \left( \frac{K_V \bar{V}_{H_0} P_x^{0.5} + \Delta V_{x,noc}}{gJ} - \frac{(K_V \bar{V}_{H_0} P_x^{0.5} + \Delta V_{x,noc})^2}{2g^2J^2} \right) + \gamma_{kam} n_0, \quad (3.15)$$

where

$$\bar{V}_{H_0} = 0.96 \rho_H^{-0.5} (1.26 K_p^2 - 0.77 K_p + 0.45)^{-0.5} \quad (3.16)$$

If the thrust-to-weight ratio of the landing power plant is assumed constant during parametric studies of different descent vehicle variants, then the altitude at which the power plant is switched on for the prelanding braking will also remain constant for vehicles with arbitrary loads on the midsection. By choosing a value of  $K_p$  close to the optimum one for the class of shapes considered, we can determine the optimum value for  $P_x$  from the condition

$$\frac{\partial}{\partial P_x} (\bar{Q}_{k,r} + \bar{Q}_{a,y}) = 0. \quad (3.17)$$

Substituting Equations 3.8 and 3.15 into Equation 3.17 and assuming that  $\Delta V_{x,noc}$  is a small quantity, we obtain the following equation for the optimum loading on the midsection:

$$(1 + a_{r,o}) \frac{K_V \bar{V}_{H_0}}{2gJ} y - \frac{K_{k,r}}{2C_x} y^3 - (1 + a_{r,o}) \frac{K_V^2 \bar{V}_{H_0}^2}{2g^2J^2} = 0, \quad (3.18)$$

where

$$y = 1/\sqrt{P_x}$$

For realistic values of  $C_x$ ,  $J$ ,  $H_0$ , and  $a_{r,o}$ , the optimum value of  $P_x$  is found to be in the range from 1,500 N/m<sup>2</sup> to 3,500 N/m<sup>2</sup> (150 kg-force/m<sup>2</sup> to 350 kg-force/m<sup>2</sup>).

FOR OFFICIAL USE ONLY

Figure 3.6 shows the typical variation in the weight constituents of the descent and landing gear as a function of vehicle lifting surface for one of the possible configurations based on the initial data given.

As already mentioned in Chapter 1, the relative weight of the descent and landing gear cannot be used as an objective criterion for comparison, and Figure 3.7 substantiates this. The figure illustrates the dependence of the ratio of the weight of the descent and landing gear to the weight of the payload of the descent vehicle as a function of the load on the midsection, that is, as a function of the dimensions of the lifting surface for a constant total vehicle weight. The optimum lies in the range of  $P_x = 1,500 \text{ N/m}^2$  to  $3,000 \text{ N/m}^2$  ( $150 \text{ kg-force/m}^2$  to  $300 \text{ kg-force/m}^2$ ), which is indicated broadly in the curves of Figure 3.6 but more distinctly in Figure 3.7.

In conclusion, let us consider the question of the best thrust-to-weight ratio of the landing rocket motor. In choosing the optimum thrust for the landing phase of a Martian landing vehicle, allowances should be made for gravitational losses during the prelanding braking and for the increase in characteristic velocity to account for changes in initial conditions at the moment the rocket motor is ignited. Inasmuch as the vehicle is actively braked by aerodynamic drag during its approach to the surface, it is more advantageous to ignite the landing rocket motor at the lowest possible altitude, thus resulting in a thrust-to-weight ratio of about 2. A typical relationship of the relative mass of the propellant section ( $G_{T0}$ ), the propulsion system  $G_{dy}$ , and the flight velocity at the instant the rocket motor is ignited is shown in Figure 3.8 as a function of the initial thrust-to-weight ratio of the landing vehicle.

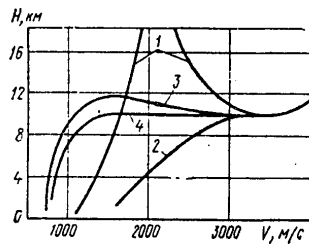


Figure 3.1. Typical Descent Trajectories Through the Martian Atmosphere. Altitude H in km, velocity V in m/s

FOR OFFICIAL USE ONLY

FOR OFFICIAL USE ONLY

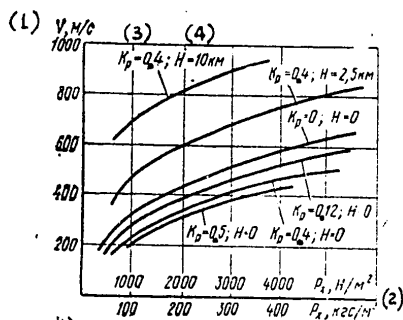


Figure 3.2. Terminal Flight Velocity as a Function of Vehicle Midsection Loading

Key:

1. Velocity,  $V$  (m/s)
2. Midsection loading,  $P_x$ , in  $N/m^2$  (upper scale) and in  $kg\text{-force}/m^2$  (lower scale)
3. Available lift-to-drag ratio,  $K_p$
4. Altitude,  $H$ , in  $km$ , for which terminal velocity is shown

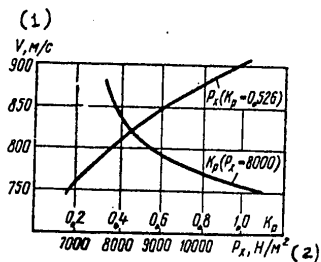


Figure 3.3. Terminal Flight Velocity at 2-km Altitude as a Function of Midsection Loading (for Constant Lift-to-Drag Ratio) and as a Function of Lift-to-Drag Ratio for Constant Midsection Loading

Key:

1.  $V$  (m/s)
2.  $P_x$  (N/m<sup>2</sup>)

FOR OFFICIAL USE ONLY

FOR OFFICIAL USE ONLY

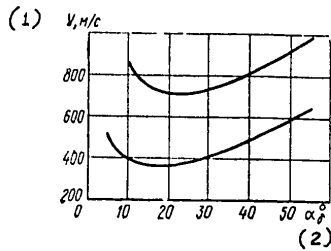


Figure 3.4. Terminal Flight Velocity as a Function of Trim Angle of Attack

Key:

1.  $V$  (m/s)
2. Trim  $\alpha$  (deg.)

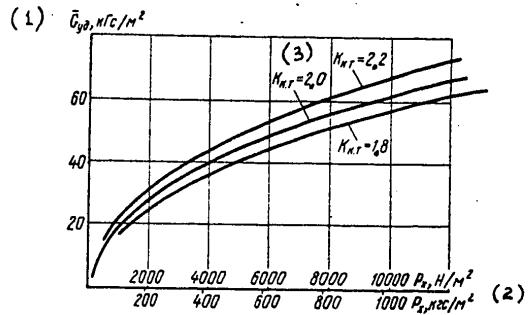


Figure 3.5. Specific Weight of  $m^2$  of Lifting Surface as a Function of Midsection Load

Key:

1. Specific weight,  $\bar{\gamma}_{y_d}$  (kg-force/ $m^2$ )
2. Midsection load,  $P_x$ , in  $N/m^2$  (upper scale) and in kg-force/ $m^2$  (lower scale)
3. Coefficient  $K_{KT}$ , defining rate of change in specific weight  $\bar{\gamma}_{y_d}$  as a function of load  $P_x$  ( $K_{KT} = 1.8, 2.0, 2.2$ )

FOR OFFICIAL USE ONLY

FOR OFFICIAL USE ONLY

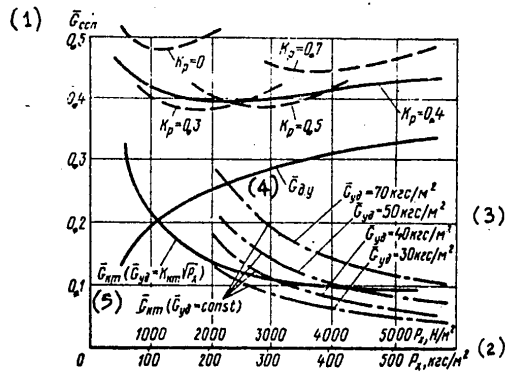


Figure 3.6. Mass Changes in the Components of the Descent and Landing Gear as a Function of Vehicle Lifting Surface

Key:

1.  $\bar{G}_{CCP}$ , relative mass of descent and landing gear
2. Midsection loading  $P_x$  in  $N/m^2$  (upper scale) and in  $kg\text{-force}/m^2$  (lower scale)
3. Specific weight  $\bar{G}_{yd}$  ( $kg\text{-force}/m^2$ )
4.  $\bar{G}_{dy}$ , relative mass of power plant
5.  $\bar{G}_{KT}$ , relative mass of thermal protection and structure (Equations 3.4 and 3.7)

FOR OFFICIAL USE ONLY



FOR OFFICIAL USE ONLY

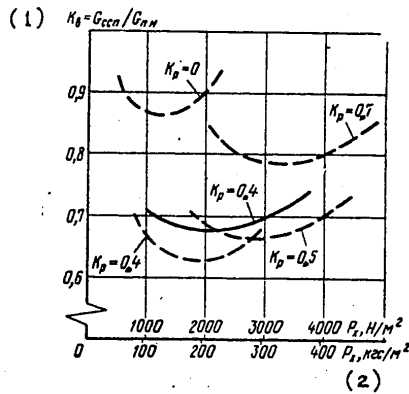


Figure 3.7. Mass of the Descent and Landing Gear as a Function of Payload for Vehicles of Different Lifting Area

Key:

1.  $K_B = G_{CCN} / G_{PN}$ , ratio of descent and landing gear mass to the payload mass
2. Midsection loading  $P_x$  in  $N/m^2$  (upper scale) and in  $kg\text{-force}/m^2$  (lower scale)

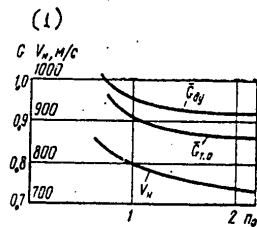


Figure 3.8. Relative Mass of Rocket Motor and Flight Velocity at the Instant of Motor Ignition as a Function of Initial Thrust-to-Weight Ratio

Key:

1.  $V_H$  (m/s)

FOR OFFICIAL USE ONLY

FOR OFFICIAL USE ONLY

## CHAPTER 4

ANALYSIS OF TRAJECTORY CHARACTERISTICS FOR CONTROLLED ENTRY  
AND DESCENT INTO THE ATMOSPHERE OF VENUS

The great density of the Venusian atmosphere determines the shape of descent vehicles and the schedule of operations to be conducted during the descent and after the landing on the surface. Contradictory requirements, which the vehicle has to satisfy at the different stages of flight, make it necessary to change the vehicle configuration as it penetrates the atmosphere. Entry into the atmosphere is made with great speed, reaching 12 km/s for direct descent from approach trajectories, 10.2 km/s for descent from highly elliptical orbits, and 7.5 km/s for descent from a near-planetary orbit. The vehicle is braked intensively in the upper layers of the atmosphere and, for a shallow entry, the conditions of motion and heat exchange resemble processes in the Earth's atmosphere. The shape of a descent vehicle designed for braking during entry into the atmosphere does not differ from the traditional shape of descent vehicles. However, the process of intensive braking is accomplished, as a rule, at altitudes of 30 to 40 km, after which the vehicle begins to descend gradually and to penetrate the dense, 700-degree-C atmosphere.

Vehicles for descent into or drift in an atmosphere whose pressure reaches 100 kg-force/m<sup>2</sup> resemble more a deep-diving bathyscaph than a flight vehicle in their structure and external appearance.

There are two groups of problems that had to be solved in designing ballistic descent vehicles and that will have to be met in the future in the design of heavy controllable vehicles for the exploration of Venus.

The first group of problems is connected with selecting the best means of braking in the upper layers of the atmosphere and with decreasing the levels of load factors and thermal stresses for the descent trajectory.

The second group of problems is defined by the operating conditions at high external pressures and temperatures, and the problems of descent and landing under these conditions.

One way of solving problems of landing on Venus is a functional separation of the planetary landing system into descent and landing vehicles, with the latter being the payload of the former. Conditions on the planet are apparently not suitable for conducting landing operations or for the design in the near future of planetary systems equipped with means of returning to Earth or to a near-planetary orbit. However, the design of heavy controllable descent vehicles capable of effectively braking in the upper layers of the planet's atmosphere, delivering there their landing or drift vehicles for flight in the denser layers of the atmosphere, appears to be one of the tasks of space flight for the near future. Let us consider the design-ballistic questions applicable to such vehicles, dealing with descent and controlled flight at the boundary of the dense atmospheric layers.

FOR OFFICIAL USE ONLY

FOR OFFICIAL USE ONLY

In contrast to a descent into the atmosphere of Mars (Chapter 3), the problem of absorbing energy of the vehicle and obtaining acceptable landing velocities for Venus is achieved without special changes in the structure and without having to perform special control operations during the descent segment. A ballistic descent vehicle entering the atmosphere within a wide range of entry angles (from  $-30$  to  $-90^\circ$ ) will decelerate to a speed required for the operation of landing systems. The speed of descent to the surface of the planet is determined by the specific loading on the vehicle's midsection and depends on the conditions of entry into the atmosphere and, for practical purposes, is independent of the lift-to-drag ratio.

The region of attainable descent velocities that are characteristic for different braking characteristics of the vehicle is shown in Figure 4.1 for variations in atmospheric parameters. It is apparent that acceptable landing velocities can be achieved without special auxiliary braking systems. The instant of terminating the intensive braking phase during atmospheric entry and transition to slow descent should be fixed, because it is precisely at this instant that a change is made in the method of controlling the trajectory, operation of descent vehicle systems is terminated, and landing gears or paraballoon systems intended for aerostatic braking of the landing vehicle begin functioning. Apparently, it is the transition to subsonic flight speeds which indicates that deployment of landing systems can be initiated. We can determine when such a moment arrives for specific conditions of atmospheric entry (entry speed of 11 km/s, trajectory flight-path angle of  $30^\circ$  at a 130-km altitude) by examining Figure 4.2. The achievement of a flight speed of 200 m/s is taken as the transition point. The curve showing the terminal flight altitude ( $H_k$ ) at this moment (for a nominal model of the atmosphere for a descent trajectory with maximum effective lift-to-drag ratio, and for vehicles with different lifting characteristics ( $K_p$ ) and specific loading ( $P_x$ ) on the lifting surface) indicates that for acceptable vehicle dimensions, the increase in the available lift-to-drag ratio makes it possible to start the descent phase at higher altitudes (and simultaneously increasing the vehicle's loiter time in the upper layers of the atmosphere and the effectiveness of operations for sounding the atmosphere of the planet). It is characteristic that even for ballistic descent the initial descent altitude is between 20 and 40 km. However, a ballistic descent in conjunction with the steep angle of entry into the atmosphere is accompanied by high load factors and heat flows. Using a small or moderate lift-to-drag ratio makes shallow entries into the atmosphere possible (entry angles less than  $30^\circ$ ), thus reducing both loading and thermal stress. The graph of Figure 4.3 illustrates the results of calculations of limiting entry trajectories attainable for motion near the upper boundary of the entry corridor (condition of capture by the atmosphere) and close to the lower boundary of the entry corridor (determined by the maximum load factor). The required dimension of the entry corridor is determined on the basis of the difference in the altitude of the theoretical perigees, and for a vehicle with braking characteristics close to conventional ones ( $P_x = 2,000$  to  $5,000$  N/m<sup>2</sup> (200 to 500 kg-force/m<sup>2</sup>)), this results in a 40-km-high entry corridor. The figure shows the relationship between the maximum load factors reached during

FOR OFFICIAL USE ONLY

FOR OFFICIAL USE ONLY

entry along the lower boundary of the corridor (entry angles of 5 to 7° at a 130-km altitude) and the available lift-to-drag ratio. This relationship is valid when, for motion along the upper boundary of the corridor of prescribed dimension, capture is provided for by the value of the lift-to-drag ratio considered (for negative lift). The region between the two curves in the figure is characteristic for most approach trajectories, with a speed of entry into the atmosphere between 11 km/s (lower curve) and 12 km/s (upper curve). Analogously to returns to Earth from interplanetary approach trajectories, an increase in lift-to-drag ratio and use of a shallow atmospheric entry result in a sharp reduction in specific loading. For example, loading is decreased by 2-1/2 to 3 times by changing from a ballistic vehicle to a vehicle with a moderate lift-to-drag ratio of about 0.6 to 0.8.

An even greater reduction in load factor is expected for descents from near-planetary orbits. The high additional energy losses of such a mode of sounding the atmosphere are justified by the added opportunities for making a circumspect choice of the region to be studied in the atmosphere and then directing the descent vehicle to that location. Figure 4.4 shows how the magnitude of the maximum load factor for vehicles with such braking characteristics changes with available lift-to-drag ratio for the case of entry from near-planetary orbits.

The cross hatch regions show what is attainable for descent vehicles entering the atmosphere from highly elliptical orbits with the lower boundaries of each zone corresponding to entry speeds into the atmosphere of 9 km/s and upper ones to entry speeds of 10 km/s. The various regions shown in Figure 4.4 are characterized by varying requirements on the control during descent and landing operations of the planetary sounder. Region 1, whose boundaries are shown by a dot-dash line, corresponds to low control requirements for descent from orbit, but entails high load factors for vehicles of traditional form, with lower load factors for vehicles with high lift-to-drag ratios. The dimensions of the required entry corridor in this case is 80 km. Region 2, bounded by dashed lines, corresponds to a 40-km entry corridor, and, finally, region 3, whose boundary is shown by solid lines, corresponds to a 20-km entry corridor. In the latter case, it is possible to reduce load factors to acceptable levels for traditionally shaped vehicles.

Proper choice of the conditions of motion during the descent phase also makes it possible for vehicles with moderate available lift-to-drag ratios to brake at higher altitudes than for constant-lift flight (Figure 4.2).

Use of leveling-off regions after passing the maximum load factor makes it possible to avoid, on one side, skipping and leaving the atmosphere, and on the other side, to avoid dives with a loss of altitude. One of the means for leveling off is control based on an isoaltitude law for changing the effective lift-to-drag ratio. For the condition that the derivative of the flight-path angle equals zero, there exists a completely defined law in the equations of motion for the variation of the available lift-to-drag ratio and drag of the vehicle. It is possible to achieve flight with a constant

FOR OFFICIAL USE ONLY

FOR OFFICIAL USE ONLY

flight-path angle and constant loading on the midsection without changing the angle of attack by controlling the roll attitude about the velocity vector for small initial flight-path angles. This has to be initiated immediately after the instant of passing maximum load factor and before the beginning of the skip. If the flight-path angle is assumed to be small, then the programmed relationship for the roll angle of the vehicle has the form

$$\gamma_{xp} = \arccos \left[ \frac{1}{K_p} \frac{1}{n_{x_T}} \left( 1 - \frac{V^2}{g_n R_n} \right) \frac{g_n}{g_3} \right],$$

where

$$n_{x_T} = \frac{n_{e \max}}{V_a^2 \sqrt{1 + K_p^2}} V^2.$$

Here  $n_{x_T}$  is the programmed instantaneous value of load factor determined by flight speed;  $g_n$ ,  $R_n$  are the acceleration of gravity and the radius of the planet;  $g_3$  is the acceleration of gravity on Earth; and  $n_{e \max}$  is the magnitude of the maximum load factor before entering the leveling-off region.

Results of the search for the best region of braking show that for the main segment of the descent trajectory it is best to use leveled-off motion or shallow descent. Figure 4.5 shows an example of an optimal trajectory for entry along the lower boundary of a 40-km corridor. Speed of atmospheric entry is 11 km/s, the loading on the midsection is 5,000 N/m<sup>2</sup>, and the available lift-to-drag ratio is 0.5.

The isoaltitude segment of leveling off is provided by changing the effective lift-to-drag ratio, whose required magnitude is shown by the dashed line in the same figure.

The isoaltitude segment of the trajectory and the isoload-factor segment that follows it are more graphically represented in Figure 4.6, where the same trajectory is shown in the altitude-vs-flight-speed coordinate system. The dashed line shows the required nominal value of the roll angle determined from the condition of implementing the design control laws. Completion of the segment of intensive braking in the atmosphere is accomplished at the maximum lift force with a zero roll angle of the vehicle.

The result of the described program of braking is the injection of the descending vehicle into the final phase of braking in a relatively short time and without significant loss of altitude, during which the landing apparatus begins to operate.

FOR OFFICIAL USE ONLY

FOR OFFICIAL USE ONLY

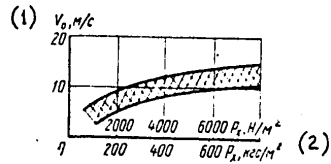


Figure 4.1. Region of Attainable Descent Velocities for Landings on the Surface of Venus

Key:

1.  $V_0$  (m/s)
2.  $P_x$  in  $N/m^2$  (upper scale) and in  $kg\text{-force}/m^2$  (lower scale)

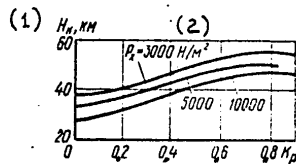


Figure 4.2. Initial Descent Altitude for Different Descent Vehicle Characteristics

Key:

1.  $H_k$  (km)
2.  $P_x$  ( $N/m^2$ )

FOR OFFICIAL USE ONLY

FOR OFFICIAL USE ONLY

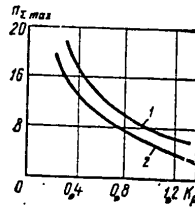


Figure 4.3. Maximum Load Factor as a Function of Available Lift-to-Drag Ratio for a 40-km Entry Corridor and Direct Descent from an Approach Trajectory. (For Vehicles with a Midsection Loading of 2,000-5,000 N/m<sup>2</sup>)

Key:

1. Speed of entry into the atmosphere: 12 km/s
2. Speed of entry into the atmosphere: 11 km/s

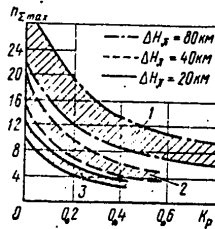


Figure 4.4. Maximum Load Factor as a Function of Available Lift-to-Drag Ratio for Descent from Near-Planetary Orbits. (For  $P_x$  of 2,000-5,000 N/m<sup>2</sup> and  $V$  of 9-10 km/s)

Key:

1. Entry corridor of 80 km
2. Entry corridor of 40 km
3. Entry corridor of 20 km

FOR OFFICIAL USE ONLY

FOR OFFICIAL USE ONLY

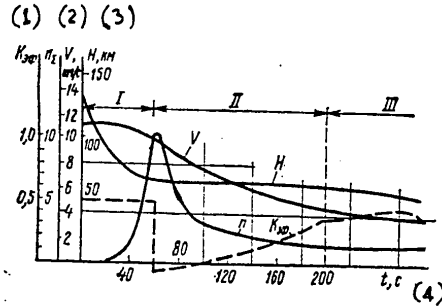


Figure 4.5. Parameters of a Descent Trajectory with Levelled-off Segment  
Key:

- |   |                                 |
|---|---------------------------------|
| I. Segment of entry into the atmosphere | 1. Effective lift-to-drag ratio |
| II. Isoaltitude segment                 | 2. $V$ (km/s)                   |
| III. Isoload-factor segment             | 3. $H$ (km)                     |
|   | 4. $t$ (s)                      |

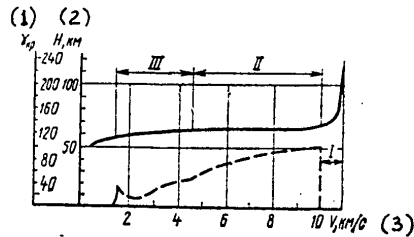


Figure 4.6. Trajectory of Descent with Isoaltitude Plateau Shown in the Altitude/Speed-of-Flight Coordinates  
Key:

- |   |               |
|---|---------------|
| I. Segment of entry into the atmosphere | 1. Roll angle |
| II. Isoaltitude segment                 | 2. $H$ (km)   |
| III. Isoload-factor segment             | 3. $V$ (km/s) |

FOR OFFICIAL USE ONLY



FOR OFFICIAL USE ONLY

CHAPTER 5

DETERMINING DESIGN PARAMETERS FOR DESCENT VEHICLES  
TO SOUND THE ATMOSPHERE OF JUPITER

The distinguishing feature of entry into the atmosphere of Jupiter is the great speed of approach to the planet. This speed is mainly dependent on the value of the parabolic escape velocity, whose magnitude is determined by the powerful gravitational field of the planet and exceeds 60 km/s.

In analyzing the conditions of entry into the Jovian atmosphere, it is necessary to consider the planet's rotation. This makes it possible to reduce the speed of atmospheric entry to a value of 49 to 50 km/s, having arranged entry along a shallow trajectory in an easterly direction in the region of the equator and in the same direction as the motion of the rotating atmosphere. The main portion of the vehicle's kinetic energy is reduced during the process of intensive braking in the upper layers of the atmosphere and before reaching the cloud layer. The distance from the planet's center to the cloud layer is usually assumed as the base or reference level of calculations, and, as in Earth conditions, the pressure at this level is said to be 1 atmosphere.

Most current models of the Jovian atmosphere assume an insignificant variation in temperature with altitude in the upper layers of the atmosphere, and the composition of the atmosphere is assumed to be basically hydrogen (70 to 85 percent) and helium (30 to 15 percent).

Implementation of descent, whose goal is the delivery of instrument containers for measuring atmospheric parameters, is complicated by the high speed of entry into the atmosphere, with attendant intensive thermal and load-factor effects on the vehicle.

In aerodynamic heating, radiative heat flows from the shock layer predominate, and, as the vehicle is braked very hard with load factors reaching hundreds of g's, the thermal effect on the surface coating has the character of a thermal shock.

In contrast to descent vehicles entering the atmospheres of Earth, Mars, and Venus, a descent vehicle for sounding Jupiter and other giant planets is subjected to a much more powerful thermal effect, and thermal protection of such a vehicle is one of the basic problems in designing it. Choice of a descent-vehicle shape constrains the task of minimizing the weights of structure and of thermal protection.

Let us imagine what the flight regimes and the shape of such a vehicle will be and in what respects this vehicle must differ from traditional descent vehicles that land on the nearby planets. It is logical to assume that for the first experiments in sounding the Jovian atmosphere preference will be given to simple and proved designs and to reliable technical solutions. We

FOR OFFICIAL USE ONLY

FOR OFFICIAL USE ONLY

can also assume that the vehicles that will be initially designed will perform ballistic, uncontrolled descents analogous to the initial Martian, Earth, and Venusian descent vehicles.

Among the systems necessary for descent and which will affect the choice of the vehicle's shape, structure and thermal protection are basic. The structure includes the envelope, the primary structure of the body, fittings for the payload, devices for attaching apparatus, hatches, and structural frames. The vehicle's envelope can be nonhermetic, but it must be rigid in order to withstand the dynamic loading during oscillation of the vehicle at the moment of atmospheric entry. Instruments and equipment, however, have to be located in hermetically sealed sections. The lifting portion of the envelope (the heat shield) affects stability due to external pressure, which attains magnitudes on the order of tens of atmospheres at the maximum dynamic pressures. Thermal protection includes the ablative surface, the heated thermal protection coating, and thermal insulation. Powerful thermal flows require the use of thermal protection coatings possessing high breakdown enthalpy, a significant working temperature of sublimation, and good solid-phase reflectivity at the exterior breakdown front of the coating and high absorption characteristics of the products of the breakdown of the coating that enter the boundary layer. The thermal-protection work process is accompanied by a significant expenditure of the coating mass as a result of which there forms in the boundary layer a bubble of pyrolytic gas, consisting mainly of products of the breakdown of the thermal protection coating.

The influx of this gas, which is cooler than the hydrogen-helium mixture in the shock layer, blocks convective heat flows, and a sheet of the products of the breakdown absorbs a part of the energy that radiates from the shock layer in accordance with the integral spectral coefficient of absorption. The linear rate of breakdown of the thermal protection material at this instant is so great that the propagation of the breakdown front into the depth of the thermal protection surface precedes the motion of the "heating wave," that is, a movement of the layer with the limiting admissible temperature for the structure.

Flow about the vehicle during the entire basic segment of the descent trajectory is hypersonic, and the aerodynamic braking force is determined by the pressure distribution over the surfaces of the vehicle, where this force is generated by a spherical or conical heat shield of either blunted or moderately pointed shape. The aft fairing of the vehicle located in the dead-flow zone can carry spoilers, which provide passive stabilization of the vehicle for a misoriented entry into the atmosphere aft end first.

In choosing design parameters, one should assume that the vehicle should be capable of moving along any trajectory within the design corridor of entry into the atmosphere. In the present case, the upper boundary of the corridor of entry is determined by the capture by the atmosphere, while the lower boundary corresponds to maximum loading. For vehicles with different shapes

FOR OFFICIAL USE ONLY

## FOR OFFICIAL USE ONLY

that have different ballistic characteristics, capture by the atmosphere can be determined by the minimum value of the specific load for a given choice of model atmosphere.

In searching for the design parameters of the descent vehicle, it is necessary to estimate the mass of structure and of thermal protection for vehicles with different configurations. In accordance with a general formulation of the design-search problems for descent vehicles, each such design estimate has to be carried out through a comparison of all possible conditions of motion with the object of eliminating those that result in the maximum values for the mass of structure and thermal protection material. It can be assumed, and the results of calculations for specific vehicle shapes support such an assumption, that the maximum mass of ablated thermal protection material will occur for a trajectory of deep immersion into the atmosphere that differs from flight during entry along the upper boundary of the corridor. The greatest mass of thermal insulation will be required for the longest trajectory, which occurs for motion close to the upper boundary of the entry corridor. Maximum external pressure on the lifting envelope of the heat shield, which is the controlling case for design of the shell, will occur at the highest dynamic pressure, that is, at the moment of maximum load factor for the steepest allowable trajectory. Let us formulate the assumptions made in the design calculations for the case of searching for best parameter values that will determine the shape, design elements, and conditions of motion of the descent vehicle. Basic among these assumptions are the following:

1. In calculating volumetric and centering characteristics, it is enough to use the dimensions of the vehicle's outline. Geometric parameters that can be varied during selection of the shape are the outlines of the external thermal protection layer before entry into the atmosphere.
2. In calculating the aerodynamic characteristics, we can assume that the shape of the vehicle remains constant, that is, the linear ablation and erosion of the surface can be neglected in calculating vehicle drag.
3. Ballistic characteristics and, in particular, loads on the midsection are determined along the descent trajectory with consideration for the dimensional changes of the lifting profile due to the linear ablation. Simultaneously, in calculating the load on the midsection, consideration is given to the decreasing weight of the vehicle during flight due to the decreasing mass of the thermal protection coating.
4. In estimating heat flows, it is necessary to account for the increase in the radius of bluntness due to the varying ablation rates of the mass of the coating at the stagnation point and along the periphery of the heat shield. This circumstance is especially important for small initial radii of bluntness for conic frontal shields. Optimum initial radius of bluntness, determined from the relationship of radiative and convective heat flows, is on the order of 0.10 to 0.20 m for vehicles with a midsection loading of from 2,000 to 5,000 N/m<sup>2</sup> (200 to 500 kg-force/m<sup>2</sup>).
5. Inasmuch as the basic part of the descent trajectory (during which the vehicle passes through maximum loading and thermal flows, and the kinetic

FOR OFFICIAL USE ONLY

energy is reduced by more than 99.8 percent) occurs at hypersonic flight velocities (for Mach numbers above the 4-to-6 range), it is adequate to use Newton's hypothesis for determining the aerodynamic characteristics. The ratio of static pressure to dynamic pressure at specific points on the surface is assumed to be constant along the descent trajectory under this condition.

6. Ablation of the thermal protection coating has to be determined considering the emission of radiation and the blocking of convective thermal flows by the layer of gas formed by the breakdown products of the thermal protection material.

The assumptions listed are, in our opinion, acceptable for estimating the conditions of motion and aerodynamic and weight characteristics of the vehicle during design calculations. More complex models of the flow and heat exchange are used for verification calculations during this stage of design.

In Figure 5.1 are shown the parameters of a descent trajectory for a vehicle with conic heat shield, which, before entry into the atmosphere, has a load of  $1,720 \text{ N/m}^2$  ( $175 \text{ kg-force/m}^2$ ) on the midsection, a bluntness radius of  $0.2 \text{ m}$  at the stagnation point, and a cone half-angle of  $70^\circ$ . Also shown in the figure is the variation in load on the midsection for such a vehicle due to ablation of the thermal protection coating during flight.

The search for the best values of parameters that determine the shape of the vehicle is broken down into a series of design calculations, during each of which mass characteristics are determined. Each of these design calculations is iterative, because in the algorithm for computing weight or mass it is necessary to assume the ballistic parameter, which, in turn, is determined by the weight or mass of the vehicle. Also, as shown earlier, determining the mass of the system should consider the worst case for each system, that is, the worst of all possible descent trajectories. One should also consider that for each new configuration of geometric parameters of the vehicle it is necessary to search for the limiting allowable trajectories corresponding to the upper and lower boundaries of the entry corridor. All the material presented above establishes the need for repeated trajectory calculations during a single pass through the design calculations. It is possible to reduce the labor in such an operation and the time lost if one foregoes accuracy in estimating descent trajectory characteristics and does not integrate the equations of motion. For estimating the mass characteristics, it is usually necessary to know the distribution of the loads on the vehicle (structural mass), flight speed, and density of the atmosphere at a given altitude (thermal flows and mass of the thermal protection layer) as functions of time. For design estimates it is desirable to determine rapidly the limiting trajectories, that is, trajectories with the largest and smallest values of maximum load factor. For such purposes, a method can be proposed for estimating trajectory parameters that uses the thermodynamic relationships involving load factor and flight time.

FOR OFFICIAL USE ONLY

FOR OFFICIAL USE ONLY

During ballistic descent, the load factor initially increases sharply and then, having passed a maximum, decreases gradually. As a rule, for maximum permissible load factors in excess of 100 g's, a single load-factor maximum occurs, and a typical expression for it (as a function of flight time) is conveniently given by a formula of the type

$$n = a\tau^2 e^{-c\tau} \quad [5.1]$$

where  $n$  is the load factor;  $\tau$  is the time of flight; and  $a$  and  $c$  are coefficients that determine the shape of the load factor curve, which depends on the assumed model for the atmosphere and the conditions of entry into the atmosphere.

If in the equations of motion we assume a load factor much greater than unity and a flight-path angle during the main segment of braking in the atmosphere as close to zero, integration of the equations of motion in velocity coordinates yields the following expressions for velocity and atmospheric density as functions of time:

$$V \approx V_{\text{BX}} - 9.8a \left[ e^{c\tau} \left( \frac{\tau^2}{c} - \frac{2\tau}{c^2} + \frac{2}{c^3} \right) - \frac{2}{c^3} \right]; \quad (5.2)$$

$$\rho \approx \rho_{xcp} n(\tau) \frac{1}{[V(\tau)]^2}, \quad (5.3)$$

where

$$c = 2/\tau_B; \quad a = 7.4n_{\text{max}}/\tau_B^2$$

$V_{\text{BX}}$  is the speed of entry into the atmosphere;  $\tau_B$  is the instant of passing the maximum load factor; and  $n_{\text{max}}$  is the maximum load factor. This load factor is less than  $n_{\text{max H}}$ , the limiting one for the vehicle (for the lower boundary of the entry corridor), and greater than  $n_{\text{max B}}$ , the minimum permissible one for the condition of capture of the vehicle by the atmosphere (upper boundary of the entry corridor); and  $P_{xcp}$  is the mean value of loading on the midsection for this trajectory. As the minimum permissible load factor,  $n_{\text{max B}}$ , we will assume 100 to 150 g's.

FOR OFFICIAL USE ONLY

FOR OFFICIAL USE ONLY

Figure 5.2 shows the results of a precise calculation of trajectory, namely: Maximum load factor as a function of the angle of entry into the atmosphere for a vehicle with a midsection load of  $1,720 \text{ N/m}^2$  ( $175 \text{ kg-force/m}^2$ ) and for a nominal atmosphere model. Reaching an altitude of 400 km above the cloud layer is assumed to be the instant of entry into the atmosphere. The same figure shows the period for braking required to reduce velocity to 1 km/s and the relative mass of the ablated thermal layer for different conditions of atmospheric entry for a vehicle that has a conic heat shield with a cone half-angle of  $70^\circ$  and a bluntness radius of 0.2 m.

In the general case, the levels of maximum load factor are related by an equation that, for design calculation, is assumed to be linear. The maximum load factor within the corridor of entry is given by the expression

$$n_{\max} = n_{\max B} (1 - \bar{K}_n \Delta\theta) \quad (5.4)$$

where  $\Delta\theta$  is the increase in the angle of atmospheric entry and determines the location of the given trajectory with respect to the upper boundary.

The coefficient  $\bar{K}_n$  depends on the assumed atmosphere model and, for practical purposes, does not depend on the vehicle's ballistic parameters. For design calculations, it can be assumed that  $\bar{K}_n = 0.19 \pm 0.03$ . The instant of passing the maximum load factor is determined within the bounds of total braking time  $\tau_E$ , which in turn depends on the velocity impulse and maximum load factor, as follows:

$$\tau_s = K_r \tau_i, \quad \tau_i = \frac{V_{ex}}{n_{\max} g} K_{cp}, \quad (5.5)$$

where  $K_{cp}$  is the coefficient determining the mean load factor or degree of "fill" of the load-factor diagram;  $K_{cp} = 0.3$  to  $0.36$ . The coefficient  $K_r$  depends on the assumed atmosphere model and lies in the range from  $0.31$  to  $0.34$ .

Methods of design estimation of the mass of the ablative and heated thermal protection layers are based on recommendations in references from home and abroad (Refs. 1, 61, 62, 63).

The main difficulty in calculating the ablation of the thermal protection layer is the need to account for weakened convective and radiative heat transfer in the layer of pyrolytic gas formed by the products of the breakdown of the coating. Estimating the rate of decrease in the mass of thermal protection, under conditions when convective heat transfer is blocked by ablation and the radiation is frequently absorbed in accordance with the integral spectrum of absorption of the breakdown products of the thermal protection layer, can be done by using expressions for the attenuation of heat transfer computed for different surfaces. These expressions take into account the feedback in the mechanism of coating breakdown and show how the relationship between thermal-protection-mass ablation and the rate of mass change in the incoming flow affects the relationship between heat transfer

FOR OFFICIAL USE ONLY

FOR OFFICIAL USE ONLY

through the vapor barrier of the coating and heat transfer due to radiation from the shock layer or due to transport by the gas in the boundary layer.

Figure 5.3 shows how the convective ( $q_k$ ) and radiative ( $q_r$ ) heat transfer and mass of the ablating thermal protection layer vary as a function of time for a trajectory with a maximum load factor of 200 g's for a vehicle of moderately pointed shape with a cone half-angle of  $50^\circ$  and midsection loading of  $2,940 \text{ N/m}^2$  ( $300 \text{ kg-force/m}^2$ ).

To draw any conclusions about the advantages of one or another aerodynamic form solely on the basis of calculations of thermal protection layer ablation (as is unfortunately done in a number of references) is premature, in that the total mass of the vehicle depends on the thickness of the heat-sink insulation, on the thickness of the envelope, and on the dimensions of the structural components of the vehicle body, as well as on the dimensions of the trim tabs of the skirt, or the ballast mass. Only by integrated accounting for all indicated factors and by considering volume-centering characteristics and heat-shield strength is it possible to judge competently the advantages of one or another aerodynamic shape.

Calculations show that for substantial pointing of the nose cone the volumetric characteristics of the vehicle worsen as the available volume and, therefore, surface of the vehicle increase. At the same time, the surface use effectiveness decreases, that is, the total surface and the heat-shield surface are increased, which can lead to a sharp increase in the mass of the structure and of thermal protection. However, in this case, the specific weight or mass of one square meter of heat-shield structure is reduced due to the increase in the curvature of the envelope, which provides resistance to external pressure. Radiative and convective heat transfer on the side surfaces of a slender cone are substantially smaller than in the stagnation region, but as the shape becomes slenderer, heat transfer in the stagnation region increases sharply because the vehicle, having small resistance and cross section (that is, a greater midsection load) moves along a steeper trajectory with higher thermal stresses at a given level of maximum permissible load factor. Also, it is necessary to account for ballast mass and means for passive stabilization (trim tabs and skirts) that increase for a slenderer nose cone.

Apparently, if no account is taken of other circumstances (descent vehicle layout as part of the spacecraft, presence of experimental and engineering sections, degree of reliability in design estimates, and so forth) and weight or mass criteria are used in choosing vehicle shape, then the optimum shape for a vehicle with a mass of 500 to 2,000 kg is the shape with a moderately slender conic heat shield having a cone half-angle of  $45^\circ$  to  $55^\circ$  and a bluntness radius of 0.15 to 0.25 m. The choice of diameter or slenderness ratio of the vehicle depends on the method used to provide static stability for noncontrolled entry into the atmosphere.

FOR OFFICIAL USE ONLY

FOR OFFICIAL USE ONLY

One should expect that the mass of structure and of thermal protection will be 110 to 140 percent of the payload mass for a descent sounder vehicle delivering measuring instruments into the Jovian atmosphere from an approach trajectory, with the mass of thermal protection coating ablated being 20 to 30 percent of the total vehicle mass.

Questions of reliability and precision of design estimates are quite important for vehicles such as Jupiter sounders being designed for flights under new and unknown conditions. The uncertainty of operating conditions, due to lack of knowledge of many parameters of the atmosphere and planet as well as to unusual, extreme conditions of entry into the atmosphere, makes caution necessary in using the results of such design calculations based on any methods, no matter how complex, because all methods have to use initial data that have substantial scatter in their values. Under such conditions, it is necessary to supplement the traditional and known design criteria by risk criteria, which directly or indirectly determine the possible variation in values of design characteristics. These risk criteria also define the degree to which the scatter in specific parameter values influences the scatter of design criteria values and the level of reliability of the relative estimates based on comparisons of possible values of such design criteria to the standardized limits established for them.

In the present case, the scatter in the values of mass or weight characteristics is primarily due to the scatter in data that determine both the atmosphere model and the parameters defining the conditions of atmospheric entry. The variations in the values of the characteristics of structural and thermal protection materials (effective enthalpy, breakdown temperature, degree of surface blackness, and so forth) and the scatter in the aerodynamic characteristics of the vehicle have a definite effect on the scatter in the mass criteria.

The distribution histogram shown in Figure 5.4 was obtained from statistical modeling of the scatter in the mass of structure and thermal protection for one type of descent vehicle. Relative mass indicators are shown, with the mass of the descent gear given as a fraction of payload mass.

One criterion that can be used to estimate risk in making decisions based on information from design calculations is the probability of coming up with design estimates that would lead to poor or simply impossible vehicle designs. Let us assume that there exists a certain limit on the total vehicle mass expressed as a fraction of the interplanetary system mass. On the other hand, there also exists a well-defined minimum mass for the instruments needed for scientific exploration. The limiting boundary for the mass of the structure with thermal protection is shown in Figure 5.4, and this boundary is determined by the minimum mass of the payload.

A situation can occur in which the mass of both the structure and the thermal protection of the vehicle exceeds the boundary established for it by the payload. In our example, the probability of such an event is quite high ( $P = 0.08$ ).

FOR OFFICIAL USE ONLY



FOR OFFICIAL USE ONLY

A change in the vehicle parameters or the establishment of better substantiated and advantageous weight reserves on part of the entire space complex will make it possible to reduce the decision-making risks during the preliminary design stage. Criteria for estimating risk when design estimates are uncertain and examples that illustrate the means of applying such criteria are described, for example, in Reference 23.

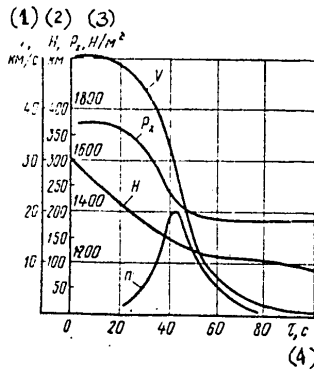


Figure 5.1. Trajectory Parameters for Descent into the Atmosphere of Jupiter

Key:

- 1.  $V$  (km/s)
- 2.  $H$  (km)
- 3.  $P_x$  ( $N/m^2$ )
- 4.  $\tau$  (s)

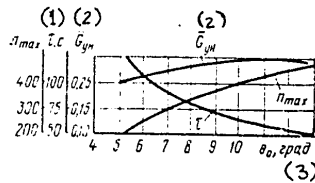


Figure 5.2. Maximum Load Factor, Time of Flight, and Relative Mass of Ablative Thermal Protection Layer as Functions of the Angle of Entry into the Atmosphere

Key:

- 1.  $\tau$  (s)
- 2. Relative ablative mass  $\overline{G}_{YH}$
- 3. Angle of entry (deg)

FOR OFFICIAL USE ONLY

FOR OFFICIAL USE ONLY

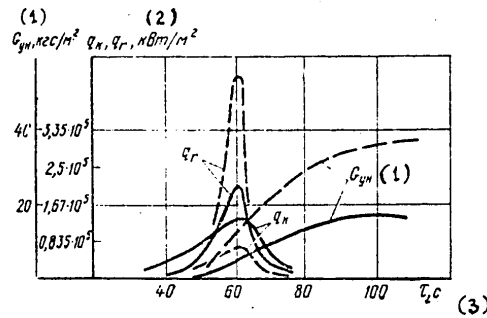


Figure 5.3. Heat Transfer and Mass of Ablative Thermal Protection Layer as Functions of Time. (Solid lines for the stagnation point; dashed lines for a point on the edge of a conic heat shield)

Key:

1. Ablative mass  $G_{YH}$  ( $kg/m^2$ )
2.  $q_k, q_r$  ( $kW/m^2$ )
3.  $\tau$  (s)

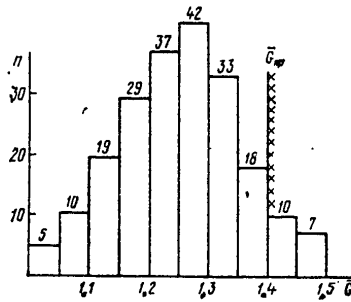


Figure 5.4. Histogram of the Distribution of Design Estimates of the Mass of Structure with Thermal Protection

Key:

1. Limiting value  $\tau_{HP}$

FOR OFFICIAL USE ONLY

PART TWO

METHODS FOR STUDYING SOFT LANDING OF SPACE VEHICLES  
ON PLANETS LACKING ATMOSPHERES

The basic questions of choice, calculation, and control along space vehicle trajectories of approach and descent to planets lacking an atmosphere and to the Moon have been described widely in both the specialized and the popular science literature (Refs. 3, 16, 17).

Strangely enough, however, the literature does not treat in sufficient depth the terminal stage of vehicle flight (starting with altitudes of 30 to 10 m above the planet) including ground contact, skidding along the ground, and coming to complete rest on the surface in an attitude that is the initial condition for subsequent vehicle operation on a given celestial body. And this, in spite of the great significance of this stage.

The ground-based experimental development of descent vehicles for interplanetary stations fared even worse in this sense, which at best was mentioned only with a hint as to its complexity and the large amount of labor required.

In view of this situation, the second part of the book will deal basically with a discussion of theoretical, experimental, and design aspects of providing the landing vehicle with a safe, soft touchdown on a planet or other celestial body to be explored.

Besides providing for "softness," the landing of the vehicle on the surface has to satisfy the following requirements: (1) Maintaining the stability of vehicle attitude during the entire landing process; (2) assuring that the vehicle will not "jump" following initial contact with the ground; (3) assuring that the attitude of the vehicle on the planet after landing will allow normal operation of all its systems (and, if provided in the program, also for the successful conditions for subsequent lift-off); (4) minimizing the likelihood of various emergencies during landing by increasing the reliability of the vehicle systems.

Analysis of the operation of landing on planets shows that the speed of approach between vehicle and ground is in the range from a few m/s up to ten and more m/s. From this it follows that the space vehicle has to be equipped with a reliable landing gear incorporating a special shock-absorbing device. Several designs exist for vehicle landing gear, for example, petal-shaped and column supports, girder structure, thin-wall envelopes, and others.

Apparently, the design of a reliably functioning landing gear for an interplanetary space vehicle is not possible without doing many studies including theoretical, experimental, design, and layout.

FOR OFFICIAL USE ONLY

FOR OFFICIAL USE ONLY

## CHAPTER 6

THEORETICAL ANALYSIS OF SOFT-LANDING DYNAMICS  
AND OF SPACE LANDING VEHICLES

## Mathematical Model of a Space Landing Vehicle

A space landing vehicle represents quite a complex, elastic system of interacting bodies due to the presence of elastic connections between its structural elements (payload, scientific equipment, propulsion and instrument sections, and supports).

The mathematical description of the dynamics of landing on a planet without an atmosphere, on Mars, for example, or on the Moon, of such a complex system for the general case of three-dimensional motion during the stage immediately preceding touchdown of the vehicle support on the ground leads to an extraordinarily cumbersome system of differential equations, including unknown magnitudes of the coefficients of elastic connection between individual elements of the space landing vehicle that can only be determined experimentally by using the full-scale object. Therefore, calculations on the dynamics of landing on planets by using such mathematical models of space landing vehicles are, due to the great effort required, possible only for checking selected critical landing cases for space vehicles already designed.

The comprehensiveness of a study of soft-landing dynamics for space landing vehicles during the preliminary design stage requires the application of simpler and less labor-consuming methods of engineering research in evaluating various structural designs of vehicle landing gears and in choosing optimum parameter values.

Let us consider the general case of three-dimensional motion of a space landing vehicle with rigid body and deformable landing gear consisting of a system of columns forming an inverse tripod. The central column of the tripod is equipped with a shock absorber and can be deformed (Figure 6.1). The complex motion of the space landing vehicle during soft landing on a planet can be represented as two less complex motions: (1) The three-dimensional motion of the body of the space landing vehicle; (2) the motion of the landing gear pads (having some equivalent mass  $m_i$ ) on the ground in any direction but with the limitation imposed by the landing surface itself.

The three-dimensional rigid body motion of the space landing vehicle is influenced by the disturbing forces and moments, which result from the interaction of the landing gear with the ground. Here the angle of inclination  $\theta$  of the landing surface and the coefficient of friction  $f$  of the landing gear pads on the surface can vary widely.

In order to describe such three-dimensional motions of the space landing vehicle during soft landing, it is necessary to formulate and solve a system

FOR OFFICIAL USE ONLY

FOR OFFICIAL USE ONLY

of  $6 + 2N$  dynamic equations, each of which is a nonlinear second-order differential equation ( $N$  is the number of landing gears). The complexity of solving such equations requires the use of numerical methods and computers.

In order to reduce these equations to the form of ordinary linear differential equations, the following assumption is made: All forces that work on the system are assumed to be constant for the duration of the sufficiently small step of integration of the differential equations. The block diagram in Figure 6.2 shows the consecutive stages of integration.

The dynamics of soft landing for a space landing vehicle are basically determined by: (1) Structural features of the vehicle and properties of its shock absorbers; (2) inclination of the planetary surface where the vehicle lands; (3) orientation of the space landing vehicle at the moment that one of its landing gears touches the surface (the instant of surface contact by the landing gear is conveniently assumed to be the beginning of time); (4) vertical and horizontal components of the space landing vehicle velocity vector at the instant of contact with the surface; (5) components of the vector of the vehicle's angular velocity at the moment of contact with the surface; and (6) external forces acting on the space vehicle during landing.

The geometric form of the design model for the space landing vehicle for any instant of time during the landing process (from the moment of first contact of any space landing vehicle landing gear with the ground until the vehicle comes to complete rest) as a whole can be characterized by the coordinates of several control points for these instants of time.

Among the control points are the following: The center of mass of the space landing vehicle (point 0) and four points on each of its landing gears  $1_i$  through  $4_i$  (Figure 6.1). The coordinates of control points  $2_i$  to  $4_i$  in the moving system of coordinates ( $U, V, W$ ) will remain constant during the landing process while the coordinates of points  $1_i$  ( $i$  is the number of the landing gear) will vary due to the changing geometry of the landing gear.

The coordinates of control points  $2_i$  through  $4_i$  are determined by the formulas

$$\begin{aligned}
 U_{2i} &= r \cos \Delta_i \\
 V_{2i} &= -h_2 \\
 W_{2i} &= r \sin \Delta_i \\
 U_{3i} &= r \cos (\Delta_i + \beta); & U_{4i} &= r \cos (\Delta_i - \beta); \\
 V_{3i} &= -h_3; & V_{4i} &= -h_3; \\
 W_{3i} &= r \sin (\Delta_i + \beta); & W_{4i} &= r \sin (\Delta_i - \beta),
 \end{aligned} \tag{6.1}$$

where

FOR OFFICIAL USE ONLY

FOR OFFICIAL USE ONLY

$$\Delta_i = (i - 1) 2\pi/N + \Delta; \Delta = \pi/N; \Delta = 0 \text{ (p. 95)}, i = 1, \dots, N.$$

Coordinates of the points  $l_i$  before ground contact by the landing-gear pads are determined by the formulas

$$\begin{aligned} U_{1_i} &= R \cos \Delta_i \\ V_{1_i} &= -H \\ W_{1_i} &= R \sin \Delta_i \end{aligned} \quad (6.2)$$

Coordinate of the points  $l_i$  following the moment of contact with the ground by the landing-gear pad is determined by solving the landing-gear equations of motion considered below.

When the coordinates of all control points are known, it is possible to calculate the length of the deforming elements of the structure by:

$$l_{1,2i} = [(U_{1i} - U_{2i})^2 + (V_{1i} - V_{2i})^2 + (W_{1i} - W_{2i})^2]^{\frac{1}{2}}. \quad (6.3)$$

The mass-inertial properties of the space landing vehicle ( $m = W_{II}/g_{II}$ ,  $J_U$ ,  $J_V$ ,  $J_W$ ,  $m_i$ , and others) are assumed to be given, because they are based on the results of design analysis and weight and centering calculations.

Special energy absorbers for absorbing energy during the soft landing of a space landing vehicle are included in the design of the landing gears. These devices absorb the main portion of the available kinetic energy of the space landing vehicle. A second, considerably smaller portion of energy is absorbed by friction in the bearings and friction with the ground and through internal friction in the structural components. Although energy absorbers of the mathematical model of a space landing vehicle can have computational force-strain characteristics of any form, in the subsequent material we will consider only energy absorbers that have force-strain characteristics in the form of a staircase function (Figure 6.3) in order to simplify the exposition. During repeated loading of the energy absorber in the landing process it is necessary to account for the magnitude of the residual strain as a result of prior loading.

For studying the dynamics of three-dimensional motion of the space landing vehicle, three coordinate systems are used (Figure 6.1): (1) A moving system of coordinates (U, V, W) rigidly attached to the vehicle (the principal inertia axes of the space landing vehicle); (2) a fixed system of

FOR OFFICIAL USE ONLY

FOR OFFICIAL USE ONLY

coordinates (X, Y, Z) fixed to the surface of the planet (axes X and Z lie in the plane of the landing surface, with the X-axis coincident with the direction of maximum surface slope and the Y-axis along the direction of the local normal); (3) a fixed system of coordinates (X', Y', Z') fixed to the surface of the planet (axes X' and Z' lie in the plane of the local horizontal, with the Z'-axis coincident with the Z-axis and the Y'-axis along the direction of the local vertical).

Transformations from the coordinate system (X, Y, Z) to the system (X', Y', Z') are written as a table of the cosines of angles between the axes of these systems

$$\begin{array}{r} \downarrow \\ X' \\ Y' \\ Z' \end{array} \begin{array}{ccc} X & Y & Z \\ \cos \theta & \sin \theta & 0 \\ -\sin \theta & \cos \theta & 0 \\ 0 & 0 & 1 \end{array} \quad (6.4)$$

During the soft landing of a space vehicle on the planet, certain forces appear in the structure of its landing gear. Generally, the magnitudes of these forces depend on the characteristics of the deforming elements used in the vehicle's landing gear. External forces applied at the instant of touchdown of the landing-gear pads on the planet have a direction opposite to the direction of the velocities of the pads on the corresponding landing gears. The external forces are determined for each integration step  $\Delta t$  as a function of conditions in which the dynamic system finds itself at that instant.

We will assume that the deforming elements of the vehicle's landing gear are made of crushable material capable of only small elastic deformation, that is, of materials that have a staircase force-strain characteristic.

Let us represent the relationship between force and strain of deforming elements of the landing gear with a staircase characteristic as follows:

$$\begin{aligned} F_p(\delta) = & \sum_{j=1}^m (F_j U(\delta - \delta^{(j+1)}) [1 - U(\delta - \delta_j)] + \\ & + [k_j (\delta - \delta^{(j)}) + F_{j-1}] [U(\delta - \delta_j) - U(\delta - \delta^{(j)})]), \end{aligned} \quad (6.5)$$

where  $U(\delta)$  is the unit step function:

FOR OFFICIAL USE ONLY

FOR OFFICIAL USE ONLY

$$U(\delta) = \begin{cases} 0 & \delta < 0 \\ 1 & \delta \geq 0. \end{cases}$$

For repeated loading, the change in the force-strain relationship is determined by the conditions:

1. when  $|\delta^{(j)}| < |\delta| < |\delta_j|$ , then  $F_{1l}^* = 0$  and  $k_{1l}^* = 0$  for  $l < j$ ;
2. when  $|\delta_j| < |\delta| < |\delta^{(j+1)}|$ , then  $F_{1l}^* = 0$  and  $k_{1l}^* = 0$  for  $l < j$

and

$$\delta_j^* = \delta_{pm}, \quad \delta^{(j)*} = \delta_{pm} - \frac{F_j - F_{j-1}}{k_j}.$$

Parameters with the index "\*" are used to determine the force in the case of repeated loading of the landing gear.

Forces acting on each landing-gear pad of the space landing vehicle ( $l_1$ ) during motion on the planet are the following: (1) The interaction force of the body of the space landing vehicle (through the elements of the landing gear); (2) the reaction of the ground; (3) the force of friction between landing-gear pad and ground.

The force interaction between landing gear and planet surface depends on surface profile, structure, and mechanical properties of the soil at the place of landing. For theoretical studies of soft-landing dynamics of a space landing vehicle, a computational model of the surface is used. The modeled surface has characteristics agreeing with current data on the planetary soil.

For a first approximation, such a landing-surface model can be an absolutely rigid surface with some slope and a high equivalent coefficient of friction, which permits accounting for resistance to the translation of the landing gear along the real planetary surface.

For each time interval during integration, we find the components of external force acting on the pad of landing gear  $l_1$ :

$$F_{11U} = (U_{11} - U_{21}) \frac{F_{1,2,t}}{l_{1,2,t}} + (U_{11} - U_{31}) \frac{F_{1,3,t}}{l_{1,3,t}} + (U_{11} - U_{41}) \frac{F_{1,4,t}}{l_{1,4,t}};$$

$$F_{11V} = (V_{11} - V_{21}) \frac{F_{1,2,t}}{l_{1,2,t}} + (V_{11} - V_{31}) \frac{F_{1,3,t}}{l_{1,3,t}} + (V_{11} - V_{41}) \frac{F_{1,4,t}}{l_{1,4,t}};$$

FOR OFFICIAL USE ONLY



FOR OFFICIAL USE ONLY

$$F_{11\bar{w}} = (W_{11} - W_{21}) \frac{F_{1,2,t}}{l_{1,2,t}} + (W_{11} - W_{31}) \frac{F_{1,3,t}}{l_{1,3,t}} + (W_{11} - W_{41}) \frac{F_{1,4,t}}{l_{1,4,t}}.$$

By using the transformation formulas, it is possible to obtain the components of the external force in any coordinate system.

Forces acting on the space landing vehicle during the soft landing can be determined from the conditions:

$$\begin{aligned} F_{1_i} &\neq 0 \text{ for } Y_{1_i} \leq 0 \\ F_{1_i} &= 0 \text{ for } Y_{1_i} > 0 \end{aligned}$$

Forces and moments referred to the center of mass of the space landing vehicle can be determined by the formulas:

$$\begin{aligned} F_U &= \sum_{i=1}^N F_{1iU}; \quad F_V = \sum_{i=1}^N F_{1iV}; \quad F_W = \sum_{i=1}^N F_{1iW}; \\ M_U &= \sum_{i=1}^N M_{1iU} = \sum_{i=1}^N (F_{1iW} V_{1i} - F_{1iV} W_{1i}); \\ M_V &= \sum_{i=1}^N M_{1iV} = \sum_{i=1}^N (F_{1iU} W_{1i} - F_{1iW} U_{1i}); \\ M_W &= \sum_{i=1}^N M_{1iW} = \sum_{i=1}^N (F_{1iV} U_{1i} - F_{1iU} V_{1i}). \end{aligned} \tag{6.6}$$

Expressions for the forces and moments are substituted into Equations 6.7 and 6.8 to find the displacements and velocities of the center of mass of the vehicle.

General Equations of Three-dimensional Motion of a Space Landing Vehicle During Soft Landing

In the general case, the motions of the space landing vehicle, when treated as a rigid body, can be described by Euler equations. We will write these equations in terms of components along the axes of the moving system of coordinates U, V, W (Figure 6.1). We obtain the following system of differential equations:

$$\left. \begin{aligned} \frac{dV_U}{dt} &= \frac{F_U}{m} - g_n \sin \theta \cos \varphi + V_V \omega_W - V_W \omega_V; \\ \frac{dV_V}{dt} &= \frac{F_V}{m} - g_n \cos \theta + V_W \omega_U - V_U \omega_W; \\ \frac{dV_W}{dt} &= \frac{F_W}{m} - g_n \sin \theta \sin \varphi + V_U \omega_V - V_V \omega_U; \end{aligned} \right\} \tag{6.7}$$

FOR OFFICIAL USE ONLY

FOR OFFICIAL USE ONLY

$$\left. \begin{aligned} \frac{d\omega_U}{dt} &= \frac{M_U}{J_U} + \omega_V \omega_W \left( \frac{J_V - J_W}{J_U} \right); \\ \frac{d\omega_V}{dt} &= \frac{M_V}{J_V} + \omega_U \omega_W \left( \frac{J_W - J_U}{J_V} \right); \\ \frac{d\omega_W}{dt} &= \frac{M_W}{J_W} + \omega_U \omega_V \left( \frac{J_U - J_V}{J_W} \right); \end{aligned} \right\} \quad (6.8)$$

$$\left. \begin{aligned} \frac{d\theta}{dt} &= \omega_W \cos \varphi - \omega_U \sin \varphi; \\ \frac{d\varphi}{dt} &= \omega_V - \omega_W \sin \varphi \operatorname{ctg} \theta - \omega_U \cos \varphi \operatorname{ctg} \theta; \\ \frac{d\psi}{dt} &= \omega_W \sin \varphi \operatorname{cosec} \theta + \omega_U \operatorname{cosec} \theta \cos \varphi. \end{aligned} \right\} \quad (6.9)$$

Equations 6.7 describe the motion of the center of mass of the space landing vehicle, Equations 6.8 describe the motion about the center of mass, and Equations 6.9 are the kinematic Euler relationships.

Because the absolute attitude and location of the vehicle cannot be expressed with respect to the moving system of coordinates U, V, W, the remaining equations will be written in the fixed system of coordinates X', Y', Z':

$$\frac{dX'}{dt} = V_{X'}; \quad \frac{dY'}{dt} = V_{Y'}; \quad \text{and} \quad \frac{dZ'}{dt} = V_{Z'}. \quad (6.10)$$

By integrating Equations 6.7, we determine the projections of the velocity of the space landing vehicle's center of mass onto the moving coordinate axes U, V, W. Components of the velocity of the center of mass in the X', Y', Z' system are determined by using the formulas

$$\begin{aligned} V_{X'} &= A_1 V_U + A_2 V_V + A_3 V_W; & V_{Y'} &= B_1 V_U + B_2 V_V + B_3 V_W; \\ V_{Z'} &= C_1 V_U + C_2 V_V + C_3 V_W. \end{aligned} \quad (6.11)$$

where

FOR OFFICIAL USE ONLY

FOR OFFICIAL USE ONLY

$$\begin{aligned}
A_1 &= \cos \psi \cos \theta \cos \varphi - \sin \psi \sin \varphi; \\
A_2 &= -\cos \psi \sin \theta; \quad A_3 = \sin \psi \cos \varphi + \cos \psi \cos \theta \sin \varphi; \\
B_1 &= \cos \varphi \sin \theta; \quad B_2 = \cos \theta; \quad B_3 = \sin \theta \sin \varphi; \\
C_1 &= -\cos \psi \sin \varphi - \sin \psi \cos \theta \cos \varphi; \\
C_2 &= \sin \psi \sin \theta; \quad C_3 = \cos \varphi \cos \psi - \sin \varphi \cos \theta \sin \psi.
\end{aligned} \tag{6.12}$$

By using Equation 6.10, we can now calculate the coordinates of the vehicle's center of mass in the fixed  $X', Y, Z'$  system.

Thus, having solved the system of equations 6.7 to 6.12, we can find all basic parameters of motion for the space landing vehicle: (1) Components of the velocity of the center of mass in the fixed  $V_{X'}, V_{Y'}, V_{Z'}$  system; (2) the coordinates of the center of mass in the fixed  $X', Y', Z'$  system; (3) the components of the instantaneous angular velocity with respect to the center of mass  $\omega_U, \omega_V,$  and  $\omega_W$ ; (4) the angular coordinates (Euler angles  $\theta, \phi,$  and  $\psi$ ) that characterize the attitude of the body with respect to a system that moves such that its origin always coincides with the center of mass and its axes remain parallel to corresponding axes of the fixed system of coordinates  $X', Y', Z'$ .

For the solution of Equations 6.7 through 6.12, it is necessary to establish the values of the following parameters at the instant  $t = 0$ :

$$\begin{aligned}
X' &= X'_0; \quad V_{X'} = V_{X'_0}; \quad \theta = \theta_0; \quad \omega_U = \omega_{U_0}; \\
Y' &= Y'_0; \quad V_{Y'} = V_{Y'_0}; \quad \varphi = \varphi_0; \quad \omega_V = \omega_{V_0}; \\
Z' &= Z'_0; \quad V_{Z'} = V_{Z'_0}; \quad \psi = \psi_0; \quad \omega_W = \omega_{W_0}.
\end{aligned}$$

If  $\theta_0 = \phi_0 = \psi_0 = 0$  when  $t = 0$ , then from Equations 6.11 and 6.12 we obtain

$$V_{X'_0} = V_{U_0}; \quad V_{Y'_0} = V_{V_0}; \quad V_{Z'_0} = V_{W_0},$$

that is, we can make immediate use of the initial data in calculating the right-hand sides of Equations 6.7.

If, however,  $\theta_0 \neq 0, \phi_0 \neq 0, \psi_0 \neq 0$  when  $t = 0$  (or any one of the angles is not equal to zero), then the values of  $V_U, V_V,$  and  $V_W$  are found from Equations 6.11 by using the initial values of the Euler angles  $\theta_0, \phi_0,$  and  $\psi_0$ .

The forces acting on the dynamic system (the body of the vehicle) during landing depend on the character of the planet's surface at the landing site (slope of the ground, physical-mechanical properties of the soil, structure

FOR OFFICIAL USE ONLY

FOR OFFICIAL USE ONLY

of the surface layer, and so forth), structural peculiarities of the space landing vehicle (the number of landing gears, location of the center of mass, characteristics of the energy absorbers, and so forth), the peculiarities of the landing-gear motion during soft landing (kinematic parameters of the component motions, which are the components of the vehicle's complex motion).

As nearly all indicated factors change during the landing process, so also do the reactions on the vehicle. This significantly complicates the problem being considered. However, it can be solved on a computer by methods of numerical integration with the assumption that the force reactions on the space landing vehicle remain constant during a sufficiently short integration step.

For this it is necessary to represent Equations 6.7 through 6.10 in the form of finite-difference equations

$$\left. \begin{aligned}
 \frac{\Delta V_U}{\Delta t} &= \frac{F_U}{m} - g_n \sin \theta \cos \varphi + V_V \omega_W - V_W \omega_V; \\
 \frac{\Delta V_V}{\Delta t} &= \frac{F_V}{m} - g_n \cos \theta + V_W \omega_U - V_U \omega_W; \\
 \frac{\Delta V_W}{\Delta t} &= \frac{F_W}{m} - g_n \sin \theta \sin \varphi + V_U \omega_V - V_V \omega_U; \\
 \frac{\Delta \omega_U}{\Delta t} &= \frac{M_U}{J_U} + \omega_V \omega_W \left( \frac{J_V - J_W}{J_U} \right); \\
 \frac{\Delta \omega_V}{\Delta t} &= \frac{M_V}{J_V} + \omega_U \omega_W \left( \frac{J_W - J_U}{J_V} \right); \\
 \frac{\Delta \omega_W}{\Delta t} &= \frac{M_W}{J_W} + \omega_U \omega_V \left( \frac{J_U - J_V}{J_W} \right); \\
 \frac{\Delta \theta}{\Delta t} &= \omega_W \cos \varphi - \omega_U \sin \varphi; \\
 \frac{\Delta \varphi}{\Delta t} &= \omega_V - \omega_W \sin \varphi \operatorname{ctg} \theta - \omega_U \cos \varphi \operatorname{ctg} \theta; \\
 \frac{\Delta \psi}{\Delta t} &= \omega_W \sin \varphi \operatorname{cosec} \theta + \omega_U \cos \varphi \operatorname{cosec} \theta.
 \end{aligned} \right\} \quad (6.13)$$

$$\left. \begin{aligned}
 X'_{(n)} &= X'_{(n-1)} + V_{X'_{(n-1)}} \Delta t + W_{X'_{(n-1)}} \left( \frac{\Delta t^2}{2} \right); \\
 Y'_{(n)} &= Y'_{(n-1)} + V_{Y'_{(n-1)}} \Delta t + W_{Y'_{(n-1)}} \left( \frac{\Delta t^2}{2} \right); \\
 Z'_{(n)} &= Z'_{(n-1)} + V_{Z'_{(n-1)}} \Delta t + W_{Z'_{(n-1)}} \left( \frac{\Delta t^2}{2} \right).
 \end{aligned} \right\} \quad (6.14)$$

FOR OFFICIAL USE ONLY

FOR OFFICIAL USE ONLY

The equations of motion for the landing-gear pads are arrived at somewhat differently from the equations of motion for the center of mass of the space landing vehicle. In the case where the landing-gear pads do not touch the planet's surface, their motion is completely described by the equations of motion of the body of the space landing vehicle, because in this case the landing gear is part of the rigid body. When the landing-gear pads are in contact with the planet's surface, they should be considered as masses moving under the influence of the forces of friction and of the deforming elements in the vehicle's landing gear (Figure 6.4).

In this case, the motion of the space landing vehicle is composed of the three-dimensional motion of the rigid body and the motion of the landing-gear pads along the surface of the planet. Forces and moments that arise during the motion of the landing-gear pads bring the space landing vehicle to rest.

Let us consider the relative motion of the landing gears along the surface of the ground. Summing forces parallel to the axes X and Z, we obtain

$$\begin{aligned} F_{ix} - F_{ix}^* - m_i \ddot{X}_i &= 0; \\ F_{iz} - F_{iz}^* - m_i \ddot{Z}_i &= 0. \end{aligned} \quad (6.15)$$

The total force of friction acts along the velocity vector, and its components are determined by the following equations

$$\begin{aligned} F_{ix}^* &= -f F_{iy} \dot{X}_i [(\dot{X}_i)^2 + (\dot{Z}_i)^2]^{-\frac{1}{2}}; \\ F_{iz}^* &= -f F_{iy} \dot{Z}_i [(\dot{X}_i)^2 + (\dot{Z}_i)^2]^{-\frac{1}{2}}. \end{aligned} \quad (6.16)$$

By substituting Equations 6.16 into the equation of motions of the landing-gear pads (Equations 6.15), we obtain

$$\begin{aligned} \ddot{X}_i - \frac{f F_{iy}}{m_i [(\dot{X}_i)^2 + (\dot{Z}_i)^2]^{\frac{1}{2}}} \dot{X}_i - \frac{F_{ix}}{m_i} &= 0, \\ \ddot{Z}_i - \frac{f F_{iy}}{m_i [(\dot{X}_i)^2 + (\dot{Z}_i)^2]^{\frac{1}{2}}} \dot{Z}_i - \frac{F_{iz}}{m_i} &= 0. \end{aligned} \quad (6.17)$$

FOR OFFICIAL USE ONLY

APPROVED FOR RELEASE: 2007/02/08: CIA-RDP82-00850R000300040031-0

LETTERS OF THE BY THE PL  
17 OCTOBER 1980 V. I. BAZHENOV AND M. I. OSIN 2 OF 3

FOR OFFICIAL USE ONLY

If we assume that forces and resulting velocities remain constant during integration over a sufficiently short time interval, we can put the equations of motion of the landing-gear pads (Equations 6.17) in the form of a system of second-order linear differential equations:

$$\begin{aligned}\ddot{X}_{1i} - a\dot{X}_{1i} - b &= 0; \\ \ddot{Z}_{1i} - a\dot{Z}_{1i} - c &= 0,\end{aligned}\tag{6.18}$$

where

$$\begin{aligned}a &= \frac{fF_{1iy}}{m_i [(\dot{X}_{1i})^2 + (\dot{Z}_{1i})^2]^{\frac{1}{2}}}; \\ b &= \frac{F_{1ix}}{m_i}; \quad c = \frac{F_{1iz}}{m_i}.\end{aligned}\tag{6.19}$$

The system of linear differential equations has solutions of the form:

$$\begin{aligned}X_{1i} &= X_{1i}^{n-1} - \frac{1}{a} \left( \dot{X}_{1i}^{n-1} + \frac{b}{a} \right) (1 - e^{at}) - \frac{b}{a} \Delta t; \\ \dot{X}_{1i} &= \left( \dot{X}_{1i}^{n-1} + \frac{b}{a} \right) e^{at} - \frac{b}{a}; \\ Z_{1i} &= Z_{1i}^{n-1} - \frac{1}{a} \left( \dot{Z}_{1i}^{n-1} + \frac{c}{a} \right) (1 - e^{at}) - \frac{c}{a} \Delta t; \\ \dot{Z}_{1i} &= \left( \dot{Z}_{1i}^{n-1} + \frac{c}{a} \right) e^{at} - \frac{c}{a}.\end{aligned}\tag{6.20}$$

Quantities with the index  $(n - 1)$  refer to the preceding integration step. Let us note that at the instant of initial ground contact by the landing-gear pad of the space landing vehicle ( $t = 0$ ), point 1 of the contacting landing gear is determined in such a fashion that  $X_{1,1} = Y_{1,1} = 0$ . When the landing-gear pads slip along the surface of the ground, the following identities hold:

$$Y_{1,1} \equiv 0 \quad \text{and} \quad \dot{Y}_{1,1} \equiv 0\tag{6.21}$$

since  $F_{1iy} = F_{1iy}^N$ .

The expressions obtained yield positions and velocities in the X, Y, Z system of the points  $1_i$  of the space landing vehicle for the case of surface contact by the pad of the  $i$ -th landing gear. Computation of the values of indicated parameters for the system of coordinates U, V, W is accomplished by using the transformation formulas.

FOR OFFICIAL USE ONLY

FOR OFFICIAL USE ONLY

If the pad of the  $i$ -th landing gear does not touch the surface of the ground, then the components of its velocity are determined by formulas

$$\begin{aligned}\dot{U}_{1i} &= \dot{U} + \omega_V W_{1i} + \omega_W |V_{1i}|; \\ \dot{V}_{1i} &= \dot{V} + \omega_W U_{1i} - \omega_U W_{1i}; \\ \dot{W}_{1i} &= \dot{W} - \omega_U |V_{1i}| - \omega_V U_{1i}.\end{aligned}\tag{6.22}$$

When the pad of the  $i$ -th landing gear of the space landing vehicle, having once touched the ground, leaves the surface, then the coordinates of points  $l_i$  of the vehicle are determined by using the formulas

$$U_{1i} = U^*_{1i}; V_{1i} = V^*_{1i}; W_{1i} = \bar{W}^*_{1i}\tag{6.23}$$

where  $i = 1, \dots, N$  and quantities with index "\*" are evaluated at the instant of separation from the surface by the  $i$ -th landing gear of the space landing vehicle.

If the indicated calculations are made for each integration step, we completely define the relationship between process parameters and time for the landing of a space landing vehicle on the surface of a planet without an atmosphere.

Having landed on the planet, the spacecraft will be in an attitude of stable equilibrium. However, not every attitude of stable equilibrium of the space landing vehicle following landing will assure normal operation of all of its systems nor the ability, should it have been planned, of a successful return lift-off from the planet. Indeed, the toppling of a space landing vehicle onto its side during landing has to be considered an unsuccessful landing (and a catastrophe if a crew is on board).

For this reason, it has come to be accepted to call "stable" only such an attitude of the space landing vehicle following landing for which all of its landing gears (or the majority of landing gears for  $N \geq 4$ ) touch the ground, and the longitudinal axis departs from the vertical by a small angle, which is determined by the conditions required for a return lift-off of the vehicle.

To evaluate the capsizing stability of the spacecraft during theoretical studies of the soft-landing process, special capsizing criteria for the space landing vehicle are defined, which determine the location of the center of mass of the vehicle with respect to the lines connecting the pads of its landing gears. The instant of coincidence of the center of mass of the vehicle with the indicated line is the critical one and is considered to be the limiting inclination such that, once it is exceeded, the vehicle will not return to an attitude of stable equilibrium. At this moment, the Euler angle  $\theta$  exceeds its critical value

FOR OFFICIAL USE ONLY



FOR OFFICIAL USE ONLY

$$|\theta_{kp}| = \arctan \frac{R \cos \phi}{|V_{1_i}|}; \quad i = 1, 2, \dots, N \quad (6.24)$$

determined by the instantaneous geometry of the vehicle and by the Euler angle  $\phi$ . The magnitude  $|\theta_{kp}|$  serves as a criterion of capsizing for the spacecraft during landing and is calculated at each integration step.

For the condition  $|\theta| \geq |\theta_{kp}|$ , the space vehicle becomes statically unstable, and the process of integration is terminated. For  $|\theta| < |\theta_{kp}|$ , the vehicle is stable. The process of integration in this case can be terminated, for example, at the moment the kinetic energy of the space landing vehicle becomes less than some sufficiently small positive quantity  $E < \eta$ .

It is necessary to note that to obtain solutions for the equations of motion (Equations 6.7 through 6.12) is generally an extremely complex problem. However, in a number of practical cases, it is enough to find the partial solutions for this system by the method of numerical integration aided by digital computers.

#### The Special Case of Two-dimensional Motion of the Space Landing Vehicle During Soft Landing

As noted earlier, the solution of dynamic equations, which describe the three-dimensional motion of a space vehicle during soft landing, is quite cumbersome and requires a considerable expenditure in machine time to calculate the regions of stability of a multilegged landing gear ( $N \geq 4$ ) space landing vehicle. This is particularly so during the analysis of the dynamics of landing as affected by various structural parameters of the vehicle and by the wide spectrum of possible landing conditions (landing speeds and orientations of the space landing vehicle, characteristics of the ground profile and of the planet's soil).

For this reason, an engineering method was developed for calculating two-dimensional landing motions of a vehicle, which is used to study the stability of a space landing vehicle with different numbers of landing gears (3 to 6) and to make a preliminary selection of the landing-gear system by using the principle of finding one of minimum mass for a given level of stability.

Inasmuch as all vehicle landing conditions in this case are symmetrical with respect to the U-axis, there is no need to determine the motion specifics for all of its landing-gear legs. If  $N$  is the number of landing-gear legs for the space landing vehicle and  $\bar{N}$  is the number of landing-gear legs whose motion should be analyzed, then  $i$  takes on values from 1 to  $\bar{N}$ . We will derive expressions to represent the relationship between  $\bar{N}$  and  $N$  (Figure 6.5):

FOR OFFICIAL USE ONLY

FOR OFFICIAL USE ONLY

$$\begin{aligned}
 &\text{When } N \text{ is even, then} && \text{a. } \bar{N} = N/2 \text{ and } \Delta = \pi/N; \\
 & && \text{b. } \bar{N} = N/2 + 1 \text{ and } \Delta = 0; \\
 &\text{When } N \text{ is odd, then } \bar{N} = (N + 1)/2 \text{ and} && \text{a. } \Delta = \pi/N; \\
 & && \text{b. } \Delta = 0
 \end{aligned}
 \tag{6.25}$$

where  $\Delta$  is the angle between the U-axis and the first landing-gear leg of the vehicle.

A substantial simplification of the mathematical model of the space landing vehicle can be achieved by using the fact that landing-gear pads translate primarily in the direction of the vehicle's longitudinal axis with negligible lateral translation, as a result of compression of the energy absorber (Figure 6.1).

In other words, we can represent the space vehicle by a model consisting of three landing-gear legs ( $\bar{N} = 3$ ), which are attached rigidly at right angles to a common base (Figure 6.6). Each of these landing gear legs contains nonelastic, crushable materials for the absorption of the vehicle's kinetic energy during the soft-landing process, which materials have a staircase relationship between force and strain and unlimited compression.

Consideration of different landing gear configurations in the planar case is made possible by an appropriate choice of linear dimensions  $L_1$ ,  $L_2$ , and  $L_3$ , and of forces  $F_{L_1}$ ,  $F_{L_2}$ , and  $F_{L_3}$ , proportional to the force of compression  $\xi$  of the energy absorber. These parameters, expressed by  $R$  (radius of the landing gear) and  $\xi$ , are shown in Table 6.1.

Table 6.1

N	Parameters					
	$L_1$	$L_2$	$L_3$	$F_{L_1}$	$F_{L_2}$	$F_{L_3}$
3	R	0.5 R	0	$\xi$	2 $\xi$	0
4	0.71 R	0.71 R	0	2 $\xi$	2 $\xi$	0
5	R	0.81 R	0.31 R	$\xi$	2 $\xi$	2 $\xi$
6	0.87 R	0.87 R	0	2 $\xi$	2 $\xi$	2 $\xi$

FOR OFFICIAL USE ONLY

For example, three-legged landing-gear configurations in motion downward along a slope correspond to a 1-2 scheme of landing-gear leg ground contact, that is, the space landing vehicle touches the ground first with one leg located higher on the slope and then simultaneously with two supports located lower on the slope. For the planar case, the two "lower" legs can be considered as a single leg, which during its deformation provides a resistance twice as large as each of the three legs of the vehicle separately. Thus, landing-gear configurations with three, four, five, and six legs can be studied in a two-dimensional problem aided by a mathematical model of a landing gear with three legs. The corresponding scheme for legs to touch ground is given in Table 6.2.

Table 6.2

Landing Gear Configuration	Landing Gear Leg Ground Contact Scheme		
Three-legged	1-2	or	2-1
Four-legged	2-2	or	1-2-1
Five-legged	1-2-2	or	2-2-1
Six-legged	2-2-2		

Also, for such a formulation of the problem, it is possible to estimate the effect of the space landing vehicle's stabilizing power plants, the so-called clamping power plants, on landing stability. The stabilizing power plants, which clamp or force the vehicle against the ground, create a moment that prevents the vehicle from capsizing during landing and tends to return it to a stable attitude.

Let us consider a simplified diagram in which the clamping propulsion system is arranged at the base of each landing-gear leg and the thrust vector is coincident with the longitudinal axis of the leg. All stabilizing propulsion systems are turned on at the instant the landing-gear leg that is lowest on the slope touches ground.

We will analyze the most dangerous case from the viewpoint of stability during landing. We will assume that the surface of the planet is an absolutely rigid surface, that is, there is absolutely no penetration of the ground by the vehicle's landing gear. For this, the coefficient of friction between landing gear and ground can vary within wide bounds. We obtain the following equation for motion of the space landing vehicle:

FOR OFFICIAL USE ONLY

FOR OFFICIAL USE ONLY

$$\begin{aligned} \frac{d\dot{X}}{dt} &= \frac{1}{m} \left[ \sum_{i=1}^3 F_{T_i} - W_n \sin \theta + \sum_{i=1}^3 T_i \sin(\gamma - \theta) \right]; \\ \frac{d\dot{Y}}{dt} &= \frac{1}{m} \left[ \sum_{i=1}^3 F_{N_i} - W_n \cos \theta - \sum_{i=1}^3 T_i \cos(\gamma - \theta) \right]; \\ \frac{d\dot{\gamma}}{dt} &= \frac{1}{J_{\gamma}} \left[ \sum_{i=1}^3 F_{T_i} Y + \sum_{i=1}^3 F_{N_i} X_i + \sum_{i=1}^3 T_i L_i \right], \end{aligned} \quad (6.26)$$

because  $\gamma < 0$  and  $\theta < 0$ , where  $i = 1, 2, 3$ ;

$$\begin{aligned} X_i &= L_i \cos(\gamma - \theta) - (H - \delta_i) \sin(\gamma - \theta); \\ \delta_i &= H + L_i \operatorname{tg}(\gamma - \theta) - Y \sec(\gamma - \theta); \\ \dot{\delta}_i &= -\sec^2(\gamma - \theta) \{ \dot{Y} \cos(\gamma - \theta) + [Y \sin(\gamma - \theta) - L_i] \dot{\gamma} \}; \\ Y &= (H - \delta_i) \cos(\gamma - \theta) + L_i \sin(\gamma - \theta). \end{aligned} \quad (6.27)$$

The force acting along the strut of the  $i$ -th landing-gear leg is determined from the conditions

$$\begin{aligned} F_{L_i} &= 0, \text{ when } \delta_i < 0; \\ F_{L_i} &= 0, \text{ when } \dot{\delta}_i \geq \varepsilon_2; \delta_i < \delta_{ipm}; \\ F_{L_i} &= C_i, \text{ when } \delta_i \geq \delta_{ipm}, \dot{\delta}_i > \varepsilon_2. \end{aligned}$$

The stabilization power plant thrust takes on the value  $T_i = K_i$  for  $t < t_{iD}$ ; and  $T_i = 0$  for  $t \geq t_{iD}$ , when  $\dot{\delta}_2 > 0$  ( $i = 1, 2, 3$ ), where  $t_{iD}$  is the time of cut-off for  $i$ -th power plant.

The sliding speed of the  $i$ -th landing-gear leg along the surface is determined by the expression

$$\dot{X}_i = \dot{X} + Y\dot{\gamma} - \dot{\delta}_i \sin(\gamma - \theta). \quad (6.28)$$

Depending on the character of motion of the landing-gear pads, the component forces  $F_{N_i}$  and  $F_{T_i}$  are determined for specific cases that frequently arise,

as follows: (1) The energy absorber collapses and the  $i$ -th landing-gear leg slides; (2) the energy absorber collapses, but there is no sliding; (3) the landing-gear leg slides, but there is no collapse.

FOR OFFICIAL USE ONLY

Characteristically,  $|\dot{X}_i| > \epsilon_1$ ;  $|\dot{\delta}_i| < \epsilon_2$ ;  $F_i (n - 1) > 0$ . In this case, we obtain a system of differential equations for each landing-gear leg; for example, for leg 1:

$$\begin{aligned} mX_1\ddot{Y} - F_L \sec \beta_1 \cos \mu_1 &= F_{N_1} + F_{N_2} - W_n \cos \theta + \\ &+ mY\dot{\gamma}^2 - (T_1 + T_2 + T_3) \cos(\gamma - \theta), \\ J_w\ddot{\gamma} + F_L \sec \beta_1 (X_1 \cos \mu_1 - Y \sin \mu_1) &= \\ &= (F_{T_1} + F_{T_2})Y + F_{N_1}X_2 - F_{N_2}X_3 + T_1L_1 - T_2L_2 + T_3L_3. \end{aligned} \quad (6.29)$$

By solving the corresponding system, we determine  $\ddot{\gamma}$  and  $F_{L_1}$ . If  $F_{L_1} > 0$ , then the value calculated for  $F_{L_1}$  is used for the integration of the system. If  $F_{L_1} < 0$ , then we should assume  $F_{L_1} = 0$ . The angle  $\mu_1$  is computed by using the formula

$$\mu_1 = -\mu_0 \frac{\dot{X}_1}{|\dot{X}_1|}.$$

Using the found values of  $\mu_1$  and  $F_{L_1}$ , we evaluate  $\beta_1 = \gamma - \theta + \mu_1$ ;  $F_i = F_{L_i} \sec \beta_i$ ;  $F_{N_i} = F_i \cos \mu_i$ ;  $F_{T_i} = F_i \sin \mu_i$ . (4) The landing-gear leg neither collapses nor slides. This is characterized by

$$|\dot{X}_i| < \epsilon_1; |\dot{\delta}_i| < \epsilon_2; F_i (n - 1) > 0.$$

For each landing-gear leg, we obtain a system of equations, for example, for leg 1:

$$\begin{aligned} F_{T_1} + mY\ddot{\gamma} &= -F_{T_1} - F_{T_2} + W_n \sin \theta - mX_1\dot{\gamma}^2 - \\ &- (T_1 + T_2 + T_3) \sin(\gamma - \theta); \\ F_{N_1} - mX_1\ddot{\gamma} &= -F_{N_1} - F_{N_2} + W_n \cos \theta - mY\dot{\gamma}^2 + \\ &+ (T_1 + T_2 + T_3) \cos(\gamma - \theta); \\ J_w\ddot{\gamma} + F_{N_1}X_1 - F_{T_1}Y &= (F_{T_1} + F_{T_2})Y + \\ &+ F_{N_1}X_2 - F_{N_2}X_3 + T_1L_1 - T_2L_2 + T_3L_3. \end{aligned} \quad (6.30)$$

By solving the corresponding system, we determine  $\ddot{\gamma}$ ,  $F_{T_1}$  and  $F_{N_1}$ . The angle  $\mu_1$  is determined by using the formula  $\mu_1 = \arctan (F_{T_1}/F_{N_1})$ . For

FOR OFFICIAL USE ONLY

$F_{N_i} > 0$ , we have (1) if  $|\mu_i| < \mu_0$ ; then the computed values for  $F_{N_i}$  and  $F_{T_i}$  are used in integrating Equation 6.26; (2) if  $|\mu_i| > \mu_0$ ; the solution is not valid because the landing gear must slide (and case 3 above applies). For  $F_{N_i} < 0$ , we should assume  $F_{N_i} = 0$  and  $F_{T_i} = 0$ .

In this chapter, we previously considered the question of determining the stable attitude of the space vehicle following a soft landing on a planet. In solving the planar problem, the criteria of capsizing of the space landing vehicle will appear slightly different from the case of three-dimensional vehicle motion. Indeed, the space vehicle moving in a vertical plane loses stability during soft landing if:

$$\alpha_1 > 0 \text{ or } \alpha_2 < 0 \quad (6.31)$$

where

$$\alpha_i = \text{arc tan } (X_i/Y) + \theta \text{ (for } i = 1, 2) \quad (6.32)$$

and where  $\alpha_1(\alpha_2)$  is the angle between the local vertical and the line passing through the center of the mass of the vehicle and the point of contact for leg 1(2) with the surface;  $X_i$  is the distance from the center of mass of the vehicle to the line of action of the force  $F_{N_i}$  ( $X_i > 0$  when the reference direction coincides with the X-axis).

The space vehicle will remain in a stable attitude following landing on the surface of a planet if the following conditions are met simultaneously:

$$\alpha_1 < 0; \alpha_2 > 0; E = \frac{1}{2} (m\dot{X}^2 + m\dot{Y}^2 + J_w \dot{\psi}^2) < \eta. \quad (6.33)$$

The integration process can be terminated at this point, because the kinetic energy of the space landing vehicle has become less than some sufficiently small positive quantity  $\eta$ , and the vehicle itself maintains a stable attitude.

The analysis of the stability of space landing vehicles during soft landing even for planar motion can be carried out only with the aid of digital computers (for example, by the method of numerical integration). Several results of studying the dynamics of soft landing of a space vehicle are given in Chapter 10.

FOR OFFICIAL USE ONLY



FOR OFFICIAL USE ONLY

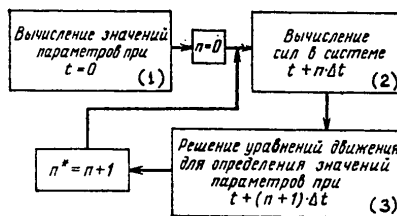


Figure 6.2. Block Diagram for the Integration Stages

Key:

1. Computation of parameter values at  $t = 0$
2. Computation of forces in the system at  $t + n\Delta t$
3. Solution of equations of motion to determine parameter values at  $t + (n + 1)\Delta t$

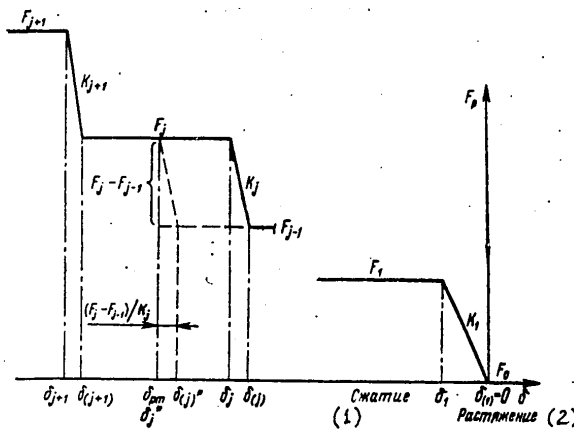


Figure 6.3. Staircase-shaped Force-strain Characteristics

Key:

1. Compression
2. Tension

FOR OFFICIAL USE ONLY



FOR OFFICIAL USE ONLY

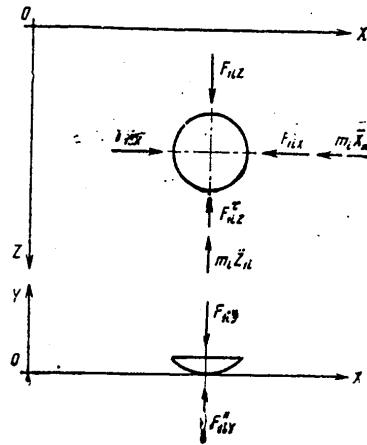


Figure 6.4. Forces Acting on the Landing Gear Pads of a Space Landing Vehicle. ( $m_i$  is the equivalent mass of the pad of the  $i$ -th landing gear)

FOR OFFICIAL USE ONLY

FOR OFFICIAL USE ONLY

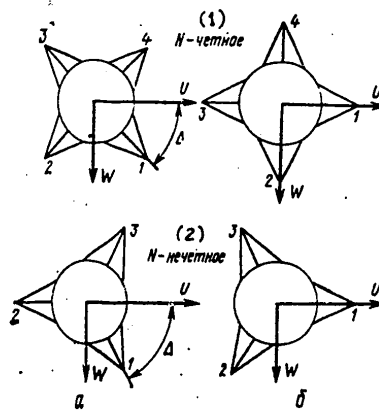


Figure 6.5. Determination of the Value of  $\bar{N}$

Key:

1. For even values of N
2. For odd values of N

FOR OFFICIAL USE ONLY

FOR OFFICIAL USE ONLY

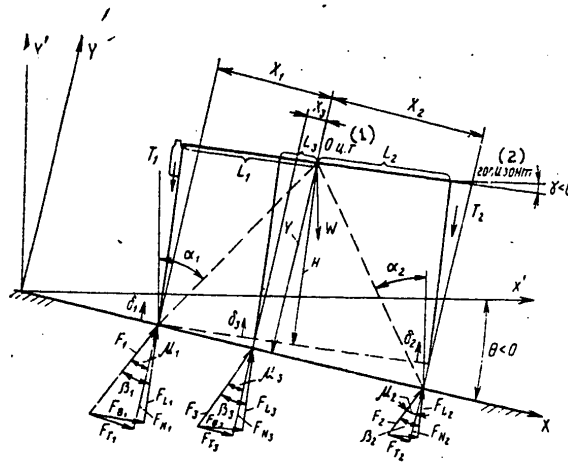


Figure 6.6. Diagrammatical Representation of a Space Landing Vehicle by a Three-legged Model

Key:

1. Center of gravity
2. Horizon

FOR OFFICIAL USE ONLY

FOR OFFICIAL USE ONLY

## CHAPTER 7

THEORETICAL FOUNDATIONS FOR PHYSICAL MODELING  
OF SOFT LANDING

Experimental verification of the efficiency and reliability of the selected structural design of the landing gear for flight vehicles (even those to the Moon) can, because of their high cost, be considered only as the final stage of a long cycle of experimental studies carried out under terrestrial conditions with dynamically similar models and full-scale mockups of space landing vehicles (Refs. 8, 10).

This circumstance is the basic distinguishing characteristic in the experimental studies of most physical phenomena associated with the invasion of interplanetary space by technology. (In addition to soft landing, these phenomena also include locomotion and construction work on the surfaces of the Moon and other heavenly bodies, docking in orbit, and so forth.)

While the use of modeling based on the theory of similarity in the study of phenomena (such as aircraft or rocket flutter, flow of fluids or gases about bodies, heat transfer in a moving medium, mechanical vibration of ground equipment and of flight-vehicle fuselages, with attention given to the motion of fuel in the tanks, and so forth) provides researchers with certain advantages before experimenting with full-scale objects (in order to choose system dimensions, rate of process development, physical means, parameter values, and so forth), the study under terrestrial conditions of phenomena of soft planetary landings using scientific modeling turns out to be the only means permitting qualitative and quantitative reproduction of the process and extrapolation of the results to full-scale phenomena.

When making experimental studies of soft landing under terrestrial conditions, similarity has to be preserved with the full-scale system in geometry and in mass-inertial parameters of the vehicle, in gravitational acceleration, in physical and mechanical properties of the planetary soil, and in the surface profile; in testing full-scale mockups of piloted vehicles (or of remotely controlled automata), similarity also has to be preserved for specific illumination of the landscape, sharply contrasting shadows, and any lack of terrestrial landmarks.

Performing such studies assumes the solution of two essentially independent problems: The representation under terrestrial conditions of a phenomenon similar to a full-scale one, and the carrying out of all necessary observations and measurements of this phenomenon.

Turning to the basic theorems of similarity and dimensional analysis, we obtain the following: If among  $n$  dimensional quantities  $y_1, y_2, \dots, y_n$  there exists a functional relationship

$$F(y_1, y_2, \dots, y_n) = 0 \quad (7.1)$$

FOR OFFICIAL USE ONLY



FOR OFFICIAL USE ONLY

Thus, the  $\Pi$ -theorem makes it possible to establish a system of nondimensional parameters to describe the given phenomenon. It is possible to show that, in order to have similarity of phenomena, it is necessary to have values for these parameters which are the same. Put differently, the parameters  $\Pi_i$  ( $i = 1, 3, \dots, m$ ) represent criteria of similarity.

The number of controlling nondimensional parameters depends on the degree and character of idealization of the physical phenomenon during its study. Thus, to speak of the totality of these parameters is possible only relative to the assumed idealized representation of the phenomenon.

#### Modeling of Soft Landing on Absolutely Rigid Simulated Planetary Surfaces

Let us consider the similarity laws for modeling under terrestrial conditions of the soft-landing dynamics for space landing vehicles.

From the viewpoint of physics, this phenomenon is determined by the following parameters: Characteristic linear dimension  $l$ , meters; mass density of the structure  $\rho$ ,  $\text{kg/m}^3$ ; the modulus of elasticity  $E$  of the material,  $\text{kg/m/s}^2$ ; the Poisson ratio  $\mu$  of the material; time  $t$ , s; acceleration of gravity  $j$ ,  $\text{m/s}^2$ ; coefficient of friction  $f$ ; thus, in our case  $n = 7$ ,  $p = 3$ .

In accordance with the  $\Pi$ -theorem (Ref. 31), we can form four nondimensional combinations ( $m = 4$ ):

$$\Pi_1 = \mu; \Pi_2 = \rho l j / E; \Pi_3 = t^2 j / l; \Pi_4 = f. \quad (7.7)$$

Equation 7.2 then takes the form

$$\Phi\left(\mu; f; \frac{t^2 j}{l}; \frac{\rho l j}{E}\right) = 0. \quad (7.8)$$

From this it follows that in order to have the modeled physical phenomenon be similar to the full-scale one, it is necessary to have these nondimensional combinations be the same, both for the full-scale one ("H") and for the modeled one ("M").

$$\begin{aligned} \mu_H &= \mu_M; \rho_H l_H j_H / E_H = \rho_M l_M j_M / E_M; \\ t_H^2 j_H / l_H &= t_M^2 j_M / l_M; f_H = f_M. \end{aligned} \quad (7.9)$$

Equations 7.9 determine the conditions of similarity for modeling phenomena for soft-landing a space vehicle on the Moon and the planets. However, they

FOR OFFICIAL USE ONLY

FOR OFFICIAL USE ONLY

are of universal character and are valid on Earth for modeling other dynamic processes (translation of a planetary surface vehicle along the surface, structural assembly work, and so forth) to be performed by space systems on any heavenly bodies whose atmosphere is less dense than that of Earth.

We will now consider methods for modeling under terrestrial conditions of soft-landing processes on the Moon, Mars, and Mercury, namely, modeling with dynamically similar models and modeling with the aid of full-scale mockups of space landing vehicles.

The simultaneous consideration of Mars and Mercury is justified by the coincidence of values of the acceleration of gravity at their surfaces (according to current data, the difference in these values is less than 1.3 percent) (Ref. 41). Of course, due to the difference of other physical characteristics (temperature and such) on these planets and the differences in the parameters of flight trajectories to them, vehicles for soft landing on their surfaces will not be identical. As far as the particulars of temperature conditions on Mercury's surface are concerned, because a "day" on that planet equals 88 Earth days and the planet is close to the Sun, the landing of the first space landing vehicles obviously should appropriately take place in the shadow zone of its surface (that is, after sunset), which has nearly Earth-like temperatures.

Modeling with the Aid of Dynamically Similar Models. As initial modeling scales we will choose the scales of the quantities with independent dimensionality: Length, modulus of elasticity of the material, and acceleration of gravity (since  $p = 3$ ), and designate them  $K_L$ ,  $K_E$ , and  $K_j$ .

Several of the derivative scales used in modeling the phenomenon under investigation are given in Table 7.1. Derivative scales of modeling are expressed in terms of initial values using the condition of similarity (Equation 7.9). For example,

$$\frac{Q_H^* f_H}{E_H} = \frac{Q_M^* f_M}{E_M}; \quad 1 = \frac{K_0 K_L K_j}{K_E}; \quad K_0 = K_E (K_L K_j)^{-1}. \quad (7.10)$$

The conditions of similarity,  $\mu_H = \mu_M$  and  $f_H = f_M$ , assume that the landing vehicle models have been manufactured of materials having the same Poisson ratio and coefficient of friction as the full-scale vehicle.

In modeling lunar surface landing phenomena under terrestrial conditions, we unambiguously obtain the scale for the acceleration of gravity as  $K_j = 6$ .

To simplify the design and manufacture of the model, it is most appropriate to have the scale of mass density equal to 1, that is,  $K_p = 1$ . With this in mind, we obtain from the formula for the scale  $K_p$  (Equation 7.10) the simple relationship  $K_E = 6K_L$ .

FOR OFFICIAL USE ONLY

## FOR OFFICIAL USE ONLY

The following cases are of practical interest: (1)  $K_\lambda = 1/6$ ;  $K_E = 1$ . In this case, the dynamically similar model has to be manufactured from the same materials as the full-scale structure (titanium and aluminum alloys, steels and others; Model DPM-A, -B, -C, Table 8-1); (2)  $K_\lambda = 1/3$ ;  $K_E = 2$ . In this case, the model of the lunar vehicle has to be manufactured from materials with a modulus of elasticity  $E$  twice as large as that of materials in the full-scale structure (for example, if the full-scale structure material is a titanium alloy with  $E = 11 \times 10^{10}$  Pa and the material of the model is steel with  $E = 22 \times 10^{10}$  Pa); (3)  $K_\lambda = 1/2$ ;  $K_E = 3$ . In this case, the material of the model must have a modulus of elasticity  $E$  three times larger than that of the material of the full-scale space landing vehicle (for example, the full-scale vehicle material is an aluminum alloy with  $E = 7 \times 10^{10}$  Pa, and the material of the model is steel with  $E = 21 \times 10^{10}$  Pa).

A wider range for choosing the linear scale of the dynamically similar model of a lunar vehicle is available, if one removes the requirement that the scale of mass densities  $K_\rho$  has to be equal to unity (Table 7.1).

Actually, from Equation 7.10 with  $K_j = 6$ , we have

$$K_\lambda = K_E(6K_\rho)^{-1} \quad (7.11)$$

Let us consider the following case: (4) Let  $K_\rho = 1/6$  and  $K_E = 1$ . We obtain  $K_\lambda = 1$ . Here we run into a contradictory requirement, namely, for full-scale dimensions for the dynamically similar model of a lunar vehicle, it is necessary to achieve a total mass of a model six times smaller than the full-scale one (Table 7.1). In order to satisfy this requirement, it is necessary to manufacture the basic portion of the lunar vehicle model, namely its landing gear and several force elements, in full scale and from materials that will actually be used, and the remaining portions of the model (payload, power plant mockup, instrument section, crew cabin, and so forth) of substantially smaller mass but in such a fashion that the total mass of the resulting dynamically similar model of the space landing vehicle maintains the scale  $K_M = 1/6$  and the model has the same centering as the actual vehicle.

The following are the particulars of a full-scale dynamically similar model of a lunar vehicle: Increase angular accelerations by a factor of 6; increase the linear and angular velocities and power by a factor of  $\sqrt{6}$ ; use full-scale values of energy (work), stress, stiffness, and forces acting on the model; reduce (compared with the actual vehicle) the test-event time scale by a factor of  $\sqrt{6}$ ; reduce mass, mass density, and moments of inertia in the model by a factor of 6.

A full-scale dynamically similar model, compared to a full-scale mockup of the space landing vehicle (page 113), does not require any mechanism for "unloading" 5/6 of the weight, which greatly simplifies test stands and



FOR OFFICIAL USE ONLY

Table 7.1

Наименование параметра (1)	Обозначение масштаба (2)	Определяющая формула (3)	(4) Луна (K <sub>J</sub> = 6)		(5) Марс (K <sub>J</sub> = 5/2)		K <sub>I</sub> = 1 K <sub>E</sub> = 1	K <sub>I</sub> = 2/5 K <sub>E</sub> = 2/5	K <sub>I</sub> = 1 K <sub>E</sub> = 1	K <sub>I</sub> = 2/5 K <sub>E</sub> = 2/5
			K <sub>I</sub> = 1/6 K <sub>E</sub> = 1	K <sub>I</sub> = 1/5 K <sub>E</sub> = 1	K <sub>I</sub> = 2/5 K <sub>E</sub> = 1	K <sub>I</sub> = 2/5 K <sub>E</sub> = 1				
(6) Коэффициент Пуассона	K <sub>p</sub>	1	1	1	1	1	1	1	1	1
(7) Время	K <sub>t</sub>	$K_I^{1/2} \cdot K_J^{-1/2}$	1/6	$(1/6)^{1/2}$	$\sqrt{2}/5$	2/5	2/5	2/5	2/5	$(2/5)^{1/2}$
(8) Массовая плотность	K <sub>q</sub>	$K_E \cdot (K_I \cdot K_J)^{-1}$	1	1/6	2	1	1	1	1	2/5
(9) Масса	K <sub>m</sub>	$K_E K_I^2 \cdot K_J^{-1}$	1/216	1/6	2/125	8/125	16/625	16/625	8/125	2/5
(10) Сила	K <sub>f</sub>	$K_E K_I^2$	1/36	1	1/25	4/25	8/125	8/125	8/125	1
(11) Момент инерции	K <sub>J</sub>	$K_E \cdot K_I^4 \cdot K_J^{-1}$	(1/6) <sup>5</sup>	1/6	2/(5) <sup>5</sup>	[2/5] <sup>5</sup>	[2/5] <sup>6</sup>	[2/5] <sup>6</sup>	[2/5] <sup>6</sup>	2,5
(12) Энергия	K <sub>s</sub>	$K_E K_I^3$	1/216	1	1/125	8/125	16/625	16/625	8/125	1
(13) Мощность	K <sub>N</sub>	$K_E \cdot (K_I \cdot K_I^5)^{1/2}$	1/36	6 <sup>1/2</sup>	$\sqrt{2}/50$	4/25	8/125	8/125	8/125	$(2,5)^{1/2}$
(14) Давление (напряже- ние)	K <sub>p</sub>	K <sub>E</sub>	1	1	1	1	2/5	2/5	2/5	1
(15) Жесткость линейная	K <sub>c</sub>	$K_E \cdot K_I$	1/6	1	1/5	2/5	4/25	4/25	4/25	1
(16) Скорость линейная	K <sub>v</sub>	$(K_I \cdot K_J)^{1/2}$	1	6 <sup>1/2</sup>	$\sqrt{2}/2$	1	1	1	1	$(2,5)^{1/2}$
(17) Угол	K <sub>g</sub>	1	1	1	1	1	1	1	1	1
(18) Скорость угловая	K <sub>g</sub>	$K_I^{1/2} \cdot K_J^{-1/2}$	6	6 <sup>1/2</sup>	5/ $\sqrt{2}$	2,5	2,5	2,5	2,5	$(2,5)^{1/2}$
(19) Ускорение угловое	K <sub>g</sub>	$K_I \cdot K_I^{-1}$	36	6	25/2	25/4	25/4	25/4	25/4	5/2
(20) Жесткость крутильная	K <sub>τ</sub>	$K_E \cdot K_I^3$	1/216	1	1/125	8/125	16/625	16/625	8/125	1
(21) Динамическая вязкость	K <sub>η</sub>	$K_E \cdot K_I^{1/2} \cdot K_J^{-1/2}$	1/6	(1/6) <sup>1/2</sup>	$\sqrt{2}/5$	2/5	4/25	4/25	4/25	$[2/5]^{1/2}$

FOR OFFICIAL USE ONLY

FOR OFFICIAL USE ONLY

Table 7.1 cont'd

Key:

1. Parameter name	12. Energy
2. Symbol of scale	13. Power
3. Defining formula	14. Pressure (stress)
4. Moon	15. Elastic stiffness
5. Mars	16. Linear velocity
6. Poisson ratio	17. Angle
7. Time	18. Angular velocity
8. Mass density	19. Angular acceleration
9. Mass	20. Torsional stiffness
10. Force	21. Dynamic viscosity
11. Moment of inertia	

methods for doing the experiments themselves. Such a model makes it possible to carry out an experimental investigation of the soft-landing process for a lunar vehicle and perfecting its full-scale landing gear by simply dropping the model from a special test stand or helicopter onto a platform that has the "full-scale profile" of the location. Experiments using the full-scale model are very interesting from the point of view of determining the probability of successful stable landing of the vehicle under conditions simulating those on the Moon.

For Mars and Mercury, the scale of gravitational acceleration takes on the value

$$K_j = j_M/j_H = g_{\text{Earth}}/g_{\text{Mars}} = 9.81/3.74 \approx 5/2$$

From Equation 7.10, we obtain the simple relationship

$$K_E = 5/2 K_p K_\rho$$

The following four cases could be of practical interest: (1)  $K_\rho = 1/5$  and  $K_E = 1$ ; then  $K_p = 2$ . Such a dynamically similar model scaled down by a factor of 5 and made of full-scale-vehicle materials but with a mass density of the structure two times that of the full-scale space landing vehicle (which is achieved by installing ballast) is very suitable for testing in a special stand with platforms simulating the soil of the planet; (2)  $K_\rho = 2/5$  and  $K_E = 1$ ; then  $K_p = 1$ . In this case, the dynamically similar model of the space landing vehicle is scaled down by a factor of 2.5 and should be manufactured of materials that are the same as the actual structure and, if possible, with the dimensions of all elements changed proportionately (Models DPM-A, -B, -C, Table 8.1); (3)  $K_\rho = 2/5$ ,  $K_E = 2/5$ ; then  $K_p = 2/5$ . In contrast to the preceding case, such a dynamically similar model of the space

FOR OFFICIAL USE ONLY

FOR OFFICIAL USE ONLY

landing vehicle scaled down by a factor of 2.5 can be manufactured from materials with a modulus of elasticity  $E$  that is 2.5 times smaller than that of the materials in the full-scale structure. This has the added result that the weight of the basic elements of the model decreases by a factor of 2.5 compared to case 2 (Models DPM-G1 and -G2, Table 8.1); (4)  $K_\lambda = 1$ ,  $K_E = 1$ ; then  $K_\rho = 2/5$ . In this case, the landing gear and several force elements of the model have to be manufactured with full-scale dimensions of the actual materials and the weights of the remaining portions of the model (payload, power plant mockups, instrument section, and so forth) have to be significantly reduced such that the overall mass obtained for the space landing vehicle model maintain the scale  $K_M = 2/5 = 0.4$  and that the model have the same center of mass as the full-scale vehicle (Model DPM-G3, Table 8.1). This case is analogous to case 4 for soft landing on the Moon.

It is worth noting that for a scaling of  $K_\lambda = 1/6$  (for Mars,  $K_\lambda = 2/5$ ), the scale of linear velocity takes on the value  $K_V = 1$ , that is, the dynamically similar model will have the same velocities during landing as the actual space landing vehicle making a soft landing on the Moon (or on Mars). This simplifies the experimental investigation and recalculation of results therefrom for the full-scale phenomenon. Let us assume that during an experiment such a model of a space landing vehicle is dropped from  $1/6$  ( $2/5$ ) altitude, which it would have on the Moon (on Mars), and the experiment is filmed from a distance of  $1/6$  ( $2/5$ ) of the actual distance and 6 times (2.5 times) faster than normal; then in viewing the film at standard speed one can see the process of soft landing equivalent to the actual one of a lunar (Martian) space landing vehicle (Figure 7.1). A reduction in linear dimensions of the model by a factor of 6 (2.5) compared to the actual one makes it possible to carry out several experimental studies of soft landing in a special altitude chamber, which simulates the lunar (Martian) vacuum.

Modeling with the Aid of Full-scale Mockups of Space Landing Vehicles. In modeling with this method, the same conditions for similarity (Equations 7.9) have to be satisfied.

Because soft landing is studied in mockups of space landing vehicles manufactured from the same materials and having full-scale mass and volumetric dimensions, the initial scales of modeling are determined directly:  $K_\lambda = 1$ ;  $K_\rho = 1$  and  $K_E = 1$  (as before,  $p = 3$ ). From the conditions of similarity (Equations 7.9), we obtain the following relationships:

$$K_\mu = 1; K_\rho K_\lambda K_j K_E^{-1} = 1; K_t^2 K_j K_\lambda^{-1} = 1; K_f = 1$$

from which

$$K_j = K_E (K_\rho K_\lambda)^{-1}; K_t = K_\lambda K_\rho^{1/2} K_E^{-1/2} \quad (7.12)$$

FOR OFFICIAL USE ONLY

FOR OFFICIAL USE ONLY

Substituting the values of the initial scales into Equations 7.12, we find that  $K_j = 1$  and  $K_t = 1$ , that is, similarity of phenomena while modeling soft landing using full-scale space-landing-vehicle mockups can only be preserved under conditions of artificially creating the planetary acceleration of gravity on Earth (this results in a full-scale time scale). This can be achieved in a number of ways. The only strict path of obtaining planetary gravitational acceleration is by putting the full-scale mockup into a flying laboratory similar to laboratories that create weightlessness. However, flying laboratories are most unsuitable for experimental studies of soft landing.

Simpler ways, from the point of view of technology, although less strict, are the various methods of "unloading," in which correspondence with the actual vehicle is obtained only in terms of the total weight of the mockup, which is influenced by terrestrial gravitation (the full-scale mockup has to be "unloaded" by the  $[1 - K_j^{-1}]$  portion of the total weight). In this case, in order to achieve a similarity of phenomena more fully, the selected method of unloading should be applied to a large number of the elements in the mockup.

Methods for unloading can be implemented by a number of designs:

(1) Installing additional jet engines onboard the mockup; (2) using counterbalances (it is desirable to have a system of unloading counterweights for each element of the mockup); (3) using electrodynamic brakes; (4) employing hydropneumatic mechanisms of unloading; (5) using inclined walls; and so forth.

We will note that in the case of full-scale-mockup modeling of the landing process for a piloted ship intended to provide cosmonauts with a complete simulation of planetary conditions during training, it is necessary also to provide for the following: (1) Manual controls with characteristics identical to the actual ones; (2) identical view from the cabins of the mockup and the piloted ship; (3) the cosmonaut in the cabin of the full-scale mockup in an identical attitude as in the actual piloted ship.

The first method of unloading in essence presumes creation of a flying, full-scale, turbojet type of mockup of the space landing vehicle (Ref. 46). In spite of the significant difficulties connected with its implementation, this method opens broad possibilities for studying the soft-landing process itself and permits training the cosmonauts in perfecting the concluding flight stage of a piloted ship including checking the effectiveness of the manual and automatic control systems, the quality of the view from the cabin, and so forth and maneuvers for choosing the landing site.

Specific variants of unloading using jet engines might be of special interest: (1) A jet engine located in the center of mass of the flying mockup in a gimballed suspension with 2 degrees of freedom, maintained in a vertical attitude by a control system during the entire flight. The engine provides thrust of 83.3 percent (for the Moon) or 60 percent (for Mars) of the

FOR OFFICIAL USE ONLY

FOR OFFICIAL USE ONLY

terrestrial weight of the mockup. In this variant, it is necessary to have a system of auxiliary power plants rigidly attached to the mockup that produce linear translations of the mockup for rotations in pitch and roll; (2) a jet engine located at the center of mass of the flying mockup in a gimbaled suspension with 2 degrees of freedom and connected to it by hydraulic actuators in the longitudinal and transverse planes. By using a composite control system, which includes a jet vane and booster as the basic actuating elements, mockup and power plant can be controlled to have such an angular attitude in space for which the kinematic parameters of the mockup's motion equal the kinematic parameters of the space landing vehicle's motion; (3) the jet engine rigidly attached to the flying mockup at its center of mass. The pilot cabin, however, is attached to the mockup with a gimbaled system with 2 degrees of freedom. The control system, using jet vanes with the jet engine and hydraulic actuators connecting the movable pilot cabin to the mockup, provides for such attitude of mockup and cabin in space for which the linear kinematic parameters of mockup motion and the turn angles of the cabin equal the corresponding parameters of motion for the manned space vehicle.

For all other methods of unloading, the full-scale mockup is supported at all times by cables from the unloading mechanism, as a result of which the maneuvering capability of the mockup is limited by the dimensions of the test stand. However, the absence of the unloading jet engine greatly simplifies the design of a full-scale mockup and test equipment (Figure 7.2).

We should note the negative side of the second unloading method, namely, that at the moment the mockup touches the surface, that is, during the period of meeting the barrier, of energy absorption, and of deformation of landing gear and ground, the unloading becomes ineffective due to inertia of the counterbalance weights.

In this sense, it is better to use the third and, especially, the fourth methods of unloading, which are distinguished by small inertias in the unloading mechanisms used. By using a wall slightly deflected from the vertical, it is possible to obtain a simulation of a reduced gravitational force by decomposition of the weight of the space-landing-vehicle mockup into its components. However, this method of unloading makes it more difficult to simulate the profile of the landing surface and the properties of a loose, deformable planetary soil.

By making the scale  $K_j = 1$  during these experiments, we simultaneously achieve the condition where the magnitudes of the remaining derived scales also equal unity. Of course, for such tests, it is impossible to maintain similarity in the temperature regime or space vacuum, because the performance of full-scale landing experiments is impractical in heat-altitude chambers.

The experimental investigations of soft landing by using full-scale mockups is one of the final stages in the experimental development of landing gears

FOR OFFICIAL USE ONLY

FOR OFFICIAL USE ONLY

under terrestrial conditions. Such studies make it possible to draw definitive conclusions on the suitability of a particular landing-gear design as well as on that of its structures for successful planetary landing. They also permit the crew training necessary for a manned vehicle (or for a remotely controlled automaton) to accomplish soft landings. These studies also improve the operational reliability of the landing-gear system and reduce the number of expensive spacecraft tests required within the framework of the test program.

#### Modeling of Soft Landings on a Deformable, Simulated Soil of Planetary Surfaces

We will now consider the question of modeling several mechanical characteristics of planetary soils under terrestrial conditions. These characteristics influence the soft-landing process for a space landing vehicle. The following quantities are of essence: The mass density of the soil,  $\rho_r$  ( $\text{kg}/\text{m}^3$ ); the coefficient of soil compressibility,  $a$  ( $\text{ms}^2/\text{kg}$ ); the coefficient of internal friction in the soil,  $\psi$  [0], and also  $\ell$ ,  $t$ ,  $f$ , and  $j$ .

It is known that for small changes in pressure, one can consider soils as linearly deformable bodies, and assume, with an accuracy sufficient for practical purposes, that there is a linear relationship between stress and strain (Ref. 39). Figure 7.3 shows the relationship between total soil deformation under a die as a function of external pressure. The curve showing soil deformation has two main parts: (1) From zero to some pressure  $p_0$ , which for all practical purposes can be approximated with sufficient accuracy by a straight line (the dashed line in the figure), and (2) a curved portion for pressures greater than  $p_0$ . Practically all soils have a "region of proportionality" between pressure and settlement  $\delta$  for low values of external pressure (up to  $\sim 3 \times 10^5$  Pa) (Ref. 35). The theory of linearly deformable semi-infinite solids gives analytical expressions for a fully stabilized compression  $\delta$  of a uniform soil under the action of external pressure  $p$ :

$$\delta = h_\delta a p \quad (7.13)$$

where  $h_\delta$  is the equivalent thickness of the soil layer whose compression under continuous load will be the same as the subsidence of a layer of soil under loading action on an area of given dimensions.

Equation 7.13 is valid for all soils and accounts for the finiteness of lateral expansion of the soil, dimensions, shape, rigidity of the base of the body acting on the soil, and the effect of all components of stress on soil settlement.

The tangent of angle  $\alpha$ , considering Equation 7.13, is given by  $\tan \alpha = h_\delta a = \text{const}$  when  $0 < p \leq p_0$ . Because the quantity  $h_\delta$  is constant for a given soil and given base of a body acting on the ground, we have  $a = \text{const}$  for  $0 < p \leq p_0$ . Equation 7.13 can be written as

FOR OFFICIAL USE ONLY

FOR OFFICIAL USE ONLY

$$p = \delta/ah_\delta = \lambda/a \quad (7.14)$$

where  $\lambda = \delta/h_\delta$  and is the relative deformation of the soil under compression.

The coefficient of internal soil friction  $\psi$ , given by  $\psi = \tan \phi$  where  $\phi$  is the angle of internal soil friction, characterizes the resistance of the ground to slipping.

The internal soil friction represents the resistance to relative sliding of particles and, within certain ranges, is directly proportional to the normal pressure being transmitted to the solid skeleton of the soil (Coulomb's law):

$$\tau = \psi p \quad (7.15)$$

where  $\tau$  is resistance to slipping (slipping stress in the soil).

We will now, in accordance with the  $\Pi$ -theorem, form nondimensional expressions to supplement Equations 7.7 that will characterize the process of interaction of the soil with the parts of the vehicle's landing gear:

$$\Pi_5 = \psi; \Pi_6 = a\rho r_j l, \text{ and also } \Pi_3 = t^2 j/l; \Pi_4 = f \quad (7.16)$$

In order that the behavior of the soil during experimental studies of soft landing under terrestrial conditions be similar to the behavior of the actual soil, it is necessary to maintain equivalency in the nondimensional expressions for the actual and modeled phenomena:

$$\psi_n = \psi_m; a_n \rho_n r_n j_n l_n = a_m \rho_m r_m j_m l_m; t_n^2 j_n / l_n = t_m^2 j_m / l_m; f_n = f_m. \quad (7.17)$$

Characteristics of Modeling Using Dynamically Similar Models. The initial scales of modeling are conveniently chosen to be the scales of the following quantities of independent dimensionality: Length, mass density of the soil, and acceleration of gravity,  $K_\rho$ ,  $K_{\rho_T}$ , and  $K_j$ . The derived scales of model-

ing are expressed by using the initial scales and the similarity conditions given in Equations 7.17.

The conditions of similarity,  $\psi_H = \psi_M$  and  $f_H = f_M$ , assume the use of simulated soils with coefficients of internal and external friction identical to those of the soil on the planet. The scale for the acceleration of gravity is uniquely determined from the conditions of the experiment ( $K_j = 6$  for the Moon,  $K_j = 2.5$  for Mars, and so forth).

FOR OFFICIAL USE ONLY

FOR OFFICIAL USE ONLY

Considering the need to preserve the condition  $\psi_H = \psi_M$  and the fact that the surface layers of the planets being considered have small density, it is desirable when creating simulated soils to use low-density materials. Therefore we assume that  $K_{\rho\Gamma} = 1$ . Substituting into the expression for the

scale  $K_a$  the values of  $K_j$  and  $K_{\rho\Gamma}$ , we obtain

$$\begin{aligned} K_a &= (K_\lambda K_{\rho\Gamma} K_j)^{-1}; K_a = (6K_\lambda)^{-1} \text{ (for the Moon)} \\ K_a &= (2.5K_\lambda)^{-1} \text{ (for Mars)} \end{aligned} \quad (7.18)$$

Equations 7.18 show that, in using dynamically similar models of the space landing vehicle with a scale  $K_\lambda = K_j^{-1}$ , the scale  $K_a = 1$ . In other words, in experimental studies of the soft-landing process, simulated soils having mechanical characteristics identical to the soil of the planet should be used. For this goal, it is necessary to use several special materials (natural and artificial) with characteristics corresponding to the latest data on the properties of the planet's surface layers (Table 7.2). In the case when (for example, for the Moon)  $K_\lambda > 1/6$ , then  $K_a < 1$ , that is, the simulated soil has to be less compressible (less yielding) than the actual one. The soil has to be less porous (spongy) and of greater structural stiffness for given values of mass density and coefficients of internal and external friction corresponding to the planet's soil.

The final choice of the magnitude of the initial scale  $K_\lambda$  considers the dimensions of the test stands and runways and the capability to prepare and use corresponding simulated planetary soils.

Characteristics of Modeling by Using Full-scale Mockups of the Space Landing Vehicle. In studying the soft landing with full-scale mockups of the space landing vehicle, the same similarity conditions (Equations 7.17) have to be met. Simulation of the planetary soil in this case demands particular consideration. Because the full-scale mockup to be tested simulates the dynamics of landing on the planet due to unloading by a factor of  $(1 - K_j^{-1}) \times 100\%$  of its weight, it is only natural to explore the possibility of using simulated soil whose properties correspond as closely as possible to the planetary soil during this experiment. Therefore, the initial scales to be used in the simulation take on the following values:  $K_\lambda = 1$ ;  $K_{\rho\Gamma} = 1$ , and

$K_a = 1$ . With this in mind, we obtain  $K_{j\Gamma} = (K_\lambda K_{\rho\Gamma} K_a)^{-1} = 1$  from the similarity conditions.

In other words, for a simulation with full-scale mockups and soft, deformable, simulated soils, full similarity of phenomena can be preserved only by simulating the planetary gravitational forces under terrestrial conditions. Because it is impossible to "unload" every soil particle by a factor of

FOR OFFICIAL USE ONLY



FOR OFFICIAL USE ONLY

Table 7.2. Physical Conditions on the Surfaces of Planets, Basic Properties of Their Soils and of Several Simulated Soils

Материал (1)	Параметры (2)										(11) Средство исследования
	(3) С/м г/см <sup>3</sup>	(4) Темпе- ратура, К	(5) Давление, Па	(6) Плот- ность, кг/м <sup>3</sup>	(7) Несущая способ- ность, Па	(8) Угол внут- реннего трения, град	(9) Кoeffи- циент трения	(10) Структура; происхож- дение аналога			
Лунный грунт (12)	1,62	123÷403	1,33·10 <sup>-9</sup> —10 <sup>-10</sup>	700—1620	(0,2—1,5) ×10 <sup>5</sup>	15—40	0,25—0,55	Мелкозернистый слабо- вязкий грунт с при- месяью гравия и камней. Соответствует пылевато- му песку [21, 70] (22)	КА типа «Луна», «Луноход», «Сер- вентер», «Аполлон» (23)		
Марсианский грунт (13)	3,74	173÷298	(6—13) × 10 <sup>2</sup>	1000— 1650	~1·10 <sup>5</sup> *	—	0,2—0,5*	Грунт изменяется от весьма рыхлого до плот- ного (скальные породы); во многом напоминает поверхность Луны [25] (24)	КА типа «Марс», «Викинг» (25)		
Грунт Меркурия (14)	3,78	250÷673	~10 <sup>-6</sup> *	800— 1500*	~1·10 <sup>5</sup> *	—	—	Близок к горным поро- дам Луны. По микро-наблде- ниям Луны, чем на Марс (26)	Радиофизические наблюдения: «Ма- ринер-10» (27)		
Грунт Венеры (15)	8,43	753	~90·10 <sup>5</sup>	2700— 2900	>2·10 <sup>5</sup> *	—	—	Напоминает гранитные породы и земные мало- пористые базальты с мас- сивной текстурой. Более плотный, чем на Луне, [2] (28)	«Венера-9», «Ве- нера-10» (29)		

FOR OFFICIAL USE ONLY

FOR OFFICIAL USE ONLY

Table 7.2 cont'd

Песок + минеральное масло (16)	9,81	290	~ 105	1420	0,29 · 10 <sup>5</sup>	27	~ 0,35	Искусственный аналог грунта [26] (30)
Андезит-базальтовый вулканический песок (17)	9,81	290	~ 105	1290—1620	0,71 · 10 <sup>5</sup>	—	0,25—0,65	Естественный аналог грунта [17] (31)
Пенобетон (18)	9,81	290	~ 105	700	0,78 · 10 <sup>5</sup>	—	~ 0,4	Искусственный аналог грунта (32)
Базальт (раздробленный) (19)	9,81	290	~ 105	1040—1890	0,79 · 10 <sup>5</sup>	—	0,2—0,5	Естественный аналог грунта (33)
Газосиликатный (20)	9,81	290	~ 105	650	1,25 · 10 <sup>5</sup>	—	—	Искусственный аналог грунта [37], рис. 7.4 (34)
Лава андезитовая базальтовая (плотная пористая) (21)	9,81	290	~ 105	2650 2150	2 · 10 <sup>5</sup> 0,5 · 10 <sup>5</sup>	—	—	Естественный аналог грунта (35)

• Примечание. Предположительная оценка по косвенным данным (36)

FOR OFFICIAL USE ONLY

FOR OFFICIAL USE ONLY

Table 7.2 cont'd

## Key:

1. Material
2. Parameters
3.  $g_{\text{planet}}$  ( $\text{m/s}^2$ )
4. Temperature ( $^{\circ}\text{K}$ )
5. Pressure (Pa) [pascals]
6. Density ( $\text{kg/m}^3$ )
7. Load-carrying capacity (Pa)
8. Angle of internal friction (degrees)
9. Coefficient of friction
10. Structure; source of analogy
11. Means of study
12. Lunar soil
13. Martian soil
14. Mercurial soil
15. Venusian soil
16. Sand plus mineral oil
17. Andesite-basaltic volcanic sand
18. Cellular foam concrete
19. Basalt (crushed)
20. Gas-silicalcite
21. Andesite-basaltic lava (dense/porous)
22. Fine-grained, loosely bound soil with admixture of gravel and rocks. Corresponds to powdery sand (Refs. 21, 70)
23. Luna, Lunokhod, Surveyor, and Apollo spacecraft
24. Soil varies from quite friable to dense (rocky minerals); in many ways reminiscent of the lunar surface (Ref. 25)
25. Mars and Viking spacecraft
26. Close to the rocky minerals of the Moon; in microstructure more similar to the Moon than to Mars
27. Mariner-10 radiophysical observations
28. Reminiscent of granite minerals and massively textured terrestrial low-porosity basalts. Denser than the Moon (Ref. 2)
29. Venera-9 and Venera-10
30. Simulated soil made of artificial materials (Ref. 26)
31. Simulated soil made of natural materials (Ref. 17)
32. Simulated soil made of artificial materials
33. Simulated soil made of natural materials
34. Simulated soil made of artificial materials (Ref. 37); also Figure 7.4
35. Simulated soil made of natural materials
36. Note: Tentative estimate based on indirect data

FOR OFFICIAL USE ONLY

FOR OFFICIAL USE ONLY

$(1 - K_j^{-1})$  under terrestrial conditions, and the creation of artificial gravitation by a flying laboratory or by an electromagnetic field acting on the particles of a special soil is impractical during experiments with full-scale mockups, the only remaining approach is to estimate the magnitude of the error introduced into the experiment by the peculiarities of the dynamics of the simulated-soil particles in the terrestrial gravitational field.

In this case, the soil subsidence under action of the space-landing-vehicle mockup can be determined by Equation 7.13 but will differ from that of the actual soil due to the  $K_j$ -fold increase in the weight of the soil particles. The pressure  $p$  used in Equation 7.13 consists of two parts (Ref. 39): The external pressure on the soil by the vehicle mockup, which pressure is the same as the real one, namely,  $p_{a\pi}$  and the internal pressure  $p_T$  in the soil due to the weight of the overlying layer of thickness  $h$ , and which is different from that of the actual soil:

$$p = p_{a\pi} + p_T = p_{a\pi} + \rho_T h g$$

From this we can find the error in the magnitude  $p$  incurred during simulation:

$$\Delta = (p_M - p_H)/p_H = [\rho_T h (g_M - g_H)] / (p_{a\pi} + \rho_T h g_H) \quad (7.19)$$

where  $g_M = g_{\text{Earth}} = 6 g_{\text{Moon}} = 2.5 g_{\text{Mars}}$  and  $g_H = g_{\text{Moon}}$  (or  $g_H = g_{\text{Mars}}$ ). Equation 7.19 can be written as follows for Mars:

$$\Delta = 1.5 g_{\text{Mars}} \rho_T h / (p_{a\pi} + \rho_T h g_{\text{Mars}}) = 1.5 / [1 + (p_{a\pi} / \rho_T h g_{\text{Mars}})] \quad (7.20)$$

or for the Moon:

$$\Delta = 5 g_{\text{Moon}} \rho_T h / (p_{a\pi} + \rho_T h g_{\text{Moon}}) = 5 [1 + (p_{a\pi} / \rho_T h g_{\text{Moon}})]^{-1} \quad (7.21)$$

Equation 7.19 shows that the error in the magnitude of the pressure  $p$  increases with an increase in the depth of the soil layer. If we let  $h \approx 0$  at the surface and in the near-surface layers, we have  $\Delta \approx 0$ . Let us determine the magnitude of the error in soil pressure at a depth of  $h = 1$  m. Assuming that  $p_{a\pi} = 1 \times 10^5$  Pa,  $\rho_T = 1,200$  kg/m<sup>3</sup>, and  $g_{\text{Moon}} = 1.62$  m/s<sup>2</sup>,  $g_{\text{Mars}} = 3.74$  m/s<sup>2</sup>, we obtain  $\Delta = 0.095$  or 9.5% (for the Moon) and  $\Delta = 6.5\%$  (for Mars).

Inasmuch as subsidence  $\delta$  and shear resistance  $\tau$  are both directly proportional to normal pressure  $p$  acting on the soil, the error in their magnitudes during experiments using a soft soil will be of the same order. Consequently, with a degree of precision adequate for practical purposes, use is made of the simulated soil "without unloading" during experimental studies of the soft-landing process (and also of locomotion) when full-scale mockups of the space landing vehicles are used.

FOR OFFICIAL USE ONLY

## FOR OFFICIAL USE ONLY

It is of interest to note that an analogous result is obtained when questions of simulating planetary soils are considered during soft-landing studies using dynamically similar full-scale models of the space landing vehicle. In this case, mass is reduced  $K_j$ -fold and the external pressure by the model on the soil is the same as for the actual vehicle.

However, the use of a simulated soil corresponding in its properties to the actual soil during experiments with dynamically similar models (constructed with the scaling  $K_j^{-1} < K_\lambda < 1$ ) leads to a substantially distorted picture of the interaction between the landing gear and the soil of the planet. Thus, for a model scale (for the Moon) of  $K_\lambda = 1/2$ , the error in the magnitude of pressure on the soil (and, consequently, in the magnitude of soil subsidence) is about 200 percent. It is therefore necessary to create special model soils for such tests in accordance with the magnitude of the scale  $K_a$  ( $K_a < 1$ ).

Experimental studies under terrestrial conditions of the soft-landing process using a deformable soil whose properties simulate the characteristics of the planet's surface layer make it possible to obtain a complete analogy of the vehicle landing, to estimate the depth to which the landing gear will sink into the soil under different conditions of motion (especially when liftoff for the return flight is required), and to identify more precisely the zones of stable landing, which was done earlier for solid soils.

## Simulation of Surface Layer Characteristics of Planets Under Terrestrial Conditions

In considering the simulation of planetary soils, it was emphasized that for an experimental study of the soft-landing dynamics of space landing vehicles, it was important to develop a completely valid simulation of planetary soils with properties corresponding to the current knowledge of soils on the Moon and planets in the terrestrial group.\*

In spite of the fact that observations of heavenly bodies with the aid of terrestrial facilities have been carried out for a very long time, that the space age has already entered its third decade, and that mankind has made more than 25 soft landings of automated and manned vehicles on the Moon and the planets of the terrestrial group, our knowledge of the structure and properties of the surface layers of the planets (Table 7.2) is far from being complete enough to allow a correct solution of the many engineering problems arising during the design of future planetary landing systems and systems of locomotion on planets' surfaces.

\*Although the Moon is a satellite and not a planet, nevertheless, because in its physical characteristics it is close to the planets of the terrestrial type, wherever the term "planet" is used in the subsequent material it will also imply that the Moon is included.

FOR OFFICIAL USE ONLY

However, the available results of studies of the surface-layer characteristics of planets attest to the fact that in spite of their substantial differences (related to the individual planet's geological development, atmospheric conditions, forces of gravity, distance from the Sun, and so forth), the planets have much in common, especially in regard to the physical-mechanical soil properties. For this reason, structures and properties of planetary soils are usually stated in comparison with either the lunar soil or with various Earth rocks.

It thus seems useful to develop several variants of simulated soils (Table 7.3) for the simulation of planetary soils during terrestrial testing of space landing vehicles. Such soils should encompass in their physical-mechanical characteristics the full spectrum of values of these properties for planets of the terrestrial type (let us also remember that such properties of planetary soils as albedo, color, polarization angle, electrical and thermal characteristics, and so forth are not very significant in studying dynamic processes). By combining these simulated soils, we can obtain multilayer models of the planets' surfaces with the required changes of property as a function of depth and given profile (slopes, rocks, craters, and so forth).

Table 7.3

Parameters	Simulated Soil Variants		
	I	II	III
Density (kg/m <sup>3</sup> )	(0.4 to 0.8) x 10 <sup>3</sup>	(0.7 to 1.4) x 10 <sup>3</sup>	(1.5 to 3.0) x 10 <sup>3</sup>
Load-carrying capacity (Pa)	(0.2 to 0.6) x 10 <sup>5</sup>	(0.7 to 2.0) x 10 <sup>5</sup>	(2.0 to 5.0) x 10 <sup>5</sup> and higher

It is necessary to note that the simulated soil variants shown in Table 7.3 represent a refinement of a preliminary three-layer model based on contemporary data of the lunar surface structure proposed in the mid-1960's by V. S. Troitskiy, a member-correspondent of the USSR Academy of Sciences, and based on an analysis of results of radio sounding of the Moon and on measurements of the variation in the RF radiation temperature during the course of a lunar day (Refs. 19, 70).

For terrestrial perfection of the soft landing of a space landing vehicle, it is appropriate to choose the least favorable variant of the simulated soil. Thus, during studies of the performance capability of the energy absorbers, the determination of maximum stresses in the structural elements of the landing gear and maximum loading in the vehicle modules should be done with the densest simulated soil (variant III), made with monolithic

FOR OFFICIAL USE ONLY

FOR OFFICIAL USE ONLY

materials such as concrete, asphalt, and so forth. These same (least favorable) materials should also be used in determining the zone of stability of the vehicle by using models and full-scale mockups for landings on surfaces with various slopes, projections, and coefficients of friction.

In experimenting with dynamically similar models for studying the effectiveness of one or another landing-gear design using porous, loose soils, as well as during tests of flying vehicle mockups for estimating the specifics of landing and, in particular, return lift-off from such soils, it is necessary to use variants I and II of the simulated soils. Materials belonging to these variants can either occur naturally or be man-made.

Among the porous-foamy materials manufactured commercially are foamed concrete and gas-silicalcite, whose characteristics are given in Table 7.2.

The foamed concrete is a monolithic materials whose mechanical properties are close to variant II of the simulated soils manufactured from cement using a simple process.

The gas-silicalcite is made by a special process developed along the following methodology (Ref. 37). For certain ratios of CaO, SiO<sub>2</sub>, and Al<sub>2</sub>O<sub>3</sub> (without cement) and depending on heat treatment, materials with different mechanical characteristics are obtained. The common gas-silicalcite used for construction has a strength of (5 to 8) x 10<sup>5</sup> Pa. By changing the process and the composition of the mixture, it was possible to obtain gas-silicalcite (Figure 7.4) with a strength of ~ 10<sup>5</sup> Pa (chemical composition of the mixture: CaO, 31.5%; SiO<sub>2</sub>, 68.37%; Al<sub>2</sub>O<sub>3</sub>, 0.13%; and H<sub>2</sub>O, 42% of the dry weight of the mixture).

The man-made simulated soil, from a base of fine sand whose cohesion is provided by adding a quantity of mineral oil, possesses a porous, finely dispersed grain-aggregate cohesive structure. In its physical-mechanical properties, it can be classified under the first variant of simulated soils (Table 7.2). The sand-oil mixture is prepared in small portions and after thorough mixing is placed on the solid subsurface of the soil platform.

The comparison of the obtained simulated soil with the porous planetary soil in terms of grain/particle-size distribution shows a sufficient degree of correspondence. Data given in Table 7.2 refer to a simulated soil deposited on a soil platform by free pouring without additional processing (the average coefficient of porosity of the simulated soil in this case is 0.81). By compacting the simulated soil or by loosening it by different degrees, we can change its properties by varying the density of packing (Ref. 26). The method of preparing the soil platform for the tests also affects the relationship between density and porosity of the simulated soil as a function of depth.

FOR OFFICIAL USE ONLY

FOR OFFICIAL USE ONLY

Reference 26 gives the following relationship between pressure in the simulated soil under the die as a function of subsidence:  
$$p = 8.5 h^{1.01646} \times 10^5 \text{ Pa (where h is in meters).}$$

Reliability estimates of the constants (8.5 and 1.01646) using the Student criterion show that with a likelihood of 95 percent the relative errors amount to 10 percent and 8.1 percent, respectively.

In creating man-made simulated planetary soils, it is necessary to keep in mind that the basic factors that affect their physical-mechanical properties are the specific conditions on the surface of a given planet.

FOR OFFICIAL USE ONLY



FOR OFFICIAL USE ONLY

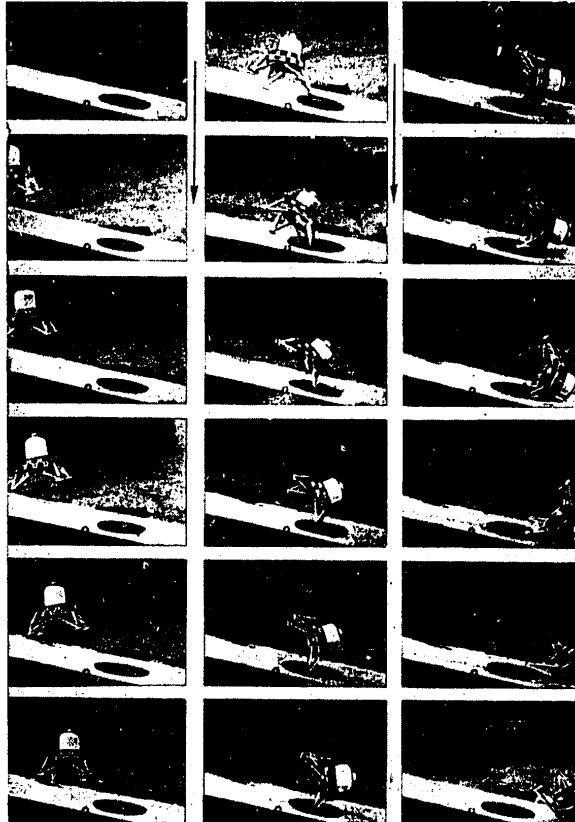


Figure 7.1. Unstable Landing of Dynamically Similar Model DPM-B in a Crater Located on a 15° Slope with Velocities  $V_{\text{vert}} = 2.5$  m/s and  $V_{\text{hor}} = 2.0$  m/s. (The landing configuration is "2-2", the soil rigid, depth of the crater 0.15 m, and the frame interval ~ 0.06 s)

FOR OFFICIAL USE ONLY

FOR OFFICIAL USE ONLY

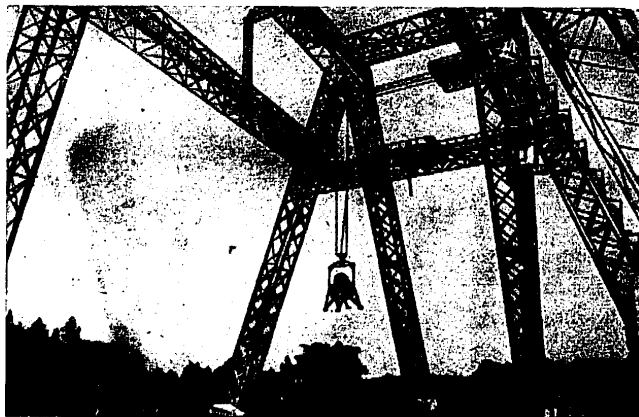


Figure 7.2. Overhead Test Stand for Developing the Pretouchdown Maneuver and Landing of a Full-scale Mockup of the Apollo Spacecraft

FOR OFFICIAL USE ONLY

FOR OFFICIAL USE ONLY

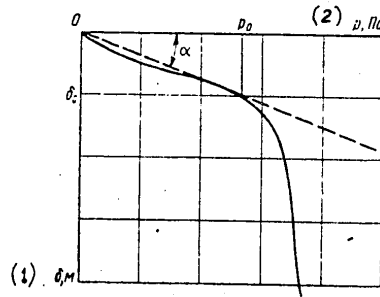


Figure 7.3. Deformation of Soil Under a Die as a Function of External Pressure ( $0 < p < p_0$ )

Key:

1.  $\delta$  (m)

2.  $p$  (Pa)



Figure 7.4. Reduced-strength Gas-silicalcite

FOR OFFICIAL USE ONLY

FOR OFFICIAL USE ONLY

CHAPTER 8

EXPERIMENTAL STUDIES OF SOFT LANDINGS USING DYNAMICALLY  
SIMILAR MODELS OF SPACE LANDING VEHICLES

Experimental studies of the soft-landing process for space vehicles using dynamically similar models are carried out with the following basic goals:

1. To study the effect of the vehicle's landing stability on the following: The vehicle's landing-gear system (number of legs in the landing gear, the size of the landing-gear leg pad, and so forth); both mass and inertial characteristics of the space landing vehicle (magnitudes of the moments of inertia, location of the center of mass, tank filling, and so forth); structure of the energy-absorbing devices and their energy capacity; variation in initial attitude of the vehicle during landing; initial angular velocities of the vehicle; direction of the horizontal component of the landing velocity relative to the vehicle and the surface; inclination of the surface and its unevenness ("profile"); and load-carrying capacity of the soil surface and the coefficient of friction.

It is necessary to conduct tests for different combinations of vertical and horizontal components of the velocity of approach to the surface, as provided by the test stand.

2. To study the effect on the vehicle mass of various landing-gear designs and structures, as well as the kinematics of its deployment.
3. To check out and refine the mathematical model assumed during the theoretical studies of the vehicle's landing gear on a digital computer (comparison and analysis of theoretical and experimental results).
4. To find the rapid and most effective way to develop the full-scale landing gear of the vehicle experimentally.
5. To prepare recommendations on the choice of landing-gear design and its geometric parameters, which will provide stability of the vehicle against toppling during landing, and recommendations on the strength of its structural elements and on the choice of scientific equipment.

The entire range of experimental studies of the soft-landing process using dynamically similar models is appropriately divided into two phases: (1) The study of the effect of the conditions of landing the vehicle on the planet's surface; (2) the study of the effects on the landing process of the vehicle's structural parameters.

In carrying out the first phase of the studies, it is necessary to vary the following: (1) Magnitude and direction of the landing velocity relative to the vehicle and to the surface; (2) surface slope angle and unevenness (simulating the "profile" of the landing area); (3) magnitude of the coefficient of friction between the landing gear and the soil; the load-carrying capacity and density of the upper soil layer; (4) initial orientation angles (pitch, yaw, and roll) and the initial angular velocities of the vehicle

FOR OFFICIAL USE ONLY

FOR OFFICIAL USE ONLY

during the drop. During the tests, the vertical and horizontal components of landing velocity are usually taken at discrete points (for example, in increments of 0.5 to 1.0 m/s).

During the phase in which the effect of structural parameters of the vehicle on the stability of landing is studied (second phase), such parameters are varied within ranges specified by the designers. In this case, in order to reduce the number of experiments, values of a whole group of parameters that characterize the vehicle's landing conditions are either fixed or are reduced in range to the maximum possible extent. As a rule, the values of parameters in this group are taken close to the critical ones so that the effect of structural parameters on the stability of the vehicle during landing will be most clearly manifested. The parameter values usually chosen are the maximum values of load factors, forces, and strains in the landing-gear elements.

Should excessive load factors, strains, or instability of the model be discovered during such tests within the range of velocities that can be encountered with the full-scale phenomena, changes of specific structural parameters of the model's landing gear are made (location of the center of gravity, magnitude of the support base, characteristics of energy absorption, and so forth), and an attempt is made to obtain favorable characteristics for a stable landing of the model in all required ranges of landing velocity. The structural changes made during this process are valuable recommendations for modification of the actual landing gear.

#### Dynamically Similar Models

We will briefly consider the particulars of the layout and structure of dynamically similar models intended for studying a soft landing on the Moon and on Mars (and Mercury). Characteristics (averaged data from various sources) for the three models, A, B, and C, corresponding to three lunar landing vehicles (with linear dimensions decreased by a factor of 6, and thus  $K_g = 1/6$ ) are shown in Table 8.1 for masses of from 5.6 to 16 tons at the time of landing (Refs. 8, 47, 55).

In its characteristics, the heavy vehicle (variant C) approaches the Apollo spacecraft, which was used for the first manned flight to the Moon (Ref. 55). Vehicle variant A (with a mass of about 5 tons) belongs to a class of automated vehicles capable of delivering large, unmanned stations and mobile laboratories to the Moon's surface (Ref. 47).

The methods-research model B was developed for studying the physical pattern of the soft-landing process on planets lacking atmospheres. It made possible a wide-range variation of basic structural parameters of the landing gear (for example, the number of landing-gear legs was varied from 3 to 6, and so forth) and was tested under different landing conditions using both rigid and deformable simulated planetary soils. Data are given in Table 8.1 on a four-leg modification of the model. The full-scale lunar vehicle of

FOR OFFICIAL USE ONLY

FOR OFFICIAL USE ONLY

Table 8.1

	Варианты КПА (1)		Параметры (20)											
			$m$ , кг (21)	$J_{\phi}$ , кг·м <sup>2</sup> (22)	$J_{\psi}$ , кг·м <sup>2</sup> (22)	$J_{\omega}$ , кг·м <sup>2</sup> (22)	$H$ , м (23)	$R$ , м (23)	$\bar{R}$	$N$ , шт (24)	$\epsilon$ , кН (25)	$\delta$ , м (25)	$f$	$V_{br}$ , м/с (26)
(2)	—	—	26,0	1,96	1,89	0,46	0,6	1,31	4	0,56	0,12	0-∞	0-3	0-1,5
(3)	—	—	5616	15246	14700	2,75	3,6	1,31	4	20,0	0,72	0-∞	0-3	0-1,5
(4)	—	—	1625	3062	2953	2,3	3,0	1,31	4	14,0	0,6	0-∞	0-4,2	0-2,1
(5)	—	—	406	191	185	1,15	1,5	1,31	4	3,5	0,3	0-∞	0-3	0-1,5
(6)	—	—	35,2	2,54	3,22	0,49	0,5	1,02	4	0,28-0,83	0,12	0,7-1,3	0-5	0-5
(7)	—	—	7600	19750	25040	2,94	3,0	1,02	4	10-30	0,72	0,7-1,3	0-5	0-5
(8)	—	—	2200	3969	5031	2,45	2,5	1,02	4	7-21	0,6	0,7-1,3	0-7	0-7
(9)	—	—	550	248	314	1,225	1,25	1,02	4	1,7-5,2	0,3	0,7-1,3	0-5	0-5
(10)	—	—	74,1	3,09	3,87	0,63	0,72	1,14	4	1,19	0,133	0,4-1,0	0-6	0-3
(11)	—	—	16000	24000	30100	3,8	4,32	1,14	4	43	0,8	0,4-1,0	0-6	0-3
(12)	—	—	4630	4828	6047	3,15	3,6	1,14	4	30	0,66	0,4-1,0	0-8,5	0-4,2
(13)	—	—	1158	302	378	1,575	1,8	1,14	4	7,5	0,33	0,4-1,0	0-6	0-3
(14)	—	—	11,3	0,99	0,477	0,2480	0,5685	2,29	3	0,47-1,89	0,133	0,4; 0,8	~7	0; 2
(15)	—	—	441,0	242	117	0,620	1,4212	2,29	3	7,4-30	0,33	0,4; 0,8	~7	0; 2
(16)	—	—	12,7	1,47	1,02	0,378	0,654	1,73	3	0,71-1,74	0,124	0,4; 0,8	~7	0; 2
(17)	—	—	496,0	359	219	0,944	1,636	1,73	3	11,1-27	0,31	0,4; 0,8	~7	0; 2
(18)	—	—	192	117	73,7	0,65	1,45	2,23	3	8,9-35,6	0,30	0,4-0,7	11,5	3
(19)	—	—	480	292,5	184,3	0,65	1,45	2,23	3	8,9-35,6	0,30	0,4-0,7	7,2	1,9

FOR OFFICIAL USE ONLY

FOR OFFICIAL USE ONLY

Table 8.1

Key:

1. Space landing vehicle variant
2. Model A [DPM = dynamically similar model]
3. Lunar space landing vehicle (scaled for  $K_L = 1/6$ )
4. Martian space landing vehicle (scaled for  $K_L = 1/5$ )
5. Martian space landing vehicle (scaled for  $K_L = 2/5$ )
6. Model B
7. Lunar space landing vehicle (scaled for  $K_L = 1/6$ )
8. Martian space landing vehicle (scaled for  $K_L = 1/5$ )
9. Martian space landing vehicle (scaled for  $K_L = 2/5$ )
10. Model C
11. Lunar space landing vehicle (scaled for  $K_L = 1/6$ )
12. Martian space landing vehicle (scaled for  $K_L = 1/5$ )
13. Martian space landing vehicle (scaled for  $K_L = 2/5$ )
14. Model D-1
15. Martian space landing vehicle (scaled for  $K_L = 2/5$  and  $K_E = 2/5$ )
16. Model D-2
17. Martian space landing vehicle (scaled for  $K_L = 2/5$  and  $K_E = 2/5$ )
18. Model D-3
19. Martian space landing vehicle (scaled for  $K_L = 1$  and  $K_M = 2/5$ )
20. Parameters
21. Units: kg
22. Units:  $\text{kg-m}^2$
23. Units: m
24. Units: number [of landing-gear legs]
25. Units: kN
26.  $V_{\text{vert}}$  in m/s
27.  $V_{\text{hor}}$  in m/s

variant B (obtained by scaling model parameters to correspond with criteria of similarity) having a landing mass of 7.6 tons can be assigned to the class of automated cargo vehicles intended to supply future lunar stationary bases.

By using conditions of similarity (Chapter 7, p 108), results of experiments (and of calculations) for model B can be generalized to the case of soft landing of dynamically similar Martian vehicles with a landing mass of 2,200 kg and 550 kg. The table also shows results of an analogous computation of characteristics for models A and C for Martian (and for Mercurial) conditions (for two linear scale values,  $K_L = 1/5$  and  $K_L = 2/5$  when  $K_E = 1$ ).

U. S. scientists designed and tested dynamically similar models of the Viking space vehicle specifically for studying the particulars of soft landing on Mars by using several configurations of this vehicle's landing gear. Three such models with scales  $K_L = 2/5$ ,  $K_E = 2/5$  and  $K_L = 1$ , and  $K_M = 2/5$  are also included in Table 8.1 (vehicle variant D [Refs. 50, 69]).

FOR OFFICIAL USE ONLY

FOR OFFICIAL USE ONLY

Let us present a brief description of the models mentioned.

Model A consists of a lifting body, landing-gear legs with energy absorbers, fuel tanks, suspension system, and load-centering system. Each of the four legs has three rods (strut and bracing struts) with collapsible devices and semispherical "shoes" to which crushable aluminum honeycombs are glued.

Model B has a rigid cylindrical body of aluminum alloy, to which from three to six landing-gear legs can be attached, a device for suspending the model, several variants of fuel tanks, and centering and balancing weights (Figure 8.1). The interchangeable legs consist of two lower side struts (bracing struts) and a central strut (stanchion) with an energy absorber (shock absorber). The energy absorber consists of a turned aluminum cylinder, inside of which is a freely moving piston with a piston rod. Inside the cylinder and under the piston is placed the aluminum honeycomb, which is crushed when the model lands on the surface. Instead of using an energy absorber with crushable aluminum honeycomb, the legs of the A and B models will use friction energy-absorbing devices.

The C model also has a light, rigid, cruciform body with cantilevers of A-shaped cross section. The four legs, consisting of a main strut (stanchion) and two lateral bracing struts, are connected to the cruciform body. All struts are equipped with shock absorbers for absorbing the energy of impact using aluminum honeycomb cartridges. Each strut of the model carries a small spike for modeling the increased coefficient of friction of the leg in contact with the surface, in lieu of a landing-gear-leg foot. At the model's center of gravity, a vertical strut is attached, which carries the model suspension mechanism for attaching to the test stand. The strut at the same time also serves for the attachment of balance weights at the required position.

The D models simulate the basic configurations of the Viking vehicle's landing gear. Two early models (D-1 and D-2) have identical truss type of bodies welded of aluminum tubing and triangular in layout, rigid and lightweight, and convenient for attaching centering and balancing weights. Models D-1 and D-2 differ from each other in the design of the landing gear, namely: The first model has landing-gear legs shaped like an inverted tripod, to whose apex a hinged foot is connected; the landing-gear legs of the second model are of cantilever design (two side braces attach to the main strut of the landing-gear leg somewhat below its middle, forming a bracket in the main strut) and also have a hinged foot.

The landing-gear main strut shock absorber is a cylinder into which four aluminum honeycomb cartridges, strung on a thin rod, are loaded. Each honeycomb cartridge deforms under the action of the applied force. During deformation of the shock absorber, the relationship between the force of compression and the displacement of the piston rod forms a staircase function (Figure 6.3).

FOR OFFICIAL USE ONLY



FOR OFFICIAL USE ONLY

Each energy absorber of the lateral struts (braces) of the landing-gear leg carries two honeycomb cartridges, one of which is used during compression of the brace and the other during extension.

The last model (D-3), in contrast to the two preceding ones, is a full-scale dynamic model of the Viking space landing vehicle with a landing gear in the form of an inverted tripod. The D-3 model has the dimensions and balance of the actual space landing vehicle; however, its mass is about 2.5 times less than that of the actual Martian vehicle (Table 7.1). The model has a rigid and very strong body of aluminum sheet and tubing welded together. The body carries balancing weights in order to give the model the necessary mass inertial characteristics. Honeycomb units (cartridges) are installed in the energy absorbers of the struts on each landing-gear leg to simulate four different values of compression force.

#### Operation Particulars for the Simulated Energy Absorbers

The landing gear of a space landing vehicle must have special energy absorbers to provide soft landing on the planet. The following requirements are placed on the energy absorbers: Small mass and small stowed volume; performance reserves for the case of premature shutdown of the retro power plant; the ability to operate under conditions of deep vacuum and rapid temperature drop; and strength and survivability for unanticipated landing conditions (hitting a stone, landing in a crevasse, landing on only some of the legs, and so forth).

During experimental studies under terrestrial conditions of the planetary soft-landing process (using models or full-scale mockups of space landing vehicles), special attention has to be given to so-called "modeled" energy absorbers, which are to simulate the actual ones in respect to forces and kinematics. Removing the requirement that they operate in a deep vacuum expands the available choices (Ref. 14) of methods that can be used for absorbing the kinetic energy in efficient model energy absorbers. Let us note, however, that specific results of such studies can be successfully generalized to full-scale energy absorbers (for example, honeycomb absorbers, extrusion type of devices, metallic torroidal and spherical envelopes, steel rods, and so forth).

Given below are only the basic results of the experimental studies of several types of model energy absorbers such as those that use a honeycomb cell structure made from different thicknesses of aluminum foil or sintered aluminum powder (Figure 8.2), those using collet friction energy absorbers, extrusion type of devices (Figure 8.6), and steel rods that deform plastically during extension.

Honeycomb energy absorbers, which are either completely or partially crushed during the landing of a model space landing vehicle, belong to the class of one-shot energy absorbers. The low proper mass, convenience of use, and nearly constant force of crushing during the process of compression--these are but a few of their positive qualities (Ref. 22).

FOR OFFICIAL USE ONLY

FOR OFFICIAL USE ONLY

The relationship between the force of crushing the honeycomb energy absorber and the magnitude of its deformation can be obtained experimentally with the aid of static (using test machines) and dynamic (using pile drivers) tests. During such tests, the compressive force is applied along the axis cells of the honeycomb unit.

The experimental equipment for static tests consists of a hydraulic press and a model cylinder with a piston (model of the leg of the full-scale landing gear), into whose open end the honeycomb units are inserted.

A pile-driver installation, in which the weight  $m_T$  free-falls onto the cylinder containing the honeycomb unit, is used for dynamic tests.

The motion of the weight following the instant of impact on the piston rod of the cylinder is described by the expression

$$m_T \ddot{y} = F_p - m_T g \quad (8.1)$$

where  $m_T$  is the mass of the weight,  $y$  is the coordinate of its center of gravity,  $F_p$  is the crushing force of the honeycomb unit (or the force of frictional resistance of the energy absorber), and  $g$  is the free-fall acceleration.

From Equation 8.1, we obtain the computational formula for

$$F_p = m_T g (\ddot{y}/g + 1) \quad (8.2)$$

where the value of  $\ddot{y}$  is determined from oscillograms, with the reading taken incrementally from the line  $n = +1$  (where  $n$  is the load factor).

Typical results of pile-driver tests on honeycomb energy absorbers are shown in Figure 8.3. Let us note the presence of a characteristic "small shelf" in the acceleration during the plastic deformation of the honeycomb unit and the subsequent "overshoot" of acceleration in the case when the energy of the falling weight is greater than the energy absorption capacity of the absorber (in this case, "elastic" collision is possible). Analysis of results of these studies allows the following conclusions to be made: Sufficiently good agreement exists between data from dynamic and static tests of the honeycomb energy absorbers; the resistance of the honeycomb unit to crushing is practically invariant for the entire distance of crushing (the scatter in force values is about 10 percent); in a number of cases, there is a "peak" in the force function during the initial period of compression of the honeycomb. However, this phenomenon can be eliminated by slightly prestressing the honeycomb; there occurs an occasional loss of stability in the honeycomb unit, accompanied by a sharp reduction in the force of resistance. The indicated loss of stability could have a number of causes: Distortion in the shape of the honeycomb-unit cells, initial deformation of one of the sides of the unit (due to faulty insertion of the unit into the cylinder), errors in manufacturing the honeycomb unit (gluing of the foil, cutting of the unit, and so forth).

FOR OFFICIAL USE ONLY

FOR OFFICIAL USE ONLY

We will develop an analytical expression for estimating an approximate value of the mean crushing stress  $\sigma_{cp}$  of a hexagonal honeycomb structure when subjected to a static axial load and freely supported at the end faces (Ref. 22):

$$\sigma_{cp} = 40.5 (t^2/d^2) \sigma_{0.2} + 1.155 (t/d) \tau_{0.3} \quad (8.3)$$

where  $t$  is the thickness of the cell wall (thickness of the foil),  $d$  is the diameter of a circle inscribed within the cell,  $\sigma_{0.2}$  is the yield point in tension, and  $\tau_{0.3}$  is the yield point in shear.

In deriving this equation, the material of the structure was assumed to have elastic plasticity with equal yield points in tension and in shear, and the effect of axial stresses on the character of the process of yielding was neglected.

A comparison of results from calculations using Equation 8.3 with data from the tests described above has shown that Equation 8.3 yields inflated and rather coarse estimates of the magnitude of the mean crushing stress of honeycomb structures (the overestimate reaches 50 to 70 percent). Comparison of calculations with experiments also attests to the significant overestimate in computed values (Ref. 22).

Frictional energy absorbers. Along with honeycomb energy absorbers, use is being made of model landing-gear legs that use dry friction. The elements, which provide absorption of kinetic energy in this landing-gear design, consist of tapered inserts made of polycaprolactam and are drawn up to the piston rod by a special nut (Refs. 7, 13).

Testing of friction energy absorbers can be carried out by using the same equipment and the same methods as for the honeycombs. Typical results of static and dynamic tests of model space landing vehicle landing-gear legs with such a design are shown in Figures 8.4 and 8.5.

The following are results of testing friction energy absorbers: (1) Motion of the piston rod during the energy-absorption process draws the insert material into the cylinder of the absorber and causes an increase in resistance (this is the "self-tightening" phenomenon in the energy absorber). For the same reason, resistance during "compression" of the absorber is larger than during its "extension" (that is, during extraction of the piston rod from the cylinder), with this increase in some cases reaching 30 percent. Absence in the oscillograms of the "small shelf" of accelerations also is proof of the continuous growth in the resistance force (a comparison with honeycomb absorbers is interesting); (2) for impacts with large initial velocity (about 4.0 m/s), movement of the absorber piston rod begins when the value of the resistance force is somewhat smaller than the static force of the initial tightening; (3) a damped oscillation in acceleration (and in the force of resistance) takes place during the initial moment of piston-rod movement, which cannot be natural oscillations of the seismic mass of

FOR OFFICIAL USE ONLY

FOR OFFICIAL USE ONLY

the transducer (because the latter is well damped). These oscillations are apparently connected with the elastic properties of the inserts, which are rubbing against the piston rod and are being pulled into the cylinder (a variety of free oscillations); (4) a substantial influence on the character of the change in the force of resistance during the energy-absorption process is produced by the manufacturing deviations during the manufacture of piston rods and polycaprolactam inserts of this series of energy absorbers; (5) model friction energy absorbers with inserts of polycaprolactam assure, under full-scale conditions, a sufficiently high stability for the energy-absorbing device during repeated tests (this results in a multiple-use model energy absorber).

The shear type of energy absorbers use the "broach" principle (Ref. 42). The moving rod of the energy absorber, which consists of a broach with cutting edges (teeth), is connected to the landing-gear leg of the vehicle. At the moment of landing, the landing-gear leg becomes loaded and is compressed. The rod of the energy absorber translates inside a special bushing and its cutting teeth sequentially cut some layer of metal (Figure 8.6).

The magnitude of resistance force  $F_p$ , which is developed by such an energy absorber, depends on the bushing material, the number of simultaneously engaged teeth, the length of their cutting edges, and the thickness of the layer of metal being cut, that is:

$$F_p = \pi p_{\text{IIp}} \sum_{i=1}^{i=N} C_i d_i t_i, \quad (8.4)$$

where  $p_{\text{IIp}}$  is the pressure of the broach tooth applied to the bushing material during compression of the energy absorber (being tested) (Ref. 42);  $N$  is the number of simultaneously engaged teeth of the piston rod;  $d_i$  is the diameter of the cutting edge of the  $i$ -th tooth;  $C_i$  is the length coefficient of the cutting edge of the  $i$ -th tooth ( $C_i \leq 1$ ; when  $C_i = 1$ , the cutting edge goes completely around the tooth); and  $t_i$  is the thickness of the layer of metal being cut by the  $i$ -th tooth.

Typical results of tests to determine the relationship between resistance force  $F_p$ , developed by a shear type of energy absorber and the translation of its rod, are shown in Figure 8.7. Interchangeable bushings of various materials (D16T, AMg-6, D16M, AK-6, and others) were used during the tests. Oscillograms obtained during pile-driver tests, which showed a clear "shelf-like" acceleration, strongly resemble oscillograms from tests of honeycomb energy absorbers.

Experimental tests have established the following basic characteristics of the shear type of energy absorbers: (1) Small mass and small dimensions for large energy capacity; (2) ease of obtaining the necessary resistance force and desired characteristics for its variation (by selecting material and the width of the interchangeable bushing and by profiling the teeth of

FOR OFFICIAL USE ONLY

FOR OFFICIAL USE ONLY

the broach); (3) adequate agreement between the resistance force for dynamic and static compression of the energy absorber (differences can reach about 15 percent); (4) lack of sharp oscillations in acceleration (and of the force of resistance) during the initial moments of energy absorption; (5) insignificant effect of environmental conditions (temperature, humidity, and others) on the characteristics of the absorber; (6) high stability of the absorber characteristics during repeated tests (for the same material of the interchangeable bushings); (7) convenience (ease of reloading, "calibration," and so forth).

The features of the shear type of energy absorber suggest the possibility of its successful use not only during terrestrial development of the soft-landing process but also directly in the actual space landing vehicle.

Energy absorbers using deformable steel struts can be of different designs whose basic elements are two telescoping, connected tubes with an internal rod. The steel rod is connected to both tubes by special transition units.

The impact load arising during landing of the model space landing vehicle is transmitted via the internal tube (piston rod) of the energy absorber to the rod. When this happens, the rod is stretched, because its other end is rigidly connected to the outside tube. If the load stretching the rod exceeds the yield point of its material, plastic deformation of the rod is initiated, which results in the absorption of the energy of impact.

The magnitude of the force  $F_p$  resisting compression in such an energy absorber depends on the tension yield point of the rod material,  $\sigma_{0,2}$ , and on the rod diameter,  $d_{plast}$ , in the segment where plastic deformation occurs, that is,

$$F_p = 0.25\pi\gamma\sigma_{0,2}d_{plast}^2 \quad (8.5)$$

where  $\gamma$  is an empirical coefficient, which accounts for the effect of friction between the elements of the shock absorber on the magnitude of the compression force ( $\gamma \geq 1$ ).

By using pile-driver and static tests, it is possible to determine the characteristics of energy absorption of such a shock absorber with rods made of different steels (for example, 1Kh18N9T, Kh17G9AN4, and others) that possess good plasticity properties. As results of the tests show, the energy absorber being considered is distinguished by: High energy capacity for small dimensions and mass; high compression diagram block coefficient; good agreement between results of dynamic and static testing; low elastic properties when external loads are removed; small effect of environmental conditions (positive and negative temperatures, humidity, and so forth) on the characteristics of energy absorption; and simple design from the point of view of manufacturing technology and application.

FOR OFFICIAL USE ONLY

## FOR OFFICIAL USE ONLY

It should be noted that energy absorbers with deformable rods (as well as honeycomb shock absorbers) have been used successfully for the Luna-16, -17, -20, -21, and -24 automated space vehicles (Ref. 16), all of which made soft landings in various regions of the lunar surface.

## Model Test Stands

Test stands are used for the experimental study of the soft-landing process of space vehicles on the Moon, on Mars, and on other planets using free-falling, dynamically similar models. Test stands make it possible to study, under terrestrial conditions, the stability of a space vehicle during soft landing, to estimate the loads acting on it, to select an optimum landing gear in terms of structural mass, and to develop its energy-absorbing elements. An interchangeable ground simulating the surface layer of the Moon, Mars, or other planets substantially expands the usefulness of the stand.

Such a test stand consists of: A special turntable (platform) with the planetary soil simulator, a pendulum system for suspending and dropping the space landing vehicle model, and a measuring and recording system (Figure 8.8).

The height  $h$  for lifting the model of the vehicle above the turntable is determined by the required magnitude of the vertical component  $V_B$  of the landing velocity and is controlled by rotating the cantilever beam of the stand in the vertical plane. The magnitude of the horizontal component  $V_P$  of the landing velocity depends on the angle  $\beta$  of the deflection of the parallelogram of the pendulum suspension system from its vertical position.

The magnitudes of  $h$ ,  $\beta$ , and  $D$  are computed by the following formulas:

$$h = \frac{V_n^2}{2g} \left( 1 - 2 \operatorname{tg} \theta \frac{V_r}{V_n} \right); \quad \beta = \arccos \left[ 1 - \frac{V_r^2}{2gl} \right]; \quad D = \frac{V_n V_r}{g \cos \theta}, \quad (8.6)$$

where  $g = 9.81 \text{ m/s}^2$ ;  $l$  is the length of the parallelogram of the suspension system; and  $\theta$  is the angle of inclination of the planetary soil simulator.

Due to some friction in the suspension bearings and air resistance during flight of the vehicle model, the components of its landing velocity will be somewhat smaller than those assumed in Equation 8.6.

In experimental terrestrial studies of soft landing, it is common to make measurements and to record the following parameters (using oscillograms, magnetic tapes, and so forth): Angles of pitch, yaw, and roll (the orientation of the model); vertical and horizontal loads (at the center of mass of the model and at all landing-gear legs); pressure of the fuel on the walls of the model tanks; angular accelerations and velocities of the

FOR OFFICIAL USE ONLY

model; deformation of the energy absorbers; and stresses in the landing-gear structural elements of the model.

Inductive sensors (DU-5), incorporated into compact equipment such as VI6-5MA, are used for measuring vertical and horizontal load factors (accelerations) (the DU-5 sensors can also be used with tensiometric equipment).

The pressure of the simulated fuel on the tank walls of the model vehicle can be measured by pressure transducers DD-1 through DD-6 (which are included in equipment assembly VI6-5MA). The DD transducers can also be used to transform the mechanical quantities to be measured into electrical signals.

Sensors built on the gyroscope principle are unsuitable for measuring angular accelerations and velocities of the model, due to their relatively large dimensions, their pronounced influence on nearby sensors, and their low impact resistance. An angular acceleration sensor without the shortcomings indicated and insensitive to linear accelerations was proposed in Reference 36. Such a sensor consists of a stator and a rotor connected by elastic springs. The spring transverse axis passes through the rotor's center of gravity and is its axis of rotation. Responding to the angular acceleration to be measured, the rotor rotates with respect to the stator. Due to complete balancing of the rotor, this sensor is not affected by linear accelerations.

To measure the magnitude and character of the deformation of the energy absorbers of the landing-gear legs at impact, special linear potentiometer sensors are used (Figure 8.2) consisting of 0.5-mm-diameter Constantan wire, stretched along the anodized rod of the leg, and a sliding contact that grasps the wire.

The stress, which shows up in the rods of the landing-gear leg during contact of the model with the ground, is measured by calibrated wire strain-gages.

Signals from all transducers in the model are transmitted via a lightweight suspended cable to the recording equipment, which can consist of widely used loop oscillographs, electronic oscillographs, magnetic tape with video receivers, cine-cameras, or others.

The experimental development of the landing gear for the Viking automated Martian vehicle was carried out at the Langley Research Center (United States) with the pendulum type of model test stands. Several dynamically similar models were used (Table 8.1, Models DPM-G). Different pendulum stands were used for tests of the small-scale models G-1 and G-2 (with a 2.5-fold reduction in linear dimensions compared with the actual vehicle) and a full-scale model G-3 (with about a 2.5-fold reduction in mass compared with the actual vehicle).

## FOR OFFICIAL USE ONLY

Some engineering characteristics of the two model-testing stands (at the Langley Test Center; Refs. 50, 69) are shown in Table 8.2.

Table 8.2

Name of Parameter	Test Stand for Model	
	G-1, G-2	G-3
Nominal height of lifting model (m)	~ 2.5	> 7
Nominal deflection angle of the support (deg.)	~ 40	> 30
Nominal vertical touchdown velocity (m/s)	~ 7	~ 12
Nominal horizontal touchdown velocity (m/s)	~ 2	~ 3
Nominal weight of model (N)	~ 130	~ 2,000
Width of landing platform (m)	1.8	~ 4
Length of landing platform (m)	3.7	~ 7
Nominal platform slope angles (deg.)	$\pm 20$	$\pm 20$
Nominal model pitch angles (deg.)	$\pm 15$	0 to 10
Coefficients of friction between landing-gear legs and platform	0.4; 0.8	0.4-0.7

The landing platform of the first stand was made of solid wood and was covered with smooth plywood (1.9 cm thick). One end of the platform was adjustable in height in order to obtain different slope angles. The aluminum pads of the model had a coefficient of friction of 0.4 in slipping on the smooth plywood. A coefficient of friction of 0.8 was obtained when the pads of the model landing-gear legs were covered with a thin layer of rubber.

The wooden landing platform of the second stand was mounted on a rigid and more massive platform. The four-rod pendulum suspension was attached with bearings to the girder boom of a special crane at a height of about 14 m and deflected to the required angle using a cable connected to the crane winch.



FOR OFFICIAL USE ONLY

## Errors in Measuring the Basic Parameters During the Experiment

Such errors basically turn out to be errors in the measurement of physical quantities, which characterize the dynamics of soft landing of the model space landing vehicle, errors in reading oscillograms (tapes), and errors introduced by the reaction to the impact of the massive test-stand table supporting the simulated soil.

Let us estimate the error in the approximate determination of the components of the model's landing velocity by using equations

$$\begin{aligned} V_B &= [2g (h_{\text{meas.}} + D_{\text{meas.}} \sin\theta_{\text{meas.}})]^{1/2}; \\ V_\Gamma &= g D_{\text{meas.}} \cos\theta_{\text{meas.}} V_B^{-1} \end{aligned} \quad (8.7)$$

From Reference 30, we have

$$\begin{aligned} \ln V_B &= (1/2)\ln 2g + (1/2)\ln (h + D \sin\theta); \\ d(\ln V_B) &= dV_B/V_B = [dh + D \cos\theta d\theta + \sin\theta dD][2 (h + D \sin\theta)]^{-1} \end{aligned}$$

or

$$\Delta V_B/V_B = (\Delta h + D \cos\theta \Delta\theta + \sin\theta \Delta D)/[2 (h + D \sin\theta)] \times 100\% \quad (8.8)$$

As the maximum absolute errors in the measurement of the geometric parameters  $D_{\text{meas.}}$ ,  $h_{\text{meas.}}$ , and  $\theta_{\text{meas.}}$  do not exceed the values  $\Delta h = \pm 0.02$  m,  $\Delta D = \pm 0.02$  m, and  $\Delta\theta = \pm 0.5^\circ$ , the relative error on computing  $V_B$  is about 7 percent. The relative error in computing  $V_\Gamma$  can be found in the formula

$$\Delta V_\Gamma/V_\Gamma = [(\Delta D/D) + \tan\theta \Delta\theta + (\Delta V_B/V_B)] \times 100\% \quad (8.9)$$

Thus, we find that the error in computing  $V_\Gamma$  is approximately 10 percent.

The total error in measurement during dynamic tests of the model is conveniently expressed in terms of the component errors in the individual elements of the measurement system (Ref. 28).

In our case, the total error in measurement consists of the following: Errors in the sensing elements (transducers),  $\sigma_a$ ; errors in the amplification equipment,  $\sigma_a$ ; errors of the oscillograph galvanometers,  $\sigma_\Gamma$ ; and errors in recording and reading,  $\sigma_3$ .

Thus, for example, in measuring the linear acceleration using a system of inductive sensors and strain-gage equipment, the indicated component errors are as follows: (1) Errors of the DU-5 sensor for normal measuring conditions in the required range of amplitudes and frequencies are 3 percent; sensitivity to the acceleration components not being measured is 0.5 percent; error due to temperature is approximately 3 percent; and the error due

FOR OFFICIAL USE ONLY

## FOR OFFICIAL USE ONLY

to inaccurate mounting of the sensor is also approximately 3 percent. Therefore,

$$\sigma_{\Delta} = [3^2 + 0.5^2 + 3^2 + 3^2]^{1/2} = 5.2\%$$

(2) The error in the amplification equipment in the system with an inductive sensor includes the sensitivity of the output current to variations in the supply voltage of  $\pm 10$  percent, for which it is less than 1.5 percent; the sensitivity of the output current to cross-talk between channels is less than 1 percent; the error in frequency characteristics of the amplifier in the range from 0 to 500 Hz is approximately 3 percent; and the nonlinearity of the amplitude characteristics of the sensor-to-amplifier channel is about 4 percent. Therefore,

$$\sigma_{\Delta} = [1.5^2 + 1^2 + 3^2 + 4^2]^{1/2} = 5.3\%$$

(3) The error of a coil galvanometer with a natural frequency  $f_0 = 400$  Hz and a working frequency range of 0 to 200 Hz is less than 1 percent, that is,  $\sigma_{\Gamma} = 1\%$ .

(4) The absolute error in recording and reading includes the inaccuracy in locating the zero line, the deviation of the recording ordinate from the normal to the zero line, and reading errors along the ordinate and the abscissa, which is about  $\pm 0.4$  mm. Thus, the relative error in recording and reading a mean 20-mm deflection in the light beam equals

$$\sigma_3 = 0.4 : 20 \times 100 = 2\%$$

By assuming a normal distribution for the partial errors, we find the total error of measuring linear accelerations to be:

$$\sigma_y = [\sigma_{\Delta}^2 + \sigma_a^2 + \sigma_{\Gamma}^2 + \sigma_3^2]^{1/2} = 7.8\%$$

By determining analogously the error in measuring landing-gear-leg deformations and the stresses (forces) in the structural elements of the landing gear, we find the corresponding quantities to be 5.6 and 5.3 percent.

Let us estimate the effect of rigidity for one of the variants of the special test-stand platforms (simulating the planet's surface) on the dynamics of the soft-landing process. With this goal, we determine what part of the total kinetic energy of the model is dissipated by the structure of the platform during oscillations arising from the model's impact on landing.

The girder structure of the special platform, which has center and edge supports and carries the simulated soil of the planet, is laid out as a three-point support beam with equal spans  $l$  and an evenly distributed mass per unit of length ( $m_{\text{гор}}$ ). At the fundamental mode of vibration, each span of such a beam will be in the condition of a beam with free end supports (Ref. 34). It can be assumed with sufficient accuracy that, during the oscillation

## FOR OFFICIAL USE ONLY

process, the deflected axis of the rod has the shape of the static deflection curve of a beam loaded in the middle and of constant cross section, that is:

$$y(x, t) = A(t) (3l^2x - 4x^3)l^{-3}$$

where  $A(t)$  is the displacement at the center of the span of the vibrating beam with free end supports.

Let us find an expression for the kinetic energy of vibration of the platform structure:

$$\begin{aligned} E_{cr} &= \frac{1}{2} \int_0^{2l} m_{nor} \dot{y}^2(x, t) dx = \frac{2\dot{A}^2(t) m_{nor}}{l^6} \int_0^{l/2} (3l^2x - 4x^3)^2 dx = \\ &= \frac{17}{35} \dot{A}^2(t) m_{nor} l. \end{aligned}$$

If we assume that  $A(t) = A_0 \cos pt$ , we get  $\dot{A}_{max} = A_0 p$ , where  $A_0$  is the amplitude of vibration at the midpoint of the span for  $l/2$ , and  $p$  is the angular frequency of the fundamental mode of vibration of the test-stand platform. The expression for estimating the magnitude of kinetic energy dissipated by the structure of the test-stand platform during oscillations takes on the form

$$E_{cr} = \frac{17}{35} A_0^2 p^2 m_{nor} l. \quad (8.10)$$

The parameters  $A_0$  and  $p$  are determined experimentally:  $p$ , by using the resonance method of exciting the basic frequency of oscillation of the platform;  $A_0$ , during drops of dynamically similar models of the space landing vehicle onto the platform (oscillogram, Figure 8.9). For our case, we have

$$A_{0\text{experim.}} = 3.33 \times 10^{-3} \text{ m}; m_{\text{TOT}} = 540 \text{ kg/m}; l = 5 \text{ m};$$

$$p_{\text{experim.}} = 2\pi f_{\text{experim.}} = 2\pi \times 4.2 = 26.4 \text{ deg/s}$$

By substituting these values into Equation 8.10, we find that  $E_{CT} = 10.1 \text{ J}$ . The total energy of the model at the beginning of the test was

$$E_{TOT} = m_M g h = 295 \text{ J}$$

where  $m_M = 35.2 \text{ kg}$  is the mass of the DPM-B model, and  $h = 0.85 \text{ m}$  is the height to which the center of gravity of the model was raised for the test.

Thus,  $\bar{E}_{CT} = E_{CT}/E_{TOT} = 0.0342$ , or 3.42 percent of the total energy of the model is dissipated in vibrations of the structure of the test-stand platform, which attests to the suitability of using a special test-stand platform for experiments in modeling soft landings on planets.

FOR OFFICIAL USE ONLY

It is necessary to note that representing the platform, which has a camber in the cross section that decreases from the center to the edges, by a beam with constant cross section will lead to some increase in the estimate of  $\bar{E}_{CT}$ . In the case considered, the model is dropped onto the midpoint of one-half of the platform, exciting vibrations with the greatest amplitudes. If the model, however, "lands" in the area of the central support of the platform (which occurs during the majority of the tests, especially for landings downward along the slope), then the amplitude of vibrations of the table will be less by an order of magnitude. We also note that in the calculation above, no account was taken (due to its small amount) of the energy dissipated during vibration by the structure of the test-stand platform at higher harmonic frequencies (Ref. 32).



Figure 8.1. Test Facility. On the left: The test stand; on the right: The dynamically similar model B

FOR OFFICIAL USE ONLY

FOR OFFICIAL USE ONLY

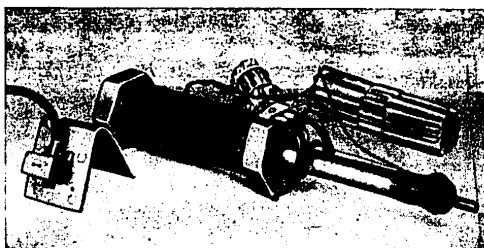


Figure 8.2. Honeycomb Energy Absorber

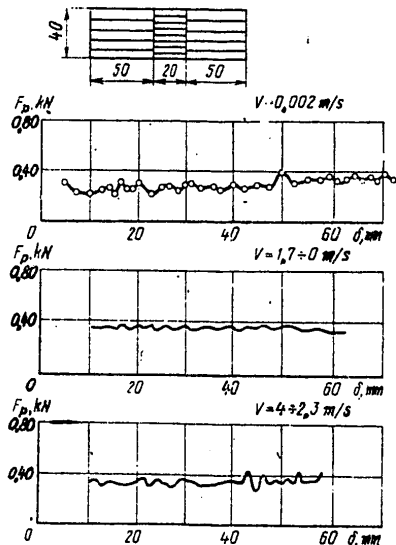


Figure 8.3. Typical Test Results for a Honeycomb Energy Absorber. Hexagon side, 6 (or 2.5) mm; foil thickness, 0.05 (or 0.15) mm; material, Al-T (SAP [sintered aluminum powder]); drop test weight,  $m_T$ , 19.3 kg

FOR OFFICIAL USE ONLY

FOR OFFICIAL USE ONLY

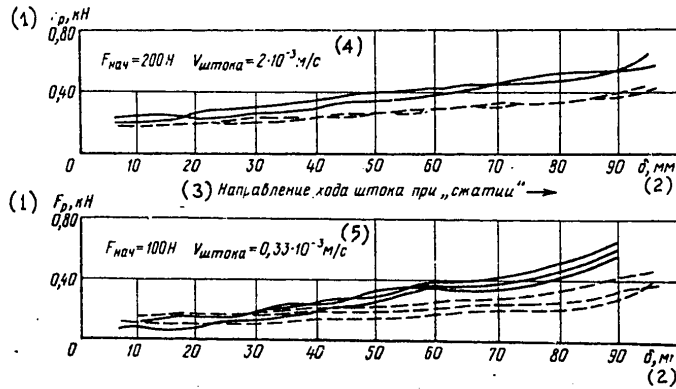


Figure 8.4. Typical Results from Static Tests of Friction Energy Absorbers

Key:

- Compression
- Tension
- 1.  $F_p$  (kN)
- 2.  $\delta$  (mm)
- 3. Direction of rod travel during compression
- 4.  $F_{initial} = 200 \text{ N}$ ,  $V_{rod} = 2 \times 10^{-3} \text{ m/s}$
- 5.  $F_{initial} = 100 \text{ N}$ ,  $V_{rod} = 0.33 \times 10^{-3} \text{ m/s}$

$\delta_k$	10	20	30	40	50	60	70	80	90
$m_F(\delta_k)$	0,127	0,135	0,164	0,209	0,245	0,295	0,322	0,376	0,476
$D_F(\delta_k) \cdot 10^4$	4,6	5,6	10,8	14,4	39,4	61,9	67,5	69,5	233
$\sigma_F(\delta_k)$	0,021	0,024	0,033	0,038	0,063	0,079	0,082	0,083	0,153

FOR OFFICIAL USE ONLY

FOR OFFICIAL USE ONLY

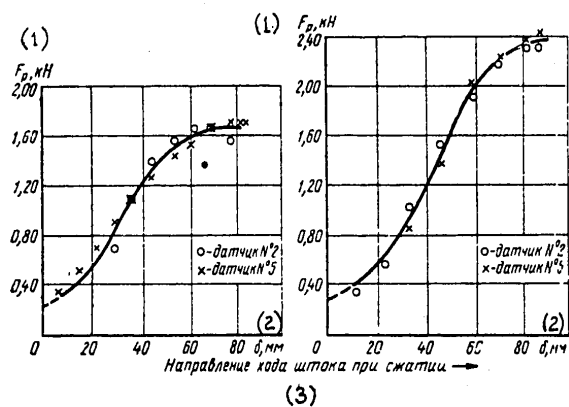


Figure 8.5. Typical Results from Dynamic Tests of Friction Energy Absorbers. Transducer No. 2 (data points shown by circles) is located on the energy absorber; transducer No. 5 (data points indicated by crosses) is located on the drop weight, of mass  $m_T = 19.3$  kg. Left figure is for test No. 105 ( $F_{initial} \approx 400$  N and  $V_{rod\ initial} = 3.1$  m/s); right figure is for test No. 104 ( $F_{initial} \approx 400$  N and  $V_{rod\ initial} = 3.8$  m/s).

Key:

1.  $F_p$  (kN)
2.  $\delta$  (mm)
3. Direction of rod travel during compression



Figure 8.6. Shear Type of Energy Absorber (Using the Broach Principle)

FOR OFFICIAL USE ONLY

FOR OFFICIAL USE ONLY

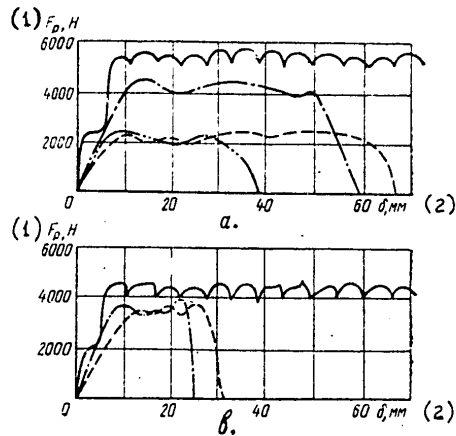


Figure 8.7. Typical Test Results for a Shear Type of Energy Absorber. (The material of the interchangeable bushings is D16T in Figure a and D16M in Figure b; the material of the broach is R18.)

Key:

1.  $F_p$  (N)
2.  $\delta^p$  (mm)

Key for Figure a:

With  $N = 2$  teeth:

- Static compression with  $V_{rod} = 2.5 \times 10^{-4}$  m/s
- - - Dynamic compression with  $V_{rod_{init.}} = 5.2$  m/s

With  $N = 1$  tooth:

- - - Dynamic compression with  $V_{rod_{init.}} = 4.0$  m/s
- · - · - Dynamic compression with  $V_{rod_{init.}} = 3.0$  m/s

Key for Figure b:

- Static compression with  $V_{rod} = 2.5 \times 10^{-4}$  m/s

With  $N = 2$  teeth:

- - - Dynamic compression with  $V_{rod_{init.}} = 3.3$  m/s
- · - · - Dynamic compression with  $V_{rod_{init.}} = 3.0$  m/s

FOR OFFICIAL USE ONLY



FOR OFFICIAL USE ONLY

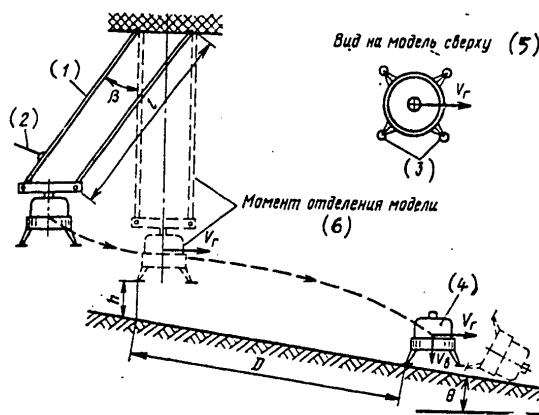


Figure 8.8. Schematic Diagram of Test Stand for Models

Key:

1. Pendulum
2. Winch cable
3. Landing-gear legs
4. Model
5. Top view of model
6. Instant of model separation

FOR OFFICIAL USE ONLY

FOR OFFICIAL USE ONLY

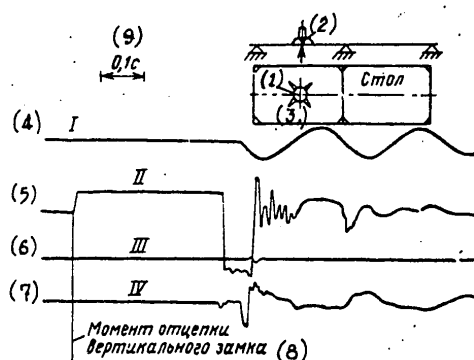


Figure 8.9. Estimating the Effect of Rigidity of the Simulated Planetary Surface. (Height of drop, 0.85 m;  $\theta \approx 0^\circ$ ; configuration, 2-2.)

Key:

1. Point at the platform center
2. Point on the model
3. Point at the platform edge
4. Trace from a translation transducer at point 1, with  $f_{\text{experim.}} = 4.2 \text{ Hz}$  and  $A_0 = 3.3 \text{ mm}$
5. Trace from an accelerometer at point 2
6. Trace from an accelerometer at point 3
7. Trace from an accelerometer at point 1
8. Moment of releasing vertical coupling
9. 0.1 s

FOR OFFICIAL USE ONLY

FOR OFFICIAL USE ONLY

CHAPTER 9

PECULIARITIES OF TERRESTRIAL EXPERIMENTAL DEVELOPMENT  
OF SOFT LANDING WITH THE AID OF FULL-SCALE MOCKUPS  
OF SPACE LANDING VEHICLES

In Chapter 7, it was indicated that preserving the similarity of phenomena during the modeling of soft landing by using full-scale mockups of space landing vehicles is possible on Earth only by creating conditions of planetary gravity. Means for "unloading" a full-scale mockup of a space landing vehicle appropriate for attaining such a goal turn out to be relatively easy from an engineering standpoint and can be implemented by different designs. Such designs fall into two groups: Unloading aided by special jet engines installed in the mockup (creation of free-flight mockups of the vehicle), and unloading aided by test-stand mechanisms consisting of a feedback device with an unloading installation (creation of a test-stand-dependent, full-scale mockup of a vehicle).

Because the permissible deviation in the value of unloading force from its nominal value as determined from similarity conditions (Equation 7.9) is 1 to 3 percent, the limiting deviations in the direction of the mockup unloading force from the vertical is limited by a cone with an apex angle of from 0.3 to 1.0 degrees.

The fundamental characteristic of experimental soft-landing studies using full-scale mockups of the vehicles is that they, apart from the final test of the performance capability of the landing gear and estimating its effectiveness and reliability, permit a full-scale development of the final stage of flight and landing on the planet's surface (which is especially valuable for piloted or remotely controlled vehicles).

Flying Mockups of Space Landing Vehicles

Flying mockups can be created in accordance with the "unloading" variants, indicated in Chapter 7, by using jet engines (it is also possible to use helicopters to replace these power plants).

The first unloading variant makes it possible to obtain the greatest accuracy in simulating the flight of an interplanetary craft. However, to use a full-scale mockup of the interplanetary vehicle as the flying mockup, it is necessary to install not just one unloading power plant but several in it, with a resultant thrust vector passing through the center of mass of the system.

For actuating elements of the control system, it is possible to use jet vanes on the landing vehicle, or control jets using compressed air bled from the jet engine, or jet vanes located downstream of the exhaust nozzles of the jet engine. Considering that there are certain difficulties in creating such a flying mockup, it is useful to consider the possibility of using

FOR OFFICIAL USE ONLY

FOR OFFICIAL USE ONLY

helicopters equipped with special mechanisms for unloading the flying mockup. The horizontal translations of the full-scale mockup caused by its motions in the gimbal support can be followed by the helicopter in such a fashion that the motions of both the helicopter and the mockup have the same kinematic parameters. The basic difficulties, which it is necessary to surmount in creating a flying mockup using this approach, include the following: Providing for synchronism of motions of the helicopter and the mockup suspended below it, preventing the mockup from swinging on the support cable, estimating the effect produced by the airstream excited by the helicopter blades and vibration of the helicopter, and problems of pilot rescue using an ejection installation in case of helicopter or mockup accident.

From the point of view of ease of building and using the flying mockup, two other variants of "unloading" that use a single unloading jet engine in the flying mockup are more advantageous (in spite of the fact that in this case the accuracy of simulating the flight of an interplanetary craft is less than during the first variant).

To make preliminary experimental tests of the dynamics of motion of the landing vehicle, to develop some of its systems, and to provide for the initial stage of crew training, a helicopter can be used as a flying mockup by installing a gimballed cabin having two degrees of freedom (pitch and yaw) on the helicopter.

Simulating the full-scale linear translations of the vehicle with corresponding kinematic parameters is provided by a special control system for the helicopter and by modifying its mass-inertial characteristics to correspond to those of the actual vehicle.

Many studies of the soft-landing process were done in the United States during the mid-1960's in connection with the Apollo program, which was planned for landing American astronauts on the Moon and subsequently return them to Earth. A special lunar vehicle was used to provide a soft landing of two astronauts on the Moon's surface, support their stay on the surface, and subsequently deliver them to a selenocentric orbit.

Four telescoping landing-gear legs of the vehicle have crushable inserts of aluminum honeycomb, which absorb the impact loads. The disk-shaped support pads are also of aluminum honeycomb.

The LLRV flying mockup (Figure 9.1) was created for developing the methods for the final flight stage of the Apollo vehicle, for training astronauts under conditions simulating the Moon landing, and for studying the controllability and stability of a lunar vehicle during landing (Ref. 46). The LLRV is a vertical take-off vehicle, at whose center of mass a CF-700-2 jet engine is suspended in a two-degree-of-freedom gimbal system. The jet engine thrust compensates for 5/6 of the vehicle's weight in order to model lunar gravity. During flight, the engine is maintained in a vertical attitude (the first variant of "unloading"). For changing the vertical velocity

FOR OFFICIAL USE ONLY

## FOR OFFICIAL USE ONLY

of the vehicle, eight rocket engines using the products of dissociation of hydrogen peroxide as fuel are used, with a thrust of about 2.25 kN.

Sixteen gas jets, with a thrust of from 80 to 410 N each, are used to provide stability and maneuverability. Dimensions of the flying mockup are height, about 3 m, and distance between landing-gear legs, about 4.0 m.

The flying characteristics of the LLRV are close to the characteristics of the Apollo lunar vehicle. The vehicle is equipped with an autopilot. Pilot rescue in an emergency is provided by an ejection seat and three or four emergency liquid-rocket engines. The vehicle is also equipped with a parachute that has a canopy 9 m in diameter, providing a descent speed of 30 m/s. Fuel supply for the jet engine provides for 10 to 15 minutes of operation. The maximum values of flight velocity are 27 m/s in the vertical direction and 21 m/s in the horizontal direction. The vehicle can ascend to 1.2 km in altitude and land within an area with a radius of 2.4 km.

One hundred ninety-seven flights at the Edwards Air Force Base and 50 flights at the Ellington base were made with this vehicle. The manufacturer, Bell Aerosystems, built two LLRV's in 1964. During 1965, this company slightly modified the flying mockup for the study of man's behavior under complex conditions of space flight during the terminal phase of controlled landing approach of the lunar vehicle. The company manufactured three modernized LLTV vehicles (cost of each vehicle was \$1.9 million). In December, 1968, the vehicle lost control during a landing approach from an altitude of about 150 m and crashed. The test pilot ejected and landed safely using a parachute.

#### Test-stand Mockups of Space Landing Vehicles

Test-stand mockups, in contrast to flying ones, are continuously connected to unloading mechanisms by support cables, as a result of which the maneuvering capability is limited by the test-stand dimensions. Depending on the complexity of the problem to be solved using test-stand mockups, the latter can be (with a known degree of arbitrariness) assigned to one of two types: Test-stand mockups intended for the development of landing procedures (the process of contact by the vehicle with the ground); and test-stand mockups intended for the development of the prelanding maneuver of the vehicle with subsequent landing.

Test-stand mockups for the development of the landing process for a space landing vehicle represent the most advanced, dynamically similar models. Thus, as models, they simulate the final stage of landing on a planet, namely, the free fall of the vehicle following the moment of engine shutdown. For such mockups, it is characteristic to have a precise correspondence with the actual vehicle, not only in the structure of the landing gear but also in terms of the basic mass-inertial parameters of the space landing vehicle. For this reason, all remaining elements of the vehicle structure (instrument section, power plants, various systems, equipment, and so forth) are modeled only in terms of their weights.

FOR OFFICIAL USE ONLY

All this materially simplifies mockup design while at the same time making it possible to carry out experimental studies of the following: Various layouts of the full-scale landing gear; the effect of the vehicle's mass-inertial characteristics on stability during landing; the effects of varying the structural parameters of the landing gears and the soft-landing conditions; the risks to which the payload of the space vehicle may be subjected (in terms of toppling, overloading, and structural damage) during emergencies. In a word, to develop fully the techniques of soft landing a vehicle, having removed the influence of scaling effects, which are significant in tests of dynamically similar models, from the test results. However, it is very difficult to use simplified test-stand mockups in the training of manned-vehicle crews.

Figure 9.2 is a schematic diagram of a typical test stand for the experimental development of the process of landing-vehicle touchdown with simplified full-scale mockups of the vehicle and for checking the effectiveness of the selected landing-gear design. For this purpose, the stand simulates, under terrestrial conditions, the forces of gravity that exist on various celestial bodies and that are significantly smaller than the force of gravity on the Earth's surface. The test stand also allows the vector of landing velocity of the space vehicle to be varied both in magnitude and direction and to simulate the relief and properties of the planet's surface layer by using interchangeable simulated grounds.

The test stand usually employs bridge-girder construction. Its basic components are a movable bridge platform carrying the unloading mechanism and the system for suspending the full-scale mockup, a special platform supporting the simulated planetary ground, and measuring and recording equipment.

The movable bridge platform located over the platform carrying the simulated ground provides the force for unloading the mockup during the entire landing process and imparts the required velocities (both horizontal and vertical components) to the mockup.

In order to achieve the required vertical landing speed during these tests, girder subassemblies can be used. By changing the length of the truss, it is possible to vary the height at which the mockup is suspended.

Unloading of the vehicle mockup is achieved by using a mechanism that can provide any force of unloading and thus simulate the effect on the mockup of reduced free-fall acceleration.

The special platform with the simulated planetary ground simulates the relief of the landing location (stones, craters, slopes), as well as the physical-mechanical properties of the planet's surface layer. This ground platform can be built as a concrete bowl or as a platform that can be adjusted to simulate local slopes of the planetary surface of up to  $\pm 20$  degrees and to simulate soil properties that change as a function of depth.

FOR OFFICIAL USE ONLY

FOR OFFICIAL USE ONLY

Control of all stages of the experiment (accelerating the platform with the mockup, dropping the mockup, breaking the platform after the drop, emergency stopping of the platform, and so forth) can be automated, while at the same time the operator can "interfere manually" from a central console.

The test stand has to be equipped with measuring and recording equipment necessary for recording the following parameters: Vertical and horizontal load factors during landing, angular velocities of the mockup, stresses in the structural elements of the landing gear, fuel pressures in the tanks, deformation of the landing gear's energy absorbers (as a function of time), penetration of the ground by the mockup's landing-gear legs, and so forth. Equipment and transducers used for measuring these parameters are, in many respects, analogous to those considered earlier (Chapter 8).

By way of illustrating, let us look at the use of simplified test-stand mockups during the terrestrial development of the space landing vehicles of the Viking-1 and -2 stations, which made soft landings on Mars in mid-1976. In Chapter 8, we presented a description of a full-scale, dynamically similar model of the Viking space landing vehicle (Table 8.1, model DPM-G3), which has a mass about 2.5-fold less than the mass of the actual space vehicle. At the Langley (United States) Research Center, this same model was transformed (by adding weight) into a full-scale test-stand mockup corresponding in its mass-inertial characteristics (480 kg of mass) to one of the variants of the Viking space landing vehicle (Ref. 50). The simplified full-scale mockup obtained in this fashion was tested during the development of the soft-landing process on a stand with 3/5 unloading (that is, by 60 percent) of its weight to imitate the Martian acceleration of the force of gravity (Figure 9.3).

The unloading of the mockup weight by 60 percent and imparting of the necessary landing velocity for a "flight" of the mockup down to contact with the landing platform were provided in the stand by using a system of cables, blocks, rollers, and weights. The cable system included dynamometers for the control of tension in the cables during the tests. The system of suspending the mockup provided five degrees of freedom (the sixth degree of freedom, the lateral translation of the mockup, was not provided by the suspension and was essentially limited). The full-scale mockup was held up by a support cable passing over an upper roller and connected to the mockup by an explosive bolt. The cable attach points made it possible to put the mockup in various attitudes before drop (for example, the mockup pitch angle was controlled within the limits of 0 to 10 degrees). Guide rails along which the rollers moved were about 60 m above the landing platform.

Before the test, the mockup was placed on the landing platform, and the force cables were stretched by winches and ropes to obtain the unloading, about 60 percent, of the mockup weight. Then the mockup was raised to the predetermined height, which provides the necessary vertical velocity for drop of the mockup (nominal value  $V_B = 7$  m/s), and the support cable was fastened. The unloading force is slightly less in this location. The drop

FOR OFFICIAL USE ONLY

FOR OFFICIAL USE ONLY

of the mockup followed the detonation of the explosive bolt of the support. Depending on the distance through which the mockup drops, the unloading force increases, reaching the necessary magnitude at the moment the landing-gear legs touch the surface. At the instant of contact, oscillations were set up in the unloading force due to inertia in the unloading cables. Such oscillations occurred during the entire landing process of the mockup. During this process, the accuracy of determining the unloading force was about  $\pm 3$  percent.

Horizontal acceleration of the mockup and trolley (9.5 kg mass) was done by using the energy of a falling weight with the aid of two stretched tow cables connecting the mockup through sheaves and trolley with the weight. When the mockup is lifted to the first position for drop, the weight is also lifted to the height necessary for obtaining the given horizontal velocity (nominal value  $V_p = 1.8$  m/s). The mockup-trolley-weight system is held in the initial position by a rope. When the rope is cut, trolley and mockup gather horizontal velocity under the action of the weight. At a predetermined moment, the weight closes the contacts of a microswitch, which explodes the connecting bolt. The now-free mockup, having attained a certain horizontal velocity, begins its fall to the platform with the simulated ground. The towing cable, connected to the trolley, is not disconnected but, being free of tension (because the weight has dropped to its support) and sufficiently light, does not affect the motion of trolley and mockup.

A rigid wooden platform of large mass is used as the landing surface and was covered by smooth plywood or by coarse gravel in order to obtain a coefficient of friction which varies between 0.4 to 0.7.

Signals carried through the cable at the time of the test from accelerometers, potentiometers, tensiometers, and so forth were recorded by a tape recorder using the frequency-modulation method.

Comparisons of tests conducted under identical conditions using free-falling, dynamically similar models and full-scale mockups with unloading have shown good agreement, with the majority of results (of measurements of acceleration of the center of mass, magnitude of landing-gear-leg compression, and forces in the energy absorbers) falling within a  $\pm 10$  percent confidence interval.

It should be noted that there is a substantial effect due to the wind on the magnitude of the horizontal landing velocity of the full-scale mockup. Thus, for winds reaching 4.5 m/s, deviations in the magnitude of horizontal velocity amount to  $\pm 0.4$  m/s.

Terrestrial development of the landing vehicles for the Venera-9 and -10 stations used a full-scale dynamic mockup without unloading, with centering and mass-inertial characteristics allowed to vary within set limits. The full-scale mockup is a simplified, rigid structure with static landing gear. The nominal mass of the landing vehicle is 660 kg. The landing gear of the

157

FOR OFFICIAL USE ONLY



FOR OFFICIAL USE ONLY

mockup consists of a thin-skinned toroidal envelope attached by a welded truss to the remainder of the body. At the moment of landing, the envelope deforms plastically, absorbing the energy of impact in this fashion. The atmospheric gas, which has penetrated during the time of descent into the inside of the envelope, is expelled through special openings, thus reducing the rebound of the landing vehicle. The body of the full-scale mockup is a weldment consisting of steel sheet bent into a cylinder with flanges. In order to obtain the necessary mass-inertial characteristics, movable balancing weights are rigidly connected to the body of the mockup. Attached to the wall of the body near the center of mass of the mockup is a beam that provides a flexible attachment of the test stand to the lifting system. Before each test (drop), the mockup is weighed, and its centering and mass moments of inertia with respect to the three orthogonal axes are determined.

To simulate the thermal effect of the Venusian atmosphere on the vehicle during test-stand tests, the full-scale mockup is heated to a certain temperature by a special oven mounted on the test stand, according to a function of interest to the designer. Mounted on the interior wall of the oven are heating elements of nichrome wire wound on ceramic tubing. The space between the double walls of the oven is filled with insulation. Testing is done by dropping the mockup from the required height under influence of terrestrial gravity (the mockup moves as a freely falling body). The difference in acceleration force due to gravity on Venus and on Earth is accounted for in calculating the kinetic energy of impact of the mockup on the landing surface, but the difference in aerodynamic drag is not accounted for due to its small magnitude as a result of low landing velocity (as is known, during the soft landings of the Venera-9 and -10 stations, the speed of contact with the surface of the planet was about 7 m/s).

To simulate the characteristics of the planet's surface layer, concrete, foamed concrete, and sintered sand are used. The platform with the simulated ground can be either horizontal or it can have various slope angles, projections, and depressions. The necessary spatial orientation of the full-scale mockup at the moment of ground impact is provided by an appropriate attachment of the mockup (which has six degrees of freedom) during the initial positioning with respect to the support stand.

The elevated portion of the test stand is made of steel and consists of support columns, transverse girders, and longitudinal beams. The full-scale mockup of the vehicle is subjected to several types of tests, among them: Tests related to landing stability at the moment of ground contact to determine limiting values of centering, moments of inertia, angles of attitude of the mockup, and soil slope; tests required for the determination of maximum impact load factors for limiting values of mockup mass and zero relative angle between the toroidal landing gear and the ground; tests connected with estimating the strength of the elements of the mockup landing gear for maximum mass and maximum relative angle between landing gear and ground.

FOR OFFICIAL USE ONLY

FOR OFFICIAL USE ONLY

Load factors during test of the full-scale mockup are measured by a DU-7 inductive sensor using the VI6-5MA equipment and recorded by an N-115 oscillograph; the temperature of the mockup elements is measured with TKKh thermocouples made of chromel-copel and recorded by EPP-09 and KSP-4 electronic potentiometers.

The mockup landing process and its results are recorded by still and cine-photography (Refs. 2, 10).

In conclusion, it is necessary to emphasize that loads acting on the space landing vehicles from the Venera-9 and -10 stations during the actual landing on Venus did not exceed the loads that occurred during tests of their full-scale dynamic mockups (Ref. 2).

Test-stand maneuvering mockups help solve the same problems as the flying mockups of the space landing vehicle, but within the bounds determined by the construction characteristics of the gantry test stands and the dimensions for maneuvering volume. In its construction, the test-stand maneuvering mockup is a full-scale copy of the vehicle being designed, and it is equipped with the actual systems necessary for performing the prelanding maneuver, among them the main and vernier engines. The mockup is suspended in a gimbal system with two degrees of freedom, on cables from a special trolley. The trolley is equipped with an unloading mechanism and is able to follow the translations of the mockup both along and across the gantry-truss structure of the stand (Figure 7.2). The safety of the test crew (during the development of manned space landing vehicles) is fully assured by using a safe and reliable cable support for the mockup in the stand.

The basic parts of a gantry stand are the same as those of a typical test stand. A translating bridge platform of the stand is automatically driven to follow the maneuvering mockup and provides, with a follower system, a constant vertical orientation of the suspension cables (with an accuracy to 1/3 degree) and unloading of the vehicle mockup. Simulation of angular motion of the space landing vehicle is accomplished by a gimbal system centered at the mockup's center of mass.

Such a test stand was constructed at the Langley Research Center in the United States (the LLRF facility) in 1965. The cost of the facility was \$3.52 million. The facility consists of a bridge crane about 76 m high, about 120 m long, and about 90 m wide at the base. The maneuvering mockup, equipped with a two-man cabin, has six degrees of freedom and, thanks to the gimbal suspension system, can simulate the angular and translational motions of the Apollo lunar ship. The astronauts can change the "flight" velocity by directing the thrust of 10 rocket motors, which use the products of dissociation of hydrogen peroxide. The "flights" of the full-scale mockup can last up to 180 s with velocities  $V_B \leq 8$  m/s and  $V_T \leq 4$  m/s (Ref. 56).

FOR OFFICIAL USE ONLY

FOR OFFICIAL USE ONLY

## Method of Performing Tests

The goals of the experimental development of both the vehicle's prelanding maneuver and the soft-landing process using full-scale mockups under terrestrial conditions are the following: (1) Final checking of the effectiveness and reliability of landing-gear function under near-actual conditions; assessment of the possibility of a successful landing in emergencies (landing on a rock, in a crevasse, with a broken landing-gear leg, and so forth); (2) determining the character and magnitude of load factors, stresses, and operation of energy absorbers under normal and emergency landing conditions; (3) better understanding of the effect that scale factor has on measurement characteristics and on the magnitude of parameters during soft landing (comparison with results of testing models); (4) evaluation of the effectiveness of using full-scale "clamping" engines from the point of view of emergency landings; (5) checking the kinematics of extending the landing-gear legs and operation of the mechanism for leveling the vehicle when such is necessary for a return lift-off from the planet; (6) development of the plan for the terminal phase of flight and landing of automatic, remotely controlled, and piloted space vehicles; (7) study of the stability and controllability of an interplanetary ship using flight and landing of flying mockups; (8) development of the detailed layout of a cabin in an interplanetary ship; (9) evaluation of the physiological capability in man for rapidly reaching correct solutions under difficult prelanding conditions (especially in the case of failure in the automatic system); (10) integrated development of the system of control for the vehicle during the landing phase (including simulation of emergency conditions, development of indicators of vehicle attitude in space, and so forth).

Corresponding to the capabilities of full-scale test stands and the peculiarities of the full-scale mockups used, the experimental development of the soft landing of space landing vehicles can be subdivided into the following phases: (1) Development of the process of vehicle contact with the ground; (2) development of the prelanding maneuver of the vehicle culminating in its landing, using test-stand maneuvering mockups; (3) development of the prelanding maneuver and soft landing of an interplanetary ship using flying mockups.

During the first phase, the process of landing itself is developed by using simplified test-stand mockups of the vehicle. During this phase, the first five of the 10 tasks indicated above can be carried out fully. A peculiarity of the first phase is the use of relatively simple full-scale mockups and test stands.

During the second phase, the development not only of the landing of the vehicle but also of its prelanding maneuver occurs. The use of a gantry test-stand and maneuvering mockup (automated or piloted) makes possible the solution of all enumerated tasks, that is, completing integrated terrestrial development of soft landing. Full-scale mockups, which are equipped with nearly all systems of the space ship as well as an elaborate test stand, are necessary for this phase.

160

FOR OFFICIAL USE ONLY

FOR OFFICIAL USE ONLY

The development of the prelanding maneuver and of the soft landing of an interplanetary ship using flying mockups (third phase) should be carried out only when it is not possible to test using the preceding phase. The availability of unlimited maneuvering space is especially favorable to the execution of the last five of the tasks mentioned. However, the building of flying mockups with special unloading engines (in essence, the creation of a new type of flying vehicle) is a task no less complex than the building of a gantry test-stand.

Let us mention the possibility of parallel execution of the phases of developing the soft-landing process by several test stands and mockups using full-scale vehicle mockups. During each phase of testing, the initial landing conditions and some structural parameters of the space landing vehicle are varied in accordance with the established program.

Only transducers that are analogous to those used for the dynamically similar models are installed on board the test-stand mockups of space landing vehicles, and all measuring and recording equipment is located remotely on the ground. In flying models, in contrast to test-stand models, it is necessary to install all equipment on board while maintaining mass similarity with the interplanetary ship.

FOR OFFICIAL USE ONLY

FOR OFFICIAL USE ONLY

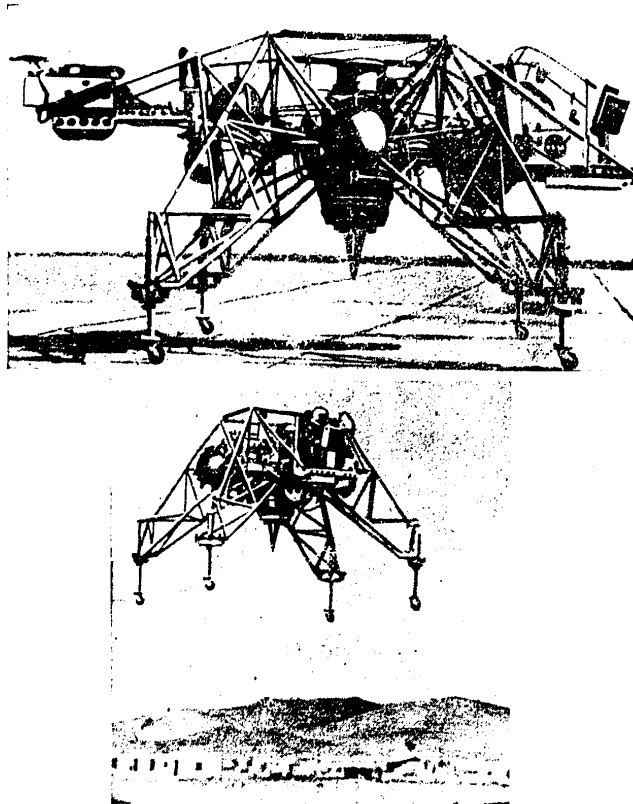


Figure 9.1. Flying Mockup of a Space Landing Vehicle (on the Ground and in Flight)

FOR OFFICIAL USE ONLY

FOR OFFICIAL USE ONLY

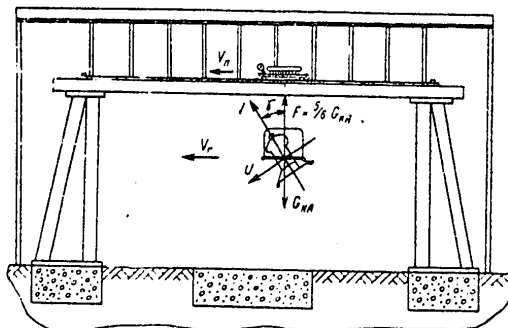


Figure 9.2. Schematic Diagram of a Full-scale Test Stand with an Unloading Mechanism

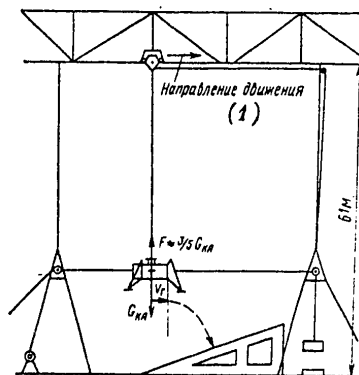


Figure 9.3. Test Stand Used in Development of Soft Landing for the Full-Scale Mockup of the Viking Spacecraft

Key:

1. Direction of motion

FOR OFFICIAL USE ONLY

FOR OFFICIAL USE ONLY

## CHAPTER 10

SEVERAL RESULTS OF THEORETICAL AND EXPERIMENTAL  
STUDIES OF SOFT LANDING

Following are the basic cases for studying dynamics of the soft landing of space landing vehicles: (1) Landing the vehicle with  $V_{\text{vert}_{\text{max}}}$  and

$V_{\text{hor}} = 0$  onto a horizontal surface ( $\theta = 0^\circ$ ) with a limited translation of the landing-gear pads along the surface plane (occurrence of maximum vertical load factors); (2) landing the vehicle with  $V_{\text{hor}_{\text{max}}}$  and small vertical

velocity onto a horizontal surface ( $\theta = 0^\circ$ ) with a limited translation of the landing-gear pads in the plane of the surface (occurrence of maximum horizontal load factors); (3) vehicle motion downward along the slope ( $\lambda = 0$ ;  $\theta_{\text{max}}$ ) with either one or two landing-gear legs leading, and with coefficients of friction  $f_{\text{max}}$  and maximum values of landing velocity components (occurrence of a critical situation due to potential toppling); (4) vehicle motion upward along the slope ( $\lambda = 180^\circ$ ;  $\theta_{\text{max}}$ ) with either one or two landing-gear legs leading, and with a coefficient of friction  $f_{\text{max}}$  and velocities  $V_{\text{vert}_{\text{max}}}$  and  $V_{\text{hor}_{\text{max}}}$  (occurrence of a critical situation due to

the maximum rate of shock absorption in the leading landing-gear leg(s) of the vehicle); (5) movement of the vehicle across the slope ( $\lambda = 90^\circ$ ;  $\theta_{\text{max}}$ ) with a coefficient of friction  $f_{\text{max}}$  and velocities  $V_{\text{vert}_{\text{max}}}$ ,  $V_{\text{hor}_{\text{max}}}$  (for

evaluating the characteristics of energy absorption and stability for such landings);  $\lambda = \arctan(V'_x/V'_y)$  is the angle that determines the direction of the horizontal component of the velocity vector of the vehicle's center of mass;  $V_{\text{vert}} = V'_y$  is the vertical component of the velocity vector of the vehicle's center of mass; and  $V_{\text{hor}} = (V_x'^2 + V_z'^2)^{1/2}$  is the horizontal component of the velocity vector of the vehicle's center of mass.

The basic theoretical and experimental study results that are characteristic of the soft-landing process for the three space landing vehicle variants, A, B, and C, described in Chapter 8 (Table 8.1), are presented in this chapter. Because these vehicle variants (in contrast to variant D) were considered as prototypes of corresponding vehicles for landing on the Moon, all results, both theoretical (computed on a digital computer) and experimental (from the tests of models DPM-A, -B, and -C), are given in terms of a full-scale lunar space landing vehicle.

By using the conditions of similarity and appropriate scales (Table 7.1), it is possible to take data from actual lunar landings and calculate corresponding model parameter values. These can, in turn, be converted to full-scale values for other planets (for example, for landing a vehicle on Mars), or even for another full-scale vehicle with different characteristics.

FOR OFFICIAL USE ONLY

FOR OFFICIAL USE ONLY

The stability zones for soft landing of the variant B space landing vehicle on slopes with  $\theta$  from  $-5$  to  $-15^\circ$  and  $\lambda = 0^\circ$  are shown in Figures 10.1 to 10.3, and are plotted in the coordinates  $V_{\text{vert}}$  and  $V_{\text{hor}}$  for the indicated parameter values and basic landing conditions. In these graphs, the area to the left of the stability curve represents stable landings, and the area to the right of the curve represents conditions under which the vehicle will topple during landing. For each value of ground slope angle, the results of the theoretical study of stability zones using a digital computer agree with the results of experiments conducted with the dynamically similar DPM-B model (Table 8.1).

The theoretical calculations involved varying the magnitude of the compression force  $\xi$  acting on the energy absorbers. As indicated in the graphs (Figures 10.1 to 10.3), the experimental results fall between the curves representing a compression force of 10 kN and 20 kN on the energy absorbers, which, recalculated for the model with  $K_0 = 1/6$ , equals a force of 280 and 560 N (a comparison of the test results for honeycomb energy absorbers is in Chapter 8).

The same figures also show the results of experimental studies of soft landing compared with theoretical calculations carried out for the condition of constant compression force on energy absorbers,  $\xi = 15$  kN, and a varying coefficient of friction between landing-gear legs and ground ( $f = 0.7-1.3$ ). Inasmuch as the model's landing-gear legs were equipped with special spikes, the legs gradually penetrated the ground during landing (that is, the effect gradually increased). Therefore, the force of friction between landing-gear leg and ground was variable and was larger for higher landing speeds. This conclusion is supported by experimental results.

Figure 10.4 shows the results of theoretical and experimental studies of the landing stability zones for a lunar vehicle. The results are presented in terms of coordinates  $V_{\text{hor}}$  and  $\theta$ , with the magnitude of  $V_{\text{vert}}$  as a parameter (for  $\xi = 15$  kN,  $f = 1.0$ , configuration 2-2, and  $\lambda = 0^\circ$ ). In such a graph, the zone of stable landings of a vehicle is represented by the area located to the left of the corresponding curve and includes the origin of coordinates. Areas beyond the curve (to the right of it) define the combinations of parameters for a lunar landing approach that lead to toppling of the vehicle during landing.

The graphs with axes  $V_{\text{hor}}$  and  $\theta$  more clearly present the relationship between the magnitude of the landing stability zone for a space landing vehicle and the slope angle of the ground, thus enhancing the graphs using axes  $V_{\text{hor}}$  and  $V_{\text{vert}}$ . These graphs can also be used to compare results of calculations with results of experiments more conveniently, because the actual angles of ground slope can be different during testing from the values used in the computer program.

Figure 10.4 also demonstrates the satisfactory agreement between results of theoretical studies and experiment. Deviations are approximately 10 percent,

FOR OFFICIAL USE ONLY



FOR OFFICIAL USE ONLY

which are due to the known limitations of the range of tests, the errors in measuring parameters, and assumptions made for the theoretical studies. Let us note that the theoretical calculation yields a stability margin for the landing of a space landing vehicle that becomes larger for small values of the components of landing velocity (for those up to 2 to 3 m/s).

Figures 7.1 and 10.5 show film frames from the soft landing of the dynamically similar DPM-B model on an inclined surface ( $\theta = -15^\circ$ ;  $\lambda = 0^\circ$ ) with a rigid simulated lunar ground (Table 7.3, third variant;  $\sigma_{gr} \geq (2-5) \times 10^5$  Pa). Stable landing (Figure 10.5) is achieved with velocities  $V_{vert} = 2.7$  m/s and  $V_{hor} = 3.7$  m/s. The landing process of the model lasted about 0.8 s with achieved maximum load factors of  $n_{vert} \approx 5$ ,  $n_{hor} \approx 6$ . The film record of the DPM-B model toppling when landing in a crater 0.15 m deep with velocities  $V_{vert} = 2.5$  m/s and  $V_{hor} = 2.0$  m/s is shown in Figure 7.1.

Figures 10.6 and 10.7 show the results of theoretical and experimental studies of the landing stability for the variant A space landing vehicle using the 2-2 configuration.

Theoretical studies of landing stability were carried out in accordance with Chapter 6. The results of experimental studies shown in Figure 10.6 have been adopted from American work (Ref. 47) for the DPM-A model (Table 8.1) for landing on slopes with  $\theta = -5$  to  $-15^\circ$ ,  $V_{vert} = 1$  to 4 m/s, and  $V_{hor} = 1$  to 3 m/s.

Figure 10.7 shows the experimental points corresponding to tests of a model space landing vehicle with "clamping" engines (in recalculating for a full-scale lunar vehicle the total engine thrust is  $T_E = 20$  kN to 36 kN) with slopes of  $-25^\circ$ ,  $-30^\circ$ , and  $-37^\circ$  for  $V_{vert} = 3$  to 4 m/s and  $V_{hor} = 1.3$  to 1.75 m/s. As we can see, results of tests with dynamically similar models agree well with the calculation of zones of landing stability made on a digital computer.

Disagreement between theoretical zones of stability and experimental results for the variant A space landing vehicle (Ref. 47) is less than 20 percent and is basically "conservative" (Figure 10.6).

Figure 10.8 presents a comparison of results of theoretical and experimental determinations of the stability zones for the landing of a heavy vehicle (variant C). Theoretical calculations were made in accordance with Chapter 6 for three-dimensional motion of the space landing vehicle. Results of experimental studies were taken from American work (Ref. 55) devoted to the analysis of the landing dynamics of the Apollo lunar vehicle with a mass of about 16,000 kg (Table 8.1). Presentation of the experimental points in the graphs with axes  $V_{hor}$  and  $\theta$  makes it possible to estimate the magnitude of the difference in results as approximately 10 percent.

Let us note that the plots representing the zones of landing stability for a space landing vehicle using coordinates  $V_{hor}$  and  $\theta$  (Figures 10.4 and 10.8)

FOR OFFICIAL USE ONLY

FOR OFFICIAL USE ONLY

that reducing the strength of an individual landing-gear leg, in spite of increasing their total number, is not permissible because the total load is redistributed to the remaining legs in the case of failure of one of the landing-gear legs. At the same time, the critical condition for absorbing energy (a landing upward along a slope with a single leg leading) remains the same, no matter what the number of legs is in a landing gear. For this reason, the choice of the optimal number of legs with the landing-gear mass as a criterion and for constant landing stability is made for the case of identical legs.

For comparing different landing gears, one can arbitrarily take the parameter  $NQ/S$ , which represents the relationship of landing-gear mass to the area of the landing stability zone. The following convention is used:  $N$  is the number of legs in the landing gear of a space landing vehicle;  $Q$  is the mass of a single landing-gear leg, in kg; and  $S$  is the area of the stability zone bounded by the ordinate axis, by the landing stability curve, and by two straight lines parallel to the abscissa axis and corresponding to arbitrarily chosen ordinates, in  $\text{mm}^2$ .

The relationships obtained for the parameter  $NQ/S$  as a function of the number of landing-gear legs for landing a vehicle on horizontal and inclined surfaces are shown in Figure 10.11. From the curves it can be seen that a landing gear with four legs is optimum in terms of mass (for equal stability) among the landing gears being considered.

Results of studying the effect on the dynamics of landing of a vehicle produced by varying the relative magnitude of the landing-circle radius of a landing gear, namely  $\bar{R} = R/H$ , show directions for effectively enlarging the landing stability zone with the goal of assuring successful vehicle landing within the required range of velocities and permissible slope angles for the planetary surface. As can be seen from Figure 10.12, an increase in the nondimensional quantity  $\bar{R}$  (by increasing radius  $R$  for a landing gear or by decreasing height  $H$  of the center of mass of the vehicle) leads to a substantial enlargement in the range of permissible landing velocities.

Another means for increasing the landing stability of a space landing vehicle (especially for landings on steep slopes, up to 30 to 35 degrees), although leading to some overdesign in the vehicle, complication of its control system, and an increase in the landing-gear mass, can be provided by using a "clamping" engine. Let us note in passing that right up to the present, no need has arisen to use such engines for landing vehicles for the Moon and planets. However, considering that space-flight technology as a whole and space vehicles for soft landing on the surfaces of celestial bodies in particular are in an early stage of their development and that the number of soft landings amounts to only one to three landings per year (in 1972, there were four soft landings; Table 10.1), there can be no doubt that the landing-vehicle design will improve and become more complex in the future. The most diverse methods for assuring successful soft landings will be developed and applied (for example, the landings on asteroids, where

FOR OFFICIAL USE ONLY

FOR OFFICIAL USE ONLY

Table 10.1. Summary of Soft Landings Accomplished by Spacecraft on the Moon and Planets

Наименование аппарата (1)	Дата мягкой посадки (2)	Масса КПА, кг (3)	Посадочная (4)		Уклон поверхности, град. (5)	Район посадки (7)	Характеристика ПУ (8)
			скорость, м/с	вертикальная (горизонтальная)			
«Луна-9» (9)	3.02.66	~100	>8 (-)		-	Океан Бурь, 7,1° с. ш.; 64,4° з. д. (36)	Баллоны со сжатым газом (сферическое) (62)
«Луна-13» (10)	24.12.66	~100	>8 (-)		-	Океан Бурь, 18,9° с. ш.; 62,0° з. д. (37)	
«Луна-16» (11)	20.9.70	1880	2,5 (0)		-	Море Изобилия, 0,7° ю. ш.; 56,3° в. д. (38)	4-х опорное стержневое, в виде треноги (63)
«Луна-17» (12)	17.11.70	~1900	2,5 (-)		-	Море Дождей, 38,3° с. ш.; 35° з. д. (39)	
«Луна-20» (13)	21.02.72	1880	2,5 (-)		-	Кратер Аполлоний С, 3,5° с. ш.; 56,5° в. д. (40)	
«Луна-21» (14)	16.01.73	~1900	~2,0 (-)		~0°	Море Ясности, 25,8° с. ш.; 30,5° в. д. (41)	3-х опорное с гидравлическими амортизаторами; в виде треноги (64)
«Луна-24» (15)	18.08.76	1880	~2,0 (-)		-	Море Кризисов, 12°45' с. ш.; 62°12' в. д. (42)	
«Сервейер 1» (16)	2.06.66	~290	~3,0 (0,5)		~0°	Океан Бурь, 2,5° ю. ш.; 43,2° з. д. (43)	
«Сервейер-3» (17)	20.04.67	~290	1+2 (0,6)		10°+15°	Океан Бурь, 3,0° ю. ш.; 23,3° з. д. (44)	
«Сервейер-5» (18)	11.09.67	~290	~3,0 (0,5)		~15°	Море Спокойствия, 1,4° с. ш.; 23,2° в. д. (45)	

FOR OFFICIAL USE ONLY

FOR OFFICIAL USE ONLY

quite graphically illustrate the dangers in landing a vehicle downward along a slope ( $\theta < 0$ ) because of possible toppling.

Let us now consider in more detail the effects of initial conditions on the soft-landing dynamics of a space landing vehicle. The term, initial landing conditions, defines the set of environmental factors not connected with the structure of the space vehicle. Among them we include: (1) The characteristics of the planet's surface layer, namely, the slope angle of the surface at the point of landing,  $\theta$ ; the coefficient of friction,  $f$ ; protrusions, depressions, or cracks; physical-mechanical properties of the ground, and so forth; and (2) kinematic parameters of vehicle motion at the moment of contact with the planet's surface, namely, linear and angular velocities, accelerations, vehicle attitudes, and so forth.

The vertical and horizontal components,  $V_{\text{vert}}$  and  $V_{\text{hor}}$ , respectively, of landing velocity of the vehicle are dominant factors defining the dynamics of the landing process.

The zones of landing stability for vehicles (variants A, B, and C) are shown in Figures 10.1 through 10.3, 10.6, and 10.8 for different slope angles on the lunar surface, for landing configuration 2-2, and for  $\lambda = 0^\circ$  and  $180^\circ$ .

For landings of the vehicle on a horizontal surface or a surface with an inclination up to  $-5^\circ$ , the allowable magnitude of horizontal velocity of the vehicle grows with an increase in its vertical landing velocity (within a range of velocities of practical interest).

It is obvious that the case of motion upward along the slope ( $\lambda = 180^\circ$ , landing configuration 2-2) is not critical in terms of vehicle stability during landing, because the region of stability grows with an increase in angle  $\theta$  (Figure 10.6).

Results of studies of the dynamics of landing for a vehicle with a 1-2-1 configuration (movement of a vehicle with a single landing-gear leg leading) are shown in Figures 10.6 and 10.9. The dashed lines in Figure 10.9 (movement of a vehicle downward along a slope with  $\theta = -15^\circ$ ) correspond to lines of equal stability of the vehicle during landing, that is, to lines whose every point determines a combination of vertical and horizontal velocity, which, during the vehicle-landing process, lead to one and the same limiting angle  $\theta$  (Chapter 6).

A comparison for the zones of vehicle stability for landing on slopes with  $\theta = -15^\circ$  and using configurations 1-2-1 and 2-2 ( $\lambda = 0^\circ$ ) (Figure 10.6) shows that the permissible values of horizontal landing velocity for a space landing vehicle with a 1-2-1 configuration are greater by 1 m/s than the corresponding permissible values of  $V_{\text{hor}}$  for the 2-2 configuration.

The magnitude of the coefficient of friction between the vehicle's landing-gear-leg pads and the lunar surface during vehicle landing onto an inclined

FOR OFFICIAL USE ONLY

FOR OFFICIAL USE ONLY

surface ( $\theta$  between  $-5$  and  $-15^\circ$ ;  $\lambda = 0^\circ$ ) affects the zone of stability, as shown in Figures 10.1 to 10.3. As can be easily seen from these diagrams, the zone of landing stability for the vehicle tends to increase for decreasing values of the coefficient of friction. This is explained by the fact that for smaller magnitudes of the coefficient of friction (and a constant normal force) there is a decrease in the component of total force (force of friction) acting on the pad of the landing-gear leg in the direction along the surface, which leads to a decrease of the overturning moment for the vehicle and to a sliding of the landing gear along the surface (with dissipation of a significant portion of the energy).

Along with the above-described effects of the initial conditions of landing, the dynamics of soft landing a vehicle are, to a large extent, determined by the structural characteristics of the vehicle and by the layout and characteristics of its landing gear, that is, by the following parameters: The number of landing-gear legs; the relative size of the radius of the circumscribing circle that passes through the landing-gear-leg pads before touchdown;  $\bar{R} = R/H$ ; the thrust of the stabilizing engines (the "clamping" engines); and the force of resistance during the compression of the landing-gear legs (the energy of deformation of the landing-gear energy absorbers).

The stability zones for the vehicle (variant A) (with the number of landing-gear legs  $N$  varied from three to six) are shown in Figure 10.10 for both a landing on a horizontal and one on an inclined surface. The diagrams were determined while keeping constant all parameters other than the number of landing-gear legs. It is obvious that the vehicle with three landing-gear legs has the lowest stability during landing on a horizontal surface. The stability zones for a vehicle whose landing gear has from four to six legs are much larger but differ little from one another.

In optimizing the number of landing-gear legs of a space landing vehicle, it is necessary to make an integrated evaluation of the stability of the vehicle during landing and landing gear mass and its reliability. It is obvious that the overall reliability of successful landing significantly increases with increases in the number of landing-gear legs up to  $N = 4$ , but for  $N > 4$  the increase in total reliability is not significant in view of the fact that failure of a single support does not necessarily lead to an emergency. Also, by increasing the number of landing-gear legs, there is an increase in the probability of landing-gear failure due to the larger number of components. As a result, any advantage in reliability that might have been gained from slightly increasing the zone of stability may be lost due to the extra landing-gear leg.

Because of this, the mass of the landing gear is the basic criterion that controls the choice of the optimum number of a vehicle's landing-gear legs. The mass of the landing gear can be held constant while increasing the number of legs only by lightening each leg (through a decrease in the cross section of its load-bearing elements), which, as a rule, leads to reduced strength in each individual landing-gear leg. However, it is commonly held

FOR OFFICIAL USE ONLY

FOR OFFICIAL USE ONLY

«Сервейер-6» (19)	10.11.67	~300	~3,0 (0,5)	~0°	Залив Центральный, 0,5° с. ш.; 1,4° з. д. (46)
«Сервейер-7» (20)	10.01.68	~300	3-4 (0,5)	—	У кратера Тихо, 40,9° ю. ш.; 11,5° з. д. (47)
«Аполлон-11» (21)	20.07.69	15100	~0 (0)	~4,0°	0°41'15" с. ш.; 23°26' в. д. (48)
«Аполлон-12» (22)	19.11.69	15100	0,6 (0)	3,08°	3,036° ю. ш.; 23,416° з. д. (49)
«Аполлон-14» (23)	5.02.71	15300	0,9 (0)	~8°	3°40'27" ю. ш.; 17°27'58" з. д. (50)
«Аполлон-15» (24)	30.07.71	~16000	1-3 (0) (расч.) (70)	~9°	26,10° с. ш.; 3,60° в. д. (51)
«Аполлон-16» (25)	21.04.72	~16000	1-3 (0) (расч.) (70)	<15° (расч.) (70)	9'0" ю. ш.; 15°35' з. д. (52)
«Аполлон-17» (26)	11.12.72	~16000	- (0) (70)	<15° (расч.) (70)	20,2° с. ш.; 30,7° в. д. (53)
«Марс-3» (27)	2.12.71	~450	8-15 (<25) (расч.) (расч.)	—	Электрик, 45° ю. ш.; 158° з. д. (54)
«Марс-6» (28)	12.03.74	~450	<12 (-)	—	Море Эригнейское, 24° ю. ш.; 19,5° з. д. (55)
«Викинг-1» (29)	20.07.76	~550	2,4 (<1,2) (расч.) (расч.)	<19° (расч.) (70)	Хризис, 19,5° с. ш.; 34° з. д. (56)
«Викинг-2» (30)	4.09.76	~550	2,4 (<1,2) (расч.) (расч.) (70) (70)	<19° (расч.) (70)	Утопия, 44,3° с. ш.; 10° з. д. (57)

FOR OFFICIAL USE ONLY

FOR OFFICIAL USE ONLY

Наименование аппарата (1)	Дата мягкой посадки (2)	Масса КПА, кг (3)	Посадочная скорость, м/с (4)		Уклон поверхности, град. (6)	Район посадки (7)	Характеристика ПУ (8)
			вертикальная (5)	(горизонтальная)			
«Венера-7» (31)	15.12.70	~495	~7	(—)	—	~2° ю. ш. (ночная сторона), ~2000 км от утреннего терминатора (58)	Амортизирующие элементы конструкции (68)
«Венера-8» (32)	22.07.72	~495	6,5	(—)	—	~10° ю. ш. (дневная сторона), ~600 км от утреннего терминатора (59)	
«Венера-9» (33)	22.10.75	660	~7	(—)	10°—15° (расч.) (70)	31°42' с. ш.; 290°50' долг. (60)	Торондальная оболочка (69)
«Венера-10» (34)	25.10.75	660	~7	(—)	10°—15° (расч.) (70)	16°02' с. ш.; 291° долг. (61)	

— данные не установлены. (35)

FOR OFFICIAL USE ONLY

FOR OFFICIAL USE ONLY

Key:

1. Vehicle name
2. Date of soft landing (day, month, year)
3. Space landing vehicle mass (kg)
4. Landing velocity
5. Vertical (horizontal)
6. Surface slope (deg.)
7. Landing location
8. Landing-gear characteristics
9. Luna-9
10. Luna-13
11. Luna-16
12. Luna-17
13. Luna-20
14. Luna-21
15. Luna-24
16. Surveyor-1
17. Surveyor-3
18. Surveyor-5
19. Surveyor-6
20. Surveyor-7
21. Apollo-11
22. Apollo-12
23. Apollo-14
24. Apollo-15
25. Apollo-16
26. Apollo-17
27. Mars-3
28. Mars-6
29. Viking-1
30. Viking-2
31. Venera-7
32. Venera-8
33. Venera-9
34. Venera-10
35. Data not determined
36. Ocean of Storms, lat. 7.1° N; long. 64.4° W
37. Ocean of Storms, lat. 18.9° N; long. 62.0° W
38. Sea of Plenty, lat. 0.7° S; long. 56.3° E
39. Sea of Rains, lat. 38.3° N; long. 35° W
40. Crater Apollonius C, lat. 3.5° N; long. 56.5° E
41. Sea of Serenity, lat. 25.8° N; long. 30.5° E
42. Sea of Crises, lat. 12° 45' N; long. 62° 12' E
43. Ocean of Storms, lat. 2.5° S; long. 43.2° W
44. Ocean of Storms, lat. 3.0° S; long. 23.3° W
45. Sea of Tranquility, lat. 1.4° N; long. 23.2° E
46. Central Gulf, lat. 0.5° N; long. 1.4° W
47. Crater Tycho, lat. 40.9° S; long. 11.5° W

FOR OFFICIAL USE ONLY



## FOR OFFICIAL USE ONLY

48. Lat. 0° 41' 15" N; long. 23° 26' E
49. Lat. 3.036° S; long. 23.416° W
50. Lat. 3° 40' 27" S; long. 17° 27' 58" W
51. Lat. 26.10° S; long. 3.60° E
52. Lat. 9° 0' S; long. 15° 35' W
53. Lat. 20.2° N; long. 30.7° E
54. Electris, lat. 45° S; long. 158° W
55. Erythraeum Mare, lat. 24° S; long. 19.5° W
56. Chryse, lat. 19.5° N; long. 34° W
57. Utopia, lat. 44.3° N; long. 10° W
58. Lat. ~ 2° S (night side) and ~ 2,000 km from the morning terminator
59. Lat. ~ 10° S (day side) and ~ 600 km from the morning terminator
60. Lat. 31° 42' N; long. 290° 50'
61. Lat. 16° 02' N; long. 291°
62. Balloons with compressed gas (spherical)
63. Four-legged, strut construction, tripod shape
64. Three-legged with hydraulic shock absorber, tripod shape
65. Four-legged (deployable) cantilevered strut construction with honeycomb shock absorber
66. Soft-landing engine and shock-absorbing structural elements
67. Three-legged (tripod shape)
68. Shock-absorbing structural elements
69. Toroidal envelope
70. (Calculated value)

there is no sensible force of gravity would be very difficult without "clamping" engines).

We now present some estimates of the effectiveness of stabilizing engines for the most critical landing conditions (downward along a steep slope,  $\lambda = 0$ ;  $\theta_{\max} = -30^\circ$ ). "Clamping" engines are installed on each of the vehicle's landing-gear legs (Figure 6.6). The duration of engine operation is limited. It is obvious (Figure 10.7) that using stabilizing engines with a total thrust of

$$T_{\Sigma} = \sum_{i=1}^4 T_i = 10,000 \text{ N}$$

enlarges the stability zone of the space landing vehicle twofold, and using engines with  $T_{\Sigma} = 20,000 \text{ N}$  increases it threefold.

Calculations show that no stability zone exists for landings on surfaces with a slope of  $-30^\circ$  (Figure 10.7) unless stabilizing engines are used (in which case, the static stability of the vehicle is preserved). Using stabilizing engines, a stable landing on a surface with a slope of  $-30^\circ$  and within the required range of velocities can be achieved.

FOR OFFICIAL USE ONLY

The change as a function of time of some parameters that characterize the dynamics of soft landing of a vehicle with a four-legged landing gear on a slope ( $\theta = -20^\circ$ , landing configuration 2-2,  $\lambda = 0^\circ$ ) is shown in Figure 10.13 (for landing velocities  $V_{\text{vert}} = \dot{Y}' = 3 \text{ m/s}$  and  $V_{\text{hor}} = \dot{X}' = 1 \text{ m/s}$ ) and in Figure 10.14 (landing velocities  $V_{\text{vert}} = \dot{Y}' = 1 \text{ m/s}$  and  $V_{\text{hor}} = \dot{X}' = 1 \text{ m/s}$ ). In these figures, solid lines represent parameters during the landing process when no stabilizing engines are used, while dot-dash lines show parameters when engines with a total thrust of 10,000 N are used. The characteristic moments during the soft landing are shown in the lower portion of the figures.

The variation of parameters for unstable landing when no stabilizing engines are used (loss of stability at the instant  $t = 1.65 \text{ s}$ , with  $\alpha_2 < 0$ ) is shown in Figure 10.13. A "clamping" engine assures stability of landing (at  $t = 1.35 \text{ s}$ ;  $\alpha_2 = 0.26 \text{ rad}$ ;  $E = 58 \text{ J}$ ).

The change in parameters for the case of a stable landing even in the absence of stabilizing engines is shown in Figure 10.14. The use of stabilizing engines leads to a faster completion of the soft-landing process.

Let us consider the main events of this process in more detail.

1. Landing-gear leg no. 1 (the doubled leg) touches the landing surface and is deformed ( $t = 0$  to  $0.1 \text{ s}$ ). As a consequence of deformation of landing-gear leg no. 1 and the presence of friction with the surface, the kinetic energy of the vehicle decreases (from 5,800 to 4,500 J). Deformation of landing-gear leg no. 1 equals  $\delta_{1m} = 0.007 \text{ m}$ .
2. The space landing vehicle rotates about the pad of landing-gear leg no. 1 ( $t = 0.1$  to  $0.7 \text{ s}$ ). The center of mass of the vehicle continues to drop until the instant when deformation of landing-gear leg no. 1 ceases. Because of this, the kinetic energy of the vehicle increases (from 4,500 to 9,210 J).
3. Landing-gear leg no. 2 (also doubled) touches the landing surface and is deformed ( $t = 0.7$  to  $0.8 \text{ s}$ ). As a result of the deformation of landing-gear leg no. 2 and because of the presence of friction with the surface, the kinetic energy of the vehicle again decreases (from 9,210 to 1,400 J). Deformation of landing-gear leg no. 2 equals  $\delta_{2m} = 0.17$ . When the pad of landing-gear leg no. 2 touches the surface, the pad of landing-gear leg no. 1 lifts off from the landing surface.

In accordance with the assumed schedule for starting the stabilizing engine, the engine is started at the instant the surface is touched by the pad of landing-gear leg no. 2. The change in the process parameters that results from starting the stabilizing engine until the instant the stability criteria (Equation 6.33) are satisfied is shown (by the dot-dash line) in Figure 10.14.

4. The vehicle rotates about the pad of landing-gear leg no. 2 ( $t = 0.8$  to  $1.0 \text{ s}$ , when stabilizing engines are used; and  $t = 0.8$  to  $1.85 \text{ s}$ , when

FOR OFFICIAL USE ONLY

FOR OFFICIAL USE ONLY

stabilizing engines are not used). During such rotation, the vehicle center of mass rises and, consequently, its kinetic energy once again decreases (from 1,400 to 50 J).

In accordance with the stability criteria (Equation 6.33), when  $\alpha_1 < 0$ ,  $\alpha_2 > 0$ , and  $E < \eta = 50$  J, the process of landing the vehicle is considered completed at the time  $t = 1.85$  s (when no stabilizing engines are used) or at  $t = 1.0$  s (when such an engine is used).

The changes in stability zones for landings of variant B space landing vehicle on inclined surfaces are shown in Figures 10.1 to 10.3 as a function of the force of resistance to the compression of the landing-gear legs ( $\xi = 10$  to 30 kN). The figures show that for landings on inclined surfaces ( $\theta = -5$  to  $-15^\circ$ ,  $\lambda = 0$ ), the vehicle's stability zone narrows significantly for increases in the force of compression on the landing-gear legs (especially for large values of landing velocity). The reason for this is the increase in the toppling moment for the vehicle, which accompanies increases in stiffness of the energy absorbers in the landing-gear legs.

In presenting this material, we have covered quite a broad range of landing velocities ( $V_{\text{vert}} = 0$  to 8 m/s and  $V_{\text{hor}} = 0$  to 5 m/s) that is significantly greater than the one that can be practically provided by the control systems for normal landings of vehicles on planetary surfaces. Also, as previously discussed (Chapter 6), the deformation of landing-gear legs was assumed to be unlimited (in order to simplify calculations).

Let us note that choosing a magnitude for the force of compression acting on the landing-gear-leg energy absorbers is appropriate not only for determining the stability zones for vehicles during landing, but also in considering the permissible load factors for the payload and for defining realistic magnitudes of deformation in the landing-gear legs.

The relative simplicity of the theoretical method presented in Chapter 6 for studying the dynamics of soft landing (and, consequently, the small expenditure of machine time when making calculations), and the ability to account for the effect of structural parameters of the vehicle and of initial landing conditions on the dynamics of landing as well as a good agreement of results with experimental data make the method fully acceptable for engineering calculations in design offices for the purpose of refining the detailed designs of space landing vehicles.

Let us now turn to the specifics of deformation of the landing-gear legs for a space vehicle with different landing conditions. In reviewing the computational and experimental data on the deformation of landing-gear legs, we note the following:

1. Deformation of all landing-gear legs of a vehicle increases with an increase in vertical landing velocity.

FOR OFFICIAL USE ONLY

FOR OFFICIAL USE ONLY

2. For vehicle landings downward along a slope ( $\lambda = 0^\circ$ , configuration 1-2-1), the largest deformation occurs for the leading landing-gear leg (no. 3) and the smallest for the trailing leg (no. 1). The deformation of leg no. 3 is two- to 2.5-fold greater than the deformation of leg no. 1. Leg nos. 2 and 4 have approximately the same deformation, which is 1.5- to twofold smaller than the deformation in leg no. 3. The deformation of leg nos. 1 and 3 increases for increasing angles of the surface slope.
3. In landing a vehicle up a slope ( $\lambda = 180^\circ$ , configuration 1-2-1), the largest deformation is experienced by the landing-gear leg (no. 1) uppermost on the slope, and the least is experienced by the lowest leg (no. 3). Deformation of landing-gear leg no. 1 is two- to 2.5-fold greater than the deformation of leg no. 3 and 1.2- to 1.5-fold greater than the deformation of leg nos. 2 and 4. For increasing surface slope angles, the deformation of leg no. 1 increases and that of leg no. 3 decreases. This case of motion represents the greatest danger during a vehicle landing, from the viewpoint of the possible failure of the leading leg no. 1 caused by the large deformation of its energy absorber (Figure 10.15).
4. For landing a vehicle across the slope ( $\lambda = 90^\circ$ ), the contact configuration of the supports is 1-1-1-1. For this, the greatest deformation occurs in the leading landing-gear leg, no. 4, and the smallest deformation in the trailing leg, no. 2. This is explained by the direction of the horizontal velocity vector in the direction of leg no. 4. The deformation of leg no. 4 is 2.5- to threefold greater than the deformation of leg no. 2 and 1.2- to 1.5-fold greater than the deformation of leg no. 1. For increased surface slope angles, the deformation of the leading leg (no. 4) and the leg uppermost on the slope (no. 1) increases, while the deformation of leg nos. 2 and 3 decreases.
5. For landings of the vehicle in configuration 2-2 downward along the slope and for different values of the component of landing velocity, the deformations of the leading landing-gear legs (nos. 3 and 4) are 2.5- to threefold larger than the deformations of the trailing landing-gear legs (nos. 1 and 2).
6. The character of the landing-gear-leg deformations of various vehicles is identical. However, the absolute magnitude of deformation of the legs decreases with increasing stiffness in their energy absorbers.

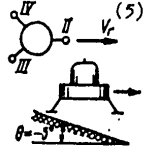
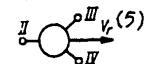
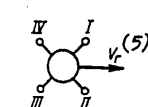
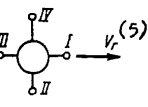
A summary of experimental values of acceleration and deformation of landing-gear legs, recorded during tests of the dynamically similar DPM-B model for  $N = 3$  and 4 during landings on a slope of  $\theta = -5^\circ$  ( $\lambda = 0^\circ$ ), is shown in Table 10.2.

It is interesting to note that the total time for the landing process of the model (including rebounds following initial contact with the ground) depends to a large degree on the magnitude and direction of the landing velocity and equals from 0.55 to 0.75 s, where the upper limit applies to the four-legged landing gear. The maximum acceleration at the model's center of mass is achieved approximately 0.1 s (recalculated for the actual space landing vehicle, this value is 0.6 s) after the first contact with the ground. Of course, the indicated time spans apply to the landing of the dynamically

FOR OFFICIAL USE ONLY

FOR OFFICIAL USE ONLY

Table 10.2

Испытание № (1)	Схема и условия испытания (2)	Показания датчиков ускорений ДУ и перемещений ДП (3)	Примечание (4)
30	 <p><math>V_r = 2,7 \text{ м/с}</math> (5)  <math>V_v = 2 \text{ м/с}</math> (6)                  Модель устойчива (7)</p>	<p>В ц. м. (9)  <math>G_r = 6 \text{ г}</math> (10)  <math>G_v = 4,5 \text{ г}</math> (11)                  На опорах  <math>G_{II} = 7 \text{ г}</math>  <math>G_{III} = 4 \text{ г}</math>  <math>G_{IV} = 3,6 \text{ г}</math> (12)  <math>\delta_{II} = 85 \text{ мм}</math>  <math>\delta_{III} = 45 \text{ мм}</math>  <math>\delta_{IV} = 45 \text{ мм}</math></p>	<p>В опоры заложены соты энергоемкостью в ~2 раза большей, чем при последующих испытаниях. ДУIII и ДУIV показывают возникновение колебаний вследствие сухого трения</p> <p>(13)</p>
31	 <p><math>V_r = 3,3 \text{ м/с}</math> (5)  <math>V_v = 2,0 \text{ м/с}</math> (6)  <math>\theta = -5^\circ</math>                  Модель неустойчива (8)</p>	<p>В ц. м. (9)  <math>G_r = 11 \text{ г}</math> (10)  <math>G_v = 9 \text{ г}</math> (11)                  На опорах  <math>G_{II} = 1,75 \text{ г}</math>  <math>G_{III} = 5,5 \text{ г}</math>  <math>G_{IV} = 5,5 \text{ г}</math> (12)  <math>\delta_{II} = 45 \text{ мм}</math>  <math>\delta_{III} = 77 \text{ мм}</math>  <math>\delta_{IV} = 75 \text{ мм}</math></p>	<p>ДПIII показывает характерное поднятие поршня задней опоры</p> <p>(14)</p>
41	 <p><math>V_r = 3,26 \text{ м/с}</math> (5)  <math>V_v = 2,2 \text{ м/с}</math> (6)  <math>\theta = -5^\circ</math>                  Модель устойчива (7)</p>	<p>В ц. м. (9)  <math>G_r = 4,6 \text{ г}</math> (10)  <math>G_v = 4 \text{ г}</math> (11)                  На опорах  <math>G_I = 3,6 \text{ г}</math>  <math>G_{II} = 3,6 \text{ г}</math>  <math>G_{III} = 1,6 \text{ г}</math>  <math>G_{IV} = 1,6 \text{ г}</math> (12)  <math>\delta_I = 75 \text{ мм}</math>  <math>\delta_{II} = 77 \text{ мм}</math>  <math>\delta_{III} = 28 \text{ мм}</math>  <math>\delta_{IV} = -</math></p>	<p>Гальванометры не зафиксировали момент касания опорами грунта вследствие нарушения гальванической связи между отдельными частями модели</p> <p>(15)</p>
42	 <p><math>V_r = 3,26 \text{ м/с}</math> (5)  <math>V_v = 2,0 \text{ м/с}</math> (6)  <math>\theta = -5^\circ</math>                  Модель устойчива (7)</p>	<p>В ц. м. (9)  <math>G_r = 5 \text{ г}</math> (10)  <math>G_v = 4 \text{ г}</math> (11)                  На опорах  <math>G_I = 5 \text{ г}</math>  <math>G_{II} = 3,6 \text{ г}</math>  <math>G_{III} = 1,7 \text{ г}</math>  <math>G_{IV} = 3,6 \text{ г}</math> (12)  <math>\delta_I = 83 \text{ мм}</math>  <math>\delta_{II} = 50 \text{ мм}</math>  <math>\delta_{III} = 40 \text{ мм}</math>  <math>\delta_{IV} = -</math></p>	<p>ДУII — «переворот» сигнала характеристикой датчика</p> <p>(16)</p>

FOR OFFICIAL USE ONLY

## FOR OFFICIAL USE ONLY

## Key:

1. Test number
2. Configuration and test conditions
3. Data from accelerometers and position transducers
4. Comments
5.  $V_{hor}$  (m/s)
6.  $V_{vert}$  (m/s)
7. Model is stable
8. Model is unstable
9. At the center of mass
10. Horizontal acceleration (g's)
11. Vertical acceleration (g's)
12. On the landing-gear legs: Accelerations, G, in g's, and compressions,  $\delta$ , in mm
13. The landing-gear legs are equipped with honeycombs having an energy capacity about twice as large as those in subsequent tests. Accelerometers III and IV show oscillations due to Coulomb friction
14. Position transducer II indicates the characteristic lifting of the piston in the trailing landing-gear leg
15. The galvanometers did not register the instant of ground contact by the landing-gear legs due to interruptions in the galvanometer leads between different parts of the model
16. The accelerometer II signal was "inverted" due to the transducer characteristic

---

similar variant B model on a surface with a slope of  $-5^\circ$ , but the order of magnitude of these time spans remains the same even when the slope of the surface is changed by  $\pm 15^\circ$ .

The results of the tests have shown that the largest load factors occur for landing-gear legs that lead when landing downward along the slope; they are two- to threefold greater than those for trailing legs. For the case of landing with a single leg leading (configurations 1-2-1 and 2-1), this difference becomes even greater. However, let us note that for a four-legged landing gear, this effect is less pronounced than in a three-legged landing gear, due to the larger number of legs. In other words, for a four-legged vehicle, the choice of landing configurations is less critical. For a vehicle with a three-legged landing gear, and a 2-1 landing configuration, the condition  $\lambda = 0^\circ$  (one leg leading downward along the slope), which otherwise has advantages from the point of view of stability in terms of toppling when compared with a 1-2 configuration, is more dangerous in terms of the larger load factors on the leading leg.

Results of landing tests downward along the slope confirm the large compression of the energy absorbers in the leading landing-gear legs. During such compression, the landing-gear legs reached the maximum values of deformation

FOR OFFICIAL USE ONLY

possible with the model, namely, 0.083 to 0.085 m (which is equivalent to about 0.5 m for the full-scale lunar vehicle). This represents a compression of the honeycomb blocks of more than 70 percent.

Based on the material presented, in conclusion we will give one of the possible development scenarios (All-Union State Standard 2.103-68) for a landing gear to be used with a future space vehicle for soft landing on a planet, its satellites, asteroids, or other celestial bodies.

1. During the phase for developing the technical proposal (All-Union State Standard 2.118-73):
  - a. Collection of data on the profile and properties of the ground at the proposed landing site;
  - b. Preliminary choice of design and dimensions for the landing gear as a function of mission, layout, and mass of the space landing vehicle and control system options;
  - c. Performance of theoretical studies on the vehicle landing dynamics for the selected configurations of its landing gear (for limiting values of landing conditions).
2. During the phase of developing the preliminary design (All-Union State Standard 2.119-73):
  - a. Collection of more-detailed information on the surface layer of the celestial body using hard landing and fly-by sounders, artificial satellites of the planet, and so forth;
  - b. Performance of a detailed theoretical analysis of the landing dynamics for the most likely landing-gear design for the space landing vehicle;
  - c. Design, manufacture, and test of dynamically similar models of the space landing vehicle with the most likely landing-gear design.
3. During the phase of engineering development (All-Union State Standard 2.120-73):
  - a. Design, manufacture, and dynamic testing of full-scale test-stand mockups of space landing vehicles (both simplified and maneuvering);
  - b. Structural testing of the full-scale landing gear at design load factors associated with landing;
  - c. Design, manufacture, and development of full-scale flying mockups of the space landing vehicle; part of the development of a piloted vehicle consists of training the cosmonauts to perform soft landings in the flying mockup and in the definition of the program of activities to be performed on the planet (crew training in a mockup is also possible in a test stand with sufficient room for maneuvering);
  - d. Final terrestrial work to assess the effectiveness of the vehicle's landing gear during emergency (unstable) landing situations by using full-scale test-stand mockups.

The landing gear, having successfully completed the cycle of terrestrial development, is now ready for the ultimate test, flight testing as part of the space vehicle.

FOR OFFICIAL USE ONLY

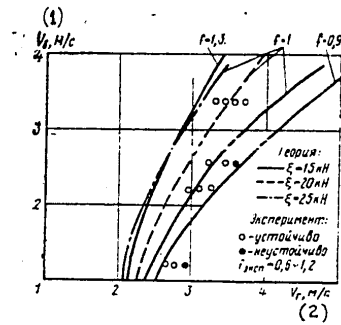


Figure 10.1. Stability Zones During Landing of the Variant B Space Landing Vehicle (downward along the slope,  $\lambda = 0^\circ$ ;  $\theta = -5^\circ$ ;  $N = 4$ ; configuration 2-2)

Key:

1.  $V_{vert}$  (m/s)
2.  $V_{hor}$  (m/s)

Theoretical results:

- for  $\xi = 15$  kN
- - - for  $\xi = 20$  kN
- . - for  $\xi = 25$  kN

Experimental results:

- stable
- unstable
- $f_{experim.} = 0.6$  to  $1.2$

FOR OFFICIAL USE ONLY



FOR OFFICIAL USE ONLY

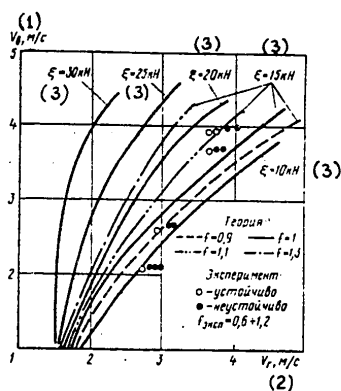


Figure 10.2. Stability Zones During Landing of the Variant B Space Landing Vehicle (downward along the slope,  $\lambda = 0^\circ$ ;  $\theta = -10^\circ$ ;  $N = 4$ ; configuration 2-2)

Key:

1.  $V_{\text{vert}}$  (m/s)
2.  $V_{\text{hor}}$  (m/s)
3.  $\xi$  (kN)

Theoretical results:

- for  $f = 0.9$
- for  $f = 1.0$
- for  $f = 1.1$
- for  $f = 1.3$

Experimental results:

- stable
- unstable
- $f_{\text{experim.}} = 0.6 \text{ to } 1.2$

FOR OFFICIAL USE ONLY

FOR OFFICIAL USE ONLY

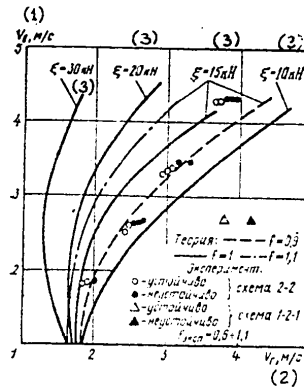


Figure 10.3. Stability Zones During Landing of the Variant B Space Landing Vehicle (downward along the slope,  $\lambda = 0^\circ$ ;  $\theta = -15^\circ$ ;  $N = 4$ ; configuration 202)

Key:

1.  $V_{vert}$  (m/s)
2.  $V_{hor}$  (m/s)
3.  $\xi$  (kN)

Theoretical results:

- for  $f = 0.9$
- for  $f = 1.0$
- .-.- for  $f = 1.1$

Experimental results:

- stable for the 2-2 configuration
  - unstable for the 2-2 configuration
  - △ stable for the 1-2-1 configuration
  - ▲ unstable for the 1-2-1 configuration
- $f_{experim.} = 0.6$  to  $1.1$

FOR OFFICIAL USE ONLY

FOR OFFICIAL USE ONLY

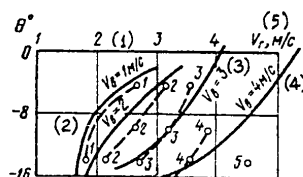


Figure 10.4. Zones of Landing Stability for the Variant B Space Landing Vehicle (plotted in the coordinates  $V_{hor}$  and  $\theta$ , with the numerals 1, 2, 3, 4, and 5 next to the data points indicating [vertical] velocities of 1, 2, 3, 4, and 5 m/s, respectively.  $\xi = 1.5 \times 10^4$  N;  $f = 1.0$ ;  $N = 4$ ; configuration 2-2)

Key:

1.  $V_{vert} = 1$  m/s
  2.  $V_{vert} = 2$  m/s
  3.  $V_{vert} = 3$  m/s
  4.  $V_{vert} = 4$  m/s
  5.  $V_{hor}$  (m/s)
- Theoretical results  
 - - - Experimental results  
 $f_{experim.} = 0.6$  to  $1.2$

FOR OFFICIAL USE ONLY

FOR OFFICIAL USE ONLY

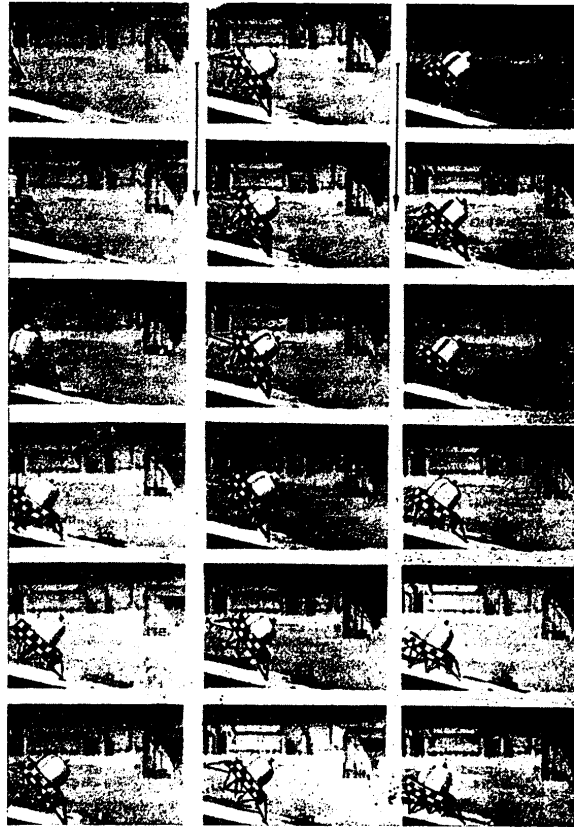


Figure 10.5. Stable Landing of the DPM-B Model (downward along the slope;  $\theta = 15^\circ$ ; velocities  $V_{\text{vert}} = 2.7$  m/s and  $V_{\text{hor}} = 3.7$  m/s; configuration 1-2-1; rigid ground; frame interval  $\sim 0.05$  s)

FOR OFFICIAL USE ONLY

FOR OFFICIAL USE ONLY

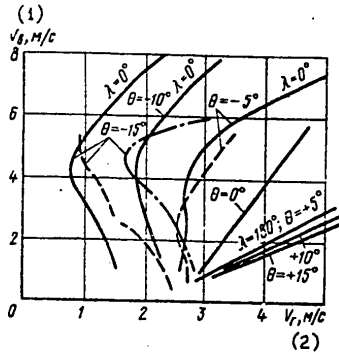


Figure 10.6. Stability Zones During Landing of the Variant A Space Landing Vehicle ( $\xi = 3 \times 10^4$  N;  $f = 0.8$ ;  $N = 4$ )

Key:

- 1.  $V_{\text{vert}}$  (m/s)
- 2.  $V_{\text{hor}}$  (m/s)

Configuration 2-2:

- Theoretical results
- - - Experimental results

Configuration 1-2-1:

- · - · Theoretical results

FOR OFFICIAL USE ONLY

FOR OFFICIAL USE ONLY

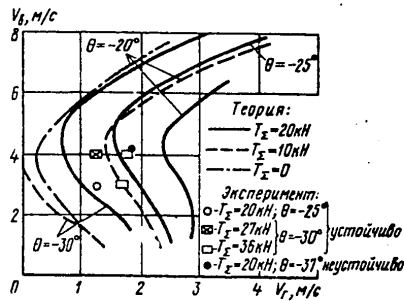


Figure 10.7. Stability Zones During Landing of the Variant A Space Landing Vehicle (using "clamping" engines;  $\xi = 3 \times 10^4$  N;  $\lambda = 0^\circ$ ;  $N = 4$ ;  $f = 0.8$ ; configuration 2-2)

Key:

1.  $V_{\text{vert}}$  (m/s)
2.  $V_{\text{hor}}$  (m/s)

Theoretical results:

- for  $T_\Sigma = 20$  kN
- - - for  $T_\Sigma = 10$  kN
- · - · for  $T_\Sigma = 0$

Experimental results:

Stable landings:

- for  $T_\Sigma = 20$  kN and  $\theta = -25^\circ$
- ◻ for  $T_\Sigma = 27$  kN and  $\theta = -30^\circ$
- ◻ for  $T_\Sigma = 36$  kN and  $\theta = -30^\circ$

Unstable landing

- for  $T_\Sigma = 20$  kN and  $\theta = -37^\circ$

FOR OFFICIAL USE ONLY

FOR OFFICIAL USE ONLY

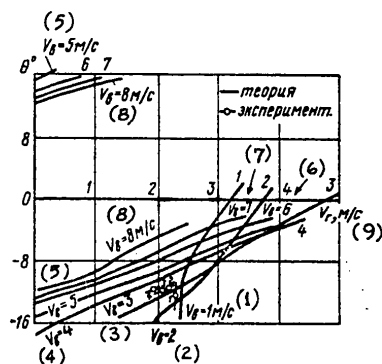


Figure 10.8. Zones of Landing Stability for the Variant C Space Landing Vehicle (plotted in the coordinates  $V_{hor}$  and  $\theta$ ; for an explanation of labeling of points see Figure 10.4;  $\xi = 42.5 \times 10^4$  N;  $N = 4$ ; configuration 2-2)

Key:

- 1.  $V_{vert} = 1$  m/s
- 2.  $V_{vert} = 2$  m/s
- 3.  $V_{vert} = 3$  m/s
- 4.  $V_{vert} = 4$  m/s
- 5.  $V_{vert} = 5$  m/s
- 6.  $V_{vert} = 6$  m/s
- 7.  $V_{vert} = 7$  m/s
- 8.  $V_{vert} = 8$  m/s
- 9.  $V_{hor}$  (m/s)
- Theoretical results
- Experimental results

FOR OFFICIAL USE ONLY

FOR OFFICIAL USE ONLY

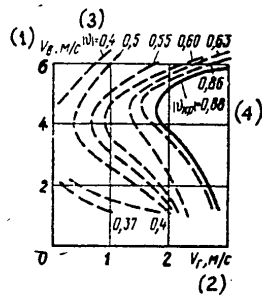


Figure 10.9. Lines of Equal Landing Stability for the Variant A Space Landing Vehicle ( $\lambda = 0^\circ$ ;  $\xi = 3 \times 10^4$  N;  $\theta = -15^\circ$ ;  $f = 0.8$ ;  $N = 4$ ; configuration 1-2-1)

Key:

1.  $V_{vert}$  (m/s)
2.  $V_{hor}$  (m/s)
3.  $\theta$
4.  $\theta_{critical}$

FOR OFFICIAL USE ONLY



APPROVED FOR RELEASE: 2007/02/08: CIA-RDP82-00850R000300040031-0

LANDING OF [REDACTED] \_ES ON PL [REDACTED]  
BY

17 OCTOBER 1980

V. I. BAZHENOV AND M. I. OSIN

3 OF 3

FOR OFFICIAL USE ONLY

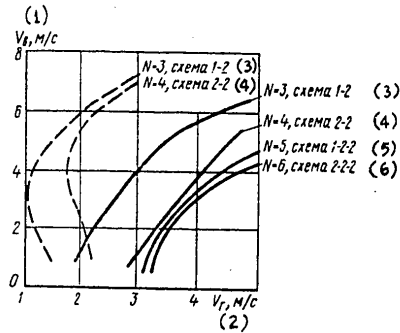


Figure 10.10. Dependence of the Size of a Space Landing Vehicle's (Variant A) Stability Zone on the Number of Landing-Gear Legs ( $\xi = 3 \times 10^4$  N;  $f = 0.8$ ;  $\lambda = 0^\circ$ )

Key:

- $\theta = 0^\circ$
- - -  $\theta = -10^\circ$
- 1.  $V_{\text{vert}}$  (m/s)
- 2.  $V_{\text{hor}}$  (m/s)
- 3.  $N = 3$ , configuration 1-2
- 4.  $N = 4$ , configuration 2-2
- 5.  $N = 5$ , configuration 1-2-2
- 6.  $N = 6$ , configuration 2-2-2

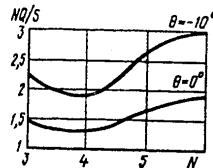


Figure 10.11. Optimizing of a Space Landing Vehicle's Landing Gear in Terms of Mass (Variant A;  $\xi = 3 \times 10^4$  N;  $f = 0.8$ ;  $\lambda = 0^\circ$ )

FOR OFFICIAL USE ONLY

FOR OFFICIAL USE ONLY

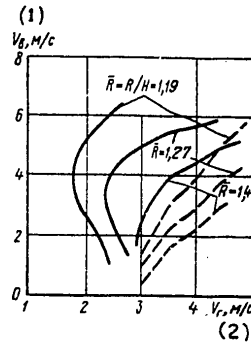


Figure 10.12. Dependence of the Size of a Space Landing Vehicle's (Variant A) Stability Zone on the Relative Magnitude of the Landing-Gear Radius ( $\lambda = 0^\circ$ ;  $\xi = 3 \times 10^4$  N;  $N = 4$ ;  $f = 0.8$ ; configuration 2-2)

Key:

- 1.  $V_{vert}$  (m/s)
- 2.  $V_{hor}$  (m/s)
- $\theta = -10^\circ$
- - -  $\theta = 0^\circ$

FOR OFFICIAL USE ONLY

FOR OFFICIAL USE ONLY

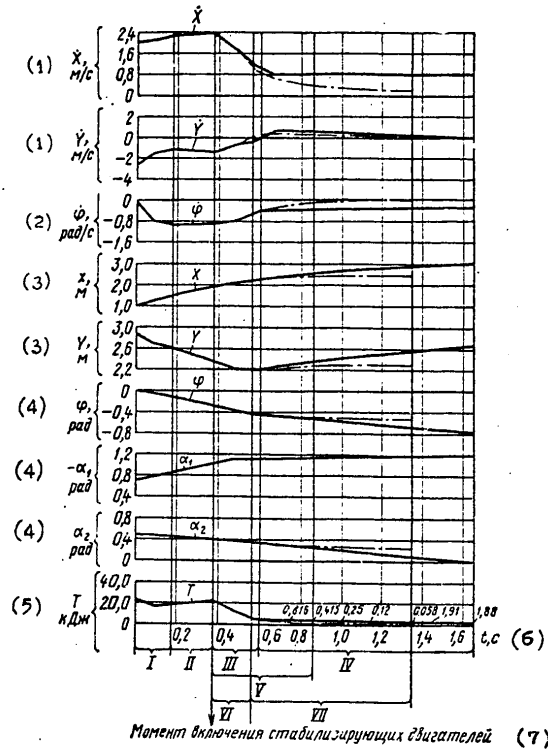


Figure 10.13. Behavior of Dynamics Parameters During an Unstable Landing of a Variant A Space Landing Vehicle (downward along the slope with  $\theta = 20^\circ$ )

Phases of the Landing Process:

- I. Crushing of landing-gear leg no. 1
- II. Rotation with respect to landing-gear leg no. 1
- III. Crushing of landing-gear leg no. 2
- IV. Rotation with respect to landing-gear leg no. 2
- V. Operating period of stabilizing engines
- VI. Crushing of landing-gear leg no. 2 when the impulse from the stabilizing engines is accounted for

FOR OFFICIAL USE ONLY

FOR OFFICIAL USE ONLY

VII. Rotation with respect to landing-gear leg no. 2 when the impulse from the stabilizing engines is accounted for

Key:

1.  $\dot{X}$  and  $\dot{Y}$  (m/s)
2.  $\dot{\phi}$  (radians/s)
3. X and Y (m)
4.  $\phi$ ,  $-\alpha_1$ , and  $\alpha_2$  (radians)
5. T (kJ)
6. t (s)
7. Instant of turning on stabilizing engines

FOR OFFICIAL USE ONLY

FOR OFFICIAL USE ONLY

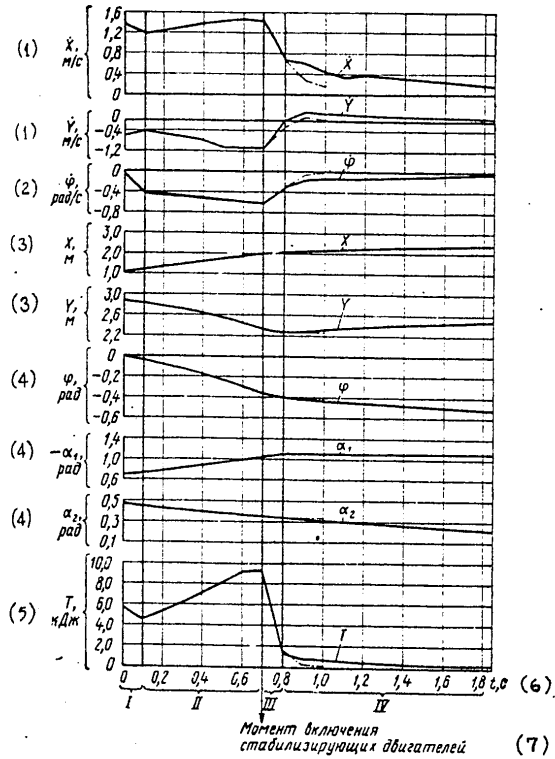


Figure 10.14. Behavior of Dynamics Parameters During a Stable Landing of a Variant A Space Landing Vehicle (downward along the slope with  $\theta = 20^\circ$ )

Phases of the Landing Process:

- I. Crushing of landing-gear leg no. 1
- II. Rotation with respect to landing-gear leg no. 1
- III. Crushing of landing-gear leg no. 2
- IV. Rotation with respect to landing-gear leg no. 2

FOR OFFICIAL USE ONLY

FOR OFFICIAL USE ONLY

Key:

1.  $\dot{X}$  and  $\dot{Y}$  (m/s)
2.  $\dot{\phi}$  (radians/s)
3. X and Y (m)
4.  $\phi$ ,  $-\alpha_1$ , and  $\alpha_2$  (radians)
5. T (kJ)
6. t (s)
7. Instant of turning on stabilizing engines

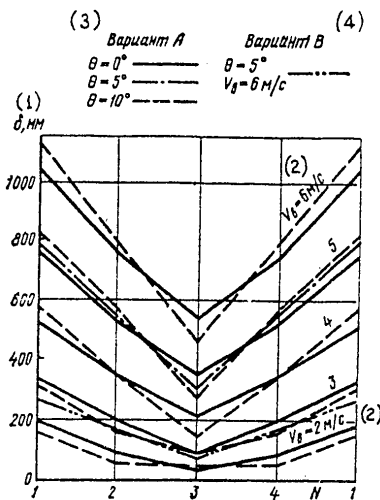


Figure 10.15. Typical Deformations of Landing-gear Legs for the Variants A and C Space Landing Vehicles (landing upward along the slope,  $\lambda = 180^\circ$ ;  $V_{\text{hor}} = 1 \text{ m/s}$ ; configuration 1-2-1)

Key:

1.  $\delta$  (mm)
2.  $V_{\text{vert}}$  (m/s)
3. Variant A
4. Variant C

FOR OFFICIAL USE ONLY

FOR OFFICIAL USE ONLY

BIBLIOGRAPHY

1. Avduyevskiy, V. S.; Anfimov, N. A.; Antonov, B. M.; and others. "Osnovy teorii poleta kosmicheskikh apparatov" [Foundations of the Theory of Spacecraft Flight], edited by G. S. Narimanov and M. K. Tikhonravov, Moscow, Mashinostroyeniye, 1972.
2. Avduyevskiy, V. S.; Marov, M. Ya.; Rozhdestvenskiy, M. K.; and others. "The Venera-9 and Venera-10 Automated Stations: The Operation of the Descent Module and the Measurement of Atmospheric Parameters," KOSMICHESKIYE ISSLEDOVANIYA, Vol 14, No 5, pp 655-666, 1976.
3. Anon. "Avtomaticheskiye planetnyye stantsii" [Automated Planetary Stations], edited by Yu. K. Khodarev, Moscow, Nauka, 1973.
4. Anon. "Algorithms and Programs for the Solution of Engineering Optimization Problems on Digital Computers, Scientific-Engineering Report," Moscow, Gosfond for Algorithms and Programs, 1970.
5. Alekseyev, K. B.; Bebenin, G. G.; and Yaroshevskiy, V. A. "Manevrirovaniye kosmicheskikh apparatov" [Maneuvering of Spacecraft], Moscow, Mashinostroyeniye, 1970.
6. Andreyevskiy, V. V. "Dinamika spuska kosmicheskikh apparatov na zemlyu" [Dynamics of Spacecraft Descent to Earth], Moscow, Mashinostroyeniye, 1970.
7. Arkhangel'skiy, B. A. "Plasticheskiye massy" [Plastics--A Reference], Leningrad, Sudpromgiz, 1961.
8. Bazhenov, V. I.; Koval', A. D.; and Straut, E. K. "From Model to Lunokhod," AVIATSIYA I KOSMONAVTIKA, No 8, pp 42-46, 1966.
9. Bazhenov, V. "Lunokhod Ground School," VESTNIK APN PO SOVETSKOMU SOYUZU, No 274, pp 1-5, 23 Nov 1970.
10. Bazhenov, V., and Sakharov, Yu. "Earth Rehearsal for Venera," Newspaper LENINSKOYE ZNAMYA, No 277, 4 p, 26 Nov 1975.
11. Bazhenov, V. I.; Goncharov, A. I.; and Osin, M. I. "Nekotoryye problemy vozvrashcheniya cheloveka iz kosmosa i ikh razvitiye ot trudov K. E. Tsiolkovskogo do nashykh dney" [Several Problems in Returning Man from Space and Their Development, Starting with the Works of K. E. Tsiolkovskiy to the Present], Works of the Tenth Tsiolkovskiy Readings, Moscow, IYET [Institute of History of Natural Sciences and Technology] of the USSR Academy of Sciences, pp 28-40, 1977.

FOR OFFICIAL USE ONLY



FOR OFFICIAL USE ONLY

12. Barer, A. S.; Sorokina, Ye. I.; and Murakhovskiy, K. I. "On the Question of Man's Tolerance for Acceleration After a Prolonged Stay Under Conditions Simulating Weightlessness," KOSMICHESKAYA BIOLOGIYA I MEDITSINA, Vol 6, No 3, pp 49-53, 1972.
13. Bilik, Sh. M. "Pary treniya metall-plastmassa v mashinakh i mekhanismakh" [Friction Between Metal and Plastic in Machines and Mechanisms], Moscow, Mashinostroyeniye, 1966.
14. Blandov, P. I. "Amortizatsiya i upravleniye vsletno-posadochnykh ustroystv samoletov" [Shock Absorption and Control of Aircraft Landing Gears], MAI, 1962.
15. Bogdanov, V. A.; Gurfinkel', V. S.; and Panfilov, V. Ye. "Test Stand for Modeling Reduced Gravity at Surface Conditions," Invention certificate no 215404, IZOBRETATEL' I RATSIONALIZATOR, No 12, p 12, 1970.
16. Borisov, M. "Na kosmicheskoy verfi" [At the Space Shipyard], Moscow, Mashinostroyeniye, 1976.
17. Kemurdzhian, A. L.; Gromov, V. V.; Cherkasov, I. I.; and others. "Avtomaticheskiye stantsii dlya izucheniya poverkhnostnogo pokrova lunny" [Automated Stations for the Study of the Surface Layer of the Moon], Moscow, Mashinostroyeniye, 1976.
18. Klimin, A. V. "Atmospheric Braking for Manned Spacecraft at the Conclusion of Interplanetary Flight," KOSMICHESKIYE ISSLEDOVANIYA, Vol 11, No 1, pp 31-37, 1973.
19. Krotikov, V. D., and Troitskiy, V. S. "Radio Emission and Nature of the Moon," USPEKHI FIZICHESKIKH NAUK, Vol 81, pp 51-56, 1963.
20. Lokh, U. Kh. T. "Dinamika i termodinamika spuska v atmosferakh planet" [Dynamics and Thermodynamics of Descent Through Planetary Atmospheres], Moscow, Mir, 1966.
21. Anon. "Lunnyy grunt iz morya izobiliya" [Lunar Soil from the Sea of Fertility], edited by A. P. Vinogradov, Moscow, Nauka, 1974.
22. Mak-Farland, R. K. "Hexagonal Honeycomb Structures Under the Action of Supercritical Axial Loads," RAKETNAYA TEKHNIKA I KOSMONAVTIKA, No 6, pp 125-131, 1963.
23. Mishin, V. P., and Osin, M. I. "Vvedeniye v mashinnoye proyektirovaniye letatel'nykh apparatov" [Introduction to Machine Design of Flight Vehicles], Moscow, Mashinostroyeniye, 1978.
24. Moroz, V. I. "Fizika planet" [Physics of Planets], Moscow, Nauka, 1967.

FOR OFFICIAL USE ONLY

25. Moroz, V. I. "Structure of the Martian Soil Based on Optical and Infrared Observations," KOSMICHESKIYE ISSLEDOVANIYA, Vol 14, Issue 1, pp 85-96, 1976.
26. Naumov, V. N.; Rozhdestvenskiy, Yu. L.; and Kharitonova, V. Ye. "Production of Artificial Soil," Transactions of MVTU [N. E. Bauman Higher Technical School in Moscow], No 231, Issue 1, Moscow, MVTU, pp 32-37, 1976.
27. Neyland, V. Ya., and Snigirev, Yu. I. "Thermal Regime of Flight Vehicles at Entry Velocities into the Earth's Atmosphere of Approximately 15 km/s," KOSMICHESKIYE ISSLEDOVANIYA, Vol 5, Issue 2, pp 205-211, 1967.
28. Pellinets, V. S. "Ob otsenke pogreshnostey pri izmerenii parametrov vibratsiy" [On Estimating Errors in the Measurement of Vibration Parameters], Leningrad, LDNTP [Leningrad House of Scientific and Technical Propaganda], 1967.
29. Anon. "Pionery raketnoy tekhniki" [Pioneers of Rocket Technology], selected works, Moscow, Nauka, 1964.
30. Sveshnikov, A. A. "Osnovy teorii oshibok" [Foundation of the Theory of Errors], Leningrad, LGU [A. A. Zhdanov State University in Leningrad], 1972.
31. Sedov, L. I. "Metody podobiya i razmernosti v mekhanike" [Methods of Similarity and Dimensional Analysis in Mechanics], Moscow, Nauka, 1972.
32. Strelkov, S. P. "Vvedeniye v teoriyu kolebaniy" [Introduction to the Theory of Oscillations], Moscow, Nauka, 1964.
33. Teyfel', V. G. "Atmosfera planety yupiter" [Atmosphere of the Planet Jupiter], Moscow, Nauka, 1969.
34. Timoshenko, S. P. "Kolebaniya v inzhenerenom dele" [Oscillations in Engineering], Moscow, Nauka, 1967.
35. Trofimenkov, Yu. G., and Vorobkov, L. N. "Polevyye metody issledovaniya stroitel'nykh svoystv gruntov" [Field Methods of Studying Structural Properties of Soils], Moscow, Stroyizdat, 1974.
36. Anon. "Angular Accelerometer, Insensitive to Linear Accelerations," U. S. Patent No 316498, kl, 73-516. [sic]
37. Khint, I. A. "Osnovy proizvodstva silikal'tsitnykh izdeliy" [Foundations of Manufacturing Silicalcite Products], Moscow, Stroyizdat, 1962.

FOR OFFICIAL USE ONLY

FOR OFFICIAL USE ONLY

38. Tsiolkovskiy, K. E. "Za atmosferu" [Beyond the Atmosphere], VOKRUG SVETA, No 1, pp 10-14, 1934.
39. Tsytoich, N. A. "Mekhanika grunta" [Soil Mechanics], Moscow, Gosstroyizdat, 1963.
40. Shkadov, L. M.; Bukhanova, R. S.; Illarionov, V. F.; and others. "Mekhanika optimal'nogo prostranstvennogo dvizheniya letatel'nykh apparatov v atmosfere" [Mechanics of Optimal Three-dimensional Motion of Flight Vehicles in the Atmosphere], Moscow, Mashinostroyeniye, 1972.
41. Shternfel'd, A. A. "Vvedeniye v kosmonavtiku" [Introduction to Space Flight], Moscow, Nauka, 1974.
42. Shchegolov, A. V. "Konstruirovaniye protyazhek" [Designing of Broaches], Moscow, Mashgiz, 1960.
43. El'yasberg, P. Ye. "Vvedeniye v teoriyu poleta iskusstvennykh sputnikov zemli" [Introduction to the Theory of Flight of Artificial Satellites of the Earth], Moscow, Nauka, 1965.
44. Admire, J., and Mackey, A. "Dynamic Analysis of a Multilegged Lunar Landing Vehicle To Determine Structural Loads During Touchdown," NASA TN D-2582, 1965.
45. Bartolomew, C. S. "Risk Appraisal for Program Planning and Management," ANNALS OF RELIABILITY AND MAINTAINABILITY, Vol 6, 1967.
46. Bellman, D. R., Matranga, G. J. "Design and Operational Characteristics of a Lunar Landing Research Vehicle (LLRV)," Edwards Flight Research Center, NASA TN D-5023, 1965.
47. Black, R. J. "Quadrupedal Landing Gear System for Spacecraft," J. OF SPACECRAFT AND ROC., Vol 1, No 2, p 196, 1964.
48. Blanchard, Ulysse, J. "Model Investigation of Technique for Conducting Full-scale Landing-Impact Tests at Simulated Lunar Gravity," NASA TN D-2586, 1965.
49. Blanchard, Ulysse J., "Evaluation of a Full-scale Lunar-Gravity Simulator by Comparison of Landing-Impact Tests of a Full-scale and a 1/6-scale Model," NASA TN D-4474, 1968.
50. Blanchard, U. J., and Stubbs, S. M. "Martian Gravity Simulator for Full-scale Viking Landing Tests." Space Simulation, NASA SP 298, pp 629-646, 1972.
51. Congelon, W. M. "Investigation of Reflecting Heat Shield Materials for Outer Planet Missions," AIAA Paper, N 74-702.

199

FOR OFFICIAL USE ONLY

FOR OFFICIAL USE ONLY

52. Douglass, D. R., and Austin, C. R. "Mission Risk Appraisal," ANNALS OF RELIABILITY AND MAINTAINABILITY, Vol 6, 1967.
53. Garden, H. D.; Herr, R. W.; and Brooks, G. W. "Technique for the Simulation of Lunar and Planetary Gravitational Fields Including Pilot Model Studies," NASA TN D-2415, 1964.
54. Herr, R. W., and Wayne, L. H. "Dynamic Model Investigation of Touchdown Stability of Lunar Landing Vehicles," NASA TN D-4215, 1967.
55. Hylderman, R.; Mueller, W.; and Mantus, M. "Landing Dynamics of the Lunar Excursion Module," J. OF SPACECRAFT AND ROCKETS, Vol 3, No 10, pp 1484-1489, 1966.
56. "Langley's Lunar Landings. Lunar Landing Research Facility (LLRF)," MISSILES AND ROCKETS, Vol 17, No 2, p 8, 1965; FLIGHT INTERNATIONAL, Vol 88, No 2940, p 111, 1965.
57. Leonard, H. W.; Walton, W. C.; and Herr, R. W. "Studies of Touchdown Stability for Lunar Landing Vehicles," J. SPACECRAFT AND ROC., Vol 1, No 5, p 552, 1964.
58. Mayo E. E., and others. "Hypersonic Reentry Vehicle," U. S. Patent 3301507.
59. McGehee, John R., and Stubbs, S. M. "Experimental Validation of a Landing Dynamics Computer Program for Legged Spacecraft Landers," NASA TN D-703, 1973.
60. Miller, R. E.; Hansen, S. D.; Kawaguchi, A. S.; Redhed, D. D.; and Southall, U. W. "Cost Effectiveness of Integrated Analysis (Design Systems/IPAD/)," AIAA Paper N 74-960.
61. Moss, I. N.; Anderson, E. S.; and Bold, C. W. "Viscous Shock Layer Solutions for Jovian Entry," AIAA Paper N 75-671.
62. Nicolet, W. E.; Morse, H. L.; Vojvodich, N. S. "Outer Planet Probe Entry Thermal Protection, Part 1: Aerothermodynamic Environment," AIAA Paper N 74-700.
63. Nicolet, W. E.; and Mizines, S. A. "Outer Planet Probe Entry Thermal Protection, Part 2: Heat Shielding Requirements," AIAA Paper N 74-701.
64. O'Bryan, T. C.; and Hewes, D. W. "Operational Features of the Langley Lunar Landing Research Facility," NASA TN D-3828, 1967.
65. Rau, T. R.; and Decker, J. P. "Optimal Design Integration System for Synthesis of Aerospace Vehicles," AIAA Paper N 74-72.

FOR OFFICIAL USE ONLY

66. Schuring, D. "Scale Model Testing of Land Vehicles in a Simulated Low-gravity Field," SAE-660148, 1966.
67. Smith, A. M. "Risk Assessment in Complex Unattended Aerospace Systems," ANNALS OF RELIABILITY AND MAINTAINABILITY, Vol 6, 1967.
68. Stubbs, S. M. "Investigation of Technique for Conducting Landing Impact Tests at Simulated Planetary Gravity," NASA TN D-6459, 1961.
69. Stubbs, S. M. "Experimental Investigation of the Landing Dynamics of Three-legged Spacecraft Models," NASA TN D-7664, 1974.
70. Troitsky, V. S. "A Four-meter Thick Porous Material Layer Covers the Moon," SPACE WORLD, Vol D-6 42, pp 44-45, June, 1967.
71. Warner, R. W.; Sorenson, R. M.; and Kaskey, A. J. "An Investigation of a Deforming Energy Absorption System for Space Vehicle Landings," NASA TN D-3061, 1966.

COPYRIGHT: Izdatel'stvo Mashinostroyeniye, Moscow, 1978

6948  
CSO: 8144/0683

END

201

FOR OFFICIAL USE ONLY